A Multi-Frequency Induction Heating System for a Thermally Triggered Gel Polymer Dynamic Vibration Absorber

by

John Israel Rodriguez

S.B. in E.E., Massachusetts Institute of Technology (1997)
M.Eng. in E.E., Massachusetts Institute of Technology (1999)

Submitted to the Department of Electrical Engineering and Computer Science
in partial fulfillment of the requirements for the degree of

Doctor of Philosophy in Electrical Engineering

at the

Massachusetts Institute of Technology

September 2003

Author _____
Department of Electrical Engineering and Computer Science
July 3, 2003

Certified by _____
Steven B. Leeb
Associate Professor
Thesis Supervisor

Accepted by _____
Arthur C. Smith
Chairman, Department Committee on Graduate Students

A Multi-Frequency Induction Heating System for a Thermally Triggered Gel Polymer Dynamic Vibration Absorber

by
John Israel Rodriguez

Submitted to the Department of Electrical Engineering and Computer Science
on July 3, 2003, in partial fulfillment of the
requirements for the degree of
Doctor of Philosophy in Electrical Engineering

Abstract

Since its invention in the early part of the twentieth century, the dynamic vibration absorber (DVA) has played an important role in vibration suppression. In its simplest form, a dynamic vibration absorber is a mechanical network consisting of a spring, a mass and sometimes a damping element. These networks have been used to successfully reduce vibrations in buildings, bridges and imbalances in rotating machinery. Because these absorbers are most effective at attenuating disturbance near or at their self-resonant frequency, there is on-going research to develop semi-active DVA's capable of adjusting their natural frequency in real time. A new semi-active DVA is described that can modify its moment of inertia, and therefore its natural frequency, by using a collection of thermo-responsive gel polymers. This thesis develops an induction heating system that is suitable for noncontact heating of these gel polymers. The proposed heating system addresses the more general problem of controllable power delivery to multiple induction targets driven by a single induction coil.

The focus of this work divides neatly between the design of the induction heating targets and the necessary power electronics. Targets that have preferential heating characteristics at particular frequencies are developed and analyzed. These targets include both resonant RLC circuits as well as conductors whose critical dimensions are much smaller than their associated skin depth. Extensive modeling of these targets is carried out and experimental results are presented. The ability to "selectively" heat these induction targets requires a power supply that can generate a sinewave with enough purity to not excessively heat unwanted targets. A 1 kW multilevel inverter topology is presented as an excellent compromise between total harmonic distortion and efficiency for this application. Referred to as the Marx inverter, this circuit can maintain its multilevel nature during real power transfer without the need for an external voltage balancing circuit or complicated control– unlike more traditional multilevel topologies. In addition to the gel vibration damper, portions of this work stand to benefit both medical and industrial venues where a desired temperature profile must be generated in a noncontact manner.

Thesis Supervisor: Steven B. Leeb
Title: Associate Professor

Once there was a well known philosopher and scholar who devoted himself to the study of Zen for many years. On the day that he finally attained enlightenment, he took all of his books out into the yard, and burned them all.

-Zen Stories to Tell Your Neighbors

Acknowledgments

In the summer of '99 I found myself in an all too familiar situation. The pursuit of my M.Eng. degree was coming to a close and I was sure that my life as an academic would end with it. I had no job prospects; I didn't even know what I wanted to do. In short, I was reluctant to leave the safety of the student life I knew and loved. It was around this time that my prayers were answered in the form of a teacher I respected and admired. His name? Steven Leeb. Professor Leeb is the person most directly responsible for my acceptance to the MIT Ph.D. program. Steve believed in me when others wouldn't, an act I have not forgotten, even now as this sojourn comes an end. Over the last four years, he has been an excellent thesis and academic advisor, my mentor and most importantly a friend. I am continually amazed by his insight and creativity. This thesis would never have come to light without his help and guidance.

Special thanks goes to my thesis committee members, Professors Kirtley and Pereault. Both are fantastic engineers and a source of inspiration to me. Their advise and comments have been a tremendous help, particularly during the final writeup.

I gratefully acknowledge that this research would not have been possible without generous support from the MRSEC Program of the National Science Foundation under award number DMR 02-13282, The Grainger Foundation, The Ford Motor Company, The U.S. Navy, and Hewlett-Packard/Agilent.

I am indebted to Ruimin He for his assistance with a number of the experiments carried out in this thesis. His unwavering work ethic is to be lauded. Ruimin is by far the most efficient UROP I've ever had the pleasure of working with.

My warmest thanks to the entire LEES community. You have made my last four years at MIT memorable ones. I will especially miss my Leeb-mates Christopher Laughman and Robert Cox. I wish them the very best with all of their future endeavors. Thanks to Ernst Scholtz and Sandip Roy who both provided me with patient explanations of the mathematical persuasion. My gratitude goes to Tim Neugabauer for his help during the preparation of my defense. I give high praise to those I owe my very sanity to, particularly Joshua Phinney, Tim Denison, and Albert Chow... good engineers, better friends. I would also like to thank, Juan Rivas, David New, Tushar Parlikar and definitely Vivian Mizuno for being, well... Vivian.

Finally, I remain forever grateful to my family for their unending love and support. May God watch over all of you, all the days of your lives.

Contents

List of Figures

List of Tables

Chapter 1

Introduction

THIS work began as an exploration of the potential use of temperature-sensitive gel polymers for designing semi-active vibration dampers. The original goal was to either augment an existing damper technology or to develop a new one that could use these "smart" materials to modify a useful parameter of the damper in real time. This thesis presents a dynamic vibration absorber (DVA) that can increase the available frequency range for damping in direct proportion to the number of heat-sensitive, polymer actuators involved. To make this DVA possible a number of technical hurdles have to be overcome. Perhaps the most prominent of these problems is how to controllably heat or "drive" the desired actuators without ruining the mechanical properties of the damper. Heating schemes that require physical contact between the polymers and the potential drive circuit(s) are undesirable for precisely this reason. Induction heating was selected as an approach that would eliminate the need for physical contact.

The decision to use induction heating led to the consideration of a more general problem: the selective heating of multiple induction seed targets in a magnetic field. A multi-frequency induction heating system, that can selectively heat individual induction targets from an array of targets, has applicability to both the DVA under consideration and other applications. For instance, consider the treatment of deep-seated tumors using inductively heated thermoseeds. By embedding these seeds in a tumor and raising their temperature above $42^{o}C$, the tumor can be destroyed by hyperthermia [41, 42]. Currently, the generation of a desired 3-D temperature profile in a tumor requires a complicated spatial distribution of induction targets. A system that gives control over the individual heating

of targets would allow for greater flexibility in the distribution of thermoseeds, since the temperature profile could be modified after target insertion.

1.1 Thesis Overview

This thesis develops a multi-frequency induction heating system that gives control over the power delivered to individual induction targets. Among other things, this system is useful for driving the gel polymer actuators in a semi-active vibration damper. Three diverse but related topics are covered:

(1) A tunable gel polymer based dynamic vibration absorber.

(2) Frequency selectable induction heating targets.

(3) A multilevel ac power supply for generating multi-frequency sums of sinewaves.

The tunable vibration damper is not the primary focus of this work, but sets the stage by providing an application for the remaining two topics. The damper is pursued as a proof-of-concept. The fundamentals concerning the damper's principle of operation are explained and analyzed in this thesis. Design equations and tools for choosing the appropriate damper dimensions are also covered. There is no attempt to completely integrate the vibration damper and heating circuit, but tests are conducted on the individual subsystems.

The induction heating system is the main focus of this work and subdivides neatly between the design of the induction targets and the necessary power electronics. Targets that have preferential heating characteristics at particular frequencies are developed and analyzed. These targets include both resonant and nonresonant structures. Because multiple targets are excited from a single primary induction coil, extensive modeling is done to not only characterize each target separately but to understand how their location in space effects the heating of the remaining targets. Construction issues relating to target geometry

and materials are also discussed.

To "selectively" heat these induction targets, an amplifier is needed that can generate sinewaves with sufficient purity to avoid stimulating unintended targets. In this regard there are a many possible choices depending on the degree of acceptable distortion. On one extreme is the linear power amplifier, offering perhaps the lowest in total harmonic distortion at the expense of efficiency. Other choices with different trade-offs include switching converters of various kinds. Switching converters have the potential for high efficiency, and many control schemes exist that allow them to trade efficiency for increased spectral purity. A multi-level inverter topology is developed in this thesis that represents an excellent compromise between total harmonic distortion and efficiency for this application.

1.2 Previous Work and Literature Review

There is an extensive body of knowledge concerning the three major topics of this thesis: dynamic vibration absorbers, induction heating targets, and multilevel inverters. The purpose of this section is to familiarize the reader with the basic concepts behind each topic and to provide a brief review of the more relevant work by others in the scientific community. Additional background may also be found in the references.

1.2.1 Dynamic Vibration Absorber

The dynamic vibration absorber[1] (or DVA for short) has played an important role in structural vibration damping since its invention in the early 20th century [7]. In its simplest form a DVA is a mechanical network consisting of a spring, a mass and sometimes a damping element [11]. These networks are attractive because of their relatively low cost and ability to be incorporated into a structure after the design phase. They have been successfully

[1]Sometimes also referred to as a tuned vibration absorber or a tuned mass damper in the literature.

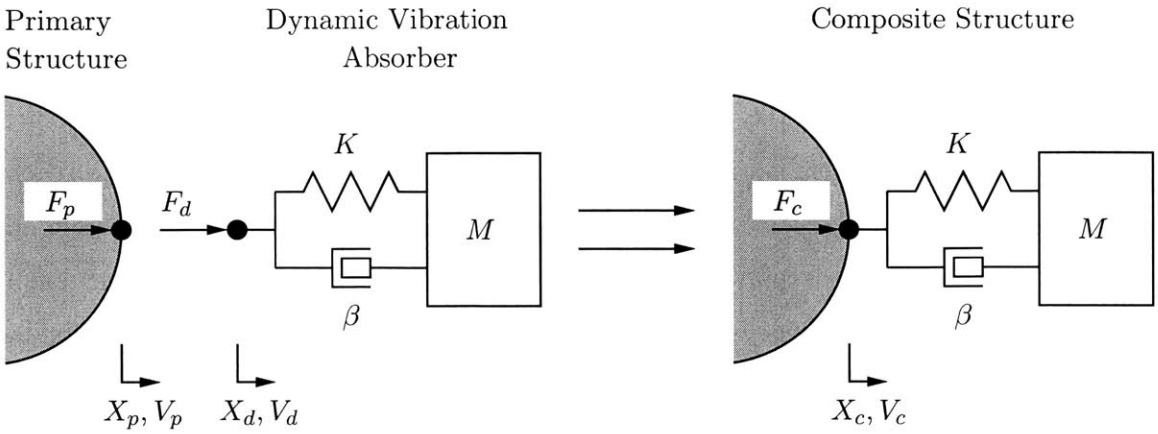

Figure 1.1: Primary structure before and after coupling with a DVA.

used to reduce vibrations in buildings, bridges and imbalances in rotating machinery. A DVA reduces vibrations by forming a composite structure whose net mechanical impedance is greater near a frequency of interest [43]. An increase in mechanical impedance is usually desired at a structure's resonant frequency where the mechanical impedance is low, or at a machine's operating frequency where the magnitude of the vibration is high. For illustration, Figure 1.1 shows a simplified primary structure and a DVA before and after coupling. If the primary structure experiences a sinusoidal force, F_p, the resulting steady-state velocity, V_p is related by

$$V_p = F_p/Z_p, \tag{1.1}$$

where Z_p is the mechanical impedance of the structure. Likewise, the velocity of the DVA can be described by

$$V_d = F_d/Z_d. \tag{1.2}$$

When the primary structure and DVA are coupled together, continuity and equilibrium require that, at the attachment point X_c,

$$V_c = V_p = V_d, \tag{1.3}$$

and

$$F_c = F_p + F_d. \tag{1.4}$$

By using (1.1) through (1.4) we see that the velocity of the composite system is now

$$V_c = F_c/Z_c, \tag{1.5}$$

where Z_c is the driving point impedance at the attachment point and is equal to

$$Z_c = Z_p + Z_d. \tag{1.6}$$

For the simple spring-mass DVA shown, the driving point impedance Z_d, is maximized at its natural frequency. As a result this type of damper loses its effectiveness when the disturbance does not coincide with the DVA's natural frequency. In fact, for some frequencies the DVA can actually exacerbate the disturbance by creating additional resonant modes in the composite system. This presents a problem if the dynamics of the primary system change with time. A common instance of this occurs during a rotating machine's startup as it accelerates to reach its nominal velocity. To overcome these limitations, there is continual, ongoing research to develop semi-active and fully-active DVA's [3, 8, 21, 45, 47, 48, 50].

A semi-active system can be defined as a system that expends energy in order to change or adapt its characteristic behavior. By analogy a fully-active system must always expend energy to do the same. An example of a semi-active DVA is one that can vary the stiffness of its spring element and/or associated viscous damping as illustrated by the left model in Figure 1.2. Adjusting the spring constant allows the natural frequency to change, permitting the DVA to track the frequency of the disturbance. A number of different schemes have been proposed to do this. In reference [48], Ting-Kong investigated using an enclosed volume of air as a variable stiffness source. By varying the volume of air, the damper could move its natural frequency from 51 Hz to 75 Hz with a reduction in vibration of 10 dB. The author also developed a dual, cantilevered mass DVA for damping beam vibrations. Unlike his first DVA, a traditional spring-mass arrangement, the behavior of the dual cantilevered mass system is described by continuum mechanics and is arguably more complex in nature. The natural frequency of this system could be adjusted by extending or retracting the positions of the masses in the cantilever. This DVA achieved a wider working

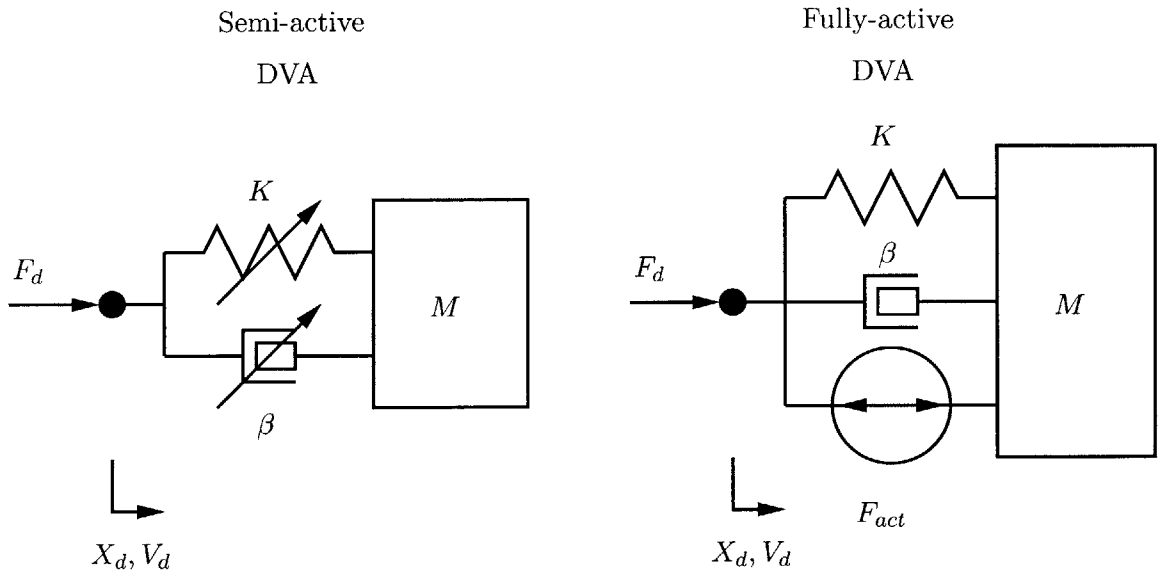

Figure 1.2: Simplified mechanical models of a semi-active and fully-active DVA.

range from 45 Hz to 90 Hz with up to a 30 dB vibration reduction.

Tentor explored another variable stiffness approach using an electromagnet as the absorber mass in [47]. Suspended by two springs, the electromagnet rests in a magnetic field generated by two stationary magnets. The repulsive forces from the stationary magnets contribute to the stiffness of the springs and can be varied by driving the electromagnet. For a +10 A input, the natural frequency of the absorber can be rapidly varied 2-3% and up to 50% by adjusting the air gap between the electromagnet and the stationary magnets. It is interesting to note that this system can behave as both a semi-active damper and a fully-active one. Adjusting the air gap constitutes semi-active control, versus actively driving the electromagnet.

Others have focused on making the damping element in the DVA adaptable. Dimarogonas and Kollias used an electrorheological (ER) fluid to control the viscous damping in a rotary DVA [3]. Applying a constant electric field resulted in a constant shear force, useful for reducing vibrations at critical speeds of a rotor. By actively controlling the electric field using feedback it was possible to obtain a substantial improvement in absorber efficacy over the constant field case. Damping schemes using magnetic dampers have also been ex-

plored. Kobayashi and Aida describe such a device, which they refer to as a Houde damper [21]. The Houde damper dissipates energy through eddy current braking as a conductor moves through a magnetic field. Unlike other DVA's, the Houde damper lacks a stiffness component, relying completely on the damping element and therefore does not need to be tuned like a conventional DVA.

In dampers that have a rotational component, varying the moment of inertia is also a possibility for changing the natural frequency. Takita and Seto developed a "pendulum-type" damper that could adjust its moment of inertia by changing the length of the moment arm using a stepper motor [45]. Other pendulum-type dampers have followed. Fujinami, Yamamoto, and Sone developed a DVA that uses a lever and pendulum mechanism for controlling the displacement of high-rise structures in [8]. Yamura, Ono, and Toyota describe an optimal tuning method for reducing swing in a gondola lift with a pendulum-type DVA [50].

Fully-active dampers have also received a great deal of attention from the vibration damping community. The model to the right in Figure 1.2, illustrates the basic concept behind the fully-active DVA. In addition to the spring-mass network, an actuator is placed in parallel with it. The presence of the actuator allows for active force cancellation while the remaining network provides filtering and acts as a fail-safe, providing a passive damper if the actuator should cease to function. These actuators are often implemented using voice-coils and are sometimes referred to as proof mass actuators or PMA's. By their nature these systems require sensing elements and some form of control to be fully useful. Sometimes the installation of the required sensors is difficult because of lack of available clearance from the structure. To address this issue and reduce the amount of hardware involved, Okada, Matsuda and Hashitani developed an actuator that incorporates the sensor [29].

Because actuators can add energy to the system they are trying to damp, care must be taken to prevent them from becoming unstable. Hence the majority of literature concerning PMA's involves control laws and optimal tunning. Nonami, Nishimura, and Cui

describe a control system using feedback and feedforward control for disturbance cancellation of a multi-degree-of-freedom system. Using a DSP controller, they successfully tested their scheme on a four-degree-of-freedom structure in real time. They observed superior control for harmonic cancellation as well as usefulness for random disturbances. Okada and Okashita applied state feedback to an active system for damping vibrations in elevators and used time-domain identification to evaluate changes in the dynamic properties of the structure in order to tune their controller [30].

This section is not exhaustive, but represents a sampling of both past and current research in the vibration damping field. As seen, the main body of research concerns itself chiefly with the development of new semi-active damper topologies or improving control laws for active dampers. By and large the number of "new" damper topologies are usually variations on existing themes– attempts to maintain performance, while meeting weight and size constraints. As will be seen in Chapter 2, the gel damper, belongs to a class of dynamic vibration absorbers that rely on variations in moment of inertia for tuning. What makes this damper unique is that it does this by using thermosensitive polymer gels to form a controllable viscosity fluid. In the next sections we examine literature relevant for thermally stimulating the gels and thereby actuating the inertia.

1.2.2 Induction Heating Targets

The term "induction heating" refers to a well known electromagnetic phenomenon whereby eddy currents are induced in a metal conductor by an externally applied time-varying magnetic field. The induced currents arise in such a way as to "buck" out the internal magnetic field, essentially "shielding" the interior of the conductor or target. During this process the induced currents lead to ohmic dissipation within the conductor (and in the case of ferromagnetic materials, hysteresis losses too) resulting in the generation of heat. Induction heating has a number of advantages over more conventional heating methods. Depending on the application it can be faster, more efficient, practically emission free and can deliver

heat where and when it is needed, reducing for example, the risk of product warpage. This phenomenon has been successfully applied in a number of industrial applications including brazing, soldering, annealing, case hardening and curing to name a few. There are also significant commercial uses (cooking units and pans designed for induction cooking) and medical applications for induction heating.

Certain *in vivo* medical applications rely on induction heating. Of particular interest is the treatment of deep-seated malignant tumors using hyperthermia. Implanting a tumor with ferromagnetic "thermoseeds" allows the cancerous cells to be heated to temperatures high enough to induce necrosis, approximately 42^oC. Kimura and Katsuki developed a low frequency (20-30 kHz) induction heating system for treating oral cancers. As a part of their investigation they considered making custom targets from a number of different materials including: powders, grains, and balls of ferromagnetic materials such as iron, steel, stainless steel, as well as wires and tapes of high conductive materials such as copper and aluminum. Because this system was intended to treat oral lesions, it was possible to monitor the localized heating using a thermocouple [20]. To address the issue of temperature regulation others have looked at designing thermoseeds with low curie points. Once the temperature of a ferromagnetic target reaches its curie point, it lose its magnetic properties. As the permeability of the target decreases so does the induced heating. In this way, the target does not exceed the curie point and can be thermally regulated without the need for additional measurement [24, 25]. While the self-regulating properties of these targets is advantageous, it is still difficult to control the temperature of the targets during a hyperthermia treatment. As a result it is necessary to predict the temperature distribution a priori via thermal models and finite element analysis [49].

In the past induction heating has also proved itself useful for driving mag-gel actuators [16, 17]. In [17], for example, Jackson, Leeb, Mitwailli, Narvaez, Fusco, and Lupton, seeded a cylindrically-shaped polymer gel with nickel flakes and used PWM position control and feedback to regulate the length and volume of the polymer. The small dimensions of the nickel flakes made for an aggregate induction target that was poorly coupled and re-

quired specialized power electronics to sufficiently heat . Unfortunately, there is very little information addressing the individual controlled heating of multiple induction targets. For applications that involve multiple targets requiring this degree of control, it is common to use a separate induction coil and inverter for each load. A good example of this is a multiple stove top induction cooking unit. One group proposed eliminating the need for multiple inverters. A single converter could drive multiple induction loads if each primary-side induction coil was resonant with a series capacitor [6]. However, this approach is not an option in applications where the individual loads are obstructed and cannot be individually coupled to separate coils. Still others have focused on making their inductively-coupled loads resonant [44]. In the latter case the authors were not concerned with induction heating different loads but selectively delivering remote power to different electrostatic actuators.

The development of induction targets that exhibit preferential heating characteristics with frequency is one that has not been fully explored to date. While the article on remote power for electrostatic actuators suggests ways that tunable induction targets can be built, these targets require capacitors to work. Capacitors are not well suited to high humidity environments or immersion in fluids, limiting their usefulness without additional protective packaging. The targets developed for *in vivo* use do not suffer from this limitation but most of the research in this area has been concerned with their thermal self-regulation and not making them frequency selectable. One of the objectives of this thesis is the development of selectable targets, both resonant and nonresonant. As will be shown, the nonresonant variety impose a special challenge on the design of the needed power electronics. To address these needs a specialized power supply is built using a novel multilevel inverter, a class of inverter we now review.

1.2.3 Multilevel Inverters

Multilevel converters have drawn recent attention in industry for synthesizing sinewaves in high-power applications. By definition a multilevel inverter is one capable of generating more than two levels, often deriving these levels from capacitor voltage sources. This is often accomplished by evenly dividing the dc bus voltage with a capacitor ladder network. A switching network is then used to connect the output of the converter to the different nodes of the capacitor network. Historically, most multilevel inverters have fallen into one of three categories: diode-clamped, capacitor-clamped and cascaded inverters with separate dc sources [22]. The first topology is implemented using the mentioned capacitor ladder while the second topology uses a slightly different approach, incorporating capacitors into the switching network to achieve the desired levels. The cascaded inverters topology does not utilize the capacitor ladder and needs separate floating dc sources per inverter in the cascade. Of these topologies the diode clamped is the oldest and its origin can be traced back to the neutral-point-clamped (NPC) inverter introduced in 1981 by Akira Nabae [28]. A single phase leg of this inverter is shown in Figure 1.3 with a table of the possible switching states.

The NPC inverter can generate three voltages (with respect to 0) at the output V_a: V_{dc}, $V_{dc}/2$, and 0 using the switching pattern shown in the appropriate table. Unique to this topology is the need for clamping diodes, D_1 and D_2, which prevent capacitors C_1 and C_2

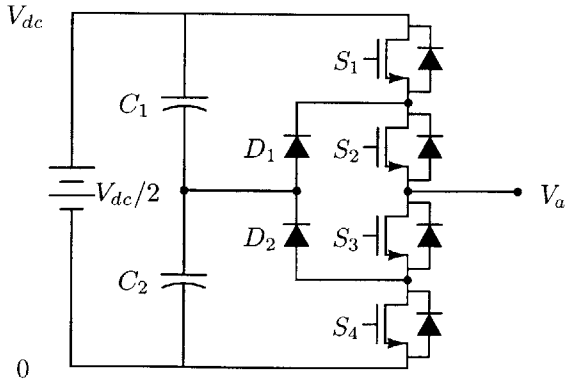

V_a	S_1	S_2	S_3	S_4
V_{dc}	1	1	0	0
$V_{dc}/2$	0	1	1	0
0	0	0	1	1

Figure 1.3: neutral-point-clamped inverter (single phase leg) with switching states.

from being discharged during the high (V_{dc}) and low (0) states and provide a bidirectional path for current during the intermediate state ($V_{dc}/2$). A variant of the npc inverter is the so-called capacitor-clamped inverter. Instead of clamping diodes, this converter employs an additional flying capacitor, nominally charged to $V_{dc}/2$ to clamp the output to the neutral voltage. This topology is shown alongside the relevant switching states in Figure 1.4. The capacitor-clamped topology has a redundant switching state for producing the intermediate voltage, $V_{dc}/2$. This is important because it provides an additional degree of flexibility for maintaining the nominal voltage on the flying capacitor. Unfortunately, the NPC inverter and all multilevel inverters that rely on capacitive division suffer from a significant (capacitor) voltage imbalance problem when delivering real power. While in the case of a three-level converter it is still possible to maintain the dc-link potential with proper control, beyond three levels, separate, isolated dc sources or a complicated voltage balancing circuit for active power transfer is required. As a result multilevel converters have found limited applications, notably as reactive power compensators.

Recently, a generalized multilevel topology [32] has been proposed from which multilevel topologies such as the diode-clamped and capacitor-clamped inverters may be derived. Of greater interest is this topology's voltage balancing capability for levels greater than three. This converter can successfully be used for real power conversion. An example of a four-level version of this converter is shown in Figure 1.5. It is apparent from this figure that

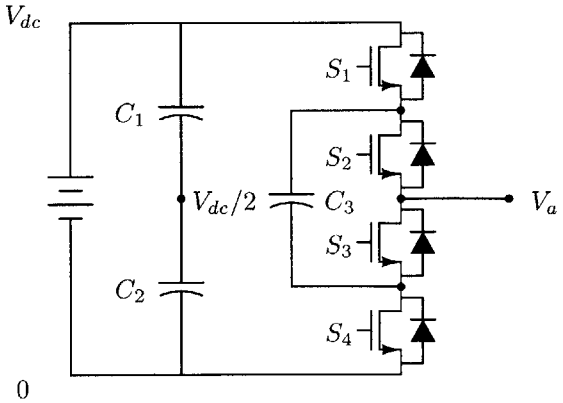

V_a	S_1	S_2	S_3	S_4
V_{dc}	1	1	0	0
$V_{dc}/2$	0	1	0	1
	1	0	1	0
$0V_{dc}$	0	0	1	1

Figure 1.4: capacitor clamped inverter (single phase leg) with switching states.

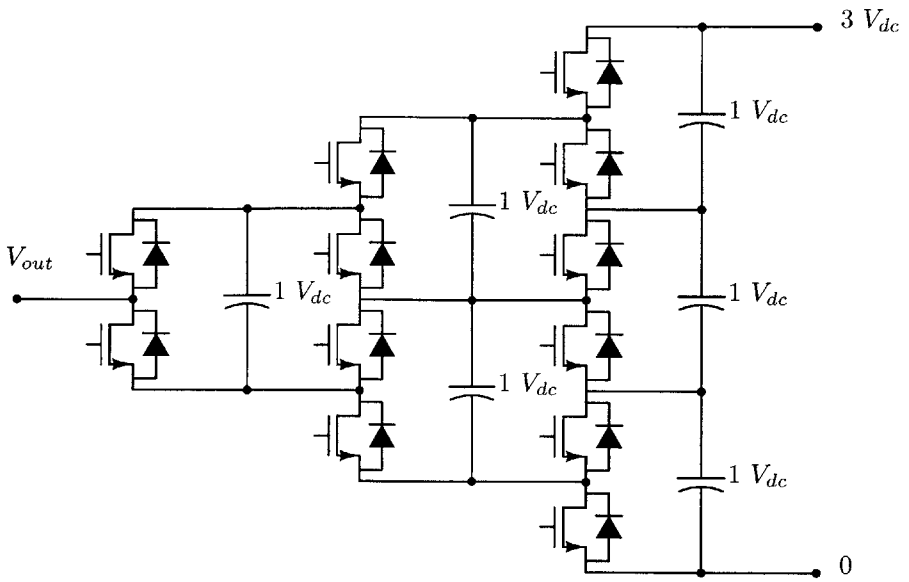

Figure 1.5: The generalized multilevel converter.

the generalized multilevel converter requires a greater number of switching devices, diodes and capacitors than traditional multilevel inverters. As a result, the immediate application for this converter includes switched-capacitor dc-to-dc converters and voltage multipliers, where the part count is less than traditional implementations. As will be seen, the multilevel inverter presented in this thesis can also be inferred from the generalized topology, but has the advantage of a substantially reduced part count while maintaining the inherent voltage balancing that makes this converter attractive.

1.3 Thesis Contributions

The gel polymer vibration damper is a cross-disciplinary project pulling together different aspects of both mechanical and electrical engineering. This work tests the validity of the gel DVA concept and lays the foundation for future work in the area of semi-active vibration damping with polymer gels. Greater emphasis is given to the development of the multi-frequency induction heating system and induction targets. The most significant contributions of this thesis are therefore in the fields of induction heating and power electronics.

The specific contributions to these three fields are summarized below.

1.3.1 Semi-Active Vibration Damping

A new type of semi-active dynamic vibration absorber is developed that uses a controllable moment of inertia to extend the absorber's useful frequency range. The damper's moment of inertia is the result of a controllable viscosity fluid composed of gel polymer beads suspended in a solvent. A prototype consisting of two separate actuating chambers is built and tested to illustrate the concept. It is hoped that the use of controllable viscosity fluids may lead to further advances in semi-active vibration damping.

1.3.2 Induction Heating

The number of potential induction heating applications is extended by the introduction of induction heating targets that are frequency selectable in nature. Both resonant and nonresonant targets suitable for heating gel polymers are built and tested. The nonresonant targets may also prove useful as potential thermoseeds for treating malignant tumors via hyperthermia. With additional work the resonant targets could be modified to act as inductively coupled networks for providing remote power to other types of actuators.

1.3.3 Power Electronics

The induction targets developed in this thesis, primarily the nonresonant ones, motivate the need for a power supply that can generate high-power, low-distortion sinewaves over a wide frequency range. A novel multilevel topology is introduced to meet these requirements. The Marx inverter overcomes the voltage balancing limitations of traditional multilevel inverters when delivering real power without the need for external balancing circuits or complicated control. When compared to over approaches, such as synthesizing sinewaves

using a pulse width modulated full-bridge inverter, this topology does so with significantly reduced switching losses. A 1 kW, seven-level, prototype Marx inverter is built, tested and compared.

1.4 Thesis Organization

This chapter introduced the need for an induction heating system that can selectively heat induction targets using a single induction coil. This system is part of a semi-active vibration damper and needed to heat the individual polymer gel actuators that modify the DVA's anti-resonant frequency. Chapter 2 reviews the fundamentals of dynamic vibration absorbers and provides a brief primer on the subject of polymer gels. A DVA that uses polymer gels is developed and the basic principle of its operation is explained. To examine its frequency response, the linearized equations of motion for the gel damper are derived. Experimental results from a damper prototype using two gel-filled chambers are presented.

Motivated by the need for induction targets that can selectively heat the various gel-filled chambers in the damper, Chapter 3, discusses one possibility. Nonferromagnetic conductors whose critical dimensions are much smaller than the corresponding skin depth at the frequencies of interest are explored. Both cylindrical shells and thin wires are used to make nonresonant targets that have preferential heating characteristics. Mathematical derivations for multiple, coupled targets are given. The consequences of generating the time-varying magnetic field with a current versus a voltage driven induction coil is examined. Two experiments (one for the cylindrical shells and one for the thin wires) are carried out to validate these mathematical models and assumptions. Chapter 4 extends induction targets to include resonant RLC circuits. Derivations analogous to Chapter 3 are presented; three experimental resonant targets are tested and their results are analyzed.

The induction targets presented in the previous chapters require a suitable power supply for heating them. The nonresonant targets in particular require a power supply

that can efficiently generate sinewaves with a low amount of total harmonic distortion. A novel multilevel inverter referred to as the Marx inverter is introduced in this chapter. The converter's mode of operation and potential for zero voltage switching (ZVS) are explained. A comparative study using this converter versus a more traditional pulse-width-modulated (PWM) full-bridge inverter is presented. Experimental results from a 1 kW prototype are examined in this chapter. Finally, Chapter 6 summarizes the contributions of this thesis and makes recommendations for future areas of work.

Chapter 2

A Gel Polymer Based Dynamic Vibration Absorber

IN Chapter 1, the dynamic vibration absorber was introduced as a passive means of vibration control. This chapter develops a semi-active DVA that utilizes a controllable viscosity fluid, composed of a collection of gel beads in a solvent, to improve damping over a user-specified range of frequencies. Before examining the gel damper in detail, the fundamental behavior of the basic dynamic vibration absorber is reviewed. After this review, two approaches for making a semi-active DVA's are covered, followed by a a brief tutorial on polymer gels. The remaining sections describe the design of a multi-compartment gel container that could be used to make a gel damper. The linearized equations of motion for this damper are subsequently derived and experimental results from a two-chamber prototype are presented.

2.1 Dynamic Vibration Absorber Fundamentals

In this section the frequency response of a mechanically resonant system is reviewed. The effects of coupling a DVA onto this system to suppress its resonant behavior is then discussed. Two tuning possible tuning schemes for the DVA are examined: constant and optimal tuning.

2.1.1 Analysis of The Primary Resonant Structure

It is typical to describe a vibrating system using the single-degree-of-freedom (SDOF) mechanical model shown in Figure 2.1. In this model, the mass of the vibrating structure, represented by M_1, undergoes a sinusoidal force of amplitude, F, and frequency ω. If the structure has compliance and some degree of damping, they are accounted for by the ideal spring, K_1, and the dashpot, β_1, respectively. Summing the forces acting on the mass gives the second-order equation of motion for this system,

$$F = M_1\ddot{X}_1 + \beta\dot{X}_1 + K_1X_1. \tag{2.1}$$

For compactness, the classic dot notation has been used to represent differentiation in the time domain. Mapping this equation to the s domain and rewriting gives the transfer function of the system,

$$\frac{X_1(s)}{F(s)} = \frac{1/M_1}{s^2 + (\beta_1/M_1)s + (K_1/M_1)}. \tag{2.2}$$

The denominator of (2.2) has been written in the canonic form,

$$Den(s) = s^2 + 2\zeta\omega_n s + \omega_n^2, \tag{2.3}$$

allowing the damping ratio, ζ, and natural frequency, ω_n, to be read directly from the equation. For this system, the damping ratio is

$$\zeta_1 = \frac{1}{2}\frac{\beta_1}{\sqrt{M_1K_1}}, \tag{2.4}$$

and the natural frequency is

$$\omega_{n,1} = \sqrt{\frac{K_1}{M_1}}. \tag{2.5}$$

Setting the complex frequency s to zero, reveals that the dc gain or the static displacement

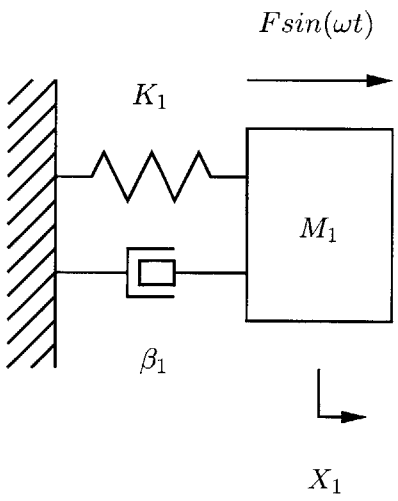

Figure 2.1: A SDOF mechanical model for a resonant primary structure.

X_{st} of the primary mass to a unit force is completely determined by the spring constant,

$$X_{st} = \frac{1}{K_1}. \tag{2.6}$$

This result make physical sense because the system will eventually come to rest (as soon as the transients decay to zero) if a constant force is applied. When the system is at rest, the constant force must be completely balanced by the restoring force of the spring, otherwise the mass will accelerate.

For the purposes of plotting the second-order frequency response of this mechanical system it is helpful to re-express (2.2) in terms of (2.4)-(2.6) and as a function of the normalized complex frequency, $\frac{s}{\omega_{n,1}}$,

$$\frac{X_1(\frac{s}{\omega_{n,1}})}{F(\frac{s}{\omega_{n,1}})} = \frac{X_{st}}{(\frac{s}{\omega_{n,1}})^2 + 2\zeta_1(\frac{s}{\omega_{n,1}}) + 1}. \tag{2.7}$$

The normalized frequency response of this transfer function is shown in Figure 2.2 for three different damping ratios[1]. In this example the static displacement has been chosen equal to unity. A damping ratio of $\zeta_1 = 0.05$ results in a displacement at the resonant

[1]The source code for this and all MATLAB generated figures can be found in Appendix B.

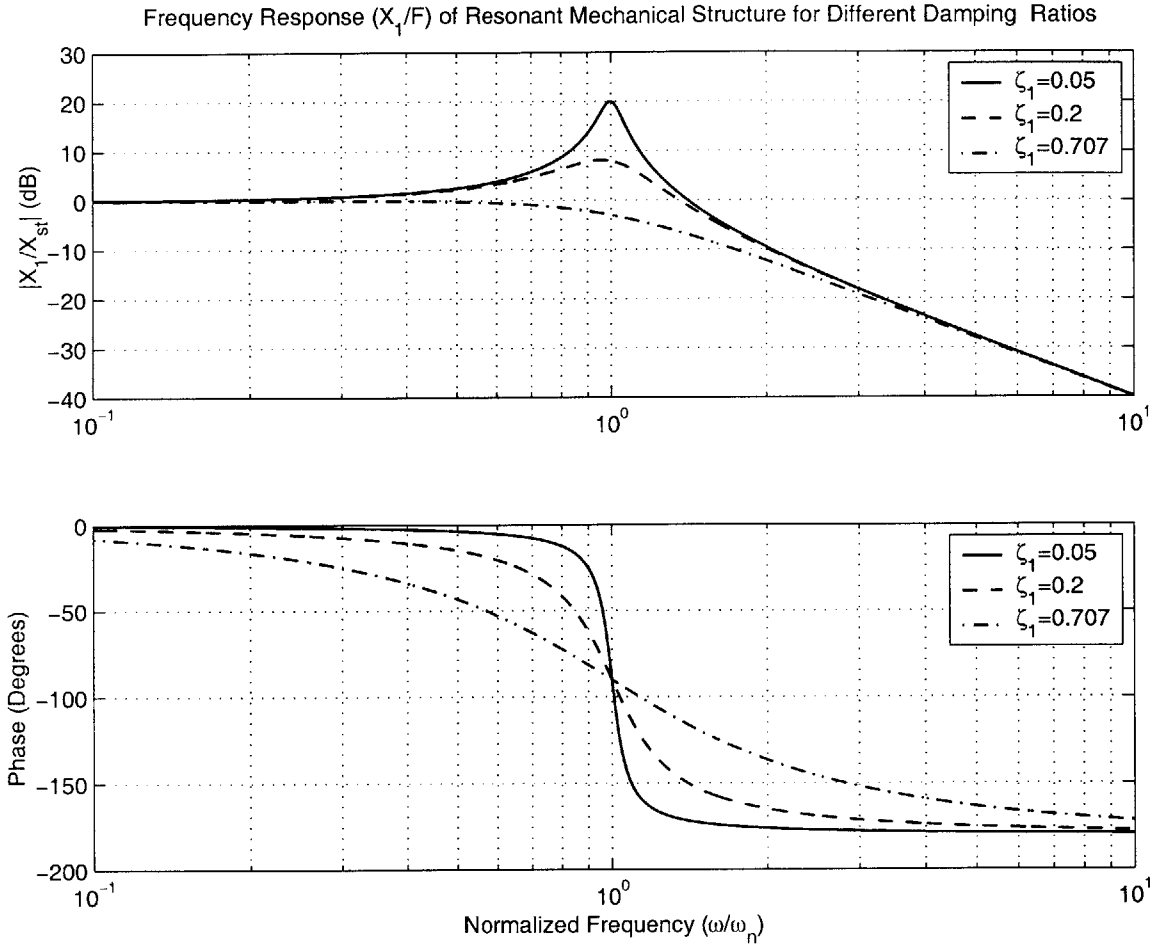

Figure 2.2: The frequency response of a primary structure's displacement due to a sinusoidal force for different damping ratios of the primary structure. ζ_1: 0.05, 0.2, and 0.707.

frequency that is ten times greater than that experienced for a constant force of the same magnitude. The height of this peak is a continuous function of the damping ratio, tending toward infinity as the damping ratio approaches zero. Likewise, when the damping ratio is equal to or larger than $\zeta_1 = 1/\sqrt{2}$ the system does not experience any peaking in the frequency domain. The system may still experience oscillatory behavior as part of its transient response to external disturbances, however. Once the damping ratio equals one, the system reaches critical damping and increased damping results in the transient behavior resembling decaying exponentials. Regardless of the damping ratio, the phase of the system always passes through -90^o at the natural frequency, i.e. the displacement of the primary

system lags the sinusoidal force by 90^o. The damping ratio does affect how quickly the phase transitions from 0^o to 180^o, with smaller damping ratios resulting in steeper transitions. For small damping ratios it is clear that the mechanical structure may experience complications in its transient or steady-state response as a result of a lightly damped resonance. A common situation where this is true is a rotating machine that must pass through its resonant frequency before reaching its final operating speed at a higher frequency.

2.1.2 Analysis Of The Primary Resonant Structure with DVA

The sinusoidal-steady-state behavior of a system that operates or experiences disturbances near a lightly damped resonance can benefit from the addition of a dynamic vibration absorber. Figure 2.3 shows the SDOF model of the primary structure from before, now coupled to a dynamic vibration absorber. The DVA is represented by the mechanical network comprised of absorber mass M_2, absorber spring K_2, and absorber damper β_1. This mechanical system is fourth order and governed by two equations of motion. Summing the forces on the primary mass M_1, gives the first equation,

$$F = M_1\ddot{X}_1 + (\beta_1 + \beta_2)\dot{X}_1 + (K_1 + K_2)X_1 - \beta_2\dot{X}_2 - K_2X_2. \tag{2.8}$$

Similarly, the second equation is found by summing the forces acting on the absorber mass M_2,

$$0 = M_2\ddot{X}_2 + \beta_2\dot{X}_2 + K_2X_2 - \beta_2\dot{X}_1 - K_2X_1. \tag{2.9}$$

rewriting these equations using Laplace transforms gives,

$$F(s) = X_1(s)\left\{M_1s^2 + (\beta_1 + \beta_2)s + (K_1 + K_2)\right\} - X_2(s)\left\{\beta_2s + K_2\right\}, \tag{2.10}$$

and

$$0 = X_2(s)\left\{M_2s^2 + \beta_2s + K_2\right\} - X_1(s)\left\{\beta_2s + K_2\right\}, \tag{2.11}$$

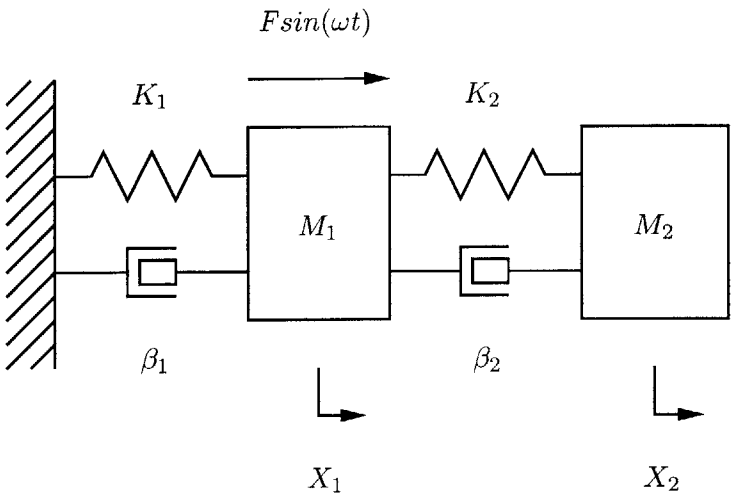

Figure 2.3: A SDOF mechanical model of a resonant primary structure coupled to a DVA.

respectively. The transfer function for the displacement of the primary mass X_1 as the result of the disturbance force F, can be found by substituting (2.11) into (2.10) and rearranging. The transfer function has the form,

$$\frac{X_1(s)}{F(s)} = \frac{M_2 s^2 + \beta_2 s + K_2}{As^4 + Bs^3 + Cs^2 + Ds + E}, \tag{2.12}$$

where the coefficients of the denominator are as follows:

$$A = M_1 M_2, \tag{2.13}$$

$$B = \beta_1 M_2 + \beta_2 (M_1 + M_2), \tag{2.14}$$

$$C = K_1 M_2 + K_2 (M_1 + M_2) + \beta_1 \beta_2, \tag{2.15}$$

$$D = \beta_1 K_2 + \beta_2 K_1, \tag{2.16}$$

and

$$E = K_1 K_2. \tag{2.17}$$

Before proceeding, it is convenient to re-express the transfer function in terms of some useful quantities, particularly the mass ratio,

$$\mu = \frac{M_2}{M_1}, \tag{2.18}$$

and the natural frequency ratio,

$$\psi = \frac{\omega_{n,2}}{\omega_{n,1}}. \tag{2.19}$$

Using these quantities, (2.12) can be rewritten as a transfer function in terms of the normalized complex frequency,

$$\frac{X_1(\frac{s}{\omega_{n,1}})}{F(\frac{s}{\omega_{n,1}})} = X_{st}\left[\frac{(\frac{s}{\omega_{n,1}})^2 + 2\psi\zeta_2(\frac{s}{\omega_{n,1}}) + \psi^2}{A'(\frac{s}{\omega_{n,1}})^4 + B'(\frac{s}{\omega_{n,1}})^3 + C'(\frac{s}{\omega_{n,1}})^2 + D'(\frac{s}{\omega_{n,1}}) + E'}\right], \tag{2.20}$$

where the coefficients of the denominator are now written as follows:

$$A' = 1, \tag{2.21}$$

$$B' = 2(\zeta_1 + (1+\mu)\psi\zeta_2), \tag{2.22}$$

$$C' = (1 + (1+\mu)\psi^2 + 4\psi\zeta_1\zeta_2), \tag{2.23}$$

$$D' = 2\psi(\psi\zeta_1 + \zeta_2), \tag{2.24}$$

and

$$E' = \psi^2. \tag{2.25}$$

2.1.2.1 Constant Tuning

The transfer function (2.20) is complicated. To understand the behavior of the composite system, it is helpful to make some additional assumptions and then examine simple cases. For many applications, the natural frequency of the DVA is chosen equal to the primary structure, such that $\psi = 1$. This is referred to as constant tuning. It is also desirable for the mass of the DVA to be a small fraction of the total mass, typical values of the mass ratio may range between 0.10 to 0.30. In our example we shall pick $\mu = 0.2$. Furthermore, let us also assume that damping of the primary structure is negligible $\zeta_1 = 0$, and that the static displacement to a unit force is again unity.

Figure 2.4 shows the normalized frequency response of such a system for three different damping ratios of the DVA, $\zeta_2 : 0, 0.1$, and ∞. When $\zeta_2 = 0$ there is no damping present in the system and the magnitude of the response can be characterized by an anti-resonant frequency at the same frequency as the DVA as well as resonant peaks at frequencies above and below the location of the anti-resonance. Because there are no losses in the system the displacement of the primary system approaches infinity at each resonant frequency and zero at the anti-resonance. If there is a finite amount of damping, $\zeta_2 = 0.1$, the amplitude of the resonant peaks become finite and the anti-resonance is greater than zero. On the other extreme, when the DVA has an infinite amount of damping, the secondary mass is rigidly fixed to the primary mass. The net result is that, at this extreme, the system has only one resonant mode at a frequency that is less than the natural frequency of the primary system. This response is expected because the network now acts like a single spring-mass system where the new mass is effectively greater by an amount determined by the mass of the DVA.

Figure 2.5 shows the frequency response for some intermediate damping ratio values: 0.1, 0.29, 1.0. Examining this figure reveals that all three curves intersect at the same two frequencies regardless of the damping ratio ζ_2. It is therefore possible to pick an optimal damping ratio ζ_2, such that the maximum peak response is minimized, i.e. equal to the

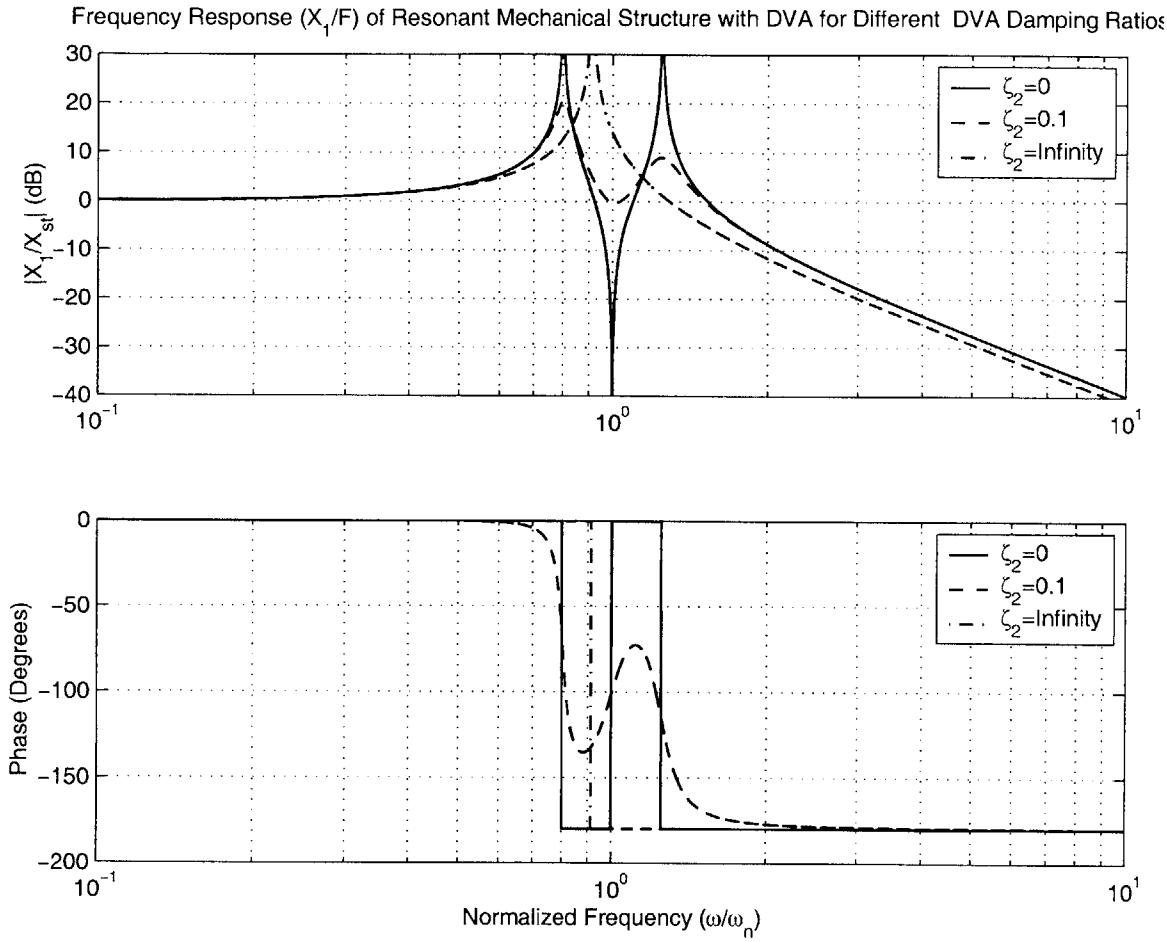

Figure 2.4: The frequency response of a primary structure coupled to a DVA with constant tuning, for different damping ratios of the DVA. ζ_2: 0, 0.1, and ∞.

amplitude of the higher of the two intersection points. For the frequency and mass ratios in this example, the optimal damping ratio is approximately 0.29.

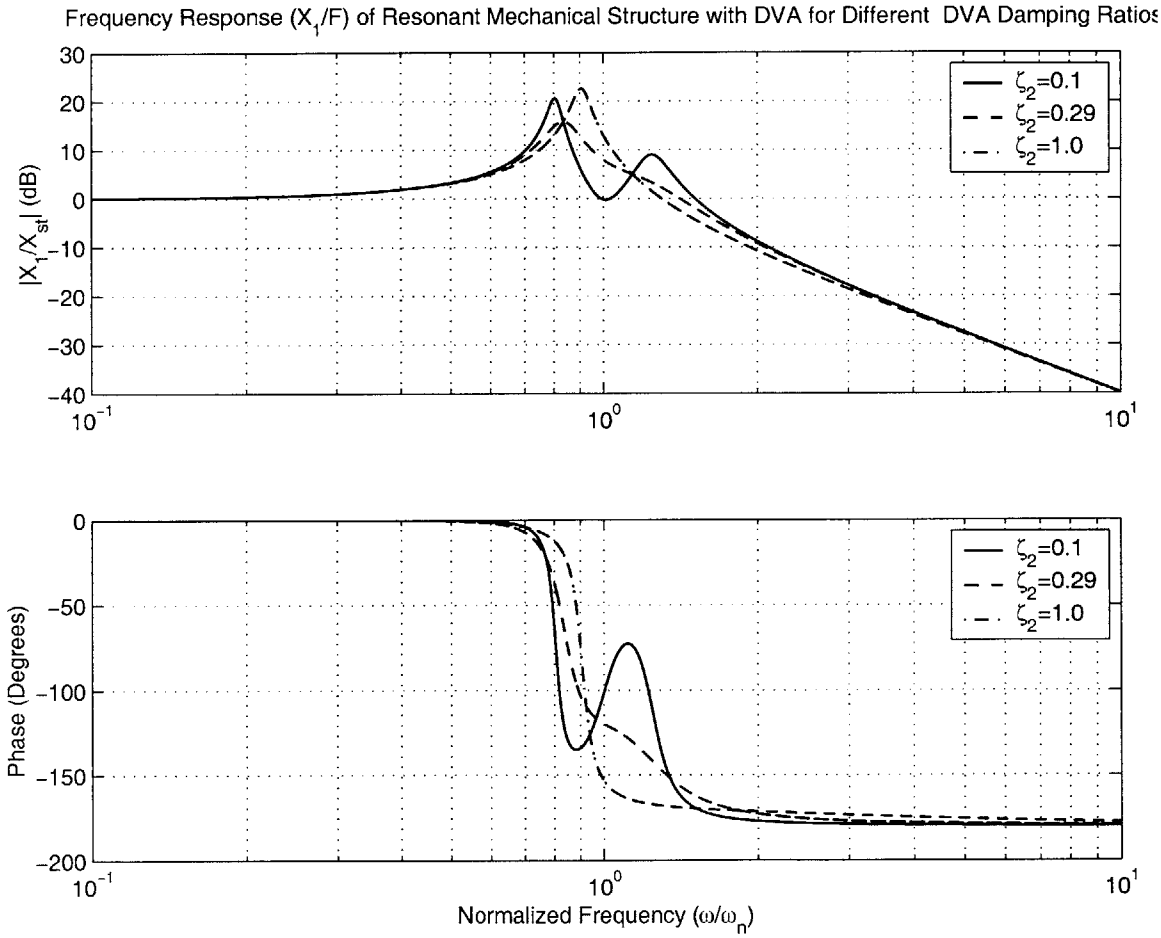

Figure 2.5: The frequency response of a primary structure coupled to a DVA with constant tuning, for different damping ratios of the DVA. ζ_2: 0.1, 0.29, and 1.0.

2.1.2.2 Optimal Tuning

For the constant tuning case it was seen that the damping ratio ζ_2, can be chosen to minimize the maximum magnitude of the frequency response. Den Hartog, showed that it is possible to lower the magnitude response even further by adjusting the frequency ratio so that the height of the intersection points is equal [12]. The optimal frequency ratio that achieves this response has been shown to be equal to,

$$\psi = \frac{1}{1+\mu}. \tag{2.26}$$

Once again it is possible to pick the damping ratio ζ_2, to optimize the response by minimizing the maximum magnitude. As the damping ratio is varied the family of curves must still pass through the two intersection points. However, there is no guarantee that when the low frequency maxima passes through its intersection point that the high frequency maxima will pass through its intersection point. The tuning is considered optimal as long as the curve passes through one of these points. The difference in performance for choosing one point over the other is considered minimal. According to Hartog [12] the amplitude of the intersection points for the optimal tuning scheme is,

$$X_1 = X_{st}\sqrt{1+\frac{2}{\mu}}. \tag{2.27}$$

Whereas in the constant tuning case, the highest amplitude (usually corresponding to the low frequency point for typical damper sizes) is

$$X_1 = \frac{X_{st}}{-\mu + (1+\mu)\sqrt{\frac{\mu}{2+\mu}}}. \tag{2.28}$$

Figure 2.6 shows the frequency response for various damping ratios ζ_2, but now using the optimal tuning law given in (2.26). In this case, a damping ratio of $\zeta_2 = 0.24$ is considered optimal because it peaks at the low frequency intersection point. If the goal of the damper is to keep the magnitude of the response below an acceptable level for all frequencies, this

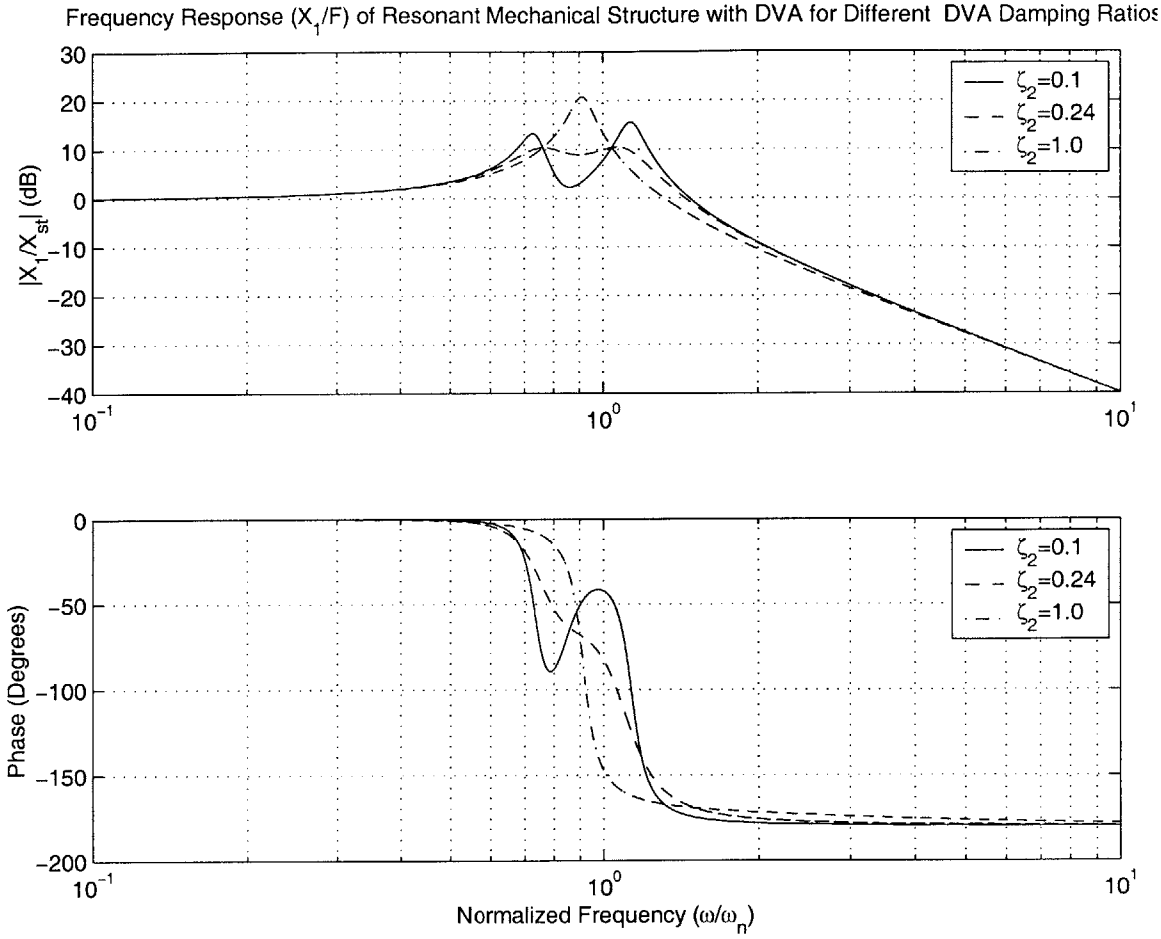

Figure 2.6: The frequency response of a primary structure coupled to a DVA with optimal tuning, for different damping ratios of the DVA. ζ_2: 0.1, 0.24, and 1.0.

tuning scheme is difficult to improve upon.

2.1.3 Analysis Of The DVA

The frequency response of the primary structure with a coupled DVA is obviously of prime consideration when designing the damper. However, the behavior of the dynamic vibration absorber must also be considered. The mechanical components of the DVA have limitations that must be observed. Of particular importance is insuring that the spring element does not exceed its rated deflection, causing it to behave in a nonlinear manner. The transfer

function for the displacement of the DVA mass is found in a similar manner to that of the primary structure. Some algebraic manipulation can be reduced by recognizing that the poles of the DVA transfer function are identical to (2.12). The numerator or zeros of the system can be found by substituting (2.11) into (2.10) for X_1 and rearranging. The transfer function is given as,

$$\frac{X_2}{F} = \frac{\beta_2 s + K_2}{As^4 + Bs^3 + Cs^2 + Ds + E}, \tag{2.29}$$

or in terms of normalized complex frequency by,

$$\frac{X_2(\frac{s}{\omega_{n,1}})}{F(\frac{s}{\omega_{n,1}})} = X_{st}\left[\frac{2\psi\zeta_2(\frac{s}{\omega_{n,1}}) + \psi^2}{A'(\frac{s}{\omega_{n,1}})^4 + B'(\frac{s}{\omega_{n,1}})^3 + C'(\frac{s}{\omega_{n,1}})^2 + D'(\frac{s}{\omega_{n,1}}) + E'}\right]; \tag{2.30}$$

the coefficients of the denominator are unchanged from before and expressed in equations (2.13)-(2.17) or (2.21)-(2.25) respectively. This transfer function is important for verifying that the displacement of the DVA mass does not exceed fixed bounds, especially if the DVA must operate in a confined space. However, if we wish to insure linear deflection of the springs, the displacement of the DVA mass with respect to the primary mass is more important and can be determined by subtracting (2.30) from (2.20) to give

$$\frac{[X_2 - X_1](\frac{s}{\omega_{n,1}})}{F(\frac{s}{\omega_{n,1}})} = X_{st}\left[\frac{(\frac{s}{\omega_{n,1}})^2}{A'(\frac{s}{\omega_{n,1}})^4 + B'(\frac{s}{\omega_{n,1}})^3 + C'(\frac{s}{\omega_{n,1}})^2 + D'(\frac{s}{\omega_{n,1}}) + E'}\right]. \tag{2.31}$$

Figure 2.7 shows the displacement of the DVA with respect to the resonant mechanical structure for the constant-tuning case and the damping ratios shown previously in Figure 2.5. Comparing these two figures for the low damping ratio $\zeta_2 = 0.1$, it can be seen that the reduction in motion of the primary structure near the natural frequency is accounted for by an increase in motion of the DVA. At this frequency the primary structure experiences an anti-resonance caused by the mass of the DVA moving in counterpoise by 90^o with the primary mass. The primary mechanical structure remains relatively stationary while the DVA oscillates as a result of "absorbing" the disturbing vibration.

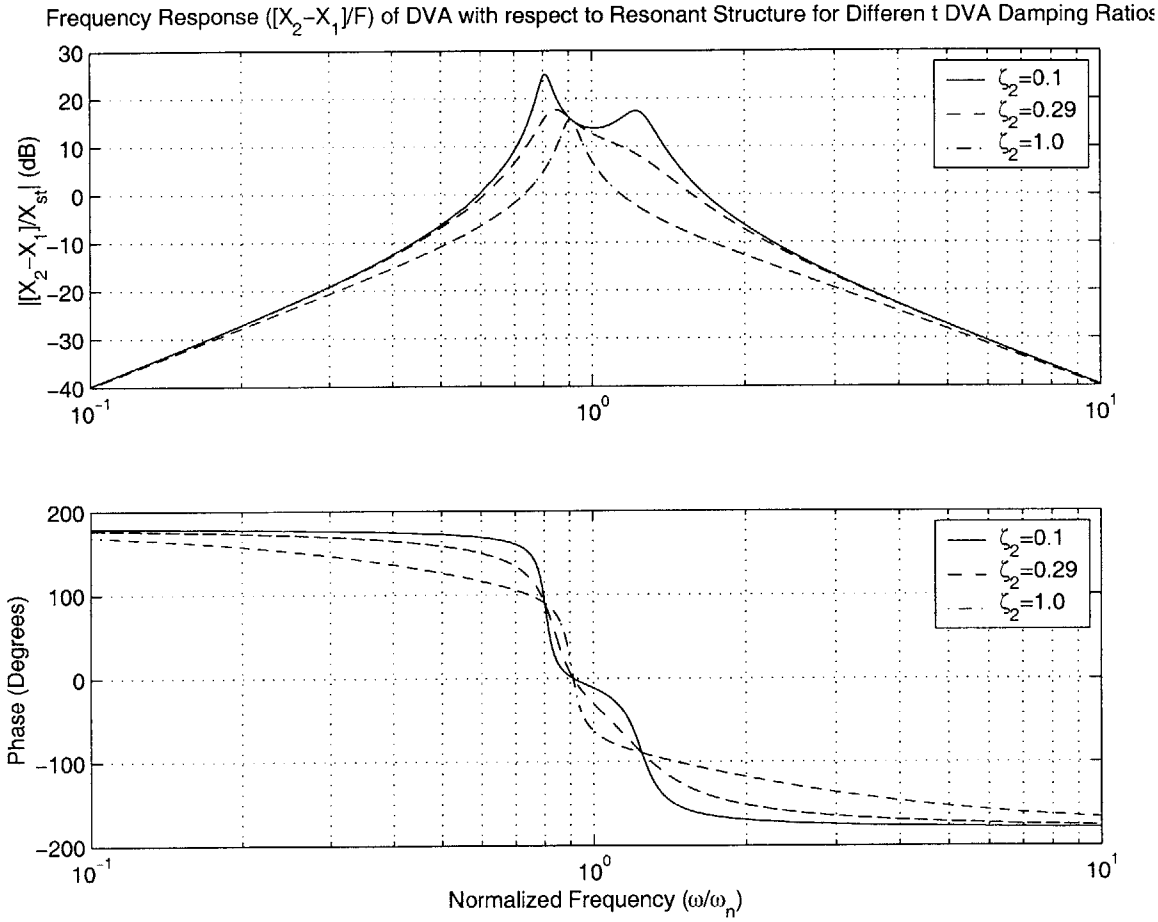

Figure 2.7: The frequency response of a DVA's displacement relative to the primary structure it is coupled to for the constant tuning case and different damping ratios of the DVA. ζ_2: 0.1, 0.29, and 1.0.

2.2 Semi-Active Dynamic Vibration Absorbers

The previous section reviewed the fundamental behavior of the dynamic vibration absorber. The constant-tuning approach can give a high reduction in vibration at the anti-resonant frequency created by the DVA. However, the new system had two resonant peaks that could be troublesome. If the disturbance is not at a frequency that is close to the anti-resonance, the DVA can actually exacerbate the disturbance, especially if some frequency component of the disturbance occurs at either of these resonant peaks, or if the dynamics of the primary system should change with time. One way to address this issue is to use the optimal tuning strategy discussed previously. Optimal tuning mitigates the height of the two resonant peaks, resulting in a less volatile system with frequency, but this reduction comes at the expense of a more shallow anti-resonance. Finding a way to maintain the effectiveness of a lightly damped anti-resonance while eliminating the concern of the two resonant peaks (at least for narrow frequency disturbances) has motivated ongoing research in the field of semi-active DVA's.

2.2.1 The Variable-Compliance Semi-Active DVA

A commonly investigated semi-active DVA topology employs a variably stiff spring element, as shown in Figure 2.8. Adjusting the spring constant allows the anti-resonant frequency to change, thereby permitting the DVA to track the frequency of the disturbance. Examples of semi-active DVA's using some variant of this idea can be found in [47, 48]. Figure 2.9 illustrates the basic concept of a variable-spring DVA. The figure shows the frequency response of the primary structure for three different values of the spring constant K_2. In this case, the three values include the nominal value as well as twice and one-half this value. If the spring compliance is allowed to vary continuously within these extremes, a narrow-band disturbance in this range can be significantly attenuated. Note that the anti-resonance is less effective at lower frequencies due to the larger damping ratio that results from a smaller spring compliance and a constant damping coefficient (assumed in this example).

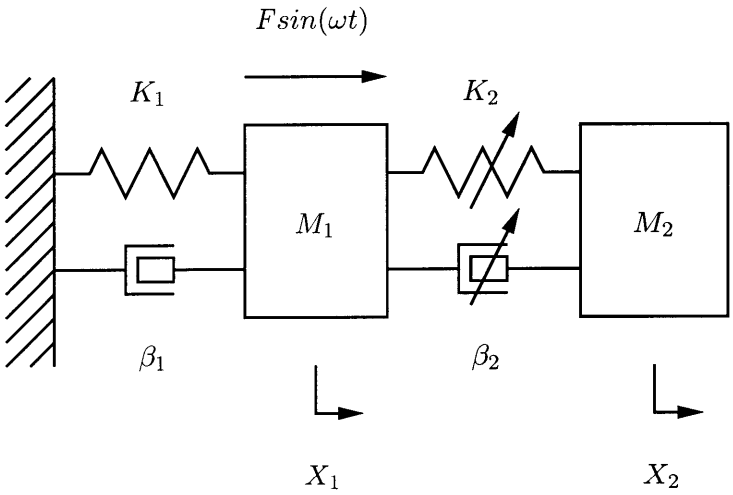

Figure 2.8: A SDOF mechanical model of a resonant primary structure coupled to a semi-active DVA.

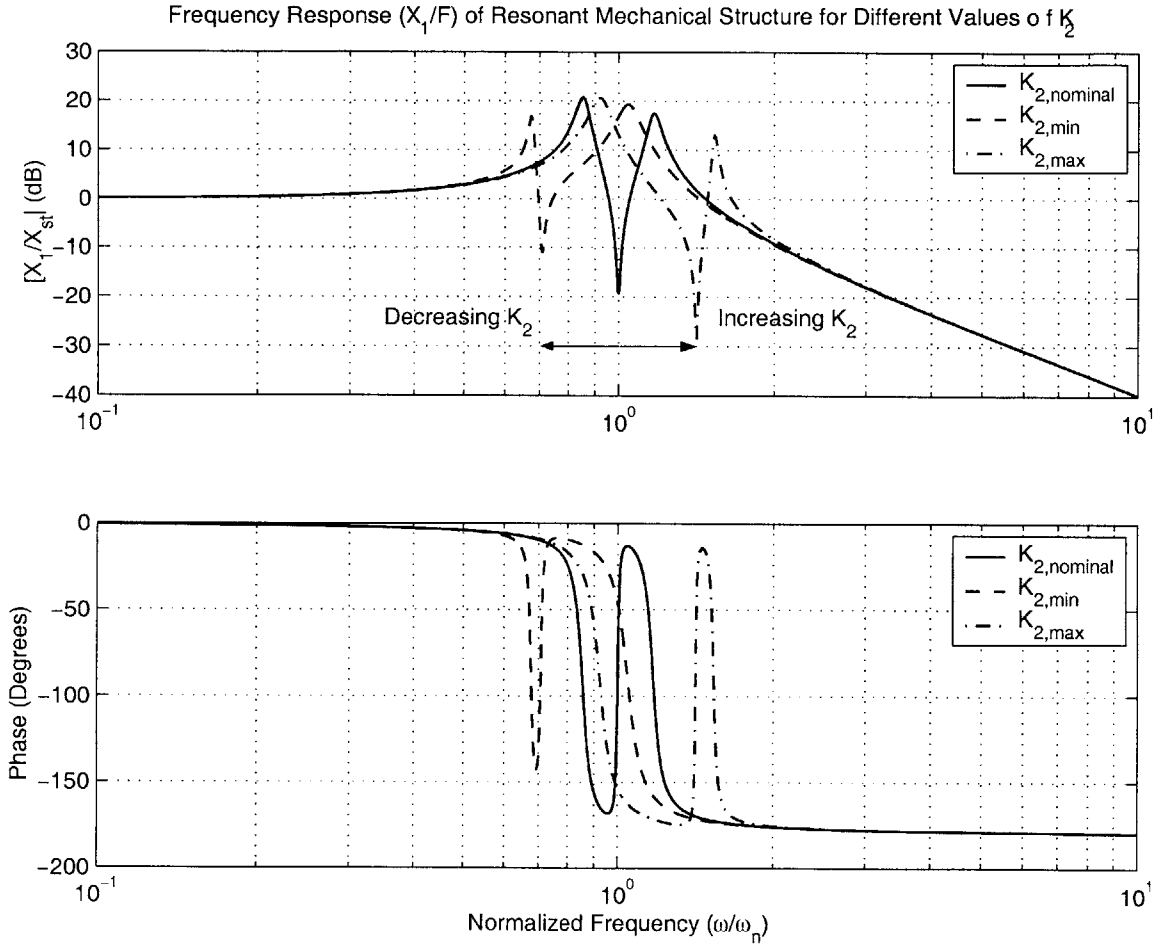

Figure 2.9: The frequency response of primary structure coupled to a semi-active DVA that can vary its natural frequency by adjusting its spring constant K_2.

2.2.2 The Variable-Inertia Semi-Active DVA

The benefits of a DVA are not limited to systems that vibrate in a linear direction. DVA's can also be used to dampen systems that experience rotational vibrations. A lumped model for the rotational SDOF analog is shown in Figure 2.10. In this case, the primary system is represented by an inertia J_1, which has a torsional compliance K_1. Likewise, the rotational DVA consists of an auxiliary inertia and compliance, J_2 and K_2 respectively. Viscous damping is not explicitly shown in Figure 2.10 but can easily be represented. The equations of motion that govern this system are identical in form to the linear one with inertia replacing mass. As before, the natural frequency of the DVA can be altered by changing the spring constant. However, rotational systems offer another potential degree of freedom. Unlike mass in a linear-motion DVA, it is much easier to manipulate the rotational analog, i.e. the moment of inertia. The pendulum-type absorbers, mentioned in Chapter 1, represent a common topology that exploits the possibility of changing the pendulum's length to adjust the absorber's natural frequency [8, 45, 50].

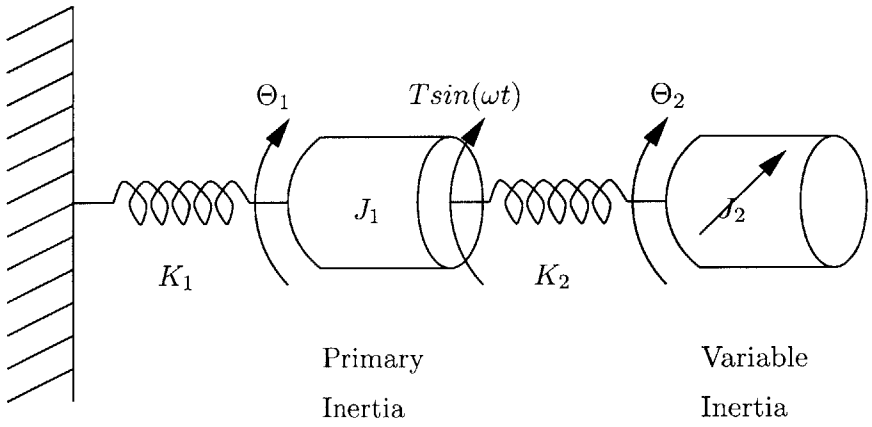

Figure 2.10: A SDOF mechanical model for a rotating resonant primary structure coupled to a a semi-active DVA with a variable moment of inertia.

Figure 2.11 shows how the frequency response of a variable-inertia DVA might differ from one that uses a variable compliance. The most noteworthy difference is that the depth of the anti-resonance for this type of DVA increases with decreasing frequency. The vibration damper topology explored in this thesis also operates using a variable moment of inertia as its basis. Instead of a variable-length pendulum, our DVA uses a container filled with a fluid whose viscosity is controllable.

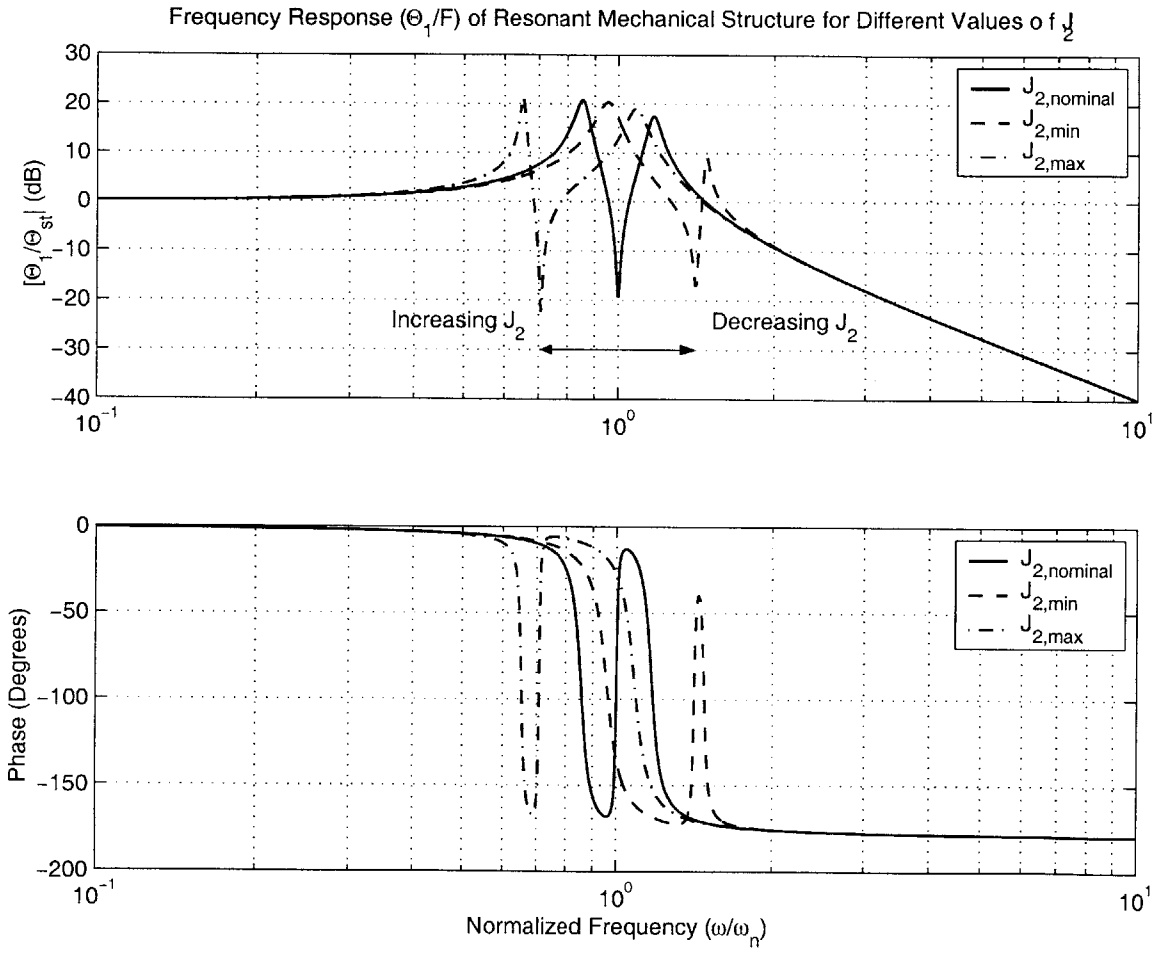

Figure 2.11: The frequency response of primary structure coupled to a semi-active DVA that can vary its natural frequency by adjusting its moment of inertia J_2.

2.3 The Rotational Gel Polymer DVA

A cylindrical container filled with a fluid has a moment of inertia that depends on the viscosity of that fluid. Fluids that exhibit a wide change in viscosity as the result of a controllable input, such as heat, provide a useful means for varying rotational inertia. If the fluid has a very high viscosity, like honey for instance, the fluid and container move together and behave much like a single, solid, fixed mass. On the opposite extreme, if the fluid has relatively low viscosity, such as alcohol, or water there is significant "slip" between the boundary of the container and the fluid. The fluid at the immediate surface of the container experiences a transfer of momentum from the cylinder as it rotates, but this transfer of energy decreases away from the boundary. If the fluid is inviscid, it does not partake in the storage of kinetic energy as the container rotates, i.e. the mass of the container and the mass of the fluid are decoupled when determining the inertia of the container. If the viscosity of the fluid is somewhere in between, as is the case with all real fluids, the system will experience an intermediate inertia as well as some degree of viscous damping due to drag and losses in the fluid. When compared to a variable-length pendulum, a DVA that uses a fluid-filled cylinder for energy storage requires potentially fewer moving parts and may offer a means of not only modifying the moment of inertia but also the associated damping.

2.3.1 The Gel Polymer Fluid

The semi-active DVA developed in this thesis uses a collection of thermally sensitive gel beads to create a fluid whose viscosity can vary with temperature. Gels are composed of a cross-linked polymer network that is suspended in a solvent [46]. In the presence of certain stimuli, a gel can exhibit reversible changes in volume, as much as a thousand-fold. Furthermore, they can be engineered to respond to desired stimuli, including changes in solvent composition, pH levels, or temperature, to name a few. The gel beads used in our prototype vibration damper respond to temperature and are composed primarily

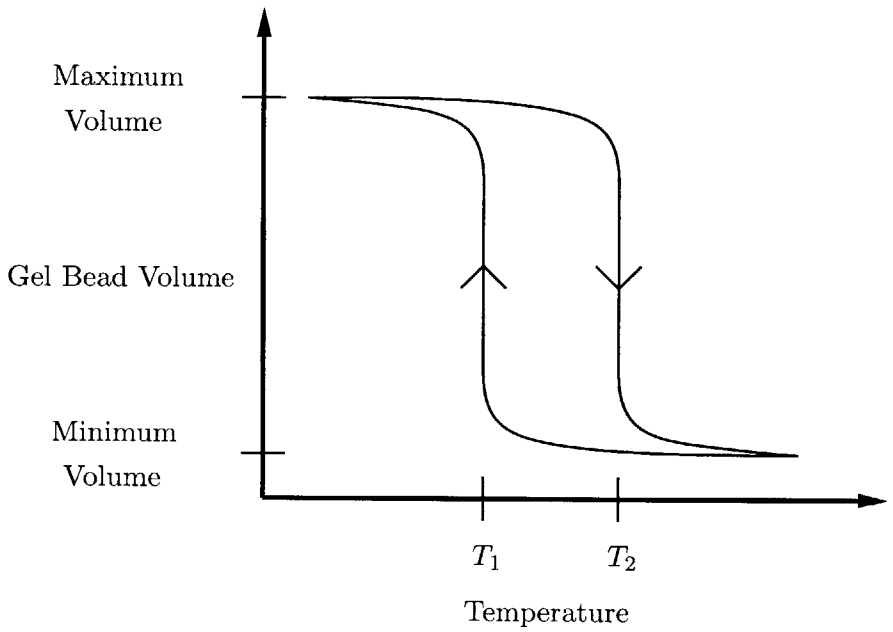

Figure 2.12: Discontinuous Gel Phase Transition

of hydroxypropyl cellulose, or HPC for short. These beads were prepared using an inverse suspension polymerization, a process outlined in Appendix A, courtesy of Dr. Bromberg [2]. The plot shown in Figure 2.12 represents a volume transition curve that is typical of many gels. Below a certain temperature a gel bead will swell, absorbing the surrounding solvent into its polymer matrix (like a sponge). When this happens the gel beads pack tightly in the container, adding significantly to the container's moment of inertia. At higher temperatures the polymer network shrinks, allowing the solvent to flow freely.

Figure 2.12 emphasizes that the transition between states is discontinuous, i.e the intermediate volumes do not represent static equilibria. The significance of this discontinuity will become more apparent in the next section. Gels may also exhibit hysteretic properties with temperature and volume, as shown. In theory, T_1 and T_2 can be engineered to assume any value within the temperature range allowing water to exist as a liquid, i.e. 0^oC to 100^oC. Although not explored in this thesis, it may be possible to exploit this type of latching phenomena as a means of maintaining a gel's present state without the need for additional energy consumption. Figure 2.13 is taken directly from Dr. Mitwalli's Ph.D.

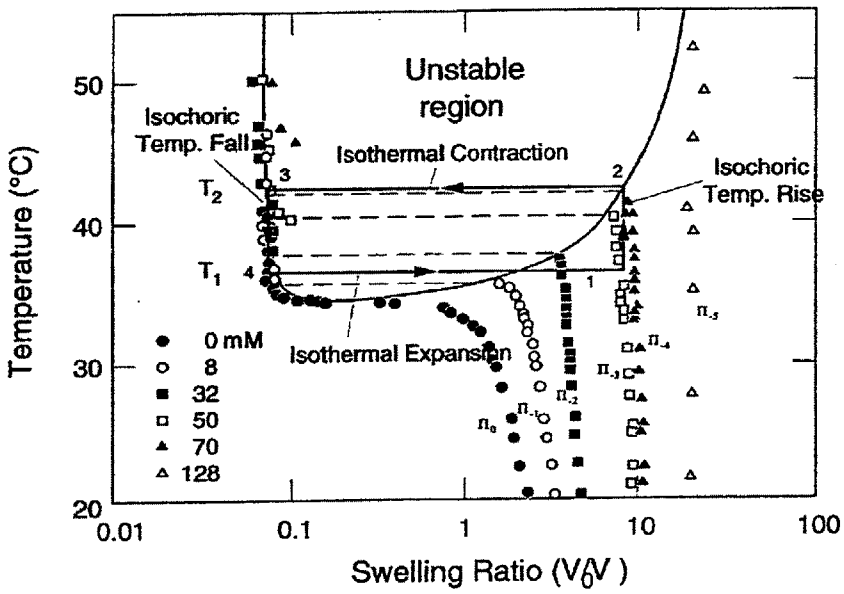

Figure 2.13: Volume transition cycle for a NIPA/sodium acrylate gel (from reference [26])

thesis [26] and shows the volume transitions for N-isopropylacrylamide (NIPA) gels with differing amounts of added sodium acrylate. NIPA gels are similar to HPC in terms of volume responsiveness, and this figure should provide the reader with an idea of some achievable values. Without any sodium acrylate, NIPA transitions at approximately $35°C$. By controlling the amount of sodium acrylate in the gel solution, transition temperatures T_1 and T_2 can be altered.

As stated, the purpose of the HPC gel mixture is to provide a fluid whose viscosity can be controlled. It is difficult to measure the viscosity associated with a gel suspension. The "two-part" fluid formed by a gel and its solvent exhibits thixotropic behavior. Thixotropy is a property that causes a gel to liquefy in the presence of a shear force. This behavior makes it difficult to obtain meaningful viscosity information using a viscometer. A typical viscometer works by measuring the retarding forces on a spindle as it rotates in a fluid at a preset speed. If the fluid being measured is thixotropic, the retarding force can change significantly under dynamic, rotating conditions. If the applied torque is low enough, the

viscosity may appear extremely high. However, once the torque is great enough to cause shearing the viscosity will drop noticeably.

The viscosity of the HPC gel solution approaches that of water, i.e. 0.89 centipoise, when the gel beads are shrunken. In this situation the gel beads occupy a small volume of the water solution and don't effect the viscosity significantly. When the gel beads are expanded, thixotropy makes viscosity measurements difficult. In this case, the solution will effectively behave as a solid as long as no significant shear forces are present. Figure 2.14 are photos taken of an HPC solution in its two phase states. Figure 2.14 (a) shows the solution at room temperature. Even in the presence of gravity the solution maintains its "shape". After heating above 40^oC, shown in Figure 2.14 (b), the solution behaves as a liquid and redistributes itself under the influence of gravity.

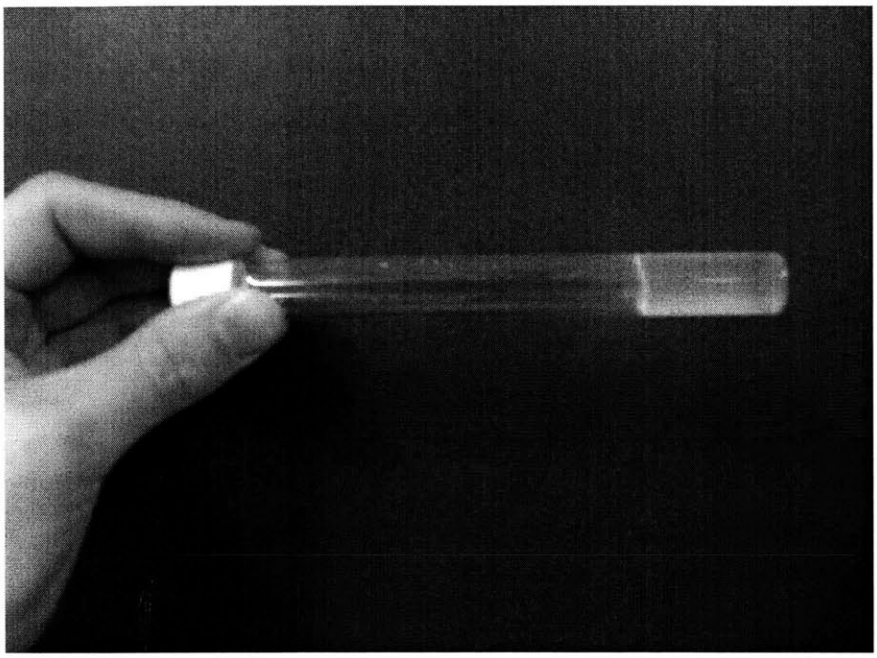

(a) Solid gel

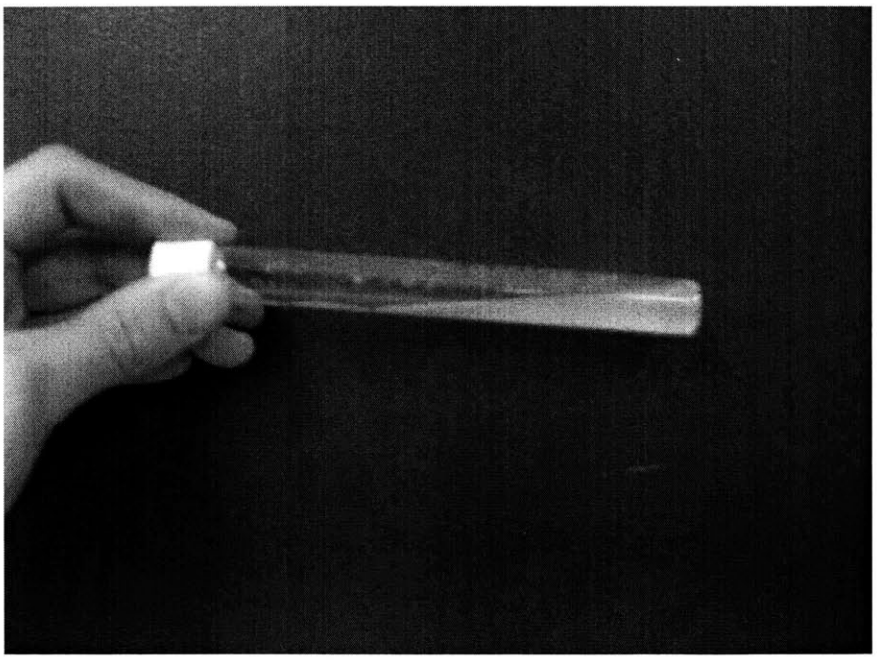

(b) Liquid gel.

Figure 2.14: HPC gel beads in H_2O

2.3.2 Principle of Operation

The HPC gel beads discussed in the previous section provide an interesting means of modulating viscosity and as a result, a DVA's moment of inertia. Because of the discontinuous or nearly discontinuous phase transition exhibited by the gel, intermediate volumes do not generally represent stable, static equilibria and cannot be maintained without some form of active control. Consequently, it is convenient to think of a polymer-filled container as taking on two possible moments of inertia, one for each gel state. This is a safe assumption providing the control scheme can adequately transition the gel back and forth between states. The ability to assume only two static states limits the number of possible anti-resonant frequencies that can be achieved. To increase this number, the number of states must also grow. A logical way to increase states using the "binary" behavior of the gel is to compartmentalize the gel container into n separate sections of varying gel mass. By subdividing the container in this way, 2^n anti-resonant states are made possible depending on the selected combination of compartments.

For the torsional damper, the natural frequency of the DVA network largely determines the anti-resonant location. Replacing the mass term in the expression for the natural frequency of the linear DVA case gives the natural frequency of the torsional case,

$$\omega_{n,2} = \sqrt{\frac{K_2}{J_2}}. \tag{2.32}$$

The possible values that J_2 can take on depend on the achievable inertias for each container when the gel is either solid or liquefied. Assume that when the gel is in its liquid state, the resulting gel inertia is small compared to the inertia of the container. The maximum anti-resonant frequency is therefore limited by the inertia of the container. The lowest anti-resonant frequency occurs when all the containers behave as solid, fixed masses. Because the natural frequency has the dependence shown in (2.32) the manner in which the compartment inertias should be picked is not obvious. While it is still possible to pick the ratios in a binary manner (making the inertia of each subsequent container twice that of the previous

one), the natural frequency will not necessarily increment in a monotonic fashion. This is further complicated by the fact that the inertia of the container is finite.

All possible anti-resonances in a band-limited frequency range can not be achieved with a discrete number of states. Instead, the goal of this idea is to rely on the non-zero width of each notch to sufficiently "bin" a range of frequencies. With an adequate number of bins, a wide and useful frequency range is possible. Figure 2.15 illustrates the basic strategy for a hypothetical three-chamber damper. Instead of showing all the states in detail, this plot shows the minimum achievable response using those states and compares it against the undamped response. This minimum response makes evident the location of the eight anti-resonant "bins." Furthermore, the minimum response eliminates the threat of the two resonant peaks normally present with only one anti-resonance, providing that the disturbance is sufficiently band-limited.

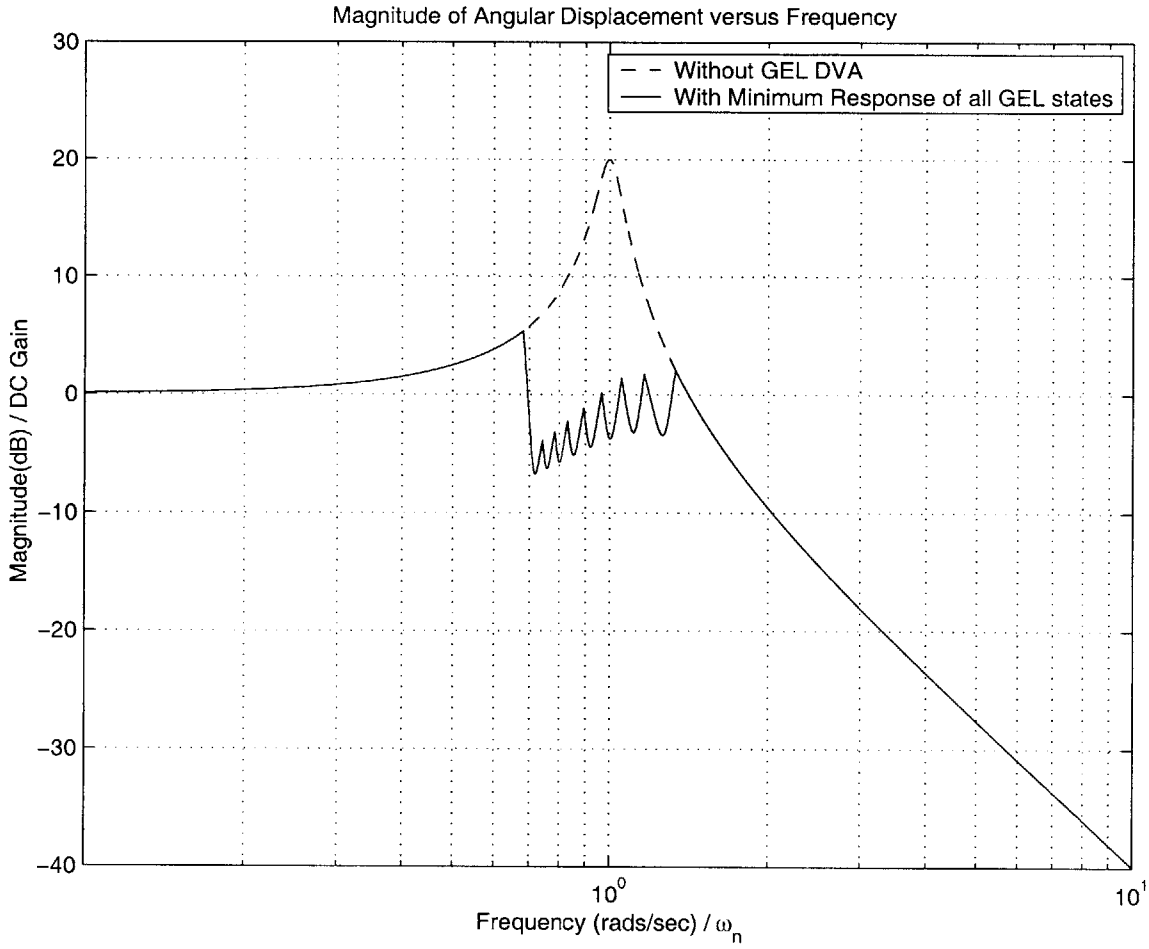

Figure 2.15: Frequency response of a servomechanism with and without a hypothetical 3-Chamber gel damper.

2.3.3 The Compartmentalized Gel Container

The design of the gel container is in many ways critical to the success of this type of damper. In order to be successful the container must meet a number of criteria.

(1) The container must subdivide the gel mass appropriately.

(2) Each compartment must be sealed to prevent the escape of solvent into the environment.

(3) The container must be mechanically sound, capable of supporting the solvents additional mass.

(4) The inertia of the container should be small compared to the inertia of a solidified gel compartment.

(5) It must be possible to integrate the induction heating elements in such as way as to not interfere with the operation of the damper.

(6) Adequate spacing or insulating materials may be needed to prevent heat from bleeding into unheated compartments.

Figure 2.16 depicts what a possible three-chamber gel container might look like. This particular arrangement consists of three annular chambers on a central hollow axis. The inertia of each gel-filled compartment can be varied by controlling the outer radius of the annulus. Surrounding the axis at the center of each annulus is the induction heating target for that chamber. To maximize coupling the induction heating coil in this system resides in the center of the hollow axis. The space inserted between chambers is meant to prevent heat transfer from one container to the next, but also to reduce inductive cross-coupling between targets– an issue discussed in Chapters 3 and 4. The largest container is placed in the center because this location gives the greatest coupling between target 1 and the induction coil. As will be shown, greater coupling translates into greater power delivered to the target. Practically speaking, the target that must heat the most gel mass should also have the best coupling to do so.

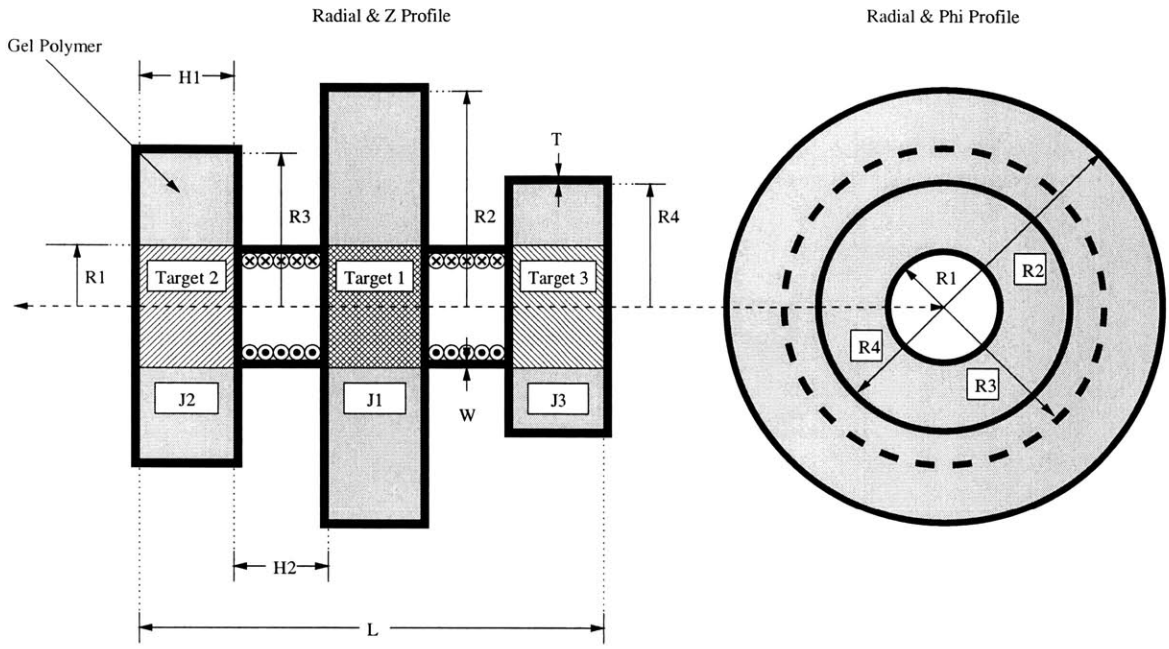

Figure 2.16: Rotational DVA SDOF model.

Designing the container to give the desired inertial states requires that the inertia of the container, with and without the gel, be calculated. In general, the inertia of an object with density ρ is defined by the volume integral,

$$J = \int \rho R^2 \, dV, \tag{2.33}$$

where R is the distance from the axis of rotation to the incremental volume. All of the important inertias for the container shown in Figure 2.16, can be calculated by knowing the inertia of the toroid-shaped mass seen in Figure 2.17. Solving (2.33) for the toroid, gives

$$J_{Toroid} = \int_{R_a}^{R_b} \rho R^2 (2\pi R l) \, dR = 2\pi\rho l \int_{R_a}^{R_b} R^3 \, dR = \frac{\rho\pi l}{2}(R_b^4 - R_a^4). \tag{2.34}$$

Referring to Figure 2.16, the inertia contributed by the immobilized gel in chamber n can be expressed using (2.34) as

$$J_{Gel-n} = \frac{\rho_{Gel}\pi H_1}{2}(R_{n+1}^4 - R_1^4). \tag{2.35}$$

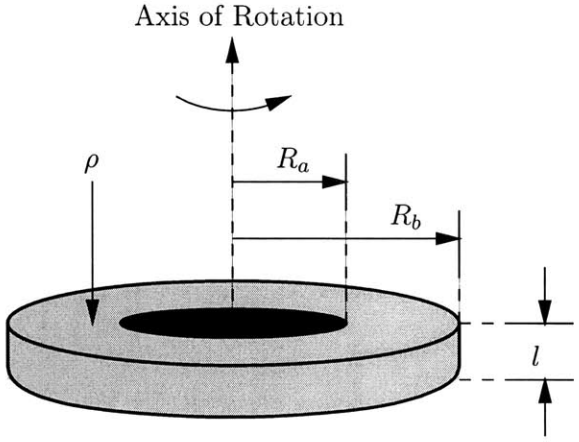

Figure 2.17: Solid Toroid

The moment of inertia for a single chamber, without the gel, can be found by decomposing the top, bottom and sidewalls of the chamber into three respective toroids and summing the inertia of each,

$$J_{Chamber-n} = \rho_{Chamber}\pi \left[\frac{H_1}{2}((R_{n+1}+T)^4 - R_{n+1}^4) + T(R_{n+1}^4 - R_1^4) \right]. \tag{2.36}$$

The hollow post that serves as the axis for the container also contributes to the inertia,

$$J_{axis} = \frac{\rho_{axis}\pi l}{2}(R_1^4 - (R_1 - w)^4). \tag{2.37}$$

The total inertia of the container, sans gel, can be found by summing the inertia of each chamber and the hollow post,

$$J_{container} = J_{axis} + \sum_n J_{Chamber-n}. \tag{2.38}$$

The maximum theoretical inertia including the gels is then given by,

$$J_{max} = J_{container} + \sum_n J_{Gel-n}. \tag{2.39}$$

2.4 Hybrid Gel Polymer DVA

Dynamic vibration absorbers that incorporate a variable moment of inertia are clearly useful for building tunable torsional dampers. This approach can also be extended to linear dampers by building a hybrid DVA that experiences both linear and rotational motion. In a hybrid system, excitations in a linear direction can be converted into rotational motion allowing the basic principle of the DVA to be applied. One such idea is presented here.

Figure 2.18 shows a simple mechanical diagram for a hybrid DVA. As before, M_1 and K_1 represent the mass and compliance of the primary structure to be damped. The DVA is more complicated than those seen previously, but can basically be described as an inverted pendulum with springs. M_2 is the mass intended as the variable-inertia component of the DVA and rotates about an axis that is fixed to the frame of the primary structure. As before, this mass is comprised of a cylindrical container filled with the gel bead fluid. Extending from the axis of rotation is an additional mass, M_3. Without the presence of this eccentric mass, the center of mass would lie at the axis of rotation and the system would be incapable of experiencing a torque as the result of a vibration in the X direction. The restoring force for the DVA is provided by two springs of value $K_2/2$ attached to a fixed point on the rotating cylinder. The distance from the pivot point to the center of mass or centroid, is denoted as l in the diagram and the pendulum has a moment of inertia J. When vertical the pendulum is chosen to be at an angle π and the direction of positive rotation is shown in the counter-clockwise direction.

The dynamic behavior of the hybrid damper is now analyzed. Summing the horizontal forces on the primary mass gives,

$$F = M_1\ddot{X} + \beta_1\dot{X} + K_1X + K_2r_1\theta + H. \tag{2.40}$$

The horizontal force H acting on the pivot point can be expressed as

$$H = (M_2 + M_3)(\ddot{X} + l\ddot{\theta}cos(\theta) - l\dot{\theta}^2sin(\theta)). \tag{2.41}$$

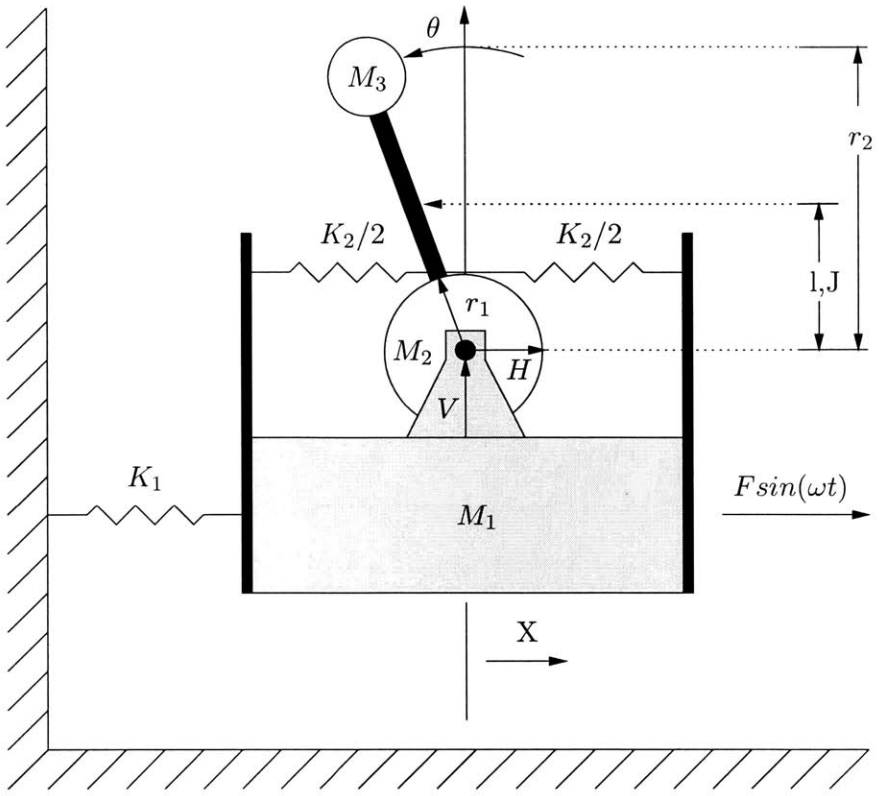

Figure 2.18: Rotational DVA SDOF Model

Substituting (2.41) into (2.40) gives the first equation of motion for the system,

$$F = M_1\ddot{X} + \beta_1\dot{X} + K_1X + K_2r_1\theta + (M_2 + M_3)(\ddot{X} + l\ddot{\theta}cos(\theta) - l\dot{\theta}^2sin(\theta)). \tag{2.42}$$

The second equation of motion can be determined by summing the forces perpendicular to the pendulum,

$$Vsin(\theta) + Hcos(\theta) = (M_2 + M_3)(gsin(\theta) + l\ddot{\theta} + \ddot{X}cos(\theta)). \tag{2.43}$$

The forces horizontal (H) and vertical (V) to the pivot point can be eliminated from equation (2.43) by summing the moments around the centroid of the pendulum. Carrying this out gives,

$$-Vlsin(\theta) - Hlcos(\theta) = J\ddot{\theta} + \beta_2\dot{\theta} + K_2r_1l\theta. \tag{2.44}$$

Combining (2.43) and (2.44) gives the second equation of motion,

$$0 = (M_2 + M_3)(gsin(\theta) + l\ddot{\theta} + \ddot{X}cos(\theta)) + J\ddot{\theta} + \beta_2\dot{\theta} + K_2r_1l\theta. \tag{2.45}$$

To analyze the system further the nonlinear equations of motion can be linearized. Let the angle θ, take the form

$$\theta = \pi + \phi, \tag{2.46}$$

where ϕ is a change in the angle from the resting position at $\theta = \pi$. For small ϕ, the following simplifications can be made,

$$cos(\theta) \approx -1, \tag{2.47}$$

$$sin(\theta) \approx -\phi, \tag{2.48}$$

and

$$\dot{\theta}^2 \approx 0. \tag{2.49}$$

Ignoring the influence of gravity and applying the above simplifications to (2.42) and (2.45) lead to the linearized equations of motions,

$$F = (M_1 + M_2 + M_3)\ddot{X} + \beta_1\dot{X} + K_1X - (M_2 + M_3)l\ddot{\phi} + K_2r_1\phi, \tag{2.50}$$

and

$$0 = (J + (M_2 + M_3)l^2)\ddot{\phi} + \beta_2\dot{\phi} + K_2r_1l\phi - (M_2 + M_3)l\ddot{X}. \tag{2.51}$$

Converting (2.50) and (2.51) to the s domain and rearranging gives the following algebraic equations,

$$F(s) = X(s)\left\{(M_1 + M_2 + M_3)s^2 + \beta_1 s + K_1\right\} - \phi(s)\left\{(M_2 + M_3)ls^2 - K_2r_1\right\}, \tag{2.52}$$

and

$$\phi(s)\left\{Js^2+\beta_2 s+K_2r_1l+(M_2+M_3)l^2s^2\right\}=X(s)\left\{(M_2+M_3)ls^2\right\}. \tag{2.53}$$

Equations (2.52) and (2.53) can now be combined to give a rational transfer function of the form,

$$\frac{X(s)}{F(s)}=\frac{N(s)}{D(s)}, \tag{2.54}$$

where

$$N(s)=[J+(M_2+M_3)l^2]s^2+\beta_2 s+K_2r_1l, \tag{2.55}$$

and the denominator is a fourth-order polynomial,

$$D(s)=As^4+Bs^3+Cs^2+Ds+E, \tag{2.56}$$

with the following coefficients,

$$A=J(M_1+M_2+M_3)+M_1(M_2+M_3)l^2), \tag{2.57}$$

$$B=\beta_2(M_1+M_2+M_3)+\beta_1(J+(M_2+M_3)l^2), \tag{2.58}$$

$$C=K_1(J+(M_2+M_3)l^2)+K_2(M_1+2(M_2+M_3))r_1l+\beta_1\beta_2, \tag{2.59}$$

$$D=K_1\beta_2+K_2\beta_1r_1l, \tag{2.60}$$

and

$$E=K_1K_2r_1l. \tag{2.61}$$

The moment of inertia J is the sum of inertias due to the eccentric point mass M_3, and cylindrical mass M_2, or

$$J=\frac{1}{2}M_2r_1^2+M_3r_2^2. \tag{2.62}$$

The centroid of the system l, can also be written in terms of other parameters as

$$l = \frac{M_3 r_2}{M_2 + M_3}. \tag{2.63}$$

The anti-resonance of the damper is determined by the zeroes of (2.54) or the roots of (2.55). The natural frequency ω_n, and damping ratio ζ, can be found by expressing (2.55) in the following form,

$$Num(s) = s^2 + 2\zeta\omega_n s + \omega_n^2. \tag{2.64}$$

Rewriting in this form and substituting (2.62) and (2.63) leads to the natural frequency,

$$\omega_n = \sqrt{\frac{K_2 M_3 r_1 r_2}{(\frac{1}{2}M_2 r_1^2 + M_3 r_2^2)(M_2 + M_3) + (M_3 r_2)^2}}, \tag{2.65}$$

and damping ratio,

$$\zeta = \frac{\beta_2(M_2 + M_3)}{2\sqrt{K_2 M_3 r_1 r_2[(\frac{1}{2}M_2 r_1^2 + M_3 r_2^2)(M_2 + M_3) + (M_3 r_2)^2]}}. \tag{2.66}$$

Alternatively, the Q associated with the anti-resonance can be written in terms of the damping ratio using the following identity,

$$Q = \frac{1}{2\zeta}. \tag{2.67}$$

As discussed previously, when the gel mass M_2 is thermally excited past the critical temperature point, it will undergo a phase change in volume. The solvent once contained within the interstitial spaces of the gel matrix, will now be free to flow and the mass will behave as a liquid once again. Because M_2 is no longer a rigid mass with respect to rotational motion, it is inertially decoupled from the system. In theory if the gel solvent behaved as an ideal fluid, the value of M_2 would now depend entirely on the mass of the gel container. This is a theoretical limit, in practice some of the fluid will experience the rotating force, particularly at the boundaries where the coupling is greatest. If the viscosity of the fluid is low enough, the term M_2 in equations (2.65) and (2.66) will effectively decrease. In this

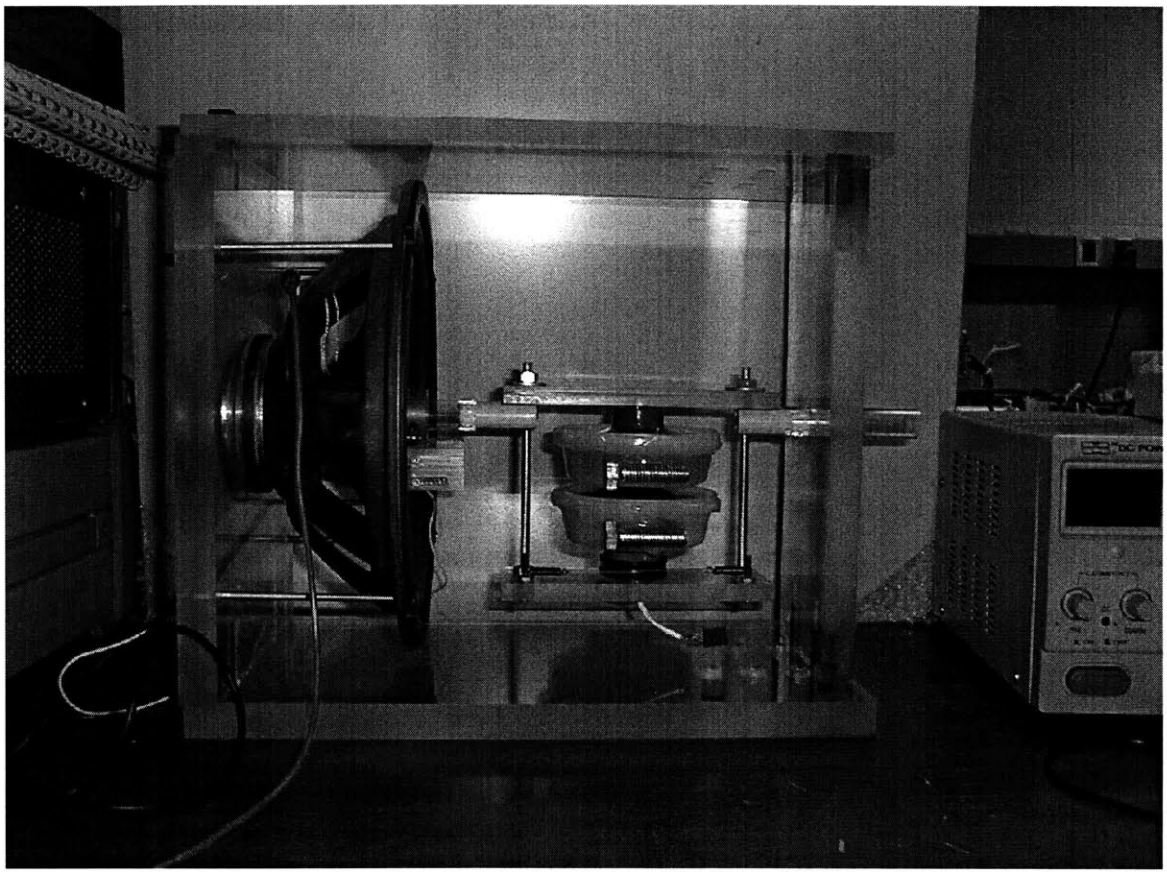

Figure 2.19: Hybrid Gel DVA prototype.

liquefied state, the gel mass will also contribute damping to the system, increasing β_2. The extent to which this is true is not quantified in this thesis and remains a subject for future work.

To test these ideas a prototype hybrid gel damper was built for experimentation. A photo of the prototype is shown in Figure 2.19. A woofer acts as the vibration source and is mechanically coupled to the damper. An Analog Devices, ADXL202EB accelerometer evaluation board [1] is used to measure the acceleration of the primary structure. The variable inertia in the prototype is the result of a two-chamber system; each chamber is filled with a different amount of gel mass. Because this system was built prior to the work on induction heating targets discussed in Chapters 3 and 4, a cruder approach was used to heat each container. A nickel sleeve was placed around the inner radius of each annulus

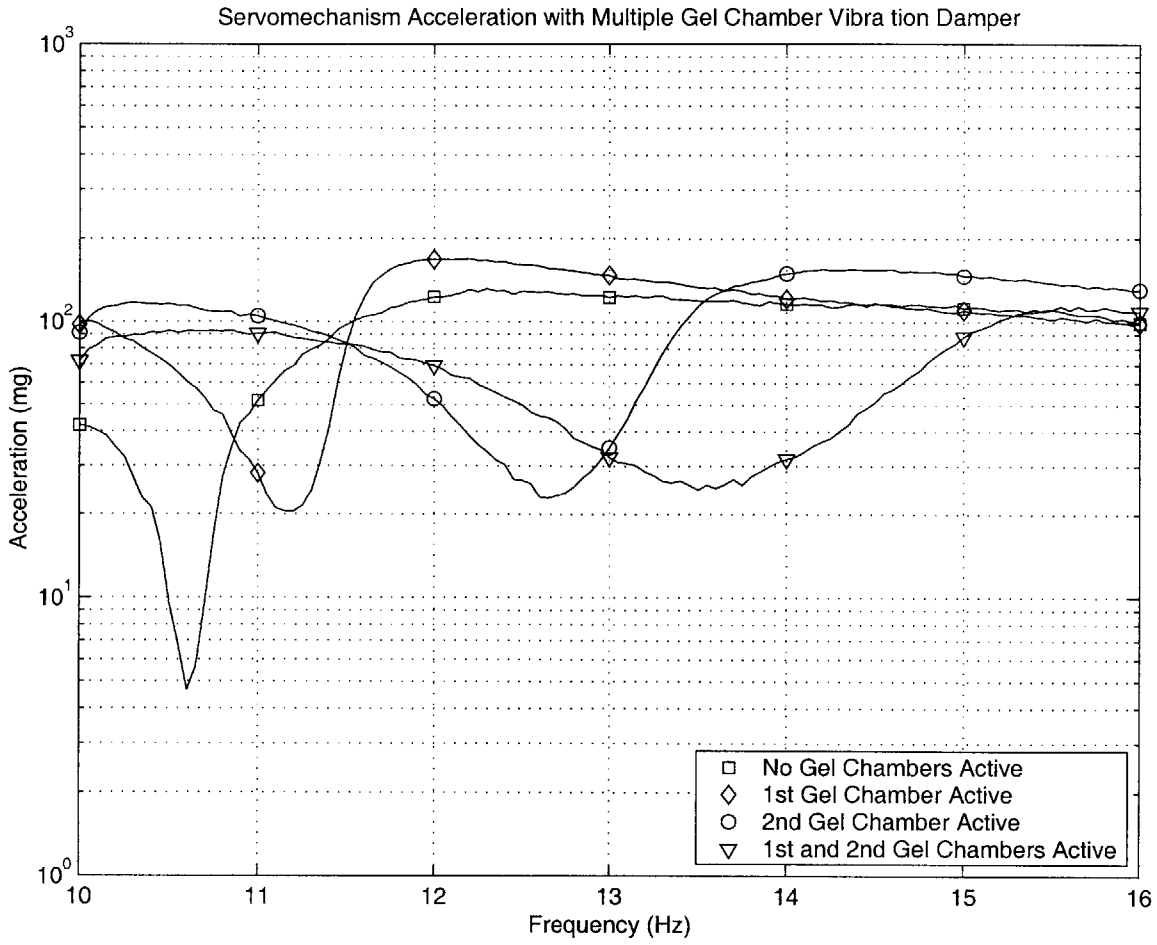

Figure 2.20: Experimental acceleration response of primary inertia with gel dynamic vibration asorber.

and a separate induction coil was used to heat each target.

The measured frequency response of the primary structure for all four combinations of liquefied gel compartments is shown in Figure 2.20. It is clear that a distinct anti-resonance exists for each possible moment of inertia. The lowest anti-resonant frequency is observed to have the highest Q. This occurs for two reasons: the Q naturally increases with a larger moment of inertia and there are less losses when the gel mass is solid. Recall that when a gel is liquefied, more damping exists because of drag forces as the liquid slides along the sidewalls of the container. Even with this additional damping most of the liquefied states achieve attenuation factors of about five.

2.5 Chapter Summary

This chapter builds up to the gel polymer vibration damper but begins by reviewing the basic fundamentals of the classic dynamic vibration absorber. Because a large number of important mechanical systems can be modeled by a second order systems, a lumped SDOF spring-mass model was first introduced and analyzed. The effect of coupling a DVA onto such a system was then considered for the case of constant tuning and for different damping ratios of the DVA. It was seen that this approach provided relief in a narrow-band of frequencies but also introduced additional resonances which may become problematic. By choosing the resonant frequency of the DVA using the optimal tuning method it was possible to lower the resonant behavior of the composite structure across all frequencies of interest.

To address the issue of the narrow-attenuation range, the notion of a semi-active damper that could adjust its spring constant was then discussed. By changing its spring constant the location of the anti-resonance could be moved to track the frequency of the disturbing resonance. The DVA concept was then extended to rotational systems where the natural frequency could also be modified by changing the moment of inertia. A variable viscosity fluid was proposed as a means of changing the inertia of the container it fills. It was seen that the one way to make a fluid whose viscosity could be varied was with a collection of HPC based gel beads suspended in water. Above a set temperature the gels shrink allowing the water to move freely, while at low temperatures the gel acts like a sponge and prevents the water from moving.

This gel solution was then utilized in a hybrid DVA that incorporated the rotational motion of the container as a way to absorb the excess linear vibrations experienced by the primary structure. The equations of motion for this system were analyzed and a prototype was built as a proof of concept. In the experiment two annular chambers of varying amounts of gel mass were used to change the inertia in discrete steps. It was observed that four distinct anti-resonant frequencies could be generated, one for all binary heating combinations.

For testing purposes the prototype used a simplistic induction heating scheme that required a separate induction coil for heating each chamber. In the remaining chapters a collection of targets and power electronics will be discussed that will allows such a damper to function with the need for only one induction coil.

Chapter 3

Nonresonant, Frequency Selectable Induction Heating Targets

IN this work, a "frequency selectable induction heating target" is a circuit that dissipates power when placed in a time-varying magnetic field and does so by heating preferentially over some frequency range (compared to other induction targets). This does not mean that the heating is necessarily exclusive. The target simply heats more than the remaining targets by a factor that is deemed large enough for a particular application. In some applications a factor of two may be sufficient, in others a larger degree of separation may be necessary. If a collection of these targets are coupled to a single induction coil, it becomes possible to excite a desired target by driving the induction coil at the target's preferred frequency. With the right frequency content powering the primary coil, combinations of targets can be heated. Placing one of these targets in each gel compartment, allows each gel-filled chamber to be individually heated.

For our purposes, frequency selectable induction targets can be divided into two categories: nonresonant and resonant. The latter involves the creation of resonant RLC circuits, each inductively coupled to a primary heating coil. In this case, a target's capacitor is chosen to give that target a unique resonant frequency where it will heat preferentially. The nonresonant approach utilizes RL circuits as targets [36]. Varying the target's resistance achieves selective heating, foregoing the need for a resonant capacitor. In general the nonresonant targets are less "selective" than their resonant counterparts, offering smaller separations in power. However, there are a number of reasons that make them well suited

to the gel damper project and other applications.

(1) Nonresonant targets are easier to construct.

(2) They can be designed to consume very little volume.

(3) Capacitors may not be well suited to immersion in solvents, water or otherwise.

(4) Capacitors impose significant limitations on the absolute power that can be dissipated.

(5) The frequency characteristics of resonant targets are more susceptible to variation because the capacitor's value may fluctuate with temperature or voltage level.

We first examine nonresonant targets and return to the resonant targets in Chapter 4.

3.1 Nonresonant Induction Heating Targets

The simplest structure that can be heated by induction is a plain metal conductor. In this case, placing the conductor in a time-varying magnetic field leads to ohmic dissipation as the result of induced eddy currents near the conductor's surface. The distribution of eddy currents is greatest near the surface, decaying into the material at a rate that is governed by the skin depth δ, of the material. Although the skin depth is geometry and material dependent, for a number of practical cases it has the form

$$\delta = \sqrt{\frac{2}{\mu\sigma\omega}}, \tag{3.1}$$

where μ and σ are the magnetic permeability and conductivity of the conductor respectively. In most induction heating applications the frequency ω of the magnetic field is high enough to cause the field to decay very quickly into the conductor. As the frequency increases, the current is forced to flow in a smaller and smaller cross-sectional area of the conductor. This results in increased dissipation, as the effective resistance seen by the current grows too. To

increase power dissipation further, conductors that are ferromagnetic are usually employed. Ferromagnetic metals have significantly higher permeabilities, leading to smaller skin depths for a given frequency. They also contribute additional loss mechanisms proportional to frequency because the magnetic domains within the material must continually do work by realigning with the magnetic field as it varies. For the purposes of this thesis we will examine nonferromagnetic materials, leaving the potential use of ferromagnetic materials for future exploration.

A conductor's geometry plays a crucial role in determining the distribution of induced eddy currents. These currents, in turn, affect how the external time-varying H-fields is terminated within the conductor. When a conductor is being used to "shield out" a magnetic field, there is a tendency to make the conductor thick enough to fully terminate the fields. However, there is an additional and often overlooked solution which involves the use of a conductor that is relatively thin. If properly designed, a thin-walled conductor whose thickness is small compared to its skin depth δ, can also act as a good shield. The explanation for this seeming paradox is borrowed from [13] and can be resolved by examining the two cases illustrated in Figure 3.1.

For each case a perfectly conducting $\supset$ - shaped conductor is driven by a sheet current $K_s = K_o sin(\omega t)$, where it is assumed that each conductor extends a long width w in the direction perpendicular to the page. In case (a) the block of conductor is surrounded by the perfectly conducting $\supset$ - shaped conductor. At low frequencies the currents flow around the perfect conductor; as the frequency is increased, currents begin to flow along the left edge of the block where the reactance is lower. For high frequencies $\delta << b$, and the current magnitude will decay exponentially as shown. At this extreme, the interior of the block will be effectively shielded from the H-field at points where the current has decayed to zero. The portion of the conductor to the right of this region could then be removed without altering the degree of shielding.

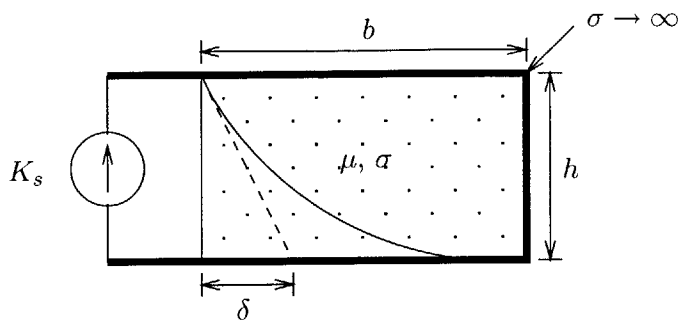

(a) Thick-walled conductor.

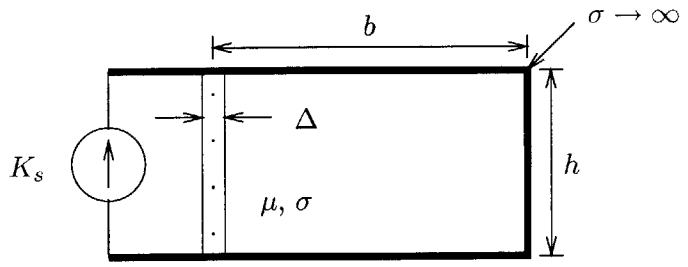

(b) Thin-walled conductor.

Figure 3.1: Shielding in thick-walled versus thin-walled conductors.

In case (b) where the conductor's thickness is consistent with $\Delta << \delta$, the conductor forms a current divider with the $\supset$ - shaped conductor. If we define the conductance per unit width $G = \sigma\Delta/h$ and the inductance times a unit width $L = \mu bh$ for these structures, the current through the thin-wall can be expressed as

$$K_{thin-wall} = \frac{j\omega LG}{1 + j\omega LG} K_o. \tag{3.2}$$

This structure will act as an effective shield as long as $\omega >> \frac{1}{LG}$. Clearly, the mechanism behind case (b) is different from (a). Unlike the previous case, this structure does not terminate the field because the conductor is thick enough, but because the associated inductance is so large that there is considerably less impedance for the current to flow through the resistive thin-wall then to store energy in the form of a magnetic field to the left of the wall. The frequency response of (3.2) has a form that is identical to the current flowing through the resistive leg of a parallel RL circuit driven by a current source. Consequently, a thin-walled conductor can be modeled as a parallel RL circuit provided that $\Delta << \delta$.

Of the two cases examined, case (b) offers promise for making a suitable induction target. "Thin-walled" conductors are ideal because they require little volume. Moreover, the assumption that the conductor thickness obeys $\Delta << \delta$ leads to a simple circuit model description for each target. The primary coil used to excite these targets can be driven with either a current or voltage source. In general, the current-drive case tends to yield simpler expressions for the behavior of the system. However, many sinusoidal drives command a voltage at the output; therefore, both drive conditions are considered in this thesis.

3.2 Current-Drive Case

Driving the primary coil with a current instead of a voltage results in fewer system dynamics and is considered first.

3.2.1 Single Target

To understand how a set of targets can be made frequency selectable, it is easiest to begin with one target. Figure 3.2 shows such a system. In this example, a sheet of metal has been formed into a single-turn inductor and placed within a solenoid. The solenoid serves as the primary-induction coil, with inductance L_0 and resistance R_0. The single-turn conductor acts as the induction target, having its own inductance L_1, and resistance R_1. Together, the solenoid and single-turn conductor can be modeled as a system of coupled inductors also shown in Figure 3.2.

The power dissipated in the induction target can be found from the $\frac{I_1}{I_0}(s)$ transfer function. To determine this transfer function an expression for the induced voltage across L_1 is first found in the s domain,

$$V_1 = L_{01} s I_0 + L_1 s I_1, \tag{3.3}$$

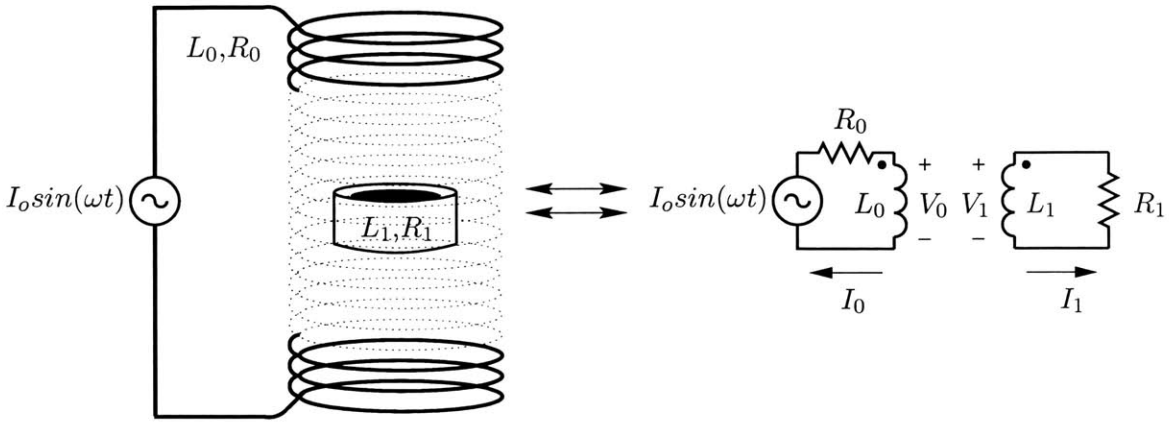

Figure 3.2: Induction heating circuit for one nonresonant target, in this case the primary coil is driven by a sinusoidal current.

where L_{01} is the mutual inductance between inductors L_0 and L_1. Next, Ohm's law gives the voltage on R_1,

$$V_1 = -I_1 R_1. \tag{3.4}$$

Substituting (3.4) into (3.3) leads to the following relationship

$$0 = L_{01} s I_0 + (L_1 s + R_1) I_1, \tag{3.5}$$

which can be rearranged to give the transfer function,

$$\frac{I_1}{I_0}(s) = -\frac{L_{01} s}{L_1 s + R}. \tag{3.6}$$

As expected (3.6) is identical in form to (3.2). To find the power dissipated, the magnitude of the transfer function is needed. Letting $s \rightarrow \omega$ and solving for the magnitude yields,

$$\left| \frac{I_1}{I_0}(j\omega) \right| = \left| \frac{L_{01} j\omega}{L_1 j\omega + R_1} \right| = \frac{L_{01}\omega}{\sqrt{(L_1\omega)^2 + R_1^2}}. \tag{3.7}$$

The current I_0 is determined by the current source,

$$I_0 = I_o sin(\omega t). \tag{3.8}$$

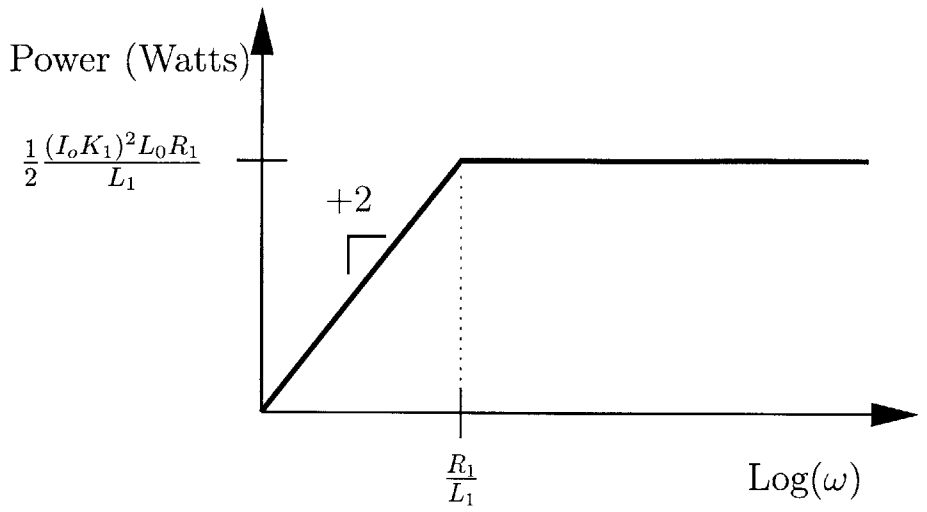

Figure 3.3: Power dissipation as a function of frequency for a single LR circuit coupled to an induction coil driven by a sinusoidal current of amplitude I_o.

Using equations (3.7) and (3.8) the time-averaged power dissipated in R_2 can be found. For a sinusoidal excitation

$$\langle P_1(\omega)\rangle = \frac{1}{2} I_1^2 R_1 = \frac{1}{2}\frac{(I_o L_{01}\omega)^2}{[(L_1\omega)^2 + R_1^2]} R_1. \tag{3.9}$$

At this point it is useful to define the coupling coefficient between L_0 and L_1 as

$$K_1 = \frac{L_{01}}{\sqrt{L_0 L_1}}. \tag{3.10}$$

The coupling coefficient is a parameter that varies from zero to one and is an indication of how much flux generated by one inductor links the other. Combing equations (3.9) and (3.10) leads to the asymptotic power-versus-frequency curve shown in Figure 3.3. As the frequency of excitation is increased from DC, the power dissipated also increases as more and more current flows in the target. Past the frequency break-point determined by the target and denoted as

$$\omega_1 = \frac{R_1}{L_1}, \tag{3.11}$$

the current asymptotically approaches its maximum value. Likewise the power dissipated

in the target reaches its maximum as $\omega \to \infty$,

$$\langle P_1(\omega \to \infty) \rangle = \frac{1}{2}\frac{(I_o K_1)^2 L_0 R_1}{L_1} = \frac{1}{2}(I_o K_1)^2 L_0 \omega_1. \tag{3.12}$$

Equation (3.12) reveals that once the break-point frequency of the target has been chosen, the only way to increase the maximum power dissipation in the target is to increase the amplitude of the current I_o, improve the coupling K_1, or make the primary inductance L_0 larger.

3.2.2 Multiple Targets

The results of the previous section apply readily to the case were multiple targets are coupled to the primary coil, providing the degree of cross-coupling between targets is weak or negligible. This can often be satisfied by spacing the targets far enough away from each other so that their respective coupling coefficients are minimized. If this restriction is met, the single load case suggests a way to make nonresonant targets that are frequency selectable. The goal is to produce a family of power curves similar to Figure 3.3, where the curves have been spaced in frequency and power such that each curve has a magnitude greater than the remaining curves for some frequency range. In the broadest sense, the only thing that can be done is to move the break-point of the curve or the curve's maximum value.

Because it is often desirable to have induction targets with similar geometries or shapes, the only useful parameter a designer might have control over is the resistance of the target. The resistance changes both the break-point and the maximum achievable power in a useful way. If each target is designed to have a similar self-inductance L_n, but a different resistance R_n, a frequency selectable heating scheme can be devised. An example is shown in Figure 3.4, where the induction coil from Chapter 3 is now coupled to three shorted wires or sheets of different alloys formed into single-turn inductors with different resistances. Once again the primary coil is driven by a sinusoidal current with amplitude I_o.

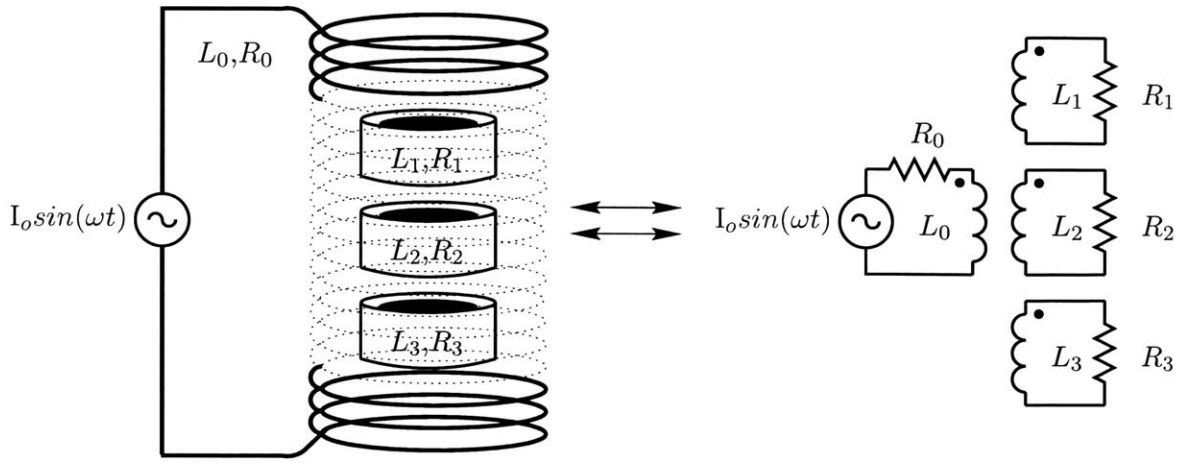

Figure 3.4: Induction heating circuit for three different targets, in this case the primary coil is driven by a sinusoidal current.

The cross-coupling between induction targets is negligible, so that the power delivered to a target is independent of the power delivered to any remaining target. In this case we may express the time average power dissipated in a target n using the results from the previous section,

$$\langle P_n(\omega) \rangle = \frac{(I_o K_n \omega)^2 L_0 L_n R_n}{2[(L_n \omega)^2 + R_n^2]}. \tag{3.13}$$

The term K_n represents the coupling coefficient between the primary coil and target n, and is defined using the mutual inductance L_{0n}, between L_0 and L_n:

$$K_n = \frac{L_{0n}}{\sqrt{L_0 L_n}}. \tag{3.14}$$

If target n (1, 2, or 3) is driven at its -3dB break-point frequency in Hertz

$$f_n = \frac{\omega_n}{2\pi} = \frac{R_n}{2\pi L_n}, \tag{3.15}$$

the equation for time average power reduces to the following:

$$\langle P_n(f_n) \rangle = \frac{\pi}{2} L_0 (K_n I_o)^2 f_n, \tag{3.16}$$

If the targets are further constrained so that the resistance between one target and the next differs by a factor of α, i.e. $R_{n+1} = \alpha R_n$, it can be shown that the time-averaged power dissipated in R_n when driven at its break-point frequency with respect to the closest higher frequency target is

$$\langle P_n(\omega_n)\rangle = \frac{\alpha^2+1}{2\alpha}\left(\frac{K_n}{K_{n+1}}\right)^2 \langle P_{n+1}(\omega_n)\rangle\,. \tag{3.17}$$

Similarly, the time-averaged power dissipated in R_n with respect to the closest lower frequency target is

$$\langle P_n(\omega_n)\rangle = \frac{\alpha^2+1}{2\alpha}\left(\frac{K_n}{K_{n-1}}\right)^2 \langle P_{n-1}(\omega_n)\rangle\,. \tag{3.18}$$

These results are more readily appreciated by plotting the power profiles for three hypothetical targets versus frequency as shown in Figure 3.5(a). The coupling coefficient of all targets has been chosen equal to 0.3 and the three targets have break-point frequencies that are separated by factors of five, specifically 4 kHz, 20 kHz, and 100 kHz. Under these constraints each target experiences preferential heating with respect to the remaining targets over some frequency range. The extent of preferential heating is given as a ratio in Figure 3.5(b) for this example. Because of the identical coupling and the even spacing in break-point frequencies, each target experiences power dissipation of at least 2.6 times more than any of the remaining targets when driven at its break-point frequency– as suggested by equations (3.17) and (3.18). Equation (3.16) makes apparent that a fixed current results in higher power dissipation at higher frequencies. In order to equalize the absolute power delivered to all targets the amplitude of the current driving the primary coil must be controlled via the following relationship:

$$I_0(\omega_{n+1}) = \frac{1}{\sqrt{\alpha}}\frac{K_n}{K_{n+1}} I_0(\omega_n). \tag{3.19}$$

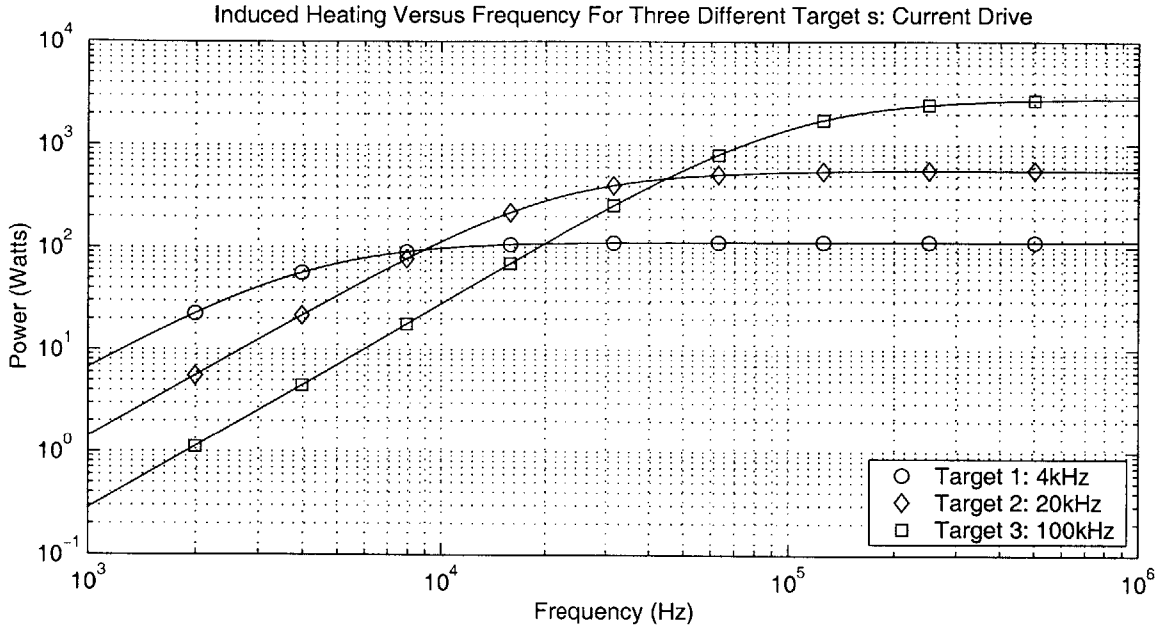

(a) Power profiles for 3 different targets.

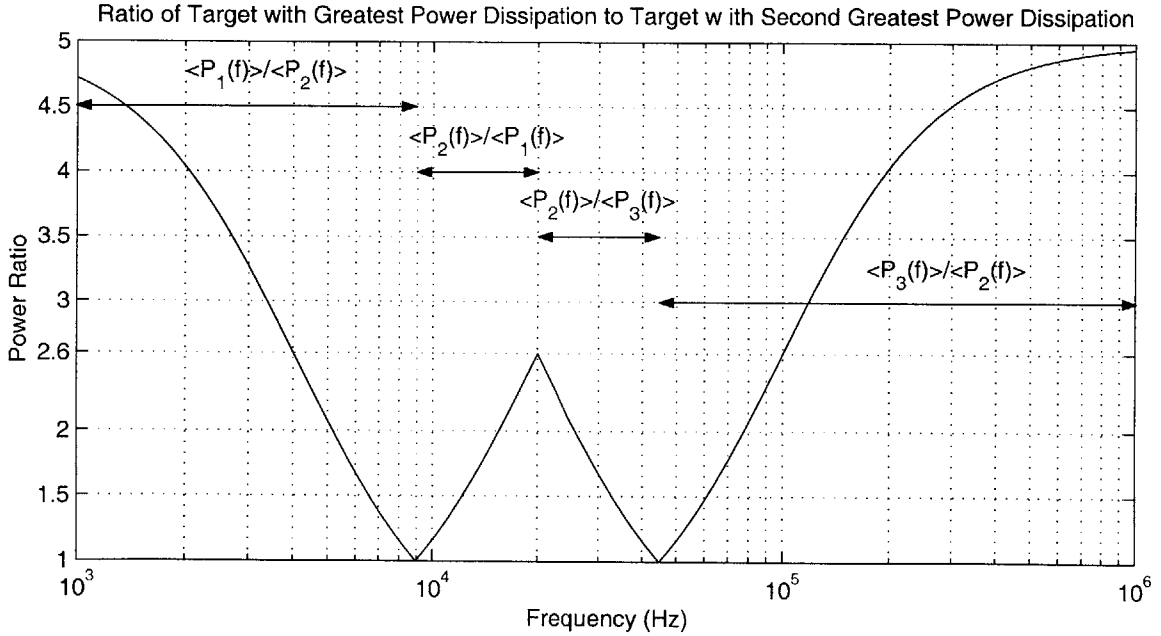

(b) Ratio of delivered power between targets.

Figure 3.5: Induction heating power curves versus frequency for 3 different targets assuming a current source drive of $I_o = 1$ A.

3.3 Voltage-Drive Case

Having considered the current-drive case, the voltage case is presented next.

3.3.1 Single Target

The current-drive case resulted in easy to understand relationships governing the power dissipation in each target. However, a number of power converters naturally apply a voltage not a current to the load they are driving. This is also true for the Marx inverter, a power circuit which will be discussed in Chapter 5. The analysis for a voltage driven induction coil is slightly more complicated than the previous case, mainly because the current is now determined by the load impedance and thus varies with frequency. For the purposes of discussion the reader is referred to Figure 3.6. To calculate the power dissipated in the load, the $\frac{I_1}{V_{in}}(s)$ transfer function is needed. Using impedances the induced voltages appearing on each inductor can be expressed as

$$V_{L_0} = L_0 s I_0 + L_{01} s I_1, \tag{3.20}$$

and

$$V_{L_1} = L_{01} s I_0 + L_1 s I_1. \tag{3.21}$$

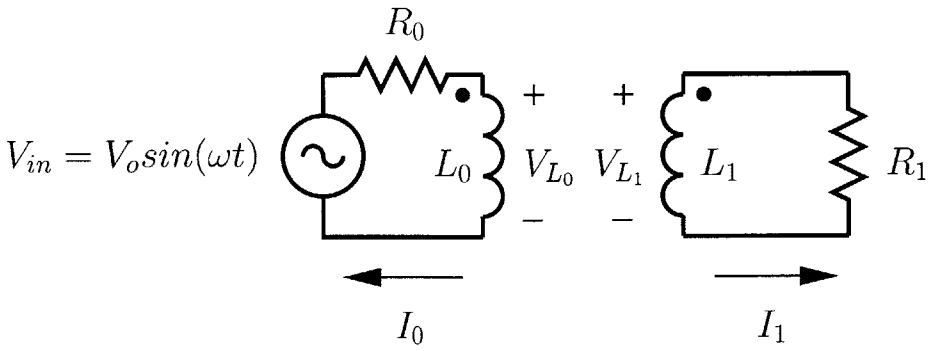

Figure 3.6: Induction heating circuit for one targets, in this case the primary coil is driven by a sinusoidal voltage.

Writing KCL around the first loop gives,

$$V_{L_0} = V_{in} - I_0 R_0, \tag{3.22}$$

while Ohm's law and KVL on the secondary side gives

$$V_{L_1} = -I_1 R_1. \tag{3.23}$$

Substituting, (3.22) into (3.20) and (3.23) into (3.21), eliminates the voltage terms and gives two equations and two unknowns,

$$V_{in} = (L_0 s + R_0) I_0 + L_{01} s I_1, \tag{3.24}$$

and

$$0 = L_{01} s I_0 + (L_1 s + R_1) I_1. \tag{3.25}$$

Equations (3.24) and (3.25) can be solved to give transfer functions from the voltage input to either current I_0 or I_1. The transfer function for the input current is

$$\frac{I_0}{V_{in}}(s) = \frac{L_1 s + R_1}{(L_0 L_1 - L_{01}^2) s^2 + (L_0 R_1 + L_1 R_0) s + R_0 R_1}. \tag{3.26}$$

The magnitude of the current drawn from the voltage source can be found from (3.26) by letting $s \rightarrow j\omega$ and solving,

$$\left| \frac{I_0}{V_{in}}(j\omega) \right| = \sqrt{\frac{(L_1\omega)^2 + R_1^2}{(L_0 R_1 + L_1 R_0)^2 \omega^2 + [R_0 R_1 - (L_0 L_1 - L_{01}^2)\omega^2]^2}}. \tag{3.27}$$

For most well designed induction coils, the impedance due to R_0 is negligible compared to $L_0\omega$. When this is true, the above equation can be reduced to,

$$\left| \frac{I_0}{V_{in}}(j\omega) \right| \approx \frac{1}{L_0\omega} \sqrt{\frac{(L_1\omega)^2 + R_1^2}{[(1 - K_1^2) L_1 \omega]^2 + R_1^2}}, \tag{3.28}$$

where the coupling coefficient K_1, has been used to further simply the expression. For a number of practical target and coil arrangements it is common to having coupling coefficients roughly equal to 0.3 or smaller. For small values the expression under the radical effectively cancels for most frequencies and the impedance seen by the source can be further simplified to

$$\left|\frac{I_0}{V_{in}}(j\omega)\right| \approx \frac{1}{L_0\omega}. \tag{3.29}$$

Under these circumstances, the driving point impedance is largely dominated by the impedance of the primary coil inductance, L_0. As a result we would expect the current drawn from the converter to decrease with increasing frequency.

To determine the power dissipation in the target the latter transfer function is needed,

$$\frac{I_1}{V_{in}}(s) = \frac{-L_{01}s}{(L_0L_1 - L_{01}^2)s^2 + (L_0R_1 + L_1R_0)s + R_0R_1}. \tag{3.30}$$

Following the previous analysis the magnitude of this transfer function is

$$\left|\frac{I_0}{V_{in}}(j\omega)\right| = \frac{L_{01}\omega}{\sqrt{(L_0R_1 + L_1R_0)^2\omega^2 + [R_0R_1 - (L_0L_1 - L_{01}^2)\omega^2]^2}}. \tag{3.31}$$

Re-expressing the above equation in terms of the coupling coefficient K_1 and assuming that R_0 can be ignored leads to

$$\left|\frac{I_0}{V_{in}}(j\omega)\right| \approx \frac{K_1\sqrt{(L_0/L_1}}{\sqrt{[(1-K_1^2)L_1\omega]^2 + R_1^2}}. \tag{3.32}$$

The voltage V_{in} is determined by the voltage source and is equal to

$$V_{in} = V_o sin(\omega t). \tag{3.33}$$

From equations (3.32) and (3.33) the power dissipated in R_2 can be determined,

$$\langle P(\omega)\rangle \approx \frac{1}{2}I_1^2R_1 = \frac{1}{2}\frac{K_1^2V_o^2(L_0/L_1)}{[(1-K_1^2)L_1\omega]^2 + R_1^2}R_1. \tag{3.34}$$

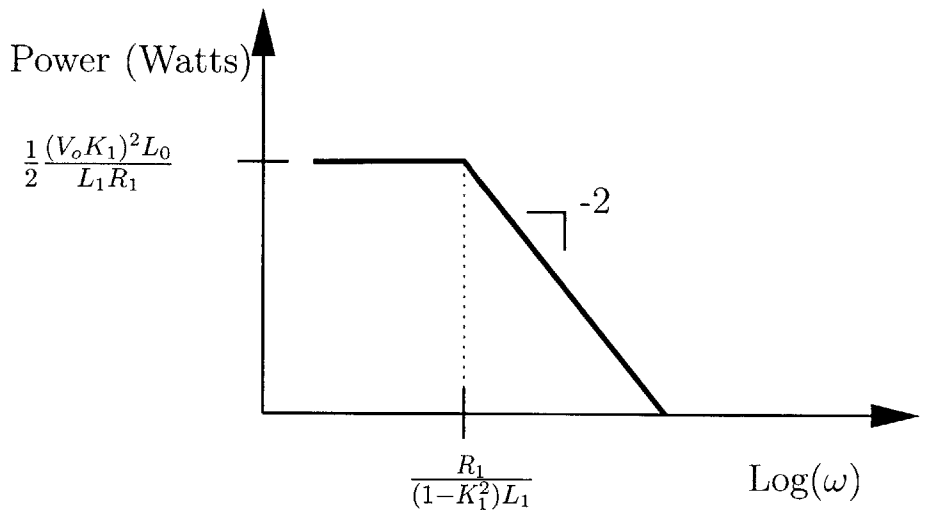

Figure 3.7: Power dissipation as a function of frequency for a single LR circuit coupled to an induction coil driven by a sinusoidal voltage of amplitude V_o.

Figure 3.7 shows what the average power-versus-frequency curve looks like for the voltage-drive case. Compared to the current-drive case, the frequency where the curve breaks is higher by a factor $(1 - K_1^2)$. Even though the pole location has shifted, the frequency that gives the greatest separation in power is still the one that corresponds to the pole location in the current-drive case, $\omega_1 = \frac{R_1}{L_1}$. If the voltage source is driven at that frequency, the average power dissipated in the target is

$$\langle P(\omega_2) \rangle \approx \frac{1}{2} \frac{K_1^2 V_o^2 (L_0/L_1)}{[1 + (1 - K_1^2)^2] R_1}. \tag{3.35}$$

3.3.2 Multiple Targets

The analysis of a multi-target voltage driven system becomes increasingly difficult to analyze by hand using SISO transfer functions. The increase in complexity can be attributed to the primary-side load impedance being a function of all the targets. Even if cross-coupling between targets is negligible, a target's presence can still impact the power delivered to other targets simply by affecting how much current is drawn from the source. Fortunately,

the ratio of power delivered between loads as indicated in Figure 3.5 remains unchanged whether a voltage or current drive is employed. Because of the multiple output nature of this system it is more convenient to analyze the voltage mode case using the following state-space description,

$$\left[\dot{I} \right] = \left[-L^{-1}R \right] \left[I \right] + \left[L^{-1} \right] \begin{bmatrix} V_{in} \\ 0 \end{bmatrix}, \tag{3.36}$$

where V_{in} is the input voltage, I is the column vector containing the systems states (the inductor currents),

$$I = \begin{vmatrix} I_0 \\ I_1 \\ I_2 \\ I_3 \end{vmatrix}, \tag{3.37}$$

and the "dot" notation has been used to indicate the derivative of those states. In the state evolution equation (3.36), L is the general inductance matrix of the system, which for the three target case takes the following form:

$$L = \begin{vmatrix} L_0 & L_{01} & L_{02} & L_{03} \\ L_{10} & L_1 & L_{12} & L_{13} \\ L_{20} & L_{21} & L_2 & L_{23} \\ L_{30} & L_{31} & L_{32} & L_3 \end{vmatrix}. \tag{3.38}$$

Likewise, the resistance matrix R for the primary coil and the three induction targets is

$$R = \begin{vmatrix} R_0 & 0 & 0 & 0 \\ 0 & R_1 & 0 & 0 \\ 0 & 0 & R_2 & 0 \\ 0 & 0 & 0 & R_3 \end{vmatrix}. \tag{3.39}$$

When expressed in this form, the system can easily be solved using a computational software package, such as MATLAB.

The transfer function from V_{in} to the current in a conductor n, denoted as I_n, was calculated in MATLAB for the hypothetical system described in Figure 3.5, using (3.36). The magnitude of these transfer functions is shown in Figure 3.8(a). Because the induction coil's impedance grows with frequency (ignoring the effect of parasitic capacitance) the current in each load must drop off at high frequencies. This results in the dissipated-power curves for each load shown in Figure 3.8(b) where, unlike the current-mode case, power decreases with increasing frequency. Note that power also rolls off at low frequencies because of the finite resistance from the primary coil. In the low frequency limit the current through the induction coil approaches a constant value, hence for low frequencies the system behavior resembles that of the current-mode case. If the effective resistance of a target is known and does not vary significantly with frequency, the induction heating profile for that target can be inferred from its V_{in}-to-I_n transfer function. For a sinusoidal voltage drive of amplitude V_o the current, I_n, flowing in conductor n can be determined and used to calculate the power dissipated according to the relationship,

$$\langle P_n(\omega) \rangle = \frac{1}{2} I_n(\omega)^2 R_n. \tag{3.40}$$

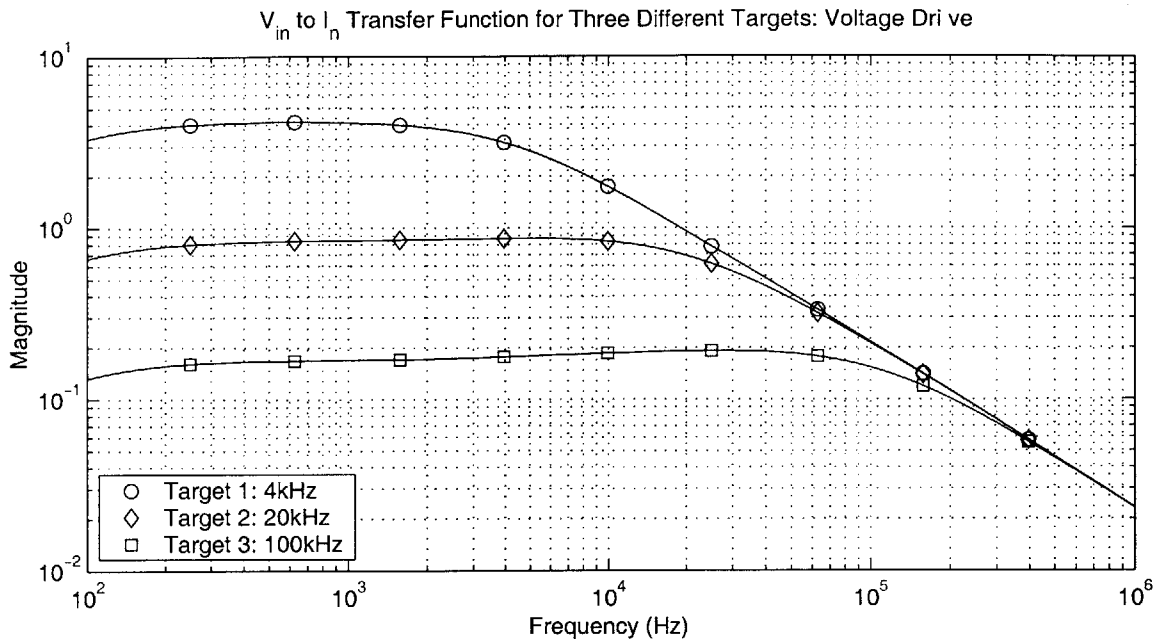

(a) Transfer function for 3 different targets.

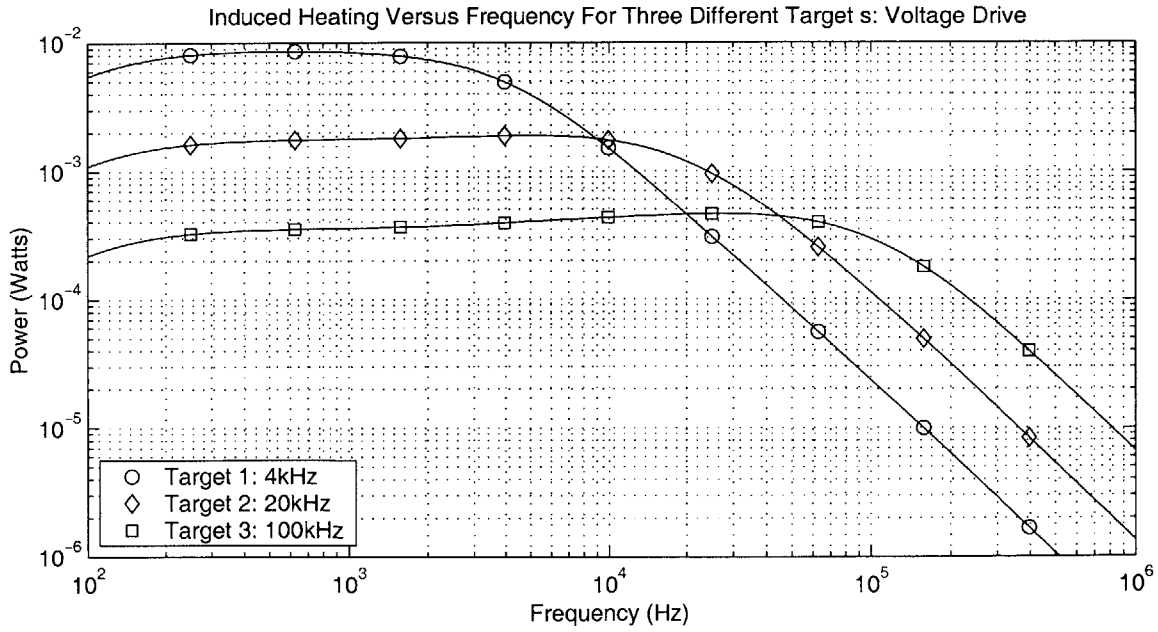

(b) Power profiles for 3 different targets.

Figure 3.8: V_{in}-to-I_n transfer function and power curves versus frequency for 3 different targets assuming a voltage drive, $V_{in} = 1$ V.

3.4 Induction Target Geometries

In this thesis two geometries were examined for making nonresonant induction targets: thin-walled cylindrical shells and thin wire loops.

3.4.1 The Thin-walled Cylindrical Shell Induction Target

A cylindrical shell is a simple geometric shape that a conductor can be made into for use as an induction target in the gel vibration damper. Figure 3.9 shows a cylinder with all of the dimensions a designer may be interested in: length, radius and thickness. As long as the thickness of the conductor is made small enough the thin-walled assumption holds and the conductor maybe treated as a simple LR circuit. This shape also provides a simple analytical expression for its resistance and inductance. To find the resistance, recall that a

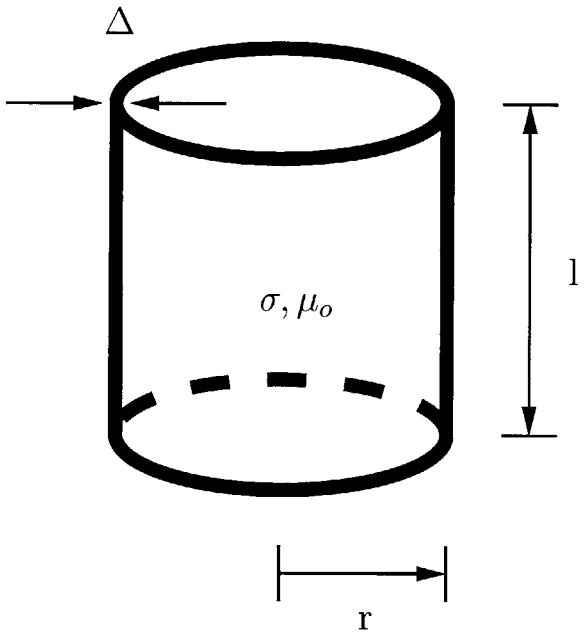

Figure 3.9: A cylindrical shell induction heating target

block with cross-sectional area A, length l, and conductivity σ has a resistance equal to

$$R = \frac{l}{A\sigma}. \tag{3.41}$$

Using this result the resistance of the shell can be calculated using the analogous expression,

$$R_{shell} = \frac{2\pi r}{\Delta l \sigma}. \tag{3.42}$$

As long as the dimensions of the shell are such that $l > 0.8r$ the Wheeler equation can be used to estimate the inductance of the shell to within about 1%,

$$L = \frac{10\pi\mu_o N^2 r^2}{9r + 10l}. \tag{3.43}$$

In equation (3.43), N represents the number of turns of the conductor which in this case is equal to one. The inductance of the shell is therefore approximately,

$$L_{shell} = \frac{10\pi\mu_o r^2}{9r + 10l}. \tag{3.44}$$

The break-point frequency (in Hertz) for this target can be found by taking the ratios of (3.42) and (3.44) and dividing by 2π to get

$$f_{shell} = \frac{\omega_{shell}}{2\pi} = \frac{R_{shell}}{2\pi L_{shell}} = \frac{9r + 10l}{10\pi\sigma\mu_o r l \Delta}. \tag{3.45}$$

This result suggests that the easiest way to adjust the break-point frequency of the target, while maintaining the same geometry from target to target is to either change the conductivity σ by using different metals or adjusting the thickness Δ[1]. When designing a cylindrical shell target, it is important to insure that the thin-walled approximation is valid. One way to verify this is to determine the ratio of the skin depth δ, to the shell thickness Δ. The skin depth of a cylindrical shell, excited at its break-point frequency can be found

[1]Technically, changing the thickness alters the geometry somewhat. However, the self-inductance of this structure is only weakly dependent upon the thickness, in fact it does not even appear as a parameter in the Wheeler equation which basically assumes the thickness of the winding is small.

by substituting (3.45) into (3.1) to give

$$\delta(\omega = \omega_{shell}) = \sqrt{\frac{10rl\Delta}{9r + 10l}}. \tag{3.46}$$

The ratio of skin depth to conductor thickness is therefore,

$$\frac{\delta}{\Delta}(\omega = \omega_{shell}) = \sqrt{\frac{10rl}{(9r + 10l)\Delta}}. \tag{3.47}$$

This ratio will be made large if the following geometric constraint is observed,

$$\Delta << \frac{10rl}{9r + 10l}, \tag{3.48}$$

and the previous constraint that $l > 0.8r$ is not violated.

3.4.2 The Thin Wire Loop Induction Target

Thin wire loops are also useful for making suitable frequency selectable induction targets. Figure 3.10 is a diagram of a wire loop induction target with all of relevant dimensions: the radius of the wire loop a, and the cross-sectional radius of the wire R. Using equation

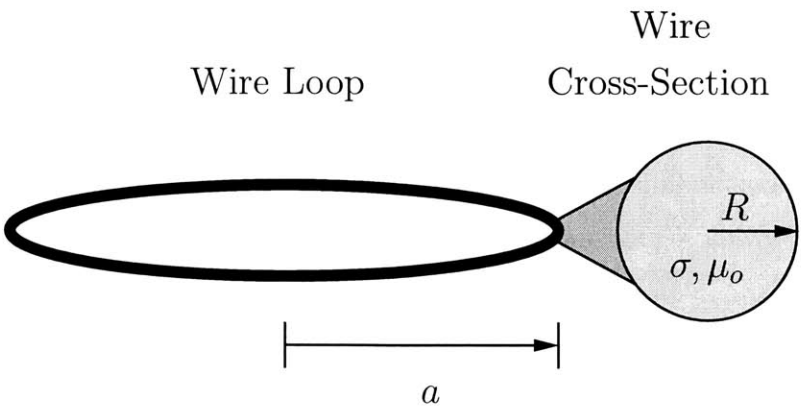

Figure 3.10: A wire loop induction heating target

(3.41) the dc resistance of a wire loop can be calculated

$$R_{loop} = \frac{2a}{R^2\sigma}. \tag{3.49}$$

The inductance of a circular loop of round wire can be estimated using the following equation

$$L_{loop} = \mu_o a \left[ln\left(\frac{8a}{R}\right) - 1.75 \right], \tag{3.50}$$

taken from [10]. The break-point frequency for this structure can be found by taking the ratios of (3.49) and (3.50),

$$f_{loop} = \frac{\omega_{loop}}{2\pi} = \frac{R_{loop}}{2\pi L_{loop}} = \frac{2}{\sigma\mu_o R^2 \left[ln\left(\frac{8a}{R}\right) - 1.75 \right]}. \tag{3.51}$$

As with the cylindrical target, it is important to know at what frequencies the ac resistance of a loop of wire will significantly impact the predicted power curves. To understand what gauge of wire to use the ac impedance of the wire must be known across frequencies. The ac impedance of a cylindrical conductor (including skin effect) is given in [4] and is expressed as,

$$Z = \frac{ml}{2\pi R\sigma} \frac{I_0(mR)}{I_1(mR)}, \tag{3.52}$$

where l is the length of the conductor and m is the reciprocal of complex depth of penetration or

$$m = \sqrt{j\omega\sigma\mu_o}. \tag{3.53}$$

$I_0(\cdot)$ and $I_1(\cdot)$ are the modified Bessel functions of the 1st kind of orders 0 and 1 respectively. This result will provide a good estimate of the ac resistance in the loop of wire provided that the radius of the loop a, is much bigger than the radius of the wire R. Substituting the length of the wire into (3.52) and taking the real part of the expression leads to the ac resistance of a loop of wire,

$$R_{loop,ac}(\omega) = Re\left\{ \frac{ma}{R\sigma} \frac{I_0(mR)}{I_1(mR)} \right\}. \tag{3.54}$$

3.5 Model Validation

To test these models, experiments were conducted on both the cylindrical shells and wire loop targets. The power dissipation in the shells was measured using a calorimetry experiment, while the frequency response of the wire loops was measured using a current probe in conjunction with a network analyzer. A more detailed description of these experiments and their results follows below.

3.5.1 Experimental Setup: Thin-walled Cylindrical Shells

Three thin-walled shells each measuring 1.25" in diameter and 1.00" in length were constructed by soldering or brazing together a single piece of 110 annealed copper, alloy 260 brass, or 302 stainless steel shim respectively. These dimensions lead to a self-inductance of about 25 nH for each target. In order to achieve a desired separation in resistance of $\alpha \approx 5$, these conductors were chosen with the following respective thicknesses (Δ): 3 mils, 2 mils, and 4 mils. These values result in nominal break-point frequencies of 5.6 kHz, 30.2 kHz, and 169.2 kHz, respectively. The power dissipation as a function of frequency for each target was determined via a careful calorimetry experiment and then tabulated [14].

Figure 3.11 shows the overall setup for the calorimetry experiment, while Figure 3.12(b) shows a closeup of the test vessel. The test is carried out using an induction coil which has been wrapped around a water-cooled glass former (A) that is maintained at a constant 25.0^oC by a Lauda Brinkman water circulator. This is done to insure that none of the power dissipated in the induction coil influences the heating of the induction target (F). The induction target is designed to fit onto an acrylic former (E) which in turn sits in a water-filled test jar (C). This arrangement insures that the position of the target with respect to the primary coil is fixed, thereby maintaining a constant coupling coefficient from target to target. A thermocouple probe (G) fits through a small hole in the top of the test jar and is used to measure the temperature of the heated water. To minimize heat transfer

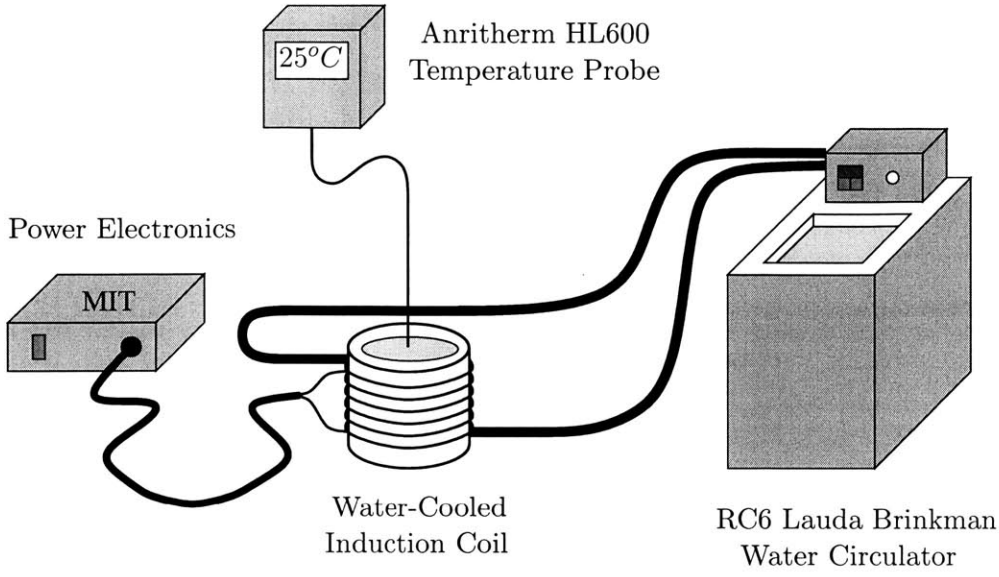

Figure 3.11: Calorimetry test setup.

between the test jar and the external surroundings, a thick layer of insulating material (B) separates the side walls and bottom of the test jar from the water-cooled glass former while a styrofoam cap (D) covers the top of the jar.

The induction coil is driven by a multilevel sinewave approximation generated by a power converter which is the subject of Chapter 5. The frequency of the sinewave is varied from 3 kHz to 300 kHz. In order to keep the amplitude of the primary current constant, the voltage amplitude is manually servoed at each frequency. At the desired frequency a fixed quantity of water (165.2 grams) is heated for exactly one hour starting from the moment it reaches 25.0^oC. At the end of this period the container is shaken to equalize the internal temperature and the final temperature is measured by the digital thermometer and recorded. Although in principle the power delivered could have been estimated based on the change in temperature by using the mass and specific heat of the water, acrylic former, and glass walls this method would only be accurate if no energy is lost to the external environment. A better way of calibrating the power delivered from the change in temperature is to run the experiment using a well defined source of power for exactly one hour. This was done by dissipating a fixed amount of power in a resistor immersed in the

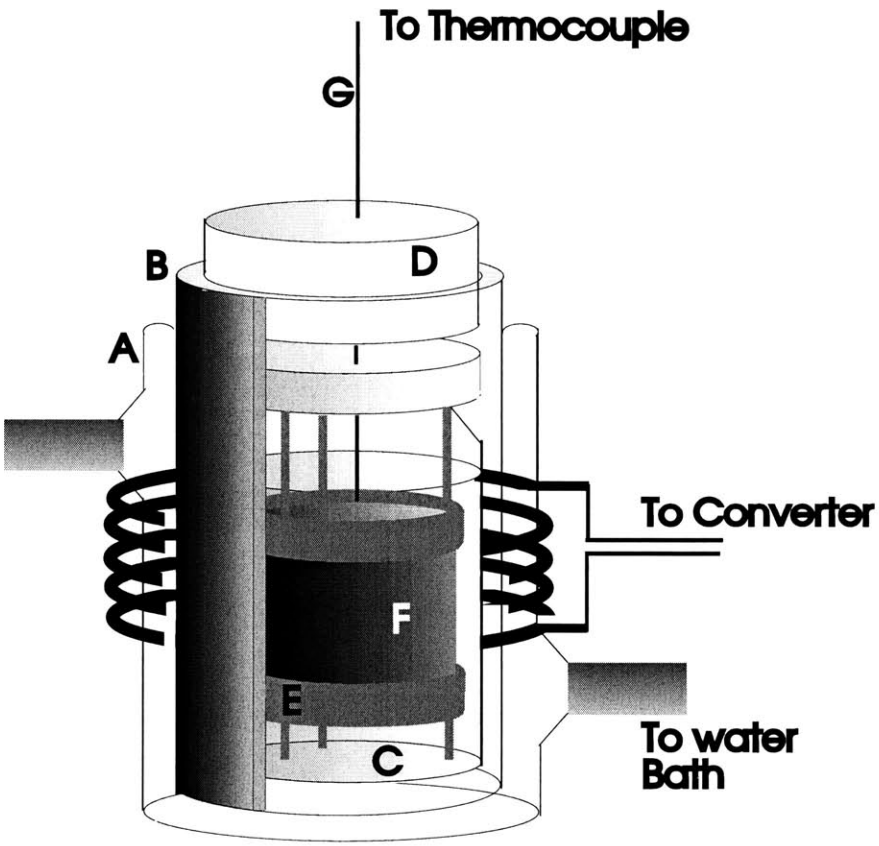

Figure 3.12: Closeup of the test vessel.

water during separate tests.

3.5.2 Experimental Results: Thin-walled Cylindrical Shells

Figure 3.13 shows the results of the calorimetry experiment for the three test metals. The simple RL model accurately predicts the power dissipation of the stainless steel and brass conductors over a wide range of frequencies. In the case of the copper target, there is a noticeable discrepancy, especially at high frequencies. This discrepancy is attributable to the fact that the skin depth is approaching the conductor thickness (at $f = 300$ kHz, $\delta_{cu} \approx 1.6\Delta_{cu}$). Table 3.1 shows the ratio of the conductor's skin depth δ, to its thickness Δ, evaluated at each of the target's corresponding break-point frequency.

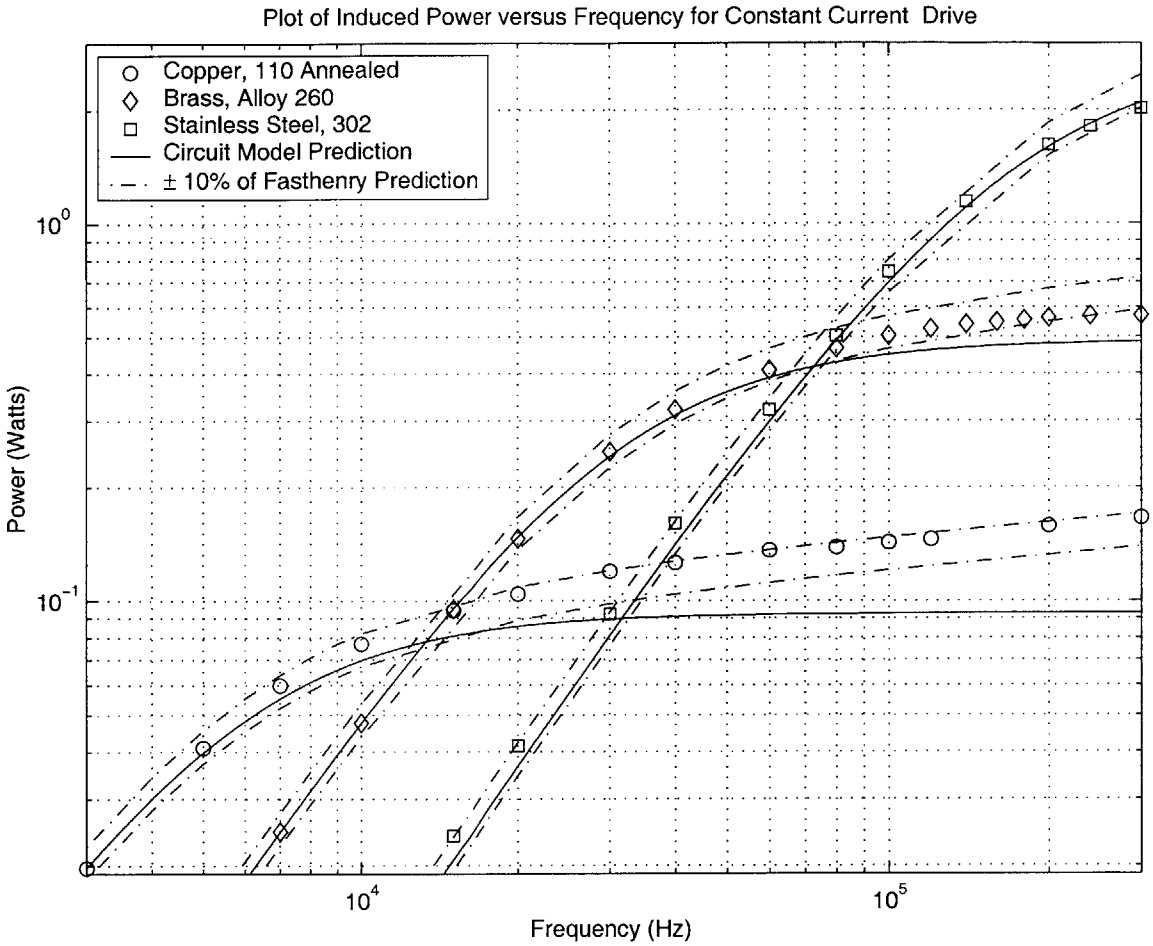

Figure 3.13: Calorimetry results for 3 different induction heating targets.

Frequency (kHz)	Cu δ/Δ	Brass δ/Δ	Steel δ/Δ
5.6	11.6	32.9	54.9
30.2	5.0	14.2	23.7
169.2	2.1	6.0	10.0

Table 3.1: Ratio of the skin depth to the conductor thickness, evaluated at each of the target's break-point frequencies.

As an additional check, a 3-D model of the water-cooled coil and shim target (shown in Figure 3.14) was evaluated using a 3-D field-solver called FastHenry [18] was used to model the ac impedance of each target[2]. The dashed lines in Figure 3.13 represent a variation in the FastHenry prediction of ±10%, and as shown, almost completely bound all of the calorimetry data. Variation in the calorimetry data can be attributed to ±10% manufacturing tolerances in the shim thickness as well as measurement error and unmodeled parasitics, such as contact resistance from soldering or brazing each conductor into a cylindrical shell.

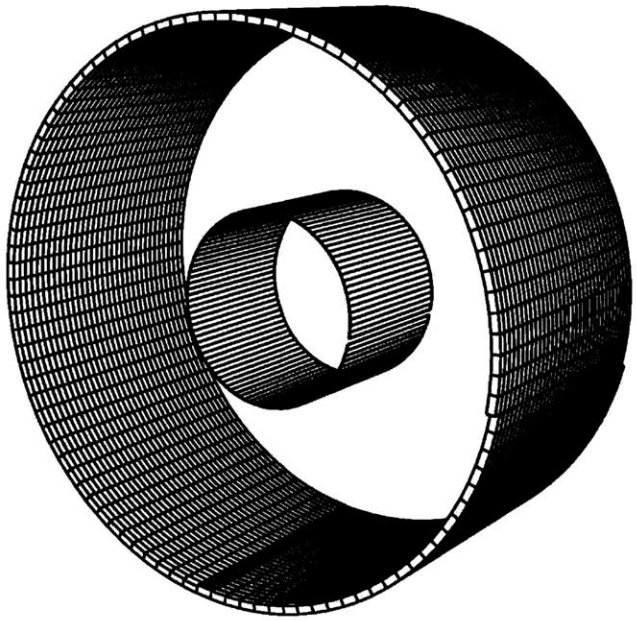

Figure 3.14: 3-D Model of the primary induction coil and an induction target as used in the calorimetry experiment.

[2]In order to work, FastHenry requires an input file that describes the conductors to be simulated. Many of the input files used in this thesis were generated with the help of Coilgen [9]. Coilgen is a C-program that acts as a preprocessor for FastHenry and provides a quick way to write FastHenry input files for simple coil structures. To verify that the input files is correct, it can be viewed using a separate program called FastModel [5]. For instance, FastModel was used to render the 3-D model of the water-cooled induction coil and target shown in Figure 3.14. Appendix B contains all of the Coilgen input files as well as some hand-edited FastHenry input files.

3.5.3 Experimental Setup: Thin Wire Loops

As a final experiment, a multi-target system was built using three different metal wires: copper, alloy 90 and alloy 800[3]. For this experiment each wire had a diameter of 0.08118 cm (20 AWG) and was wound on a PVC former into a loop measuring 6.00 cm in diameter. Each resulting target had a self-inductance of 0.169 μH as predicted by FastHenry. The resistances of these alloys are roughly factors of 8-9 apart and were chosen to yield nominal break-point frequencies of 5.98 kHz, 51.9 kHz, and 461.6 kHz respectively. The purpose of this experiment was not to measure power directly but to characterize the V_{in}-to-I_n transfer function for all of the targets so that power could be inferred later. Figure 3.15 illustrates the entire system.

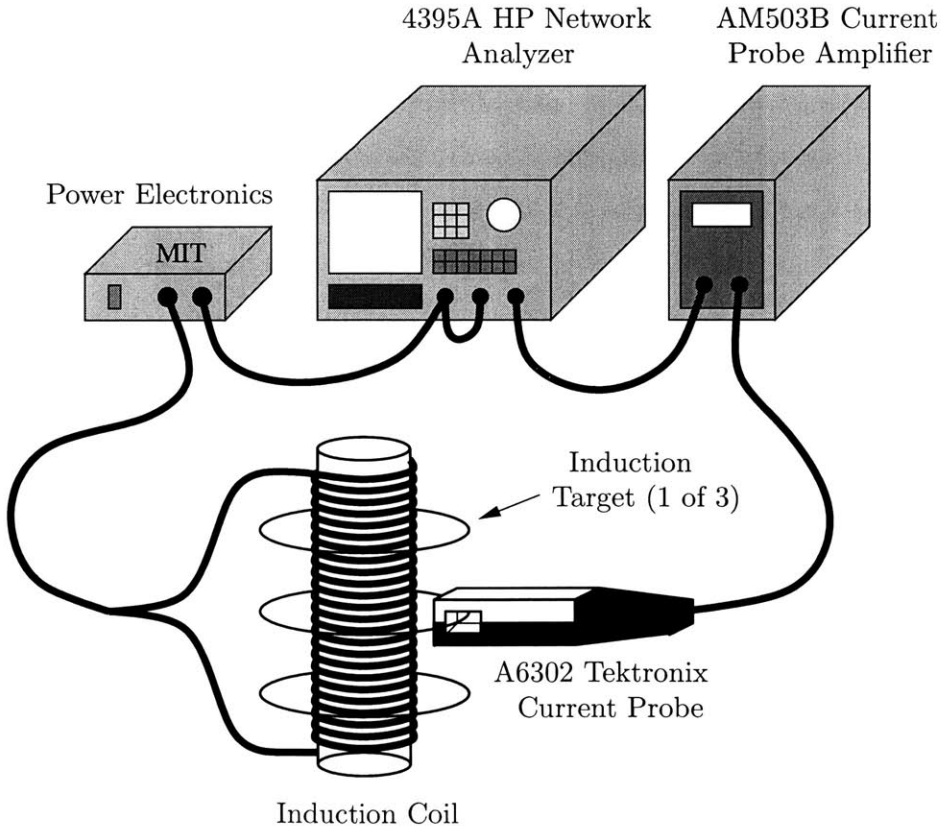

Figure 3.15: Multi-wire induction heating experiment.

[3]Alloy 90 and alloy 800 are commercially available resistance wires.

In this setup, all three wire loops are arranged on a PVC former (not shown) and coupled to a 200 μH induction coil. The center's of the targets and the induction coil are offset in order to accommodate a A6302 Tektronix current probe. An HP 4395A network analyzer determines the transfer function by sweeping the voltage reference that generates the multilevel sinewave approximation impressed across the induction coil. The current in each target is then measured via the current probe and amplified before being passed back to the network analyzer.

To calculate the theoretical transfer functions for this system, a 3-D model of this system was generated and passed to FastHenry to estimate the inductance matrix for the system. A view of the model used is shown in Figure 3.16. The Coilgen code used to produce this model can be found in Appendix B. In principle the mutual inductance could be calculated from the Neumann formula either by direct evaluation or with a numerical approach [19].

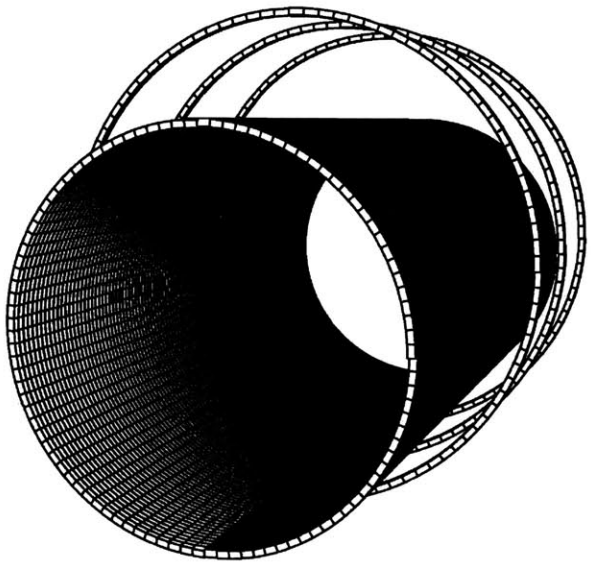

Figure 3.16: 3-D Model of the primary induction coil and targets as used in the multi-wire induction heating experiment.

3.5.4 Experimental Results: Thin Wire Loops

The experimental magnitude response of the system is shown in Figure 3.17. A discrepancy between the circuit model and the measured data was apparent for the lower resistance wires. This discrepancy can be attributed to the current probe's insertion loss during the measurement. Because the resistance of the copper wire ($R_{cu} = 6.28\ m\Omega$) was closest in magnitude to the probe's insertion loss, the copper wire data was the most distorted. This distortion was less noticeable for the remaining alloys because of their lower conductivities.

To account for this error, the insertion impedance of the probe was characterized over the relevant frequency range and used to calculate the new magnitude response. For characterization purposes, a five-turn test coil was wound around the same type of PVC former used for the induction targets. Using an HP 4192A LF impedance analyzer, the measured inductance and resistance of the test coil were zeroed at the relevant frequency. The probe insertion impedance was then determined by clamping the probe around the test coil and measuring the new resistance and inductance of the test inductor. These measurements correspond to the probe's insertion impedance scaled by the turns ratio squared. Dividing by 25 gives the correct resistance and inductances. This procedure was repeated for each desired frequency. Using these results, the corrected magnitude agreed within about $\pm 5\%$ over the entire frequency range.

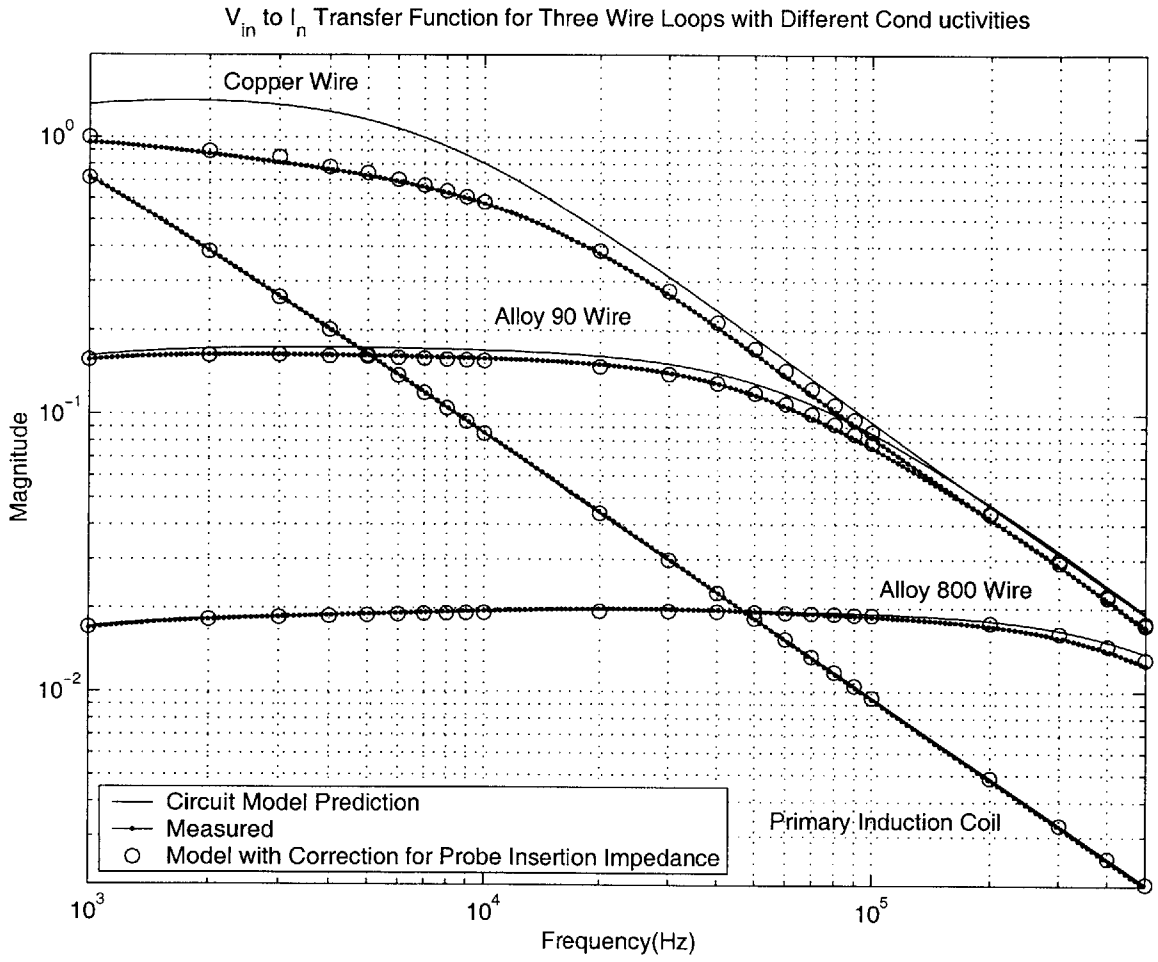

Figure 3.17: Results of multi-wire induction heating experiment.

3.6 Chapter Summary

This chapter showed how frequency selectable induction heating targets can be constructed using single-turn conductors whose critical dimensions are small compared to the skin depth at the frequency range of interest. If these single-turn conductors have similar self-inductances, with R/L break-point frequencies that are spaced evenly by factors of α, frequency selectivity can be achieved. That is a target driven at its break-point frequency will heat by an amount of $(\alpha^2 + 1)/(2\alpha)$ more than the remaining targets. These results were experimentally demonstrated for two types of induction targets, thin-walled cylindrical shells and thin wire loops. Both of these geometries are attractive targets for use in the gel damper because of their simplicity of construction, and minimal volume requirements. The major downside to these nonresonant targets results from the large spacing in frequency required for modest separations of relative heating between targets. In the next chapter resonant targets that can achieve a greater degree of selectivity with a considerably smaller spacing in frequency will be introduced.

Chapter 4

Resonant, Frequency Selectable Induction Heating Targets

IN Chapter 3, frequency selectable induction targets were developed that were nonresonant in nature. Essentially inductively coupled RL circuits, these targets achieved selective heating by varying the resistance of each target. Although these targets have a number of advantages outlined in the previous chapter, the amount of selectivity they can achieve is moderate at best. This chapter describes resonant targets that overcome this limitation at the cost of additional complexity.

4.1 Resonant Induction Heating Targets

Resonant induction heating targets are basically RLC circuits, which are inductively coupled to a primary heating coil. In this case, the target's capacitance is chosen so that the effective series resistance (ESR) in the circuit dissipates power preferentially at the circuit's resonant frequency. When compared to the RL scheme, the RLC target allows for a greater degree of preferential heating while keeping the required target frequencies in a tighter frequency band. Paralleling the development of the previous chapter, the induction coil that excites these targets can also be driven with either a current or voltage source. Once again, both drive conditions and their implications are considered.

4.2 Current-Drive Case

Because the current-drive case results in a system with fewer dynamics it is considered first.

4.2.1 Single Target

Consider the situation where only one resonant circuit exists as indicated in Figure 4.1 by R_1, L_1, and C_1. This network is coupled to a primary-induction coil L_0, which is driven by the sinusoidal current $I_o sin(\omega t)$. Paralleling the development in Chapter 3, the time averaged power dissipated in R_1 can be found from the $\frac{I_1}{I_0}(s)$ transfer function. To find this transfer function, the voltage induced on L_1 can be expressed in the s domain as

$$V_{L_1} = L_{01} s I_0 + L_1 s I_1, \tag{4.1}$$

where L_{01} again represents the mutual inductance between L_0 and L_1. Summing KVL around the components on the induction target side gives

$$V_{L_1} = -I_1 \left(\frac{1}{C_1 s} + R_1 \right). \tag{4.2}$$

Substituting (4.2) into (4.1) leads to the following relationship,

$$0 = L_{01} s I_1 + \left(L_1 s + R_1 + \frac{1}{C_1 s} \right). \tag{4.3}$$

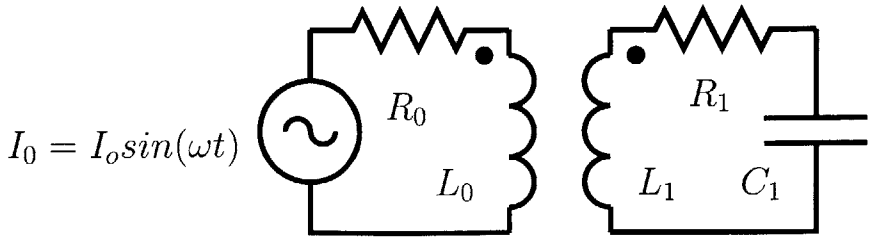

Figure 4.1: Induction heating circuit for one resonant target, in this case the primary coil is driven by a sinusoidal current.

which can be rearranged to give the desired transfer function,

$$\frac{I_1}{I_0}(s) = \frac{-L_{01}C_1 s^2}{L_1 C_1 s^2 + R_1 C_1 s + 1}. \tag{4.4}$$

The magnitude of the transfer function can be found by letting $s \rightarrow \omega$ and solving.

$$\left|\frac{I_1}{I_0}(j\omega)\right| = \left|\frac{L_{01}C_1\omega^2}{R_1 C_1 j\omega + (1 - L_1 C_1 \omega^2)}\right| = \frac{L_{01}C_1\omega^2}{\sqrt{(R_1 C_1 \omega)^2 + (1 - L_1 C_1 \omega^2)^2}}. \tag{4.5}$$

The current I_0 is determined by the sinusoidal current source,

$$I_0 = I_o sin(\omega t). \tag{4.6}$$

Using equations (4.5) and (4.6) the time-averaged power dissipation in R_1 for a sinusoidal current is

$$\langle P_1(\omega)\rangle = \frac{1}{2} I_1^2 R_1 = \frac{1}{2} \frac{(I_o L_{01} C_1 \omega^2)^2}{[(R_1 C_1 \omega)^2 + (1 - L_1 C_1 \omega^2)^2]} R_1 \tag{4.7}$$

For convenience the coupling coefficient between the two coils K_1, is again defined as

$$K_1 = \frac{L_{01}}{\sqrt{L_0 L_1}}. \tag{4.8}$$

Combining (4.7) and (4.8) the power dissipated in R_2 can be expressed in terms of the coupling coefficient,

$$\langle P_1(\omega)\rangle = \frac{(I_o K_1 \omega^2)^2 L_0 L_1 R_1}{2[(1 - L_1 C_1 \omega^2)^2 + (R_1 C_1 \omega)^2]}. \tag{4.9}$$

Maximum power is delivered at the natural frequency,

$$\omega_1 = \frac{1}{\sqrt{L_1 C_1}}, \tag{4.10}$$

simplifying (4.9) to the following

$$\langle P_1(\omega_1)\rangle = \frac{(I_o K_1 \omega_1)^2 L_0 L_1}{2R_1} = \frac{(I_o K_1)^2 L_0}{2R_1 C_1}. \tag{4.11}$$

Alternatively, (4.11) can be expressed in terms of the first target's "quality" factor,

$$Q_1 = \frac{L_1\omega_1}{R_1}, \tag{4.12}$$

to give

$$\langle P_1(Q_1)\rangle = \frac{(I_o Q_1 K_1)^2 R_1}{2}. \tag{4.13}$$

Consequently, the power dissipated in a target at its resonant frequency is commensurate with its Q.

4.2.2 Multiple Targets

The design of a multiple resonant induction target system can be a considerable challenge because of the large number of parameters an engineer must specify. A designer must simultaneously balance geometry, thermal issues, and the selection of several components all while trying to achieve a desired degree of "selectivity" in an acceptable frequency band. To make matters worse, these systems have the potential to be coupled to such an extent that a target can not be designed without taking into account its affect on the remaining targets. A designer is then forced to evaluate the design using a computer, a method that provides little insight for improvement. Fortunately, some insight can be had from examining those cases that are not highly coupled.

4.2.2.1 Targets with Negligible Cross-Coupling

For the current-drive case, the single target relationships established previously will hold equally well for multiple targets simultaneously, provided that there is no cross-coupling between targets, i.e. any mutual inductance between targets coils is identically zero. When at least two targets are present, it is useful to know the frequencies that will lead to the greatest amount of preferential heating. The degree of heating in a target n compared to a

target m can be expressed as

$$\frac{\langle P_n(\omega)\rangle}{\langle P_m(\omega)\rangle} = \frac{K_n^2 L_n R_n[(1 - L_m C_m \omega^2)^2 + (R_m C_m \omega)^2]}{K_m^2 L_m R_m[(1 - L_n C_n \omega^2)^2 + (R_n C_n \omega)^2]}. \tag{4.14}$$

Taking the derivative of (4.14) and setting it equal to zero

$$\frac{d}{d\omega}\left(\frac{\langle P_n(\omega)\rangle}{\langle P_m(\omega)\rangle}\right) = 0, \tag{4.15}$$

leads to a fifth-order polynomial in ω,

$$a\omega^5 + b\omega^3 + c\omega = 0 \tag{4.16}$$

where the coefficients are as follows:

$$\begin{aligned} a =& [(R_n C_n)^2 - 2L_n C_n](L_m C_m)^2 - [(R_m C_m)^2 - 2L_m C_m](L_n C_n)^2 \\ b =& [2(L_m C_m)^2 - 2(L_n C_n)^2] \\ c =& [(R_m C_m)^2 - 2L_m C_m] - [(R_n C_n)^2 - 2L_n C_n]. \end{aligned} \tag{4.17}$$

Only two of the polynomial's roots are relevant as one of the roots is zero and the other two are negative. The valid roots are

$$\omega = \sqrt{\frac{-b \pm \sqrt{b^2 - 4ac}}{2a}}. \tag{4.18}$$

If the Q's of the resonant targets are high enough, the solution to (4.18) will equal the natural frequencies of the two targets to a close approximation. Equation (4.11) makes apparent, that for a fixed current, the absolute power delivered to a target will vary depending on the target's component values. Targets are enumerated (beginning with the number 1) in terms of increasingly higher natural frequencies, i.e. $\omega_n < \omega_{n+1}$, then the absolute power delivered to two adjacent targets can be equalized by controlling the amplitude of the current driving

the primary coil via the following relationship:

$$I_0(\omega_{n+1}) = \frac{K_n}{K_{n+1}}\sqrt{\frac{R_{n+1}C_{n+1}}{R_nC_n}}I_0(\omega_n). \tag{4.19}$$

These results are easier to understand by examining the time-averaged power versus frequency for three hypothetical targets shown in Figure 4.2 (a). In this example the primary coil L_0 has an inductance of 10 μH, and the inductance of the three target coils (L_1, L_2, and L_3) is equal to 100 μH. The resistance of each target (R_1, R_2, and R_3) is 1 Ω. The resistance of the primary coil is $R_0 = 1\ \Omega$ but irrelevant because of the current source drive. The coupling coefficient of each target with respect to the primary coil has been arbitrarily set to 0.3 and the capacitances, C_1, C_2, and C_3 of the three targets have been chosen to give natural frequencies of 80 kHz, 90 kHz, and 100 kHz, respectively. With these constraints each target experiences preferential heating with respect to the remaining targets over some frequency range. The extent of preferential heating is given as a ratio in Figure 4.2 (b) and clearly exceeds 100 near the natural frequencies of these targets.

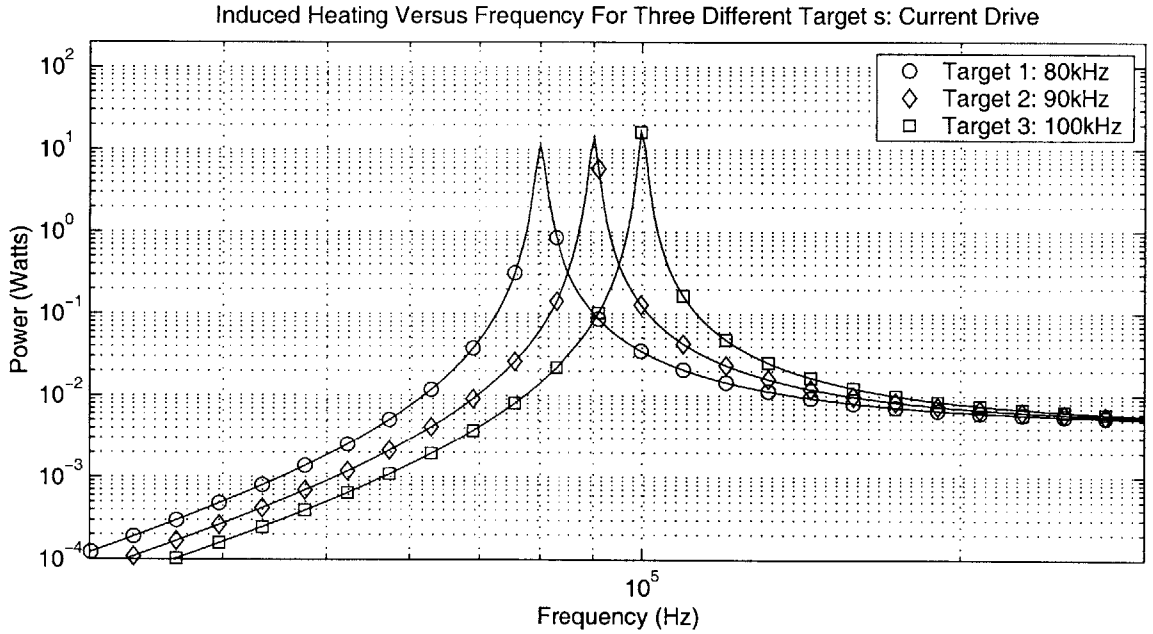

(a) Power profiles for 3 different targets.

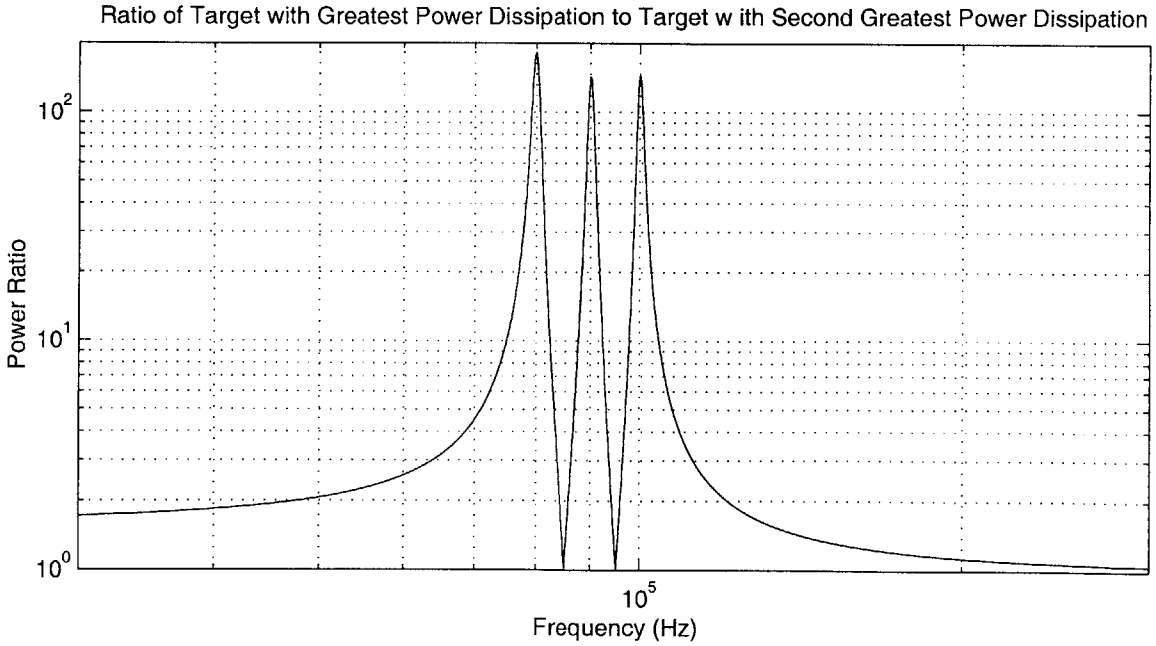

(b) Ratio of delivered power between targets.

Figure 4.2: Induction heating power curves versus frequency for 3 different targets assuming a current source drive of $I_o = 1$ A.

4.2.2.2 Targets with Cross-Coupling

So far only targets with negligible cross-coupling have been considered. In reality mutual inductance a exists between targets and cannot always be ignored. Even a small degree of cross-coupling can have a noticeable effect on the power profile of a resonant target. The inclusion of cross-coupling terms lead to increasingly complicated transfer function descriptions of the system, without much additional insight. Instead of looking at the transfer functions in detail, consider the impact of cross-coupling on the hypothetical targets discussed earlier. For simplicity target 3 has been removed and targets 1 and 2 now have a cross-coupling coefficient of 0.03, a number which is ten times smaller than their respective coupling to the primary coil.

For this example the power profiles of the two targets is shown in Figure 4.3 (a). Previously, each target exhibited one resonant frequency. Now each target has two resonant frequencies located closely at the natural frequencies of the uncoupled system examined earlier. In addition, each system also exhibits an anti-resonant frequency located to the right of the "new resonant frequency." Figure 4.3 (b) shows the ratio of heating between targets. From this figure it is apparent that the frequencies where the ratio is maximized are now higher, corresponding more closely to the location of the anti-resonant frequencies.

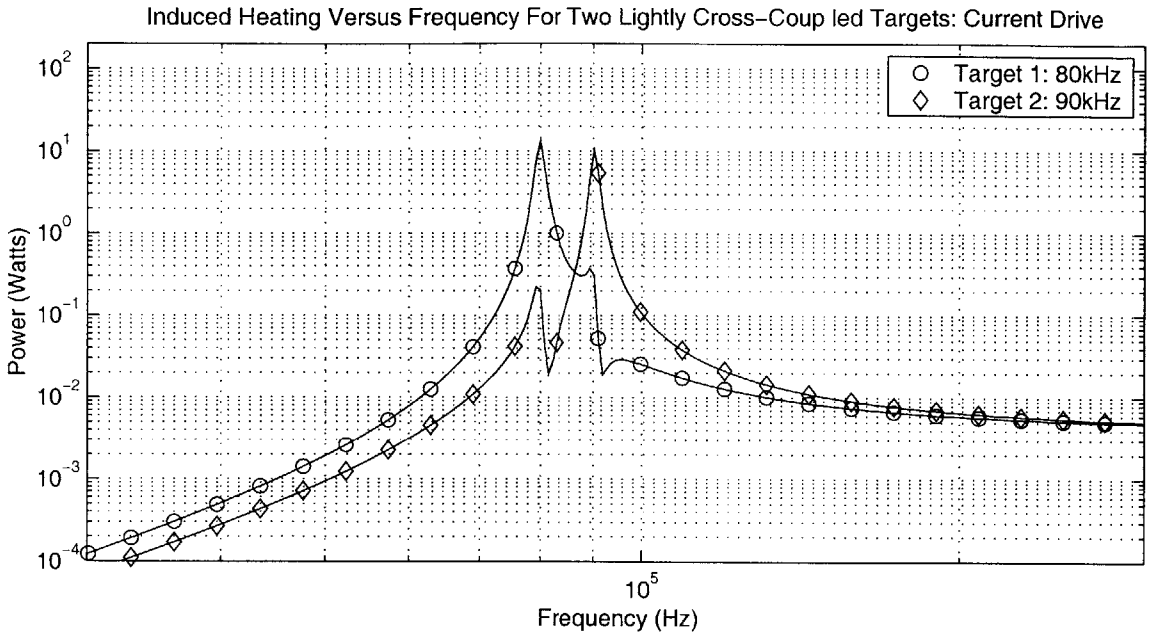

(a) Power profiles for 3 different targets.

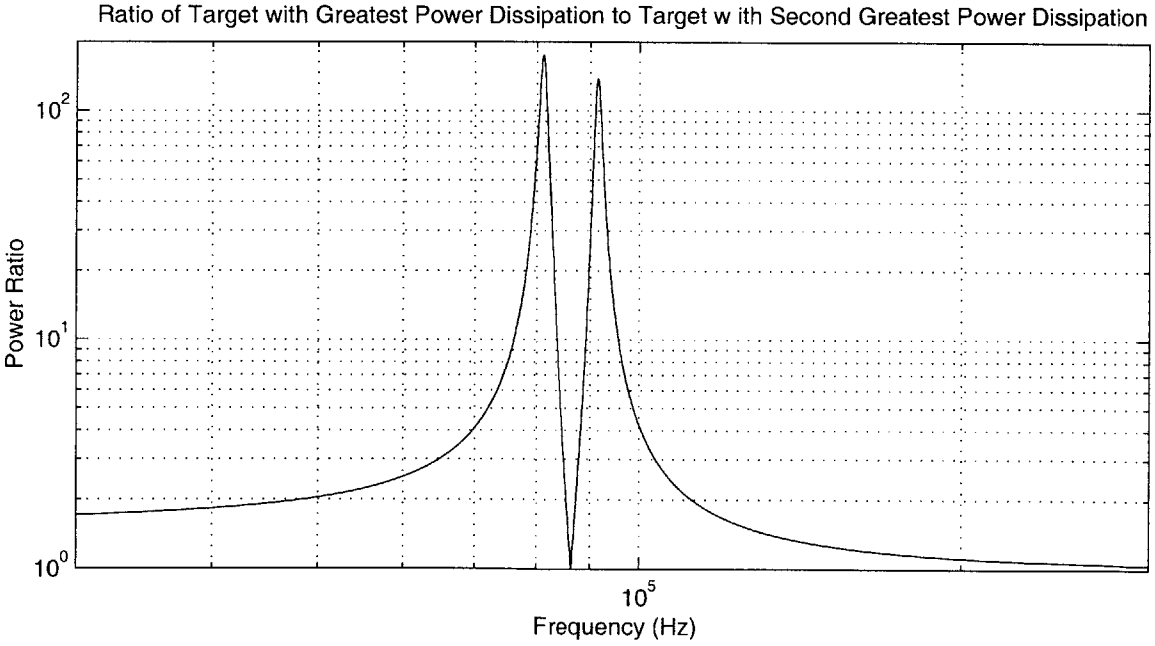

(b) Ratio of delivered power between targets.

Figure 4.3: Induction heating power curves versus frequency for 3 different targets assuming a current source drive of $I_o = 1$ A.

If a detailed analysis is needed a state-space formulation can be solved using a computational package such as MATLAB. A state-space model for the current-drive system can be derived from the following matrix relationship, which has been inferred by writing out the differential equations for a few targets and then generalizing

$$\begin{bmatrix} \dot{I} \\ \dot{V} \end{bmatrix} = \begin{bmatrix} -L_a^{-1}R & L_a^{-1} \\ -C^{-1} & 0 \end{bmatrix} \begin{bmatrix} I \\ V \end{bmatrix} - \begin{bmatrix} L_b \\ 0 \end{bmatrix} \dot{I}_0 \ . \tag{4.20}$$

In relationship 4.20, I and V are column vectors containing the inductor currents and capacitor voltages respectively. For the three-target case these vectors can be expressed in the following manner:

$$I = \begin{vmatrix} I_1 \\ I_2 \\ I_3 \end{vmatrix}, \tag{4.21}$$

and

$$V = \begin{vmatrix} V_{C_1} \\ V_{C_2} \\ V_{C_3} \end{vmatrix}. \tag{4.22}$$

In (4.20) L_a is the inductance matrix of the system without any of the primary-side terms or

$$L_a = \begin{vmatrix} L_1 & L_{12} & L_{13} \\ L_{21} & L_2 & L_{23} \\ L_{31} & L_{32} & L_3 \end{vmatrix}, \tag{4.23}$$

and L_b is a column vector containing the mutual inductance terms between the primary-side inductance and the target inductances

$$L_b = \begin{vmatrix} L_{01} \\ L_{02} \\ L_{03} \end{vmatrix}. \tag{4.24}$$

Likewise, matrices C and R are the target's capacitance and resistance matrices respectively

and are written as,

$$C = \begin{vmatrix} C_1 & 0 & 0 \\ 0 & C_2 & 0 \\ 0 & 0 & C_3 \end{vmatrix}, \tag{4.25}$$

and

$$R = \begin{vmatrix} R_1 & 0 & 0 \\ 0 & R_2 & 0 \\ 0 & 0 & R_3 \end{vmatrix}. \tag{4.26}$$

By itself, equation (4.20) does not give a proper state-space relationship because it depends on the derivative of the input. To produce a proper state-space formulation the following mathematical trick can be applied [39]. When a system has the following form

$$\dot{x} = Ax + B\dot{u}, \tag{4.27}$$

it can be recast in proper form by rewriting the state variable x as

$$x = q + Bu. \tag{4.28}$$

To see how this helps, substitute (4.28) and its derivative into (4.27) to give

$$\dot{q} + B\dot{u} = A(q + Bu) + B\dot{u}. \tag{4.29}$$

Simplifying this expression leads to

$$\dot{q} = Aq + ABu, \tag{4.30}$$

which can be solved for q using standard techniques. The desired state variables can then be calculated by plugging q back into (4.28).

4.3 Voltage-Drive Case

The current-drive case is insightful because it makes apparent the excitation frequencies that give the greatest degree of preferential heating. However many inverters naturally apply a voltage at their output and supply the required current as determined by the load impedance that is driven. This means that, unlike the current-mode case, the absolute power delivered to a target can not be analyzed without taking into consideration how all the targets contribute to the driving point impedance. If the impedance looking into the primary coil is known the current drawn from the converter can be calculated and the equations from the previous section applied.

4.3.1 Single Target

Consider Figure 4.4 which represents the induction heating circuit from before with some minor changes. The current source has been replaced with a voltage source and as a practical matter a dc blocking capacitor C_0 has been inserted on the source side. If only one target is present, the expression for the load impedance $Z_{load}(s)$ is a rational transfer function of the form:

$$Z_{load}(s) = \frac{Z_n(s)}{Z_d(s)}, \tag{4.31}$$

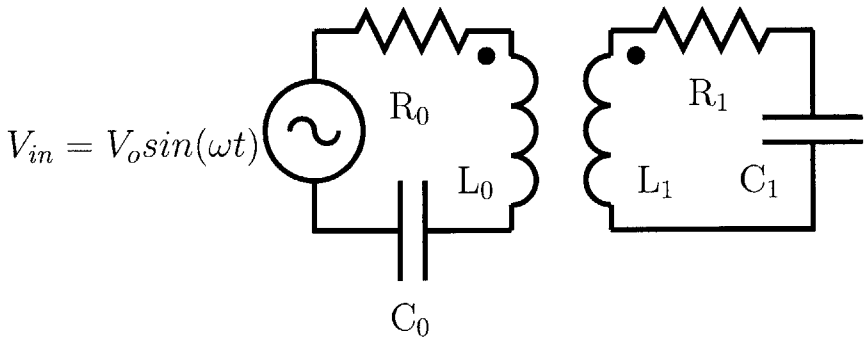

Figure 4.4: Induction heating circuit for 1 resonant target: voltage drive.

where the numerator is

$$Z_n(s) = (L_0 s + R_0 + \frac{1}{C_0 s})(L_1 s + R_1 + \frac{1}{C_1 s}) - (L_{01} s)^2, \tag{4.32}$$

and the denominator is

$$Z_d(s) = (L_1 s + R_1 + \frac{1}{C_1 s}). \tag{4.33}$$

If the impedances associated with R_0 and C_0 are small at the frequencies of interest (typical of a practical design), then (4.31) can be simplified to

$$Z_{load}(s) = \frac{L_0 s[L_1(1 - K_1^2)C_1 s^2 + R_1 C_1 s + 1]}{L_1 C_1 s^2 + R_1 C_1 s + 1}. \tag{4.34}$$

From (4.34) it can be inferred that the load impedance will experience a maximum near the natural frequency of the target,

$$\omega_{Zmax} = \omega_1 = \frac{1}{\sqrt{L_1 C_1}}, \tag{4.35}$$

and a minimum near

$$\omega_{Zmin} = \frac{1}{\sqrt{L_1 C_1 (1 - K_1^2)}} \tag{4.36}$$

In the current-drive case, a target's natural frequency yielded the greatest amount of power dissipation in that target– a result consistent with the load impedance being maximized at that frequency. In the voltage-drive case, the natural frequency no longer gives maximum power dissipation, in fact it is greatly attenuated there. Locally, the frequency that now gives the greatest dissipation is (4.36). Although power is no longer maximized at the natural frequencies, these frequencies will still give the highest amount of preferential heating regardless of the drive type (assuming negligible cross-coupling).

4.3.2 Multiple Targets

When more than one target is present and the impact of cross-coupled inductors must be taken into account, the system shown in Figure 4.5 can be analyzed using the following compact state-space formulation,

$$\begin{bmatrix} \dot{I} \\ \dot{V} \end{bmatrix} = \begin{bmatrix} -L^{-1}R & L^{-1} \\ -C^{-1} & 0 \end{bmatrix} \begin{bmatrix} I \\ V \end{bmatrix} + \begin{bmatrix} L^{-1} & 0 \\ 0 & 0 \end{bmatrix} \begin{bmatrix} V_{in} \\ 0 \end{bmatrix}, \tag{4.37}$$

where V_{in} is the amplitude of the input voltage and I and V are column vectors containing the inductor currents and capacitor voltages. For the three target case I and V are written as follows,

$$I = \begin{vmatrix} I_0 \\ I_1 \\ I_2 \\ I_3 \end{vmatrix}, \tag{4.38}$$

and

$$V = \begin{vmatrix} V_{C_0} \\ V_{C_1} \\ V_{C_2} \\ V_{C_3} \end{vmatrix}. \tag{4.39}$$

In the state-space formulation L is the general inductance matrix of the system, which for the three target case takes the following form:

$$L = \begin{vmatrix} L_0 & L_{01} & L_{02} & L_{03} \\ L_{10} & L_1 & L_{12} & L_{13} \\ L_{20} & L_{21} & L_2 & L_{23} \\ L_{30} & L_{31} & L_{32} & L_3 \end{vmatrix}. \tag{4.40}$$

Likewise, the resistance and capacitance matrices R and C for the three target network in

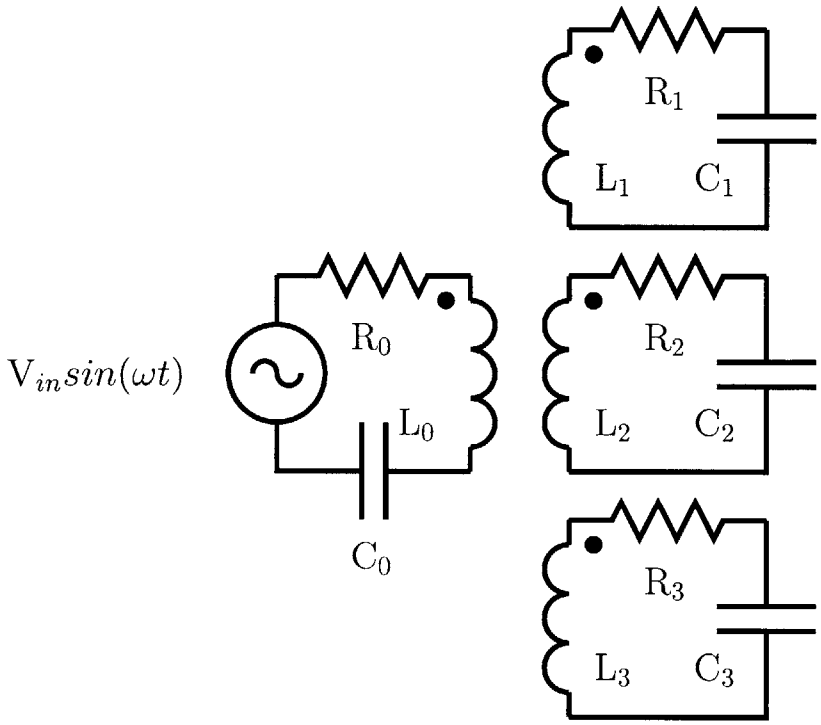

Figure 4.5: Induction heating circuit for 3 different targets.

Figure 4.5 can be expressed as

$$R = \begin{vmatrix} R_0 & 0 & 0 & 0 \\ 0 & R_1 & 0 & 0 \\ 0 & 0 & R_2 & 0 \\ 0 & 0 & 0 & R_3 \end{vmatrix}, \tag{4.41}$$

and

$$C = \begin{vmatrix} C_0 & 0 & 0 & 0 \\ 0 & C_1 & 0 & 0 \\ 0 & 0 & C_2 & 0 \\ 0 & 0 & 0 & C_3 \end{vmatrix}, \tag{4.42}$$

respectively.

Using (4.37) the transfer function from V_{in} to I_n, were I_n denotes the current in con-

ductor n, for the hypothetical system described in Figure 4.5, was calculated in MATLAB and is shown in Figure 4.6(a). This example has identical component values to the hypothetical system discussed in the current-drive case. The only difference is the addition of C_0, the dc blocking capacitor which has been chosen to yield a natural frequency with the primary-side coil of 50 kHz. If the effective resistance of a target is known and does not vary significantly with frequency, the induction heating profile for that target can be determined from its V_{in}-to-I_n transfer function. For a sinusoidal voltage drive of amplitude V_{in} the current I_n, flowing in conductor n can be found from Figure 4.6 and used to calculate the power dissipated according to the relationship,

$$< P_n(\omega) >= \frac{1}{2} I_n(\omega)^2 R_n. \tag{4.43}$$

Carrying this calculation out, results in the dissipated-power curves of each load shown in Figure 4.6(b). In this example the power curves are similar in shape to the magnitude of the transfer function because all of the targets have the same resistance. The voltage source case results in prower profiles that are arguably more complicated than the current-drive case. Although the frequencies that give the most preferential heating are unchanged from the current-drive case, they no longer maximize the amount of power delivered. As stated previously this can be explained by the variation of the load impedance as a function of frequency. The magnitude and phase of the load impedance for this example are shown in Figure 4.7 (a) and (b) respectively. As suggested earlier, the magnitude of the impedance peaks at the frequencies corresponding to the natural frequencies of the various targets. The increased impedance leads to less current drawn and hence a reduction in power. At these frequencies the phase approaches 0^o, so the impedance appears resistive here. The phase also passes through 0^o at frequencies were the power dissipated in a target is maximized. However, the degree of preferential heating is much smaller there.

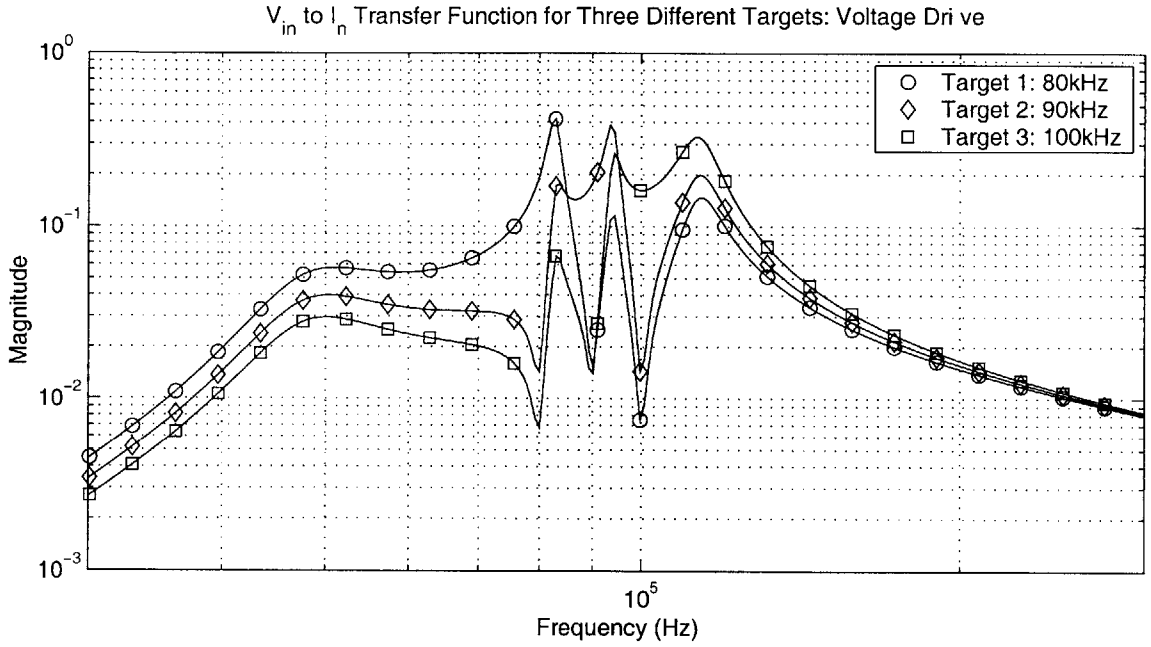

(a) Transfer function for 3 different targets.

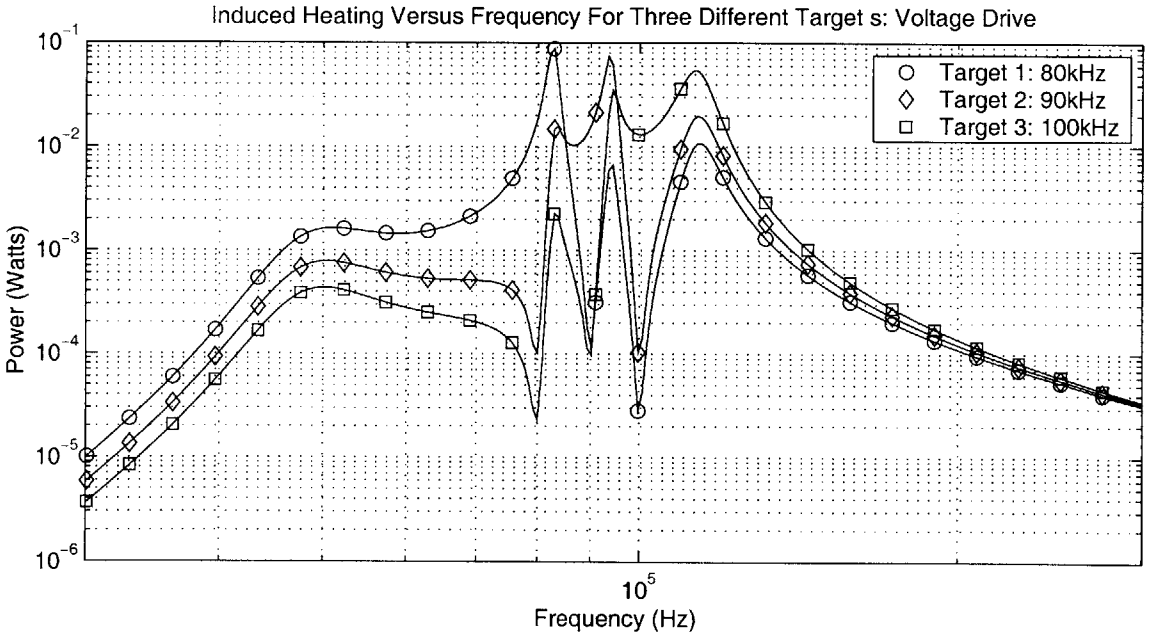

(b) Power profiles for 3 different targets.

Figure 4.6: V_{in}-to-I_n transfer function and power curves versus frequency for 3 different targets assuming a voltage drive, $V_{in} = 1$ V.

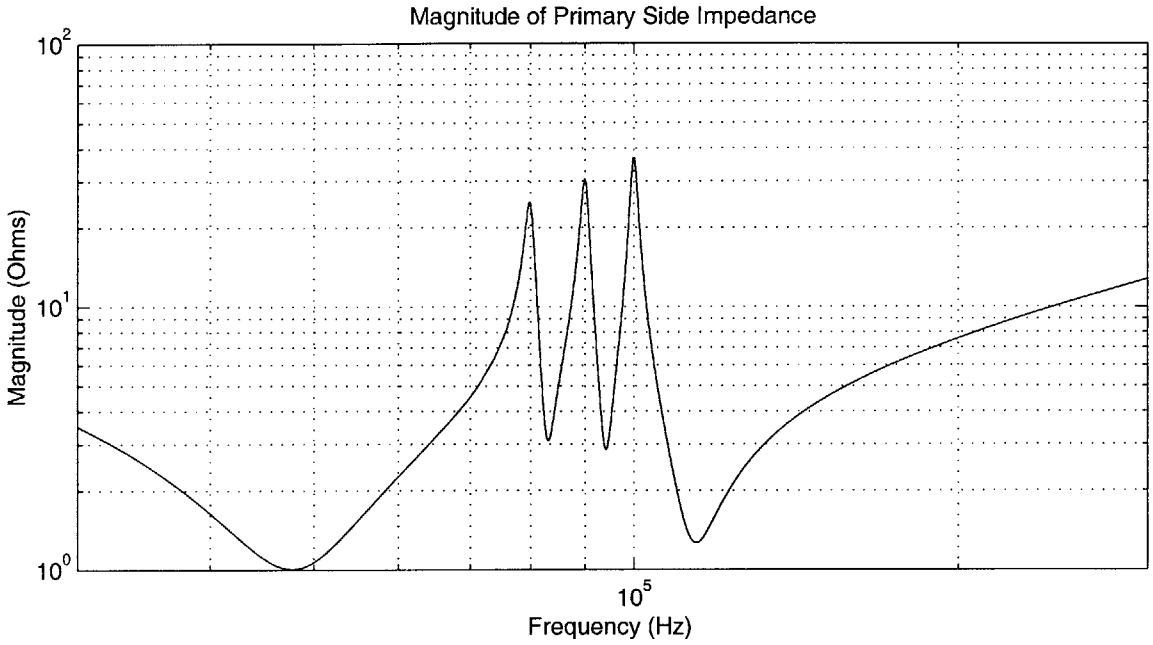

(a) Magnitude of load impedance.

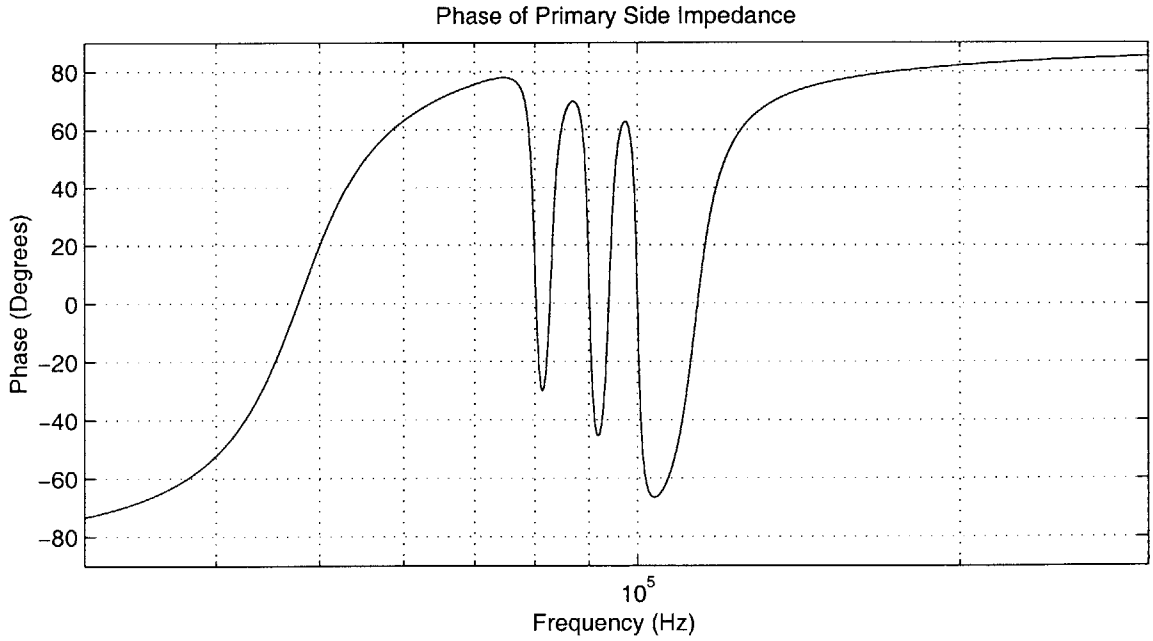

(b) Phase of load impedance.

Figure 4.7: Load impedance as seen by converter versus frequency.

4.4 Practical Issues

Resonant RLC induction targets can be constructed in a number of ways. Perhaps the easiest approach is to design each target using a passive element for each of its constituent components, i.e. a separate resistor, inductor and capacitor. For the gel damper application, this approach is less than desirable. Using a lumped resistor as the dissipative element localizes heating to a small area, while consuming precious volume in the gel chamber. A better approach is to rely on the parasitic resistance of the induction coil. If the coil windings are evenly distributed a uniform heating surface can be built. The capacitor could also be eliminated if the self-resonance of the coil is low enough. But if the inter-winding capacitance of the coil is insufficient, a lumped capacitor must be carefully selected. Because the selectivity of these targets relies on sufficiently high "Q's", it is not uncommon for the winding resistance to be small and the induced current to be high. From a practical standpoint the selected capacitor should have an ESR that is much smaller than the winding resistance. Otherwise, most of the induced heating will occur in the capacitor and not the windings. This may be undesirable for a number of reasons:

(1) Heat is localized to a small area, i.e. the capacitor.

(2) The resonant frequency may change significantly with temperature.

(3) Extreme temperature cycling can cause the capacitor to fail.

Stable capacitors with low dissipation factors such as silvered mica are ideal for this application, providing the appropriate values are available in reasonable volumes.

4.5 Model Validation

To test these models, experiments were conducted on a three resonant targets system. The frequency response of the resonant targets was estimated using FastHenry and then measured with a network analyzer. A detailed explanation of the experimental setup and results is available below.

4.5.1 Experimental Setup: Resonant Targets

A resonant multi-target system was built for testing. The primary coil has a diameter of 4.4 cm, a length of 20.4 cm and made from 48 turns of litz wire on a plexiglass former. The three resonant targets have the same 6.32 cm diameter with the following lengths: 4.0 cm, 4.1 cm, 4.2 cm. These coils were made from 57, 58, and 59 turns of 22 AWG wire, respectively. The output of these targets were paralleled using silvered mica capacitors of the following value: 30 nF, 20 nF, 40 nF. Figure 4.8 (A) shows a photo of the primary coil and targets coils. In order to calculate the theoretical transfer functions of the system, a 3-D model of each coil was generated and passed to Fasthenry to estimate the inductance matrix for the system. A view of the model used is shown in Figure 4.8 (B). The Coilgen source code for this model can be found in Appendix B.

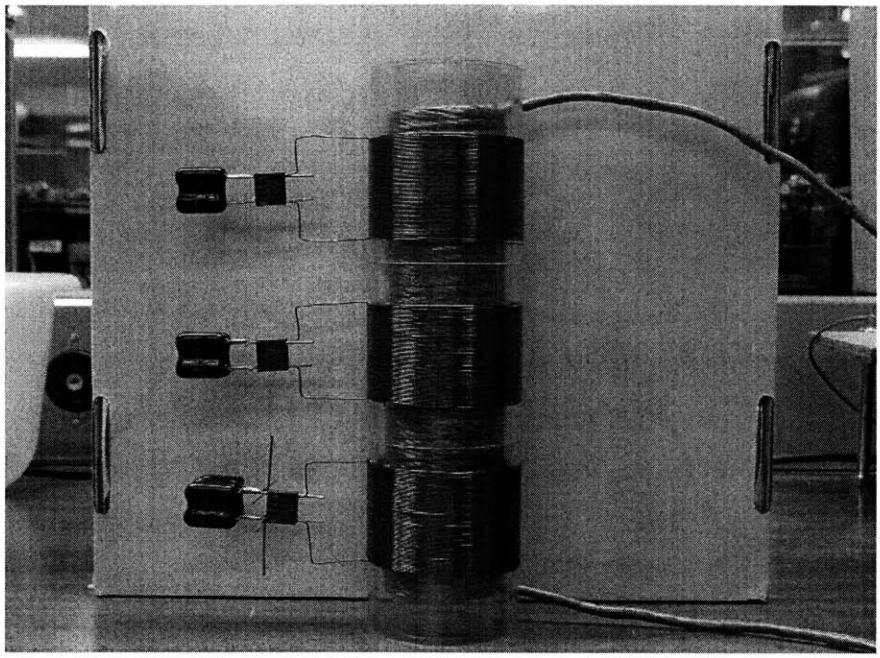

(a) Photo of system

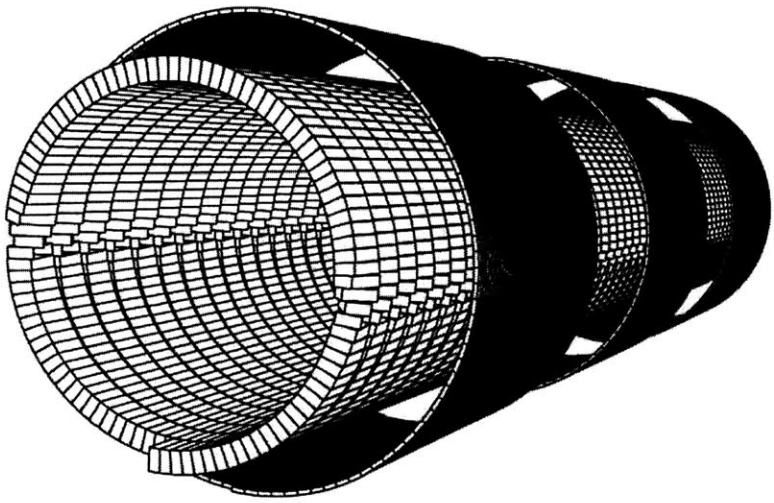

(b) 3-D FastHenry model

Figure 4.8: Photo and 3-D model of the multi-resonant induction heating system

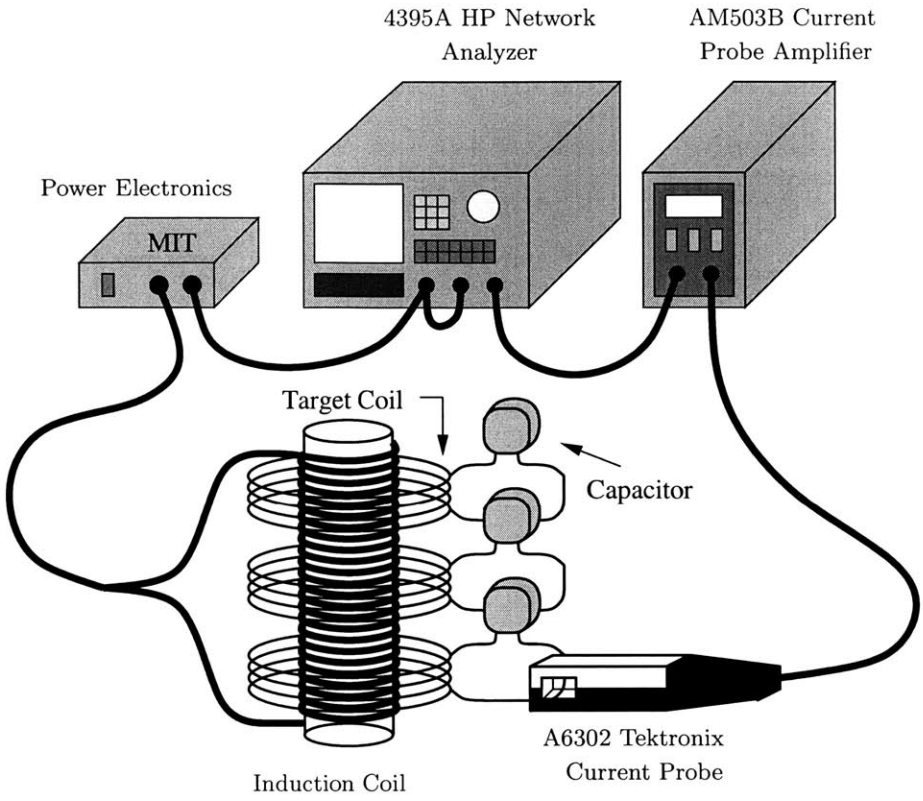

Figure 4.9: Multi-wire induction heating experiment.

The actual transfer functions were then measured for comparison using the test setup shown in Figure 4.9. An HP 4395A network analyzer determined the transfer function by sweeping the voltage reference that generates the multilevel sinewave approximation impressed across the induction coil. The current in each target was then measured via the current probe and amplified before being passed back to the network analyzer. Once all of the V_{in}-to-I_n transfer functions have been characterized, the power profiles of each target can be estimated using (4.43) as discussed previously.

4.5.2 Experimental Results: Resonant Targets

The measured results from the network analyzer are plotted against a theoretical prediction in Figure 4.10. It is clear from the figure that most of the salient features are in agreement. Notably the location of all resonances and anti-resonances are within a few percent of their predicted locations. In general the magnitude of the measured resonances and anti-resonances agree at low frequencies. However there is a growing error with increasing frequency. The reason for this discrepancy can be attributed to the additional ac losses in the windings as a result of skin and proximity effects at higher frequencies. These losses cause the measured maxima and minima to appear more damped than predicted. For

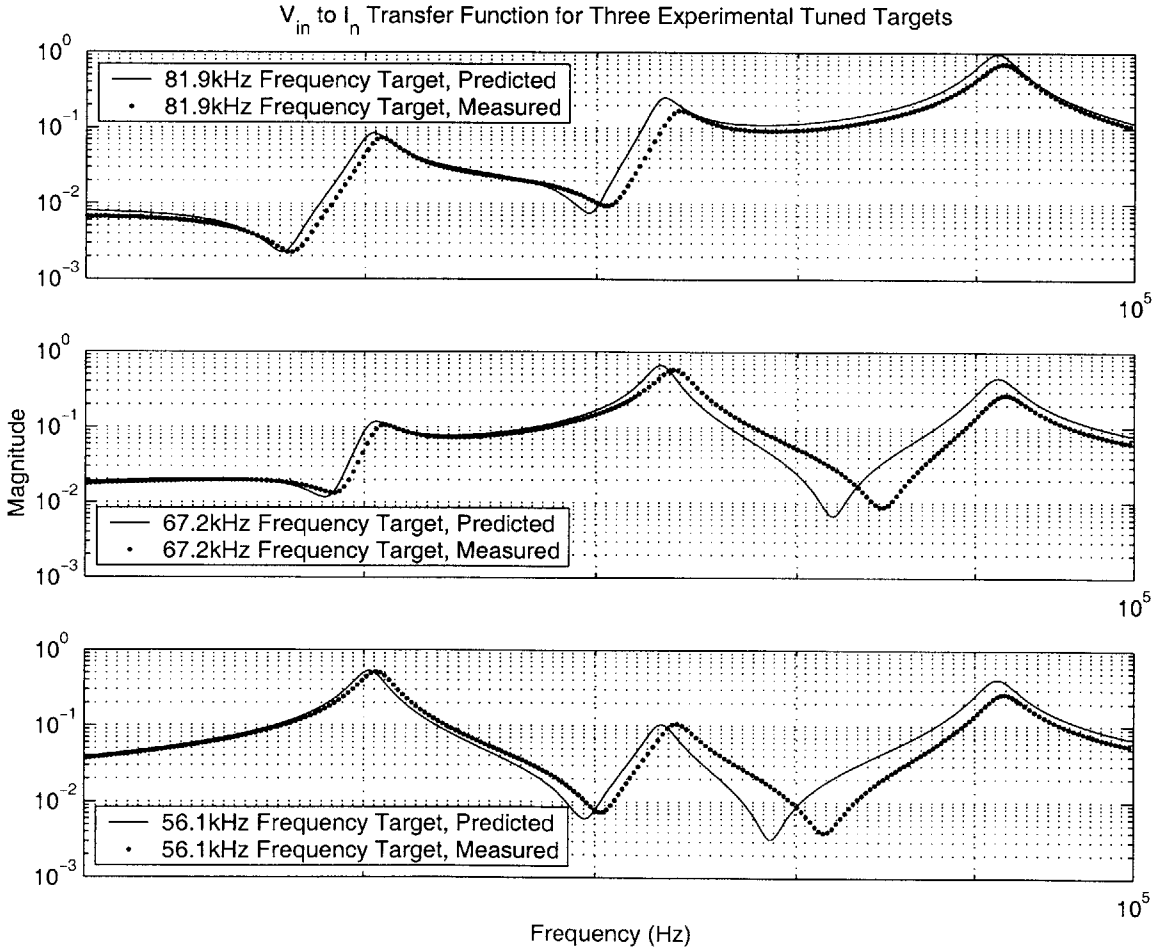

Figure 4.10: Results of multi-resonant induction heating experiment.

this particular fit, the ac resistance of the windings were measured at the low frequency resonances and used to re-estimate the transfer functions. If this resistance was measured for a higher frequency resonance, the fit would be noticeably improved there as well.

4.6 Chapter Summary

Frequency selectable induction heating targets can be constructed using resonant RLC circuits. By designing each target coil and capacitor to have a different resonant frequency, frequency selectivity can be achieved. An experimental system consisting of three resonant targets was built and tested. When compared to nonresonant selectable induction heating targets, resonant RLC circuits have the potential for considerably higher preferential heating in a smaller frequency band. Care must be taken to insure that the network is sufficiently resonant and that the majority of losses are not associated with the resonant capacitor. Thus far no details concerning the power electronics used to drive these targets has been discussed. In general, a power supply will be needed that can generate a sinewave with enough spectral purity to avoid heating unwanted targets. This is especially true for the nonresonant targets which offer very little filtering, compared to the resonant variant. A power supply that can efficiently drive these loads with low total harmonic distortion is the subject of the next chapter.

Chapter 5

The "Marx" Multilevel Inverter

THIS chapter presents a power supply suitable for driving the frequency selectable induction heating targets discussed in Chapters 3 and 4. Designing a power supply to drive the nonresonant target is especially challenging. By their very nature, these targets offer very little filtering, requiring a sinusoidal current or voltage with a low total harmonic distortion or THD. While there are many possible solutions to this problem, the "Marx" inverter [37] presented here is believed to offer an exceptional compromise between spectral purity and efficiency. This inverter, which is multilevel in nature, overcomes some of the inherent limitations of traditional multilevel inverters by taking a different approach to level synthesis. Most multilevel inverters divide down the bus to provide the needed voltage levels; the Marx inverter takes the opposite approach and "multiplies" the bus upward as necessary. Because of this approach, the Marx inverter is not a direct replacement for multilevel inverters intended to interface with medium voltage grids (2.3, 3.3, 4.16, or 6.9 kV) [34]. Rather, this topology offers an alternative option for inductively coupled power transfer in the low 100's of kHz range, were fidelity and efficiency are a premium.

The remainder of this chapter proceeds with a brief review of multilevel converters and reiterates the basic limitation of these converters for delivering real power. A high voltage pulse circuit called a Marx generator is then introduced that suggests a different approach to level synthesis. The Marx inverter is inferred from this pulse circuit as well as a more generalized topology that is capable of active power transfer. A discussion of the Marx inverter topology follows. In this section the basic implementation and control of this circuit is covered. Opportunities for achieving ZVS switching are also discussed

for the generation of staircase sinewaves. Some relevant issues concerning the gate drive requirement for this topology are also mentioned here. This chapter then spends some time comparing the performance of the Marx inverter against a more traditional power circuit– the pulse-width-modulated full-bridge inverter. The two circuits are compared on the basis of achievable efficiencies for an acceptable degree of total harmonic distortion. This comparison is first made for a simple LR load and is then extended to the case of multiple frequency selectable induction heating targets.

5.1 Background

This section provides helpful background information for understanding the role, origin and operation of the Marx inverter. The following three areas are reviewed:

(1) Multilevel Converter.

(2) The Marx Generator.

(3) The Generalized Inverter with Self-Voltage Balancing.

Additional background on these topics can be found in the references.

5.1.1 Multilevel Converters

As mentioned in Chapter 1, multilevel converters have provided an important means of approximating sinewaves in high power applications, doing so with low distortion and allowing devices with smaller breakdown voltage to be used aggregately. To review, the three most common multilevel converter topologies are the diode-clamped, capacitor-clamped and cascaded inverters with separate dc sources [22]. An example of each of these converters is shown in Figure 5.1. To understand the behavior of the first two topologies it is helpful to

realize that they have the general structure shown in Figure 5.2. Essentially, a capacitor ladder divides the bus voltage and produces the necessary voltages at the respective nodes. These nodes are then connected through a switching network, which can consist of active devices, diodes and capacitors.

Generating more than three levels with the first two topologies leads to significant capacitor voltage balancing problem when delivering real power [22]. In the case of a three-level converter it is possible to maintain the dc-link potential with proper control. This amounts to balancing the current flowing in and out of the capacitor ladder midpoint, shown in Figure 5.2. As the number of levels increases, the lack of symmetry and increased complexity make it extremely difficult to balance these currents. Consequently, beyond three levels these converters require separate, isolated dc sources or complicated voltage balancing circuits for active power transfer. For these reasons, the diode-clamped and capacitor-clamped converters have found limited use in applications that process real power, being typically used for reactive power compensation. The cascaded inverters topology is capable of active power transfer and has been used for powering large electric drives but relies on separate dc sources to work.

Table 5.1 gives a breakdown of the number of components required for these three topologies. In terms of active devices all of these multilevel inverters require the same number of components. However in terms of clamping components, both the diode-clamped and capacitor-clamped topologies have requirements that grow quadratically; the cascaded inverter does not. Another advantage of the cascaded inverter topology is that it requires half as many dc bus capacitors. While it is clear that the cascaded inverter circuit has a less stringent requirement on components, the need for isolated dc sources may be significant. Of course without isolated dc sources or at least a complicated control or external balancing circuit, none of the other topologies are suited to real power transfer, so the issue is moot.

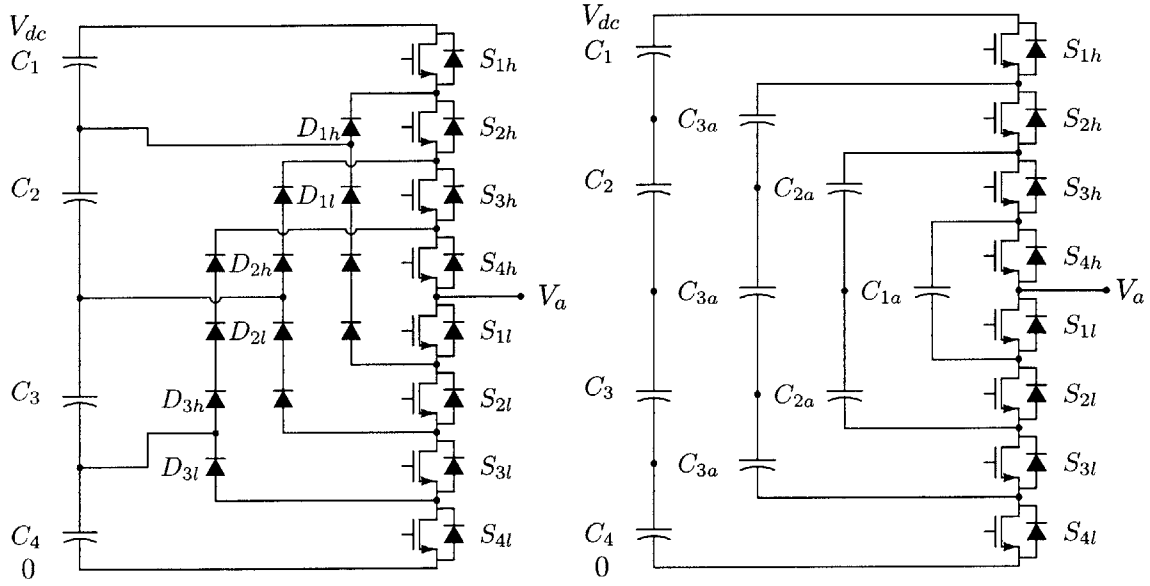

(a) Diode-Clamped.

(b) Capacitor-Clamped.

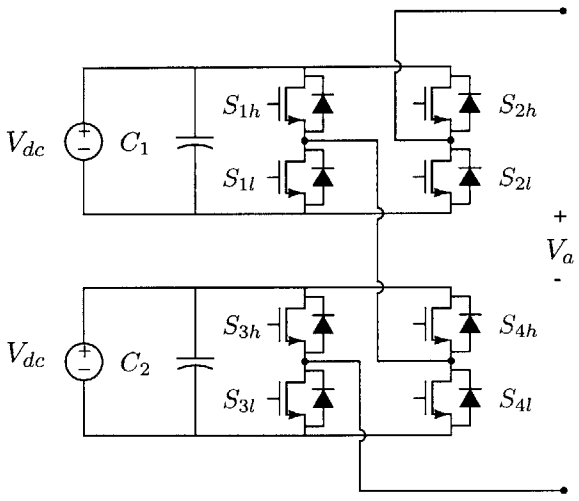

(c) Cascaded Inverters.

Figure 5.1: Examples of the three most common multilevel inverter topologies. Each of these converters can generate 5 levels.

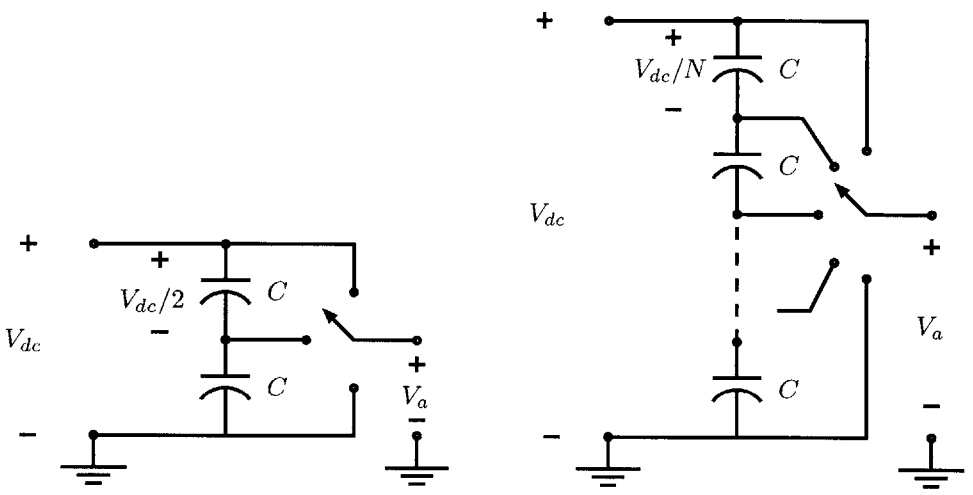

Figure 5.2: Simplified multilevel inverter topology, 3 level and N+1 level topologies shown.

Table 5.1: Comparison of part requirements among the traditional multilevel converters

Converter	Diode-Clamped	Capacitor-Clamped	Cascaded Inverters
Active Devices	$(m-1) \times 2$	$(m-1) \times 2$	$(m-1) \times 2$
Main Diodes	$(m-1) \times 2$	$(m-1) \times 2$	$(m-1) \times 2$
Clamping Diodes	$(m-1) \times (m-2)$	0	0
DC bus capacitors	$(m-1)$	$(m-1)$	$(m-1)/2$
Balancing capacitors	0	$(m-1) \times (m-2)/2$	0

5.1.2 The Marx Generator

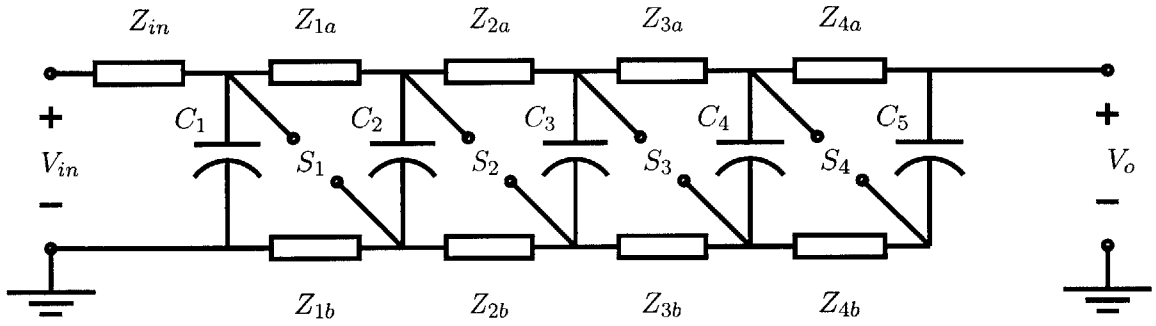

Figure 5.3: A five-stage Marx Generator.

The multilevel topology presented in this chapter is based on a high voltage pulse circuit invented in 1924 by Erwin Marx and referred to as Marx Generator [38]. Figure 5.3 shows a five-stage version of this pulse circuit. The basic idea behind the Marx Generator is that it can produce a high voltage pulse by *charging a bank of capacitors in parallel and discharging them in series.* The capacitors in a Marx Generator are normally charged through a high impedance network represented by $Z_{1a} - Z_{4a}$ and $Z_{1b} - Z_{4b}$. Typically the impedances shown are large resistances or chokes. Discharging the capacitors in series is accomplished by a switching network originally comprised of spark gaps or avalanche-type devices. When the first gap is triggered it sets into motion a cascade effect whereby each successive gap fires and all the capacitors are serially discharged.

If these spark gaps and the charging network are replaced by controllable switching devices it becomes possible to control the number of capacitors that are serially connected to the load. The result is a multilevel topology that generates the required voltage levels by multiplying the DC bus voltage as opposed to dividing it down. One way to replace the spark gaps and charging network is shown in Figure 5.4. Because the basic concept behind this inverter is similar to the Marx Generator, the topology shown here will be referred to as a "Marx" multilevel inverter. In this case, the circuit shown here constitutes a single phase leg of a four-level, Marx inverter.

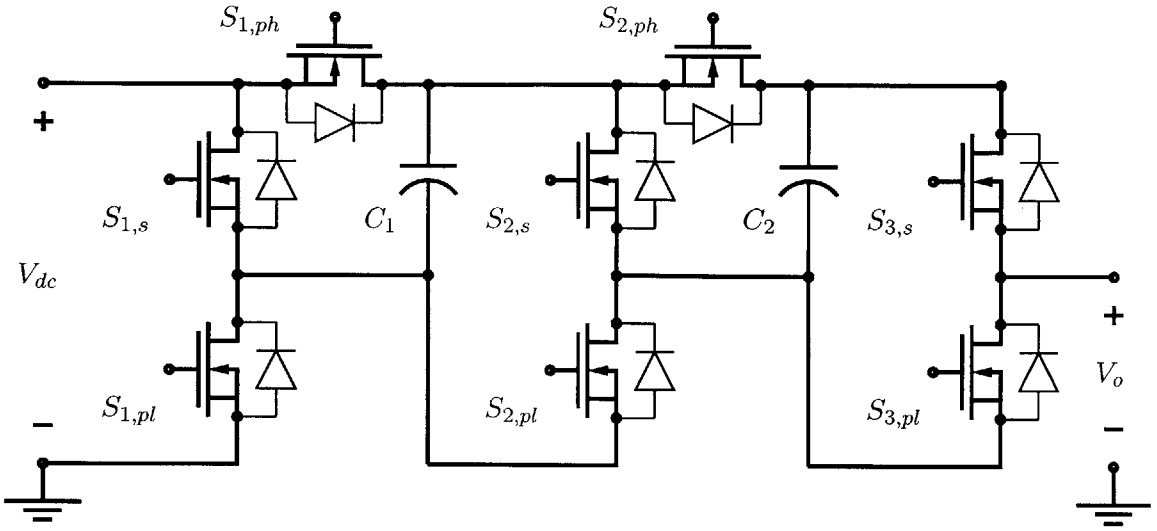

Figure 5.4: A four-level Marx inverter.

5.1.3 The Generalized Multilevel Inverter with Self-Voltage Balancing

So far, no serious discussion has been made concerning the Marx inverter's capability to process real power while maintaining the capacitor voltages needed to make multiple levels. One way to recognize, that The Marx inverter can process real power is to consider yet another multilevel topology introduced in [32]. Referred to as the generalized multilevel inverter, this circuit eliminates the voltage balancing problem for real power transfer because of its inherent auto-balancing topology. For a detailed description of how this converter works, the reader is referred to the appropriate source. Briefly speaking, every time a transition is made different capacitors are paralleled together. If any imbalance in voltage is present prior to switching it is equalized with its paralleled neighbor. In this way charge is constantly being redistributed and the voltage levels are maintained. This process is not unlike a technique presented in [31] that uses a switched capacitor network to equalize battery voltages in a series string.

The downside of the generalized topology is that that the number of active switching devices grows quadratically with the number of levels. As a result the applications that would benefit from this inverter are somewhat limited but include: switched-capacitor dc-

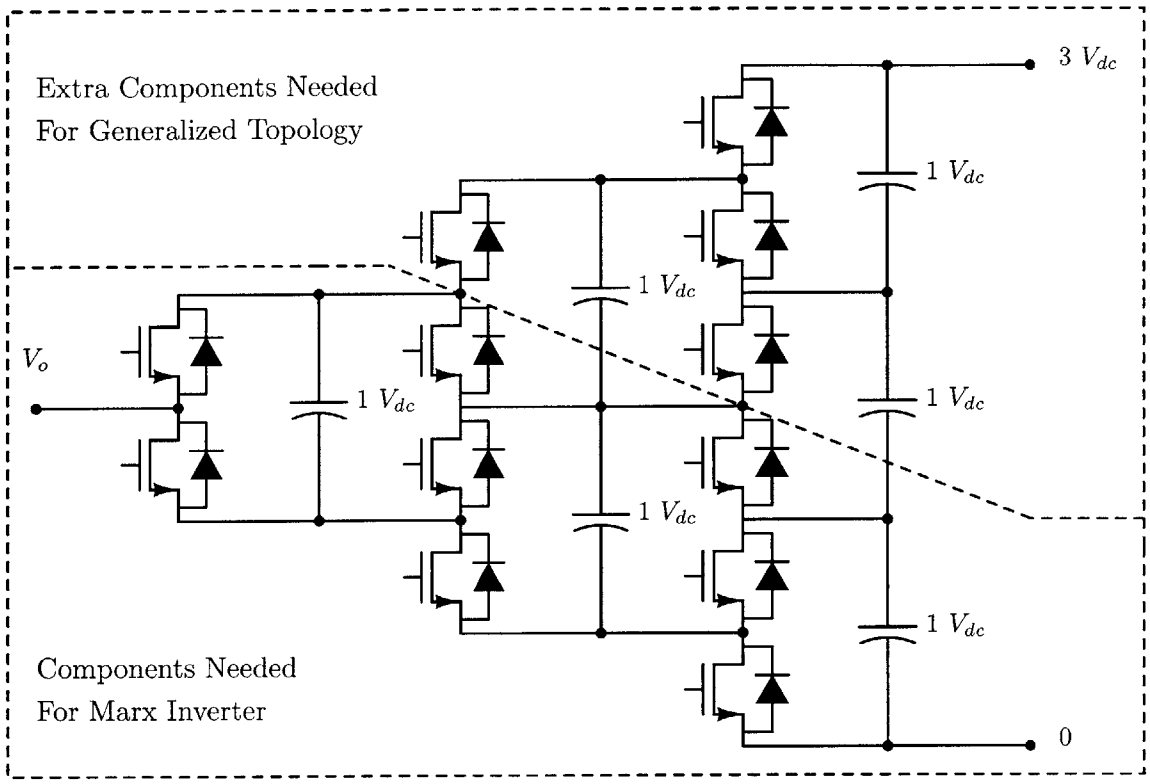

Figure 5.5: Inferring the Marx inverter from the generalized multilevel converter.

to-dc converters and voltage multipliers where the component count is less than traditional ones. Perhaps more important is that the generalized topology can be used to infer other possible multilevel inverters, some of which are less part intensive. The Marx inverter falls into this category, requiring fewer switching elements while preserving the auto-balancing feature of the generalized multilevel converter. Figure 5.5 shows a four-level generalized converter and how one-third of the switches (in this case) can be eliminated to produce a Marx inverter. Removing the extra switches forces the input side of the converter to interface with a smaller bus voltage, therefore the Marx inverter may not be suited for connecting to medium voltage grids. Fortunately, this is not a disadvantage in the induction heating application since a smaller dc voltage sources is preferable.

5.2 Marx Inverter Topology Discussion

This section provides an overview of the Marx inverter topology. First, the inverter is reduced to a basic cell structure and the overall function of this building block is described. This section then goes on to describe how the actual inverter can be constructed from these cells and how they can be switched to make multiple levels. Because this topology is part intensive, the number of devices required to construct a Marx inverter is then compared against other multilevel topologies. Next, a control scheme is described that allows the Marx inverter to quantize reference waveforms. To illustrate this behavior, some sample waveforms are provided. With proper implementation the Marx inverter can achieve ZVS switching while generating quantized sinewaves across an inductive load. A section describing the requirements for ZVS operation is therefore provided. Finally, a way to drive all of the Marx inverter's MOSFETs using floating capacitor IC's, such as the IR2125, is discussed.

5.2.1 The Marx Cell

An M-level Marx inverter can be decomposed into a cascade of M-2 Marx cells and one half-bridge inverter. Operation of this inverter can be understood by examining the basic Marx cell shown in Figure 5.6(a). Each cell is composed of a capacitor and three switches which serve to either parallel (via $S_{m,pl}$, $S_{m,ph}$) the capacitor with the cell preceding it or to connect it in series (via $S_{m,s}$) with it. When paralleled the output voltage of the m^{th} cell is

$$V_{m+1} = V_m, \tag{5.1}$$

or when in series given by

$$V_{m+1} = V_m + V_{dc}. \tag{5.2}$$

By definition $V_1 = V_{dc}$. The cascade of Marx cells can be used to generate $M - 1$ levels above ground while the final stage shown in Figure 5.6(b) is used to select one of these

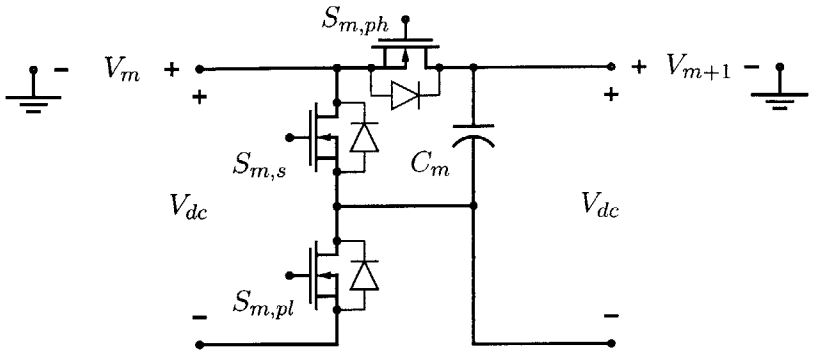

(a) Marx cell.

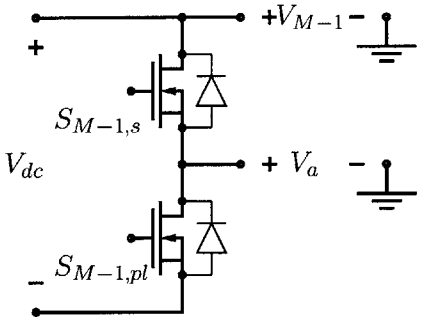

(b) Half-Bridge (M^{th} stage).

Figure 5.6: The basic Marx cell and last stage half-bridge inverter.

levels to produce

$$V_a = V_{M-1}, \tag{5.3}$$

or alternatively to select ground when all of the capacitors are in parallel,

$$V_a = V_{M-1} - V_{dc} = 0. \tag{5.4}$$

In general an M-level Marx inverter has 2^{M-1} possible switching states. Therefore, there are redundant states for some of the intermediate voltage levels. In the case of certain multilevel inverters, such as the capacitor-clamped topology, redundant switching states may be useful for capacitor voltage balancing. Because the capacitor voltages of a Marx inverter are equalized to the bus voltage whenever all the capacitors are paralleled, redundant states need not be used. Instead, it is easier to use a set of states that simplifies

the overall control. One scheme to do this is to stack the capacitors sequentially by starting from the source side. The switching states for this approach are shown in Table 5.2. Of course, different switching patterns could be chosen. For instance, instead of stacking capacitors by starting at the source side, the stacking process could also begin at the output side as listed in Table 5.3. Still other redundant states exist. These two switching approaches listed lead to the easy control implementation, however the first pattern offers the additional flexibility when implementing the high-side gate drives as will be seen. Figure 5.7 illustrates the four switching patterns for this implementation by depicting each on-switch in black, and each off-switch in gray.

Table 5.2: Switching states for a four-level Marx inverter sequentially stacking capacitors starting from the source side.

V_a	$S_{1,p}$	$S_{2,p}$	$S_{3,p}$	$S_{1,s}$	$S_{2,s}$	$S_{3,s}$
0 V_{dc}	1	1	1	0	0	0
1 V_{dc}	0	1	1	1	0	0
2 V_{dc}	0	0	1	1	1	0
3 V_{dc}	0	0	0	1	1	1

Table 5.3: Switching states for a four-level Marx inverter sequentially stacking capacitors starting from the output side.

V_a	$S_{1,p}$	$S_{2,p}$	$S_{3,p}$	$S_{1,s}$	$S_{2,s}$	$S_{3,s}$
0 V_{dc}	1	1	1	0	0	0
1 V_{dc}	1	1	0	0	0	1
2 V_{dc}	1	0	0	0	1	1
3 V_{dc}	0	0	0	1	1	1

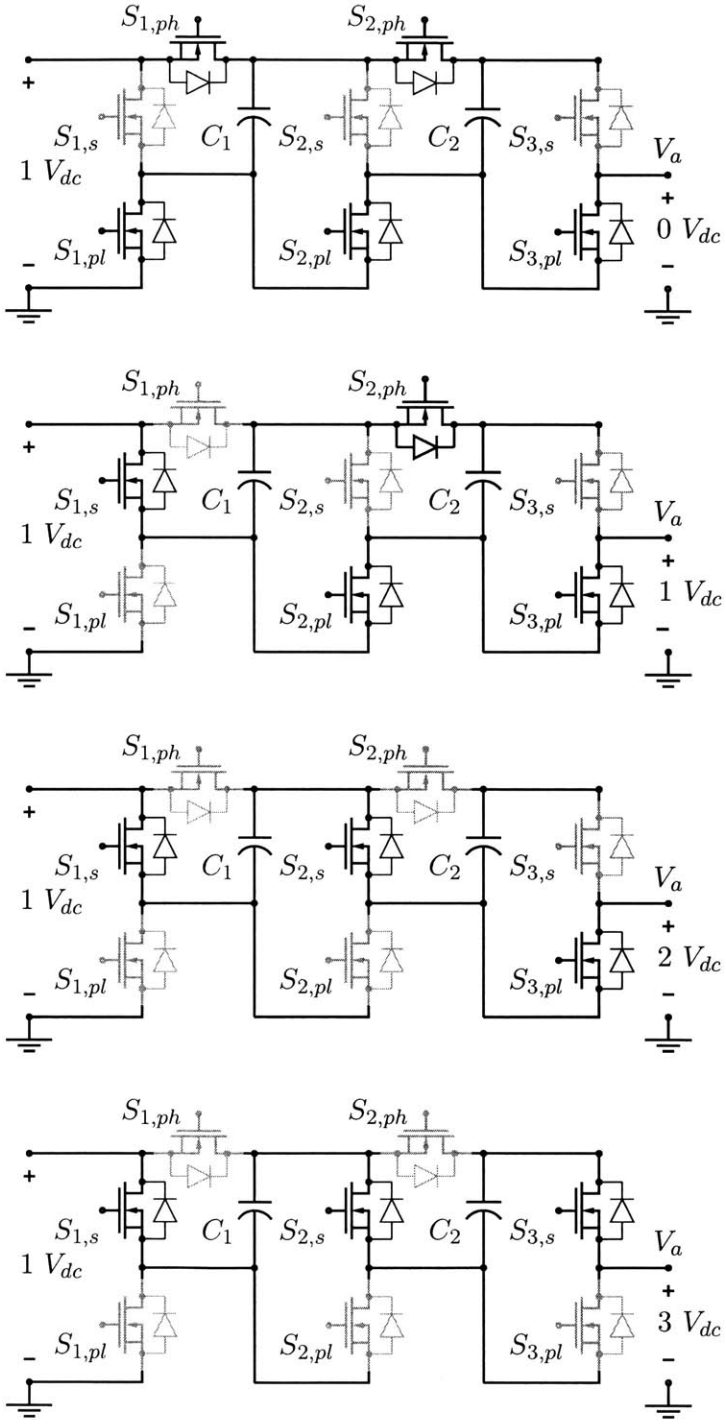

Figure 5.7: A four-level Marx inverter with various switching states shown. Switches in black are on, while switches in gray are off.

5.2.2 Comparing the Device Count

Having established the general structure of the Marx inverter, the number of components required to make this topology work can now be compared against other multilevel converters. Table 5.4 gives a breakdown for the components needed to build an M-level, diode-clamped, generalized and Marx type inverters. From this comparison it is clear that the requirement of active devices for the Marx inverter is in between that of the diode-clamped and generalized converters. With the exception of the last stage, the Marx inverter basically requires one more active device per level than the diode-clamped inverter. However the Marx inverter does not require any clamping diodes. In the case of the diode-clamped topology the number of clamping diodes grows quadratically and quickly becomes the bottleneck for implementation. In terms of the required capacitors, these two topologies are identical, although the capacitors serve different purposes in each topology.

Table 5.4: Part requirements for Marx inverter versus diode-clamped and generalized inverters

Converter	Diode-Clamped	Generalized Inverter	Marx Inverter
Active Devices	$(m-1)\times 2$	$m\times(m-1)$	$3m-4$
Main Diodes	$(m-1)\times 2$	$m\times(m-1)$	$3m-4$
Clamping Diodes	$(m-1)\times(m-2)$	0	0
DC bus capacitors	$(m-1)$	$(m-1)$	1
Balancing capacitors	0	$(m-1)\times(m-2)/2$	$m-2$

5.2.3 Control and Modulation Strategy

Most control and modulation strategies for multilevel inverters are meant for synthesizing sinewaves at low frequencies for utility or industrial applications. In general these approaches fall into two categories [34]:

- High switching frequency PWM techniques.
- Fundamental switching frequency techniques.

Two high frequency PWM methods, the classic sinusoidal PWM method and the Space Vector PWM approach, are well suited to low frequency sine generation. These schemes suffer from significant switching losses as well as switching speed limitations when trying to synthesize sinewaves in the 100-300 kHz range or higher. For high frequencies, fundamental switching frequency strategies can be advantageous, generally requiring fewer switching transitions to produce a sinusoidal approximation. A conventional six-pulse sinewave drive is a familiar example of a fundamental switching frequency technique. Recent fundamental switch frequency strategies include the selective harmonic elimination approach[40] and the Space Vector Control technique [35].

A different fundamental switching frequency strategy is explored in this thesis – using the Marx inverter as a symmetric uniform quantizer. This approach can be implemented with a minimal amount of analog hardware, is simple to understand, and can be used to approximate more complicated ac waveforms. Of particular importance are sums of sinewaves, which would allow the Marx inverter to drive multiple frequency selectable induction heating targets simultaneously. The suggested control scheme follows the block diagram in Figure 5.8. First, the amplitude of a reference waveform is compared against six decision levels to determine which level is generated at the output. This is accomplished using a bank of comparators to convert the reference waveform into a simple thermometer code, not unlike those used in flash analog-to-digital converters. The output is then decoded with an appropriate amount of dead-time inserted into the appropriate control signals to

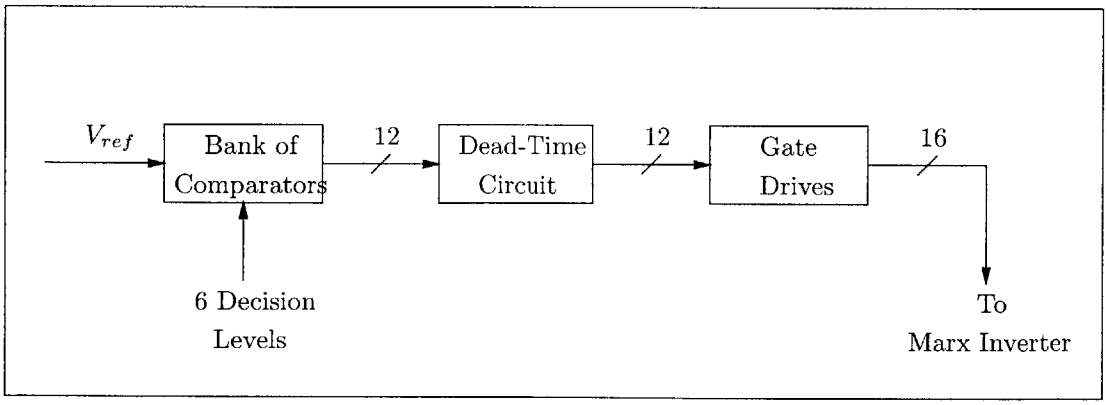

Figure 5.8: Block diagram of control strategy.

provide the correct gate drive logic for two $M = 4$, single-phase Marx inverters operated differentially. This effectively creates a seven-level, symmetric uniform mid-tread quantizer whose transfer characteristic is shown in Figure 5.9. For detailed schematics of how this control circuitry is implemented, the reader is referred to Appendix C.

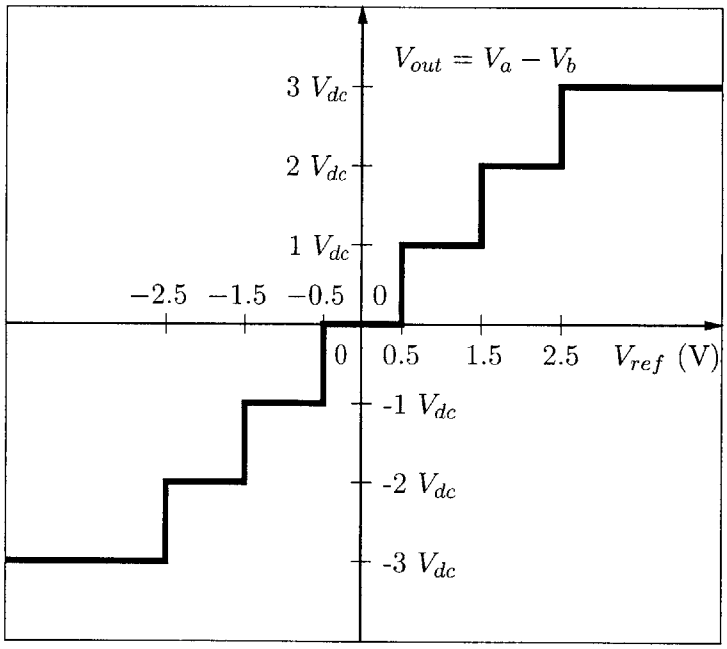

Figure 5.9: A seven-level symmetric uniform mid-tread quantizer.

5.2.4 Sample Waveforms

Figures 5.10 and 5.11 are a collection of sample waveforms generated by a 1 kW prototype Marx inverter functioning as a seven-level quantizer. Two $M = 4$ phase legs are used to drive either a 200-μH air-core inductor Figure 5.10(a-b) and Figure 5.11(c) or a 100-Ω resistor shown in Figure 5.11(d) differentially. Each snapshot shows three waveforms which correspond (from top to bottom) to the input reference waveform, a multilevel approximation and the current drawn from the converter. As seen in these various scope plots, the Marx inverter can drive a variety of AC waveforms across an inductive load, and/or deliver real power while still maintaining appropriate voltage levels.

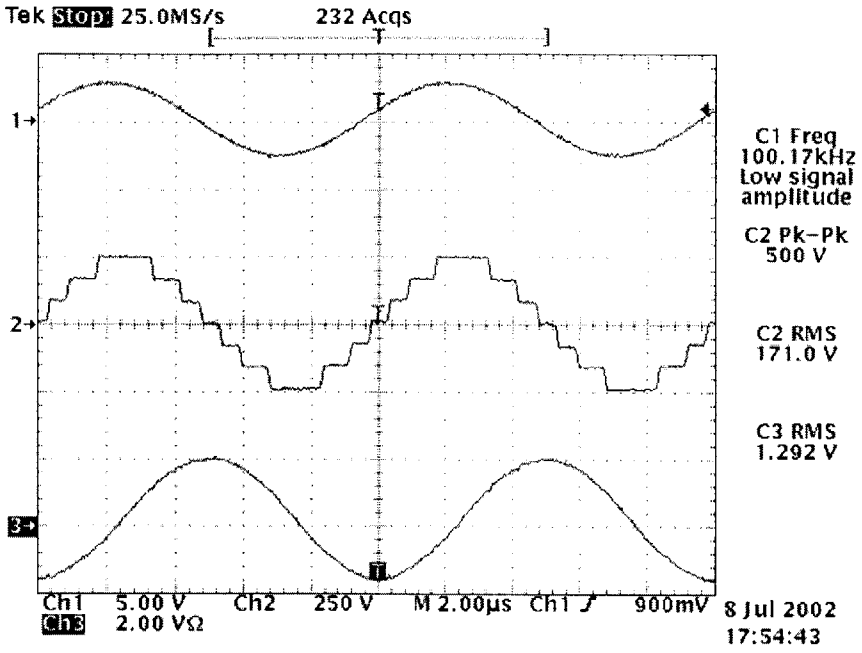

(a) 100 kHz Sinewave across a 200 μH air core inductor

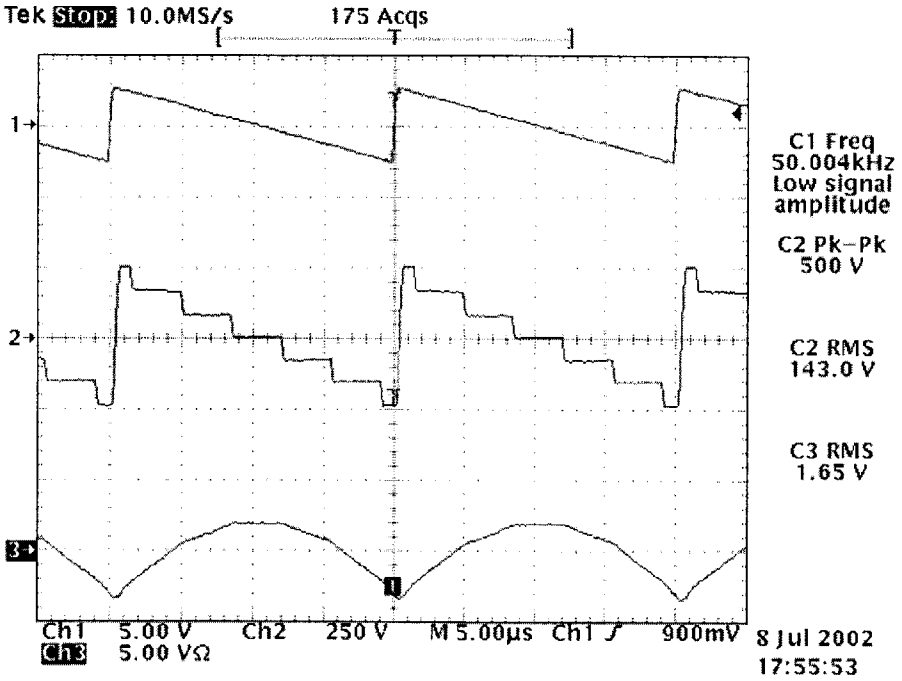

(b) 50 kHz Sawtooth across a 200 μH air core inductor.

Figure 5.10: Sample Marx inverter waveforms. Channels 1 and 2 are the reference waveform and Marx output voltage respectively. Channel 3 shows the output current of the converter on 2 A/Div scale for subfigure (a) and 5 A/Div for subfigure (b).

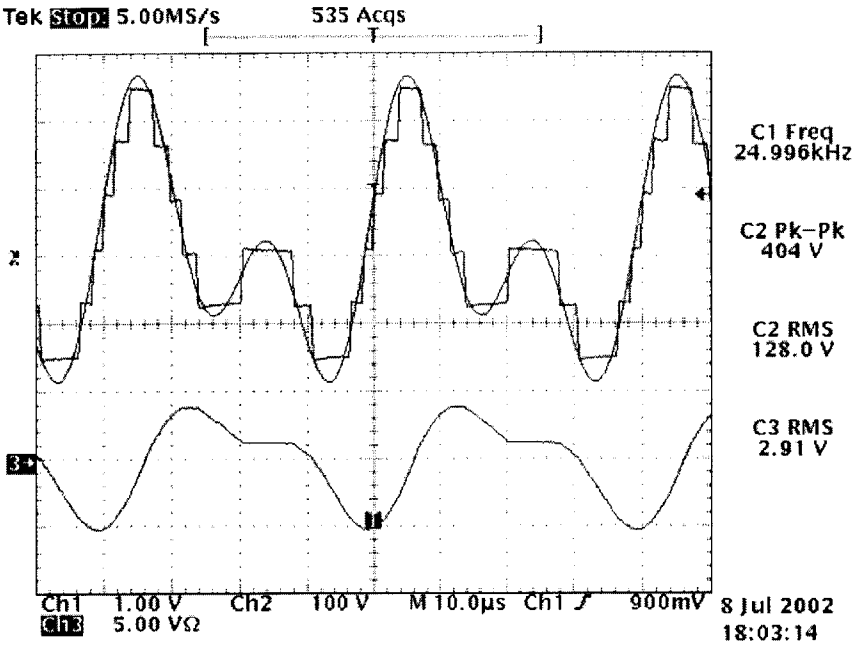

(a) A 25 kHz and 50 kHz sum of sinewaves across a 200 μH air core inductor.

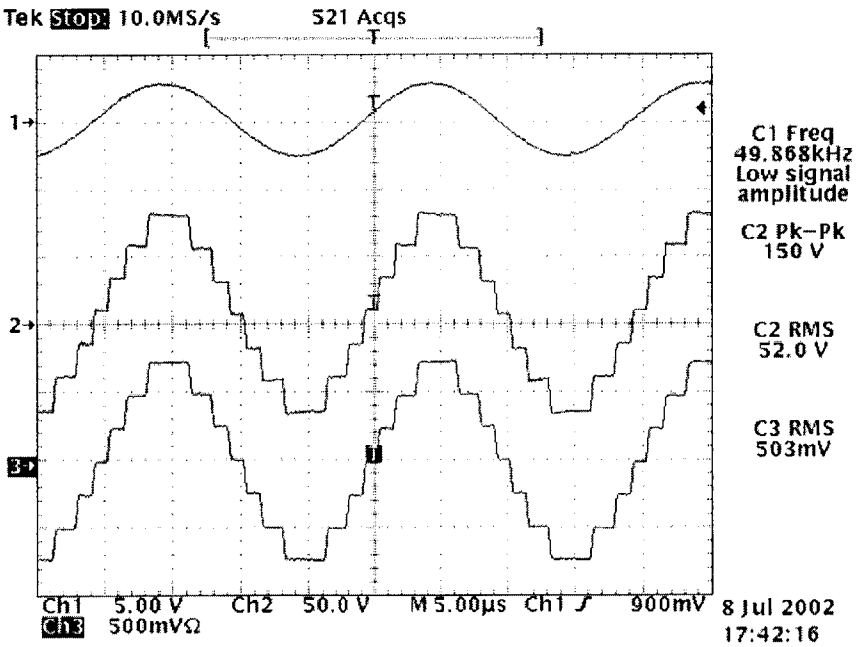

(b) A 50 kHz Sinewave across a 100 Ω resistor.

Figure 5.11: Sample Marx inverter waveforms, cont. Channels 1 and 2 are the reference waveform and Marx output voltage respectively. Channel 3 shows the output current of the converter on 5 A/Div scale for subfigure (a) and 0.5 A/Div for subfigure (b).

5.2.5 ZVS for Sinewave Generation

When driving an inductive load, the inserted dead-time between switching transitions provides an opportunity for energy stored in a body diode's capacitance to be returned to the source. This allows a switch to be turned on with zero volts across it, a process referred to as zero voltage switching or ZVS. This type of switching has long been an important means for reducing switching losses in power electronics. In the case of the Marx inverter, ZVS operation is possible as long as the load current has the "right" polarity and is of sufficient amplitude. The load current has the "right" polarity whenever it is negative (goes into the inverter phase) during switching transitions that raise the (inverter phase) output voltage and positive for transitions that lower the output voltage. To understand this it may be helpful to refer to Figure 5.12 for the remainder of this discussion.

Figure 5.12 shows the output voltage of a single Marx (M-Level) phase leg as it generates the first half-cycle of a sinewave approximation. If there are enough levels and sufficient filtering, the resulting load current will appear sinusoidal and is shown here in gray. When the load is purely inductive, the load current will lag the voltage by 90^o. If the load has a real component, i.e. real power is delivered, the phase of the current, $\theta_{I_{load}}$, will lie between 0^o and 90^o and the current may not have the correct polarity for all possible transitions.

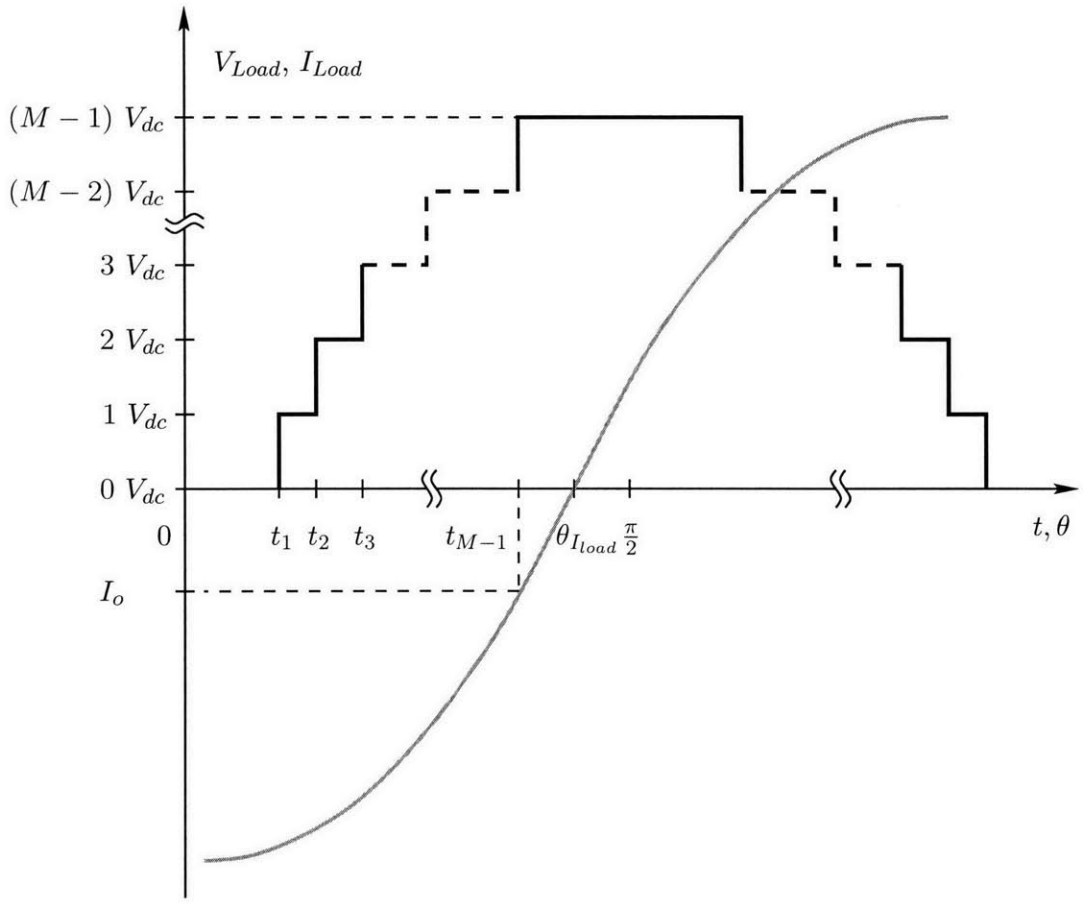

Figure 5.12: Sample voltage and current waveforms for understanding how the Marx inverter can operate with ZVS transitions when driving an inductive load.

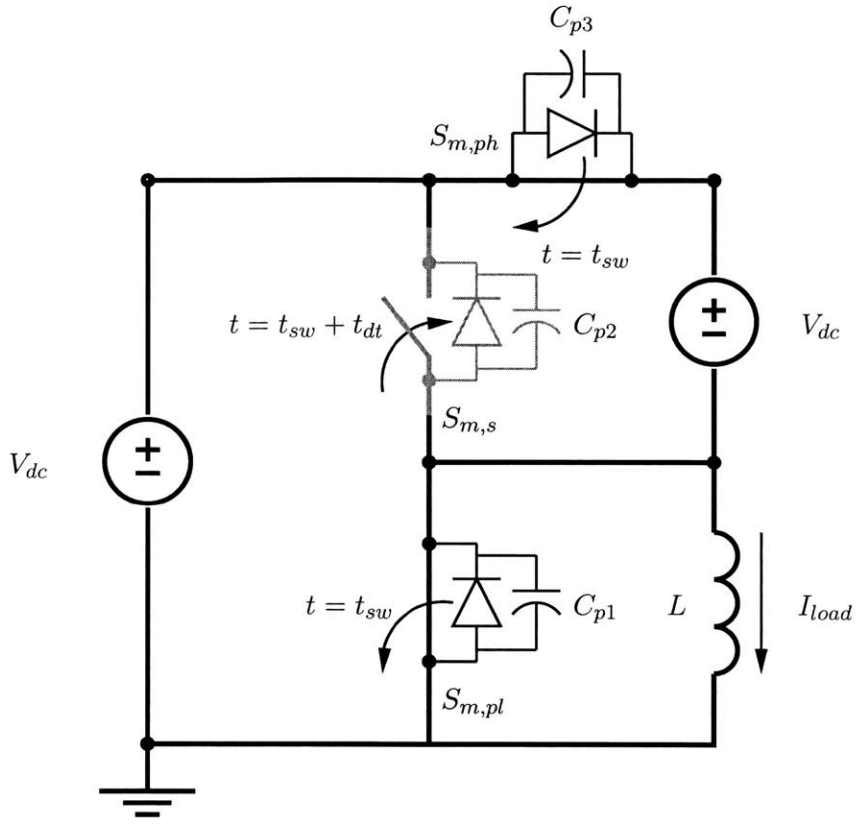

Figure 5.13: ZVS circuit

The exact requirements on the current amplitude, phase, and dead-time needed to achieve ZVS can be determined by examining the Marx inverter at the appropriate transition. For transitions that increase the output voltage, the Marx cell that is switching can be reduced to the circuit shown in Figure 5.13. For simplicity the load has been represented as an inductor and the parasitic diode capacitances are treated as linear capacitors. Because of the small time scales of interest during switching, the large Marx capacitors in the circuit are modelled as dc voltage sources. Prior to this transition, $S_{m,pl}$ and $S_{m,ph}$ are on and $S_{m,s}$ is off. At $t = t_{sw}$, switches $S_{m,pl}$ and $S_{m,ph}$ are opened and the current flowing through the inductor begins to discharge the voltage stored on capacitor C_{p2}. If there is enough initial current in the inductor, the voltage on the parasitic capacitor will ring to zero causing the D_2 body diode to conduct and clamp the voltage to the rail. Switch $S_{m,s}$ can now be turned on with zero volts across it. The change in the voltage across C_{p2} only

depends on the inductor current; this is true because if the inductor current was zero the system would be at rest with V_{dc} stored on C_{p2}. The voltage on this capacitor as a function of time is given by

$$V_{C_{p2}}(t) = V_{dc} + I_{load}(t_{sw})\sqrt{\frac{L}{C}}sin(\omega_o t), \tag{5.5}$$

where the natural frequency of oscillation is

$$\omega_o = \frac{1}{\sqrt{LC}}, \tag{5.6}$$

and

$$C = C_{p1} + C_{p2} + C_{p3}. \tag{5.7}$$

For the transitions that lower the output voltage, the Marx inverter can be simplified to the following circuit shown in Figure 5.14. Prior to this transition $S_{m,s}$ is conducting and $S_{m,pl}$ and $S_{m,ph}$ are off. At $t = t_{sw}$, $S_{m,s}$ is opened and the voltage stored on C_{p1} and C_{p3} begins to discharge. Unlike the previous case, even without any energy stored in the inductor the voltage on these parasitic capacitors would decay to zero. Current cycling through the inductor simply speeds up the process. The time evolution of the voltage on C_{p1} and C_{p3} can be expressed as

$$V_{C_{p1}}(t) = V_{C_{p3}}(t) = V_{dc}cos(\omega_o t) - I_{load}(t_{sw})\sqrt{\frac{L}{C}}sin(\omega_o t). \tag{5.8}$$

Comparing (5.5) and (5.8) it is clear that the voltage on $V_{C_{p2}}$ is the slower of the transitions for the same inductor current. Furthermore, Figure 5.12 makes clear that during a positive going transition the amount of inductor current is generally smaller then the current at the analogous negative transition. In fact, as the phase of the current approaches 0^o, the current at time $t = t_{M-1}$ may not only be too small it might actually have the wrong sign. As a result this instance is the most critical. As long as ZVS is possible during this transition, the inductor current should be large enough to ZVS any of the other transitions. Because switching at time $t = t_{M-1}$ is done by the half-bridge inverter stage, the results obtained for

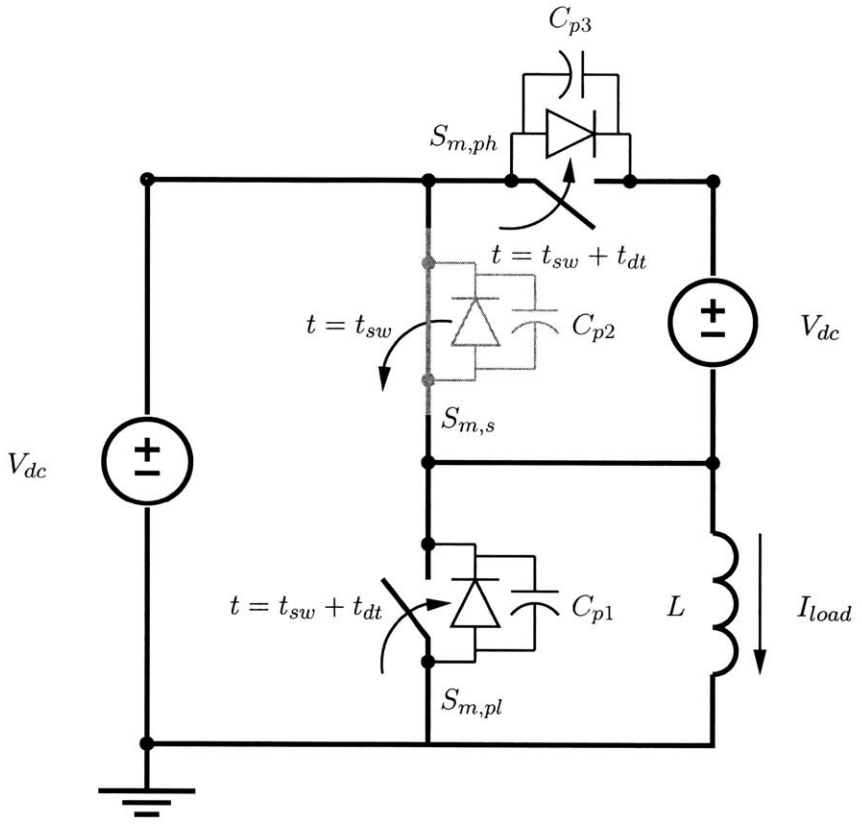

Figure 5.14: ZVS circuit

the Marx cell should be modified to reflect the lack of the additional parasitic capacitance by replacing C in equations (5.5) and (5.6) with

$$C = C_{p1} + C_{p2}. \tag{5.9}$$

Referring to Figure 5.12, the current at time $t = t_{M-1}$ is denoted as I_o. In order for equation (5.5) to reach zero, the amplitude of the current at this time, I_o, must satisfy the following inequality,

$$|I_o| \geq \frac{V_{dc}}{\sqrt{\frac{L}{C}}}. \tag{5.10}$$

Furthermore, for the inductor current to completely ring the switch voltage to zero it is also necessary for the inserted dead-time, t_{dt}, to exceed the amount of time it takes equation

(5.5) to go to zero. This leads to an additional constraint,

$$t_{dt} \geq \sqrt{LC} sin^{-1}\left(\frac{V_{dc}}{I_o\sqrt{\frac{L}{C}}}\right). \tag{5.11}$$

Earlier, we chose to model the load as a pure inductance because it lead to simple time-domain expressions for the parasitic capacitor voltages. In truth, the load must have some resistive component or no power would be delivered. A more accurate model would be to include a resistance, R, in series with the inductor. Provided the characteristic impedance $\sqrt{\frac{L}{C}}$ is large compared to the real part of the load, the results developed in (5.5) will hold approximately. Stated differently, as long as the RLC circuit formed by the load and the parasitic capacitances has a high enough Q, the solution given in (5.5) will be accurate for short times. In this case, the main purpose of including the resistance is to account for the phase shift in current and its effect on the current amplitude,

$$I_{load}(t) = \frac{(M-1)V_{dc}}{\sqrt{R^2+(L\omega)^2}} sin\left(\omega_o t - tan^{-1}\left(\frac{L\omega}{R}\right)\right). \tag{5.12}$$

The value of the current at time, $t = t_{M-1}$, can be found by evaluating the above expression at that time to give

$$I_o = I_{load}(t_{M-1}) = \frac{(M-1)V_{dc}}{\sqrt{R^2+(L\omega)^2}} sin\left(\omega_o t_{M-1} - tan^{-1}\left(\frac{L\omega}{R}\right)\right). \tag{5.13}$$

This equation can be used in conjunction with equations (5.10) and (5.11) to see if ZVS transitions are possible while generating staircase sine waves with the given circuit parameters. It is important to note that there might be additional constraints not considered here. For instance, the dead-time should also be smaller than the available time between two adjacent transitions. Lastly, these results are predicated on certain assumptions concerning the resistive component of the load. If the Q of the system is not high, as previously stated, the exact equations will have to be computed.

5.2.6 Gate Drive Implementation

All of the multilevel converters presented thus far have a large high-side switch requirement. The Marx inverter is no exception. In this thesis, the gate drives for the Marx inverter's high-side switches were implemented with floating capacitor IC's such as the IR2125. In order for these IC's to properly boot-strap themselves the cathode of the floating capacitor is periodically grounded as part of a converter's normal operational cycle. This can be problematic for a Marx inverter because the high-side paralleling switches (S_{ph}) are never grounded as the converter cycles though its different levels. One solution to this problem is shown in Figure 5.15. For the purposes of discussion the m^{th} basic Marx cell is shown[1], cells 1 through $m-1$ have been represented as a single switch $S_{1,pl} - S_{m-1,pl}$ and cells greater than m are ignored. When the output of the phase leg shown is zero, switches $S_{1,pl} - S_{m,pl}$ are on and capacitors C_{u1} and C_{u2} are replenished in the usual way as diodes D_1 and D_2 conduct. When the output level changes as the result of $S_{m,s}$ turning on in complementary fashion, C_{u3} is charged from C_{u2} through D_3. To prevent the charge on C_{u2} from dropping significantly when C_{u3} is charged, it should be over sized by at least a factor of ten, i.e.

$$C_{u2} \geq 10C_{u3}. \tag{5.14}$$

[1]The M^{th} stage of the converter, consisting of the half-bridge inverter, does not have the additional high-side switch and can therefore be implemented in the usual way.

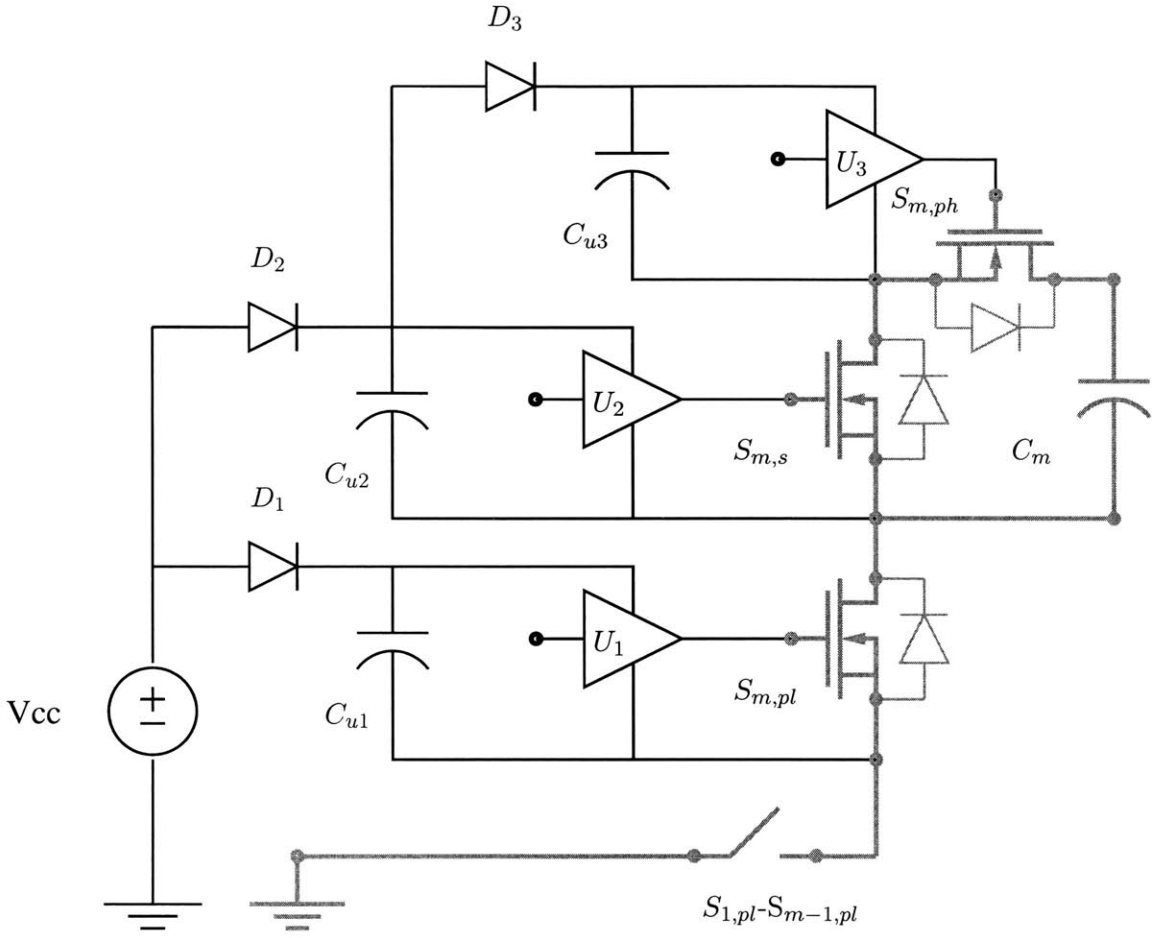

Figure 5.15: A Marx Cell GateDrive

This approach works well, but does place one limitation on the switching states. As mentioned earlier the Marx inverter has a number of redundant switching states. For instance, instead of sequentially stacking capacitors starting at the input side as shown in Figure 5.7, the capacitors could be stacked starting from the output side. Unfortunately, switching in this manner will not properly take advantage of this gate drive implementation. The bootstrap capacitors associated with those S_{ph} switches closest to the input will not have an opportunity to be charged. As a consequence of this, those switches will be forced to rely on their body diodes for balancing capacitor voltages. If the load current causes the voltage on capacitor C_m to be larger than the voltage on C_{m-1} the body diode will be reversed biased and incapable of equalizing the capacitor voltages.

5.3 Performance Comparison: PWM Full-Bridge vs. Quantized Marx

The Marx inverter is a component-intensive solution in comparison to a simple full-bridge inverter. The decision to choose this converter as a viable solution must be justified on the basis of performance versus economic trade-off. We will consider two benchmarks for circuits designed to synthesize power-level sinewaves:

(1) The spectral purity of the generated output.

(2) The converter's efficiency.

The first benchmark is measured by examining the total harmonic distortion (THD) present in the load current. In this case the distortion in the current is determined by

$$THD = \sqrt{\frac{I_{rms}^2 - I_{rms,1}^2}{I_{rms,1}^2}}, \tag{5.15}$$

where I_{rms} is the rms value of the load current and $I_{rms,1}$ is the rms value of the load current's fundamental component. The PWM Full-Bridge VSI, shown in Figure 5.16, is a prime candidate for comparison against the quantized Marx inverter because of its popularity and simplicity. There are also a number of PWM strategies that could be used for comparison and include, but are not necessarily limited to, the naturally sampled, symmetric and asymmetric regular sampled schemes [15]. The naturally sampled strategy is the traditional analog scheme that determines the switching instances by comparing a sine reference against a high frequency triangle waveform. The other two schemes are digital approaches. Our comparison will be confined to the naturally sampled case since the proposed control for the Marx inverter is also analog.

There are number of digital implementations that would allow for selective harmonic cancellation and hence improved performance in either type of converter. The analysis here

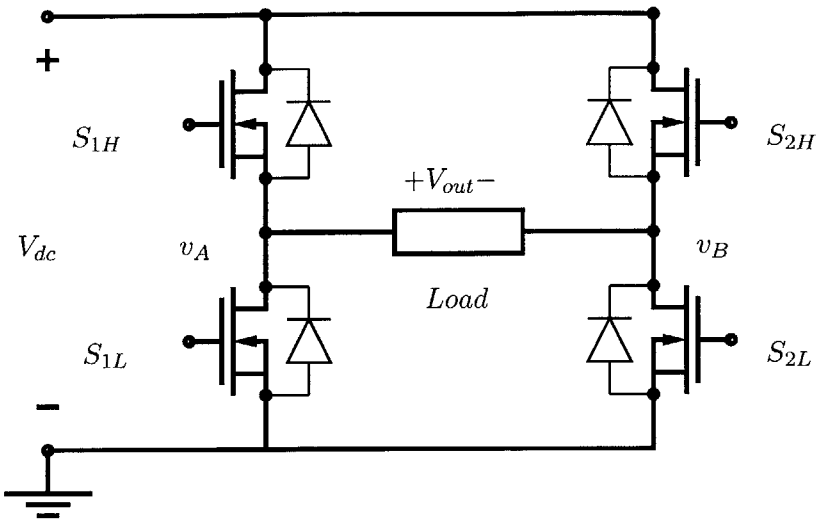

Figure 5.16: Full-Bridge inverter.

is a fair starting point for comparison. Depending on the implementation, a full-bridge can be made to produce either a bipolar or unipolar naturally sampled PWM waveform [27]. The unipolar pattern differs from the bipolar because it uses a 180^o phase-shifted version of the reference sine for determining the switching instants of the second phase leg. For clarity, Figure 5.17 shows an example of a naturally sampled unipolar PWM scheme were the modulation frequency has been arbitrarily chosen to be seven times ($M_f = 7$) faster than the carrier frequency. The unipolar pattern reduces the low frequency harmonic content for the full-bridge PWM inverter, and will be used here as a standard for comparison.

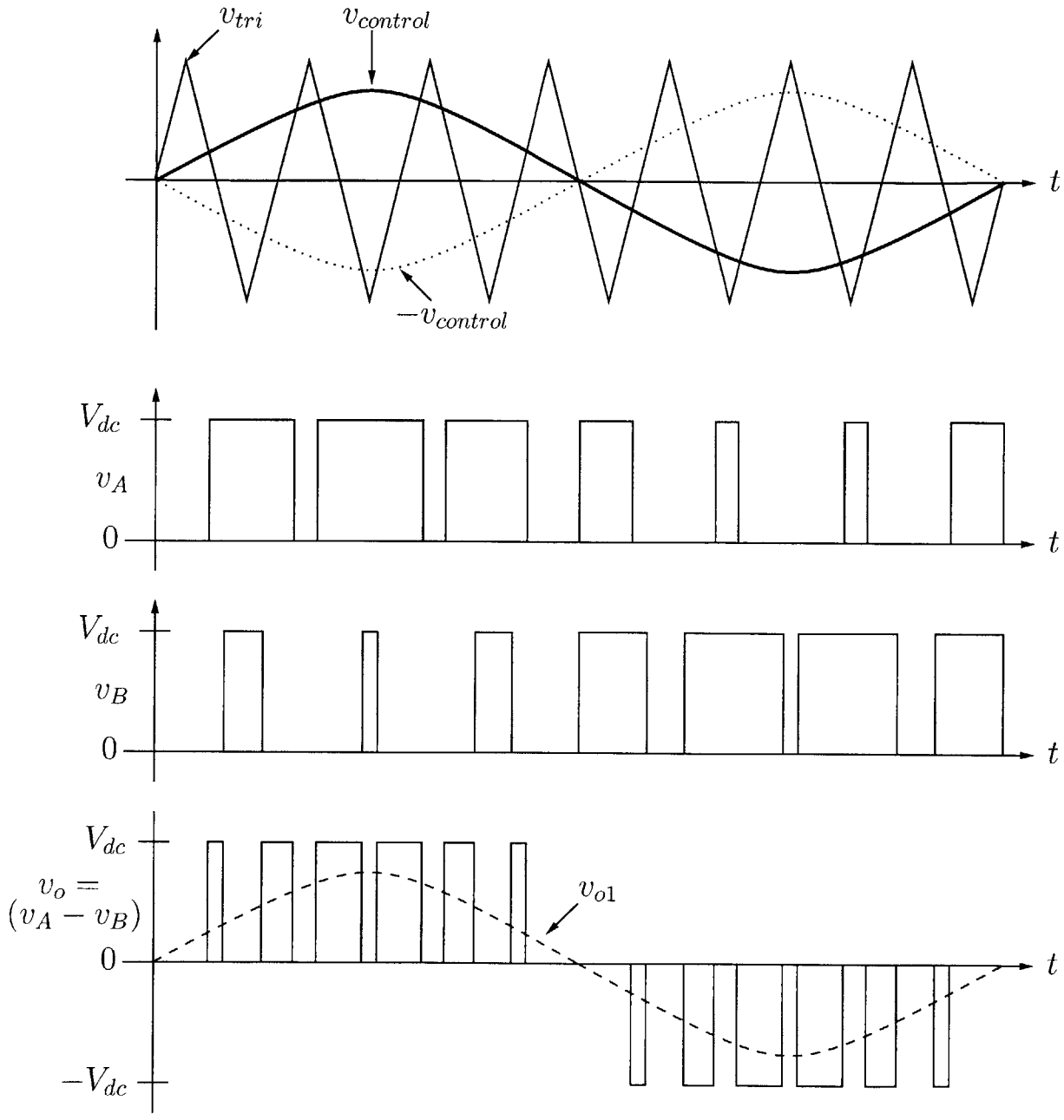

Figure 5.17: Unipolar switching scheme.

5.3.1 Total Harmonic Distortion Comparison

Ultimately, the goal is to drive a collection of induction targets, each at its own respective $R/(2\pi L)$ break-point. Before examining the multi-target case in its entirety, consider a simpler load: a resistive load R, with a series inductor L, for filtering. Such a circuit could be used to model a single induction target. The load current's THD over a normalized fundamental output voltage range was computed using MATLAB for both converters, with results shown in Figure 5.18. The MATLAB script used to produce this result is contained in Appendix B. In this plot, the THD of the full-bridge PWM inverter is shown for three different frequency modulation ratios: $M_f = 3$, 5 and 10. As expected the distortion in the PWM case decreases in response to an increase in the frequency modulation ratio M_f. In addition the distortion for a 2-phase Marx inverter functioning as a seven-level symmetric uniform quantizer is also shown. Both the quantized Marx and PWM waveforms have fundamental frequencies at the $R/(2\pi L)$ break-point frequency for the load. As shown in Figure 5.18, the quantized waveform generally gives lower THD over the upper two-thirds of the achievable amplitude range even for the $M_f = 10$ case. In fact over most of this range the percent THD is under 10%. Because the total delivered power can be expressed as

$$P = (1 + THD^2) I_{rms,1}^2 R, \tag{5.16}$$

the THD is also useful for determining how much of the total power is the result of additional harmonics. For a percent THD under 10%, less than 1% of the delivered power is carried by the higher current harmonics. Note that below this amplitude range, only one level of the Marx converter is being exercised and therefore the amount of harmonic distortion grows rapidly.

In the previous, single target case it was easy to see that for $M_f = 10$, the Marx output still gave better THD, at least over a useful range of output voltages. Such conclusions are not as easy to draw in the case of multiple targets, where the THD in all loads must be considered simultaneously. Consider once more the theoretical multiple target system

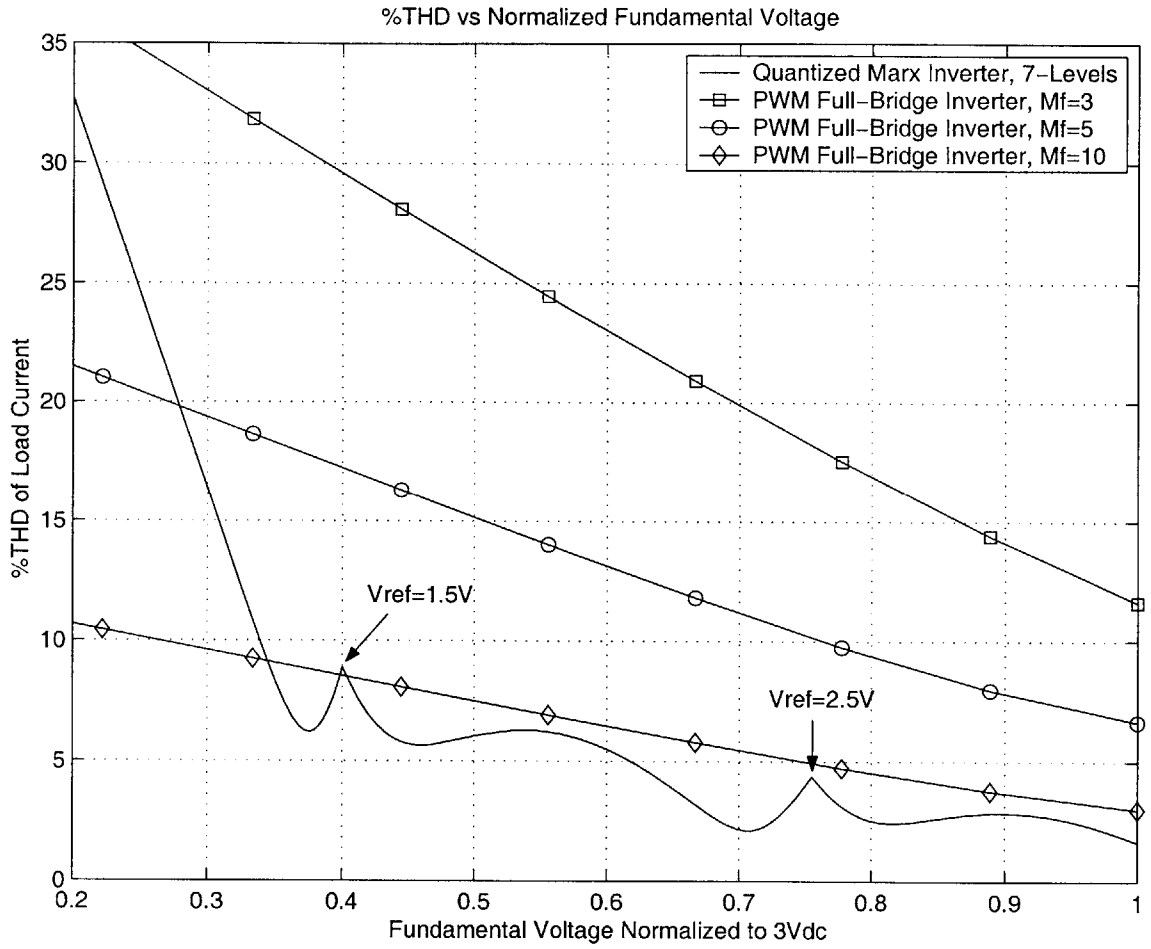

Figure 5.18: Total Harmonic Distortion for a single L-R load.

introduced in Chapter 3 and shown here in Figure 5.19 with a voltage drive. Recall that the separation between break-point frequencies is designed to be a fixed number and that the greater the separation factor α, the higher the relative heating in a target. In order for this scheme to be successful, power delivered unintentionally through higher current harmonics must be minimized.

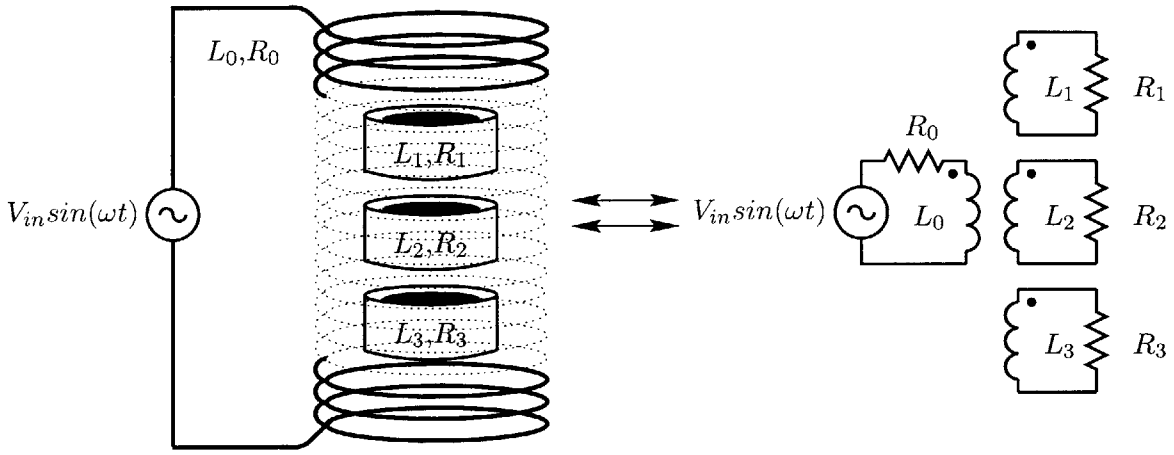

(a) Induction heating circuit for three different targets.

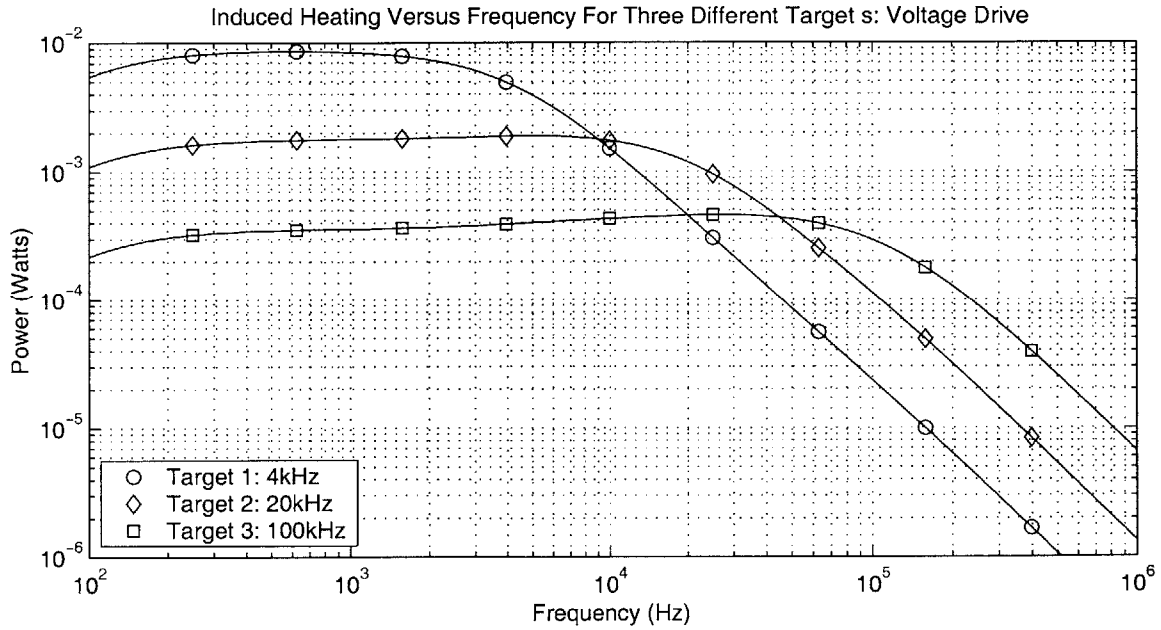

(b) Power profiles for 3 different targets.

Figure 5.19: Induction heating circuit for three different targets and their corresponding power curves versus frequency assuming a voltage drive, $V_{in} = 1$ V.

In the case of the multi-target load, a useful measure of converter performance is how much the additional harmonics impact the relative heating factor of a target. The theoretical relative heating factor for the sample case illustrated in Figure 5.19 was calculated using MATLAB. This particular system had a frequency separation factor of five which implies a nominal relative heating factor of 2.6. The PWM switching frequency was set to three times the highest target frequency in order to produce the three plots shown in Figures 5.20-5.22. This number avoids excessive PWM switching losses, yet is large enough to limit unwanted heating due to higher harmonics when driving the low and middle frequency induction targets.

Figure 5.20 shows the relative heating factor for the lowest frequency target when driven by both a quantized Marx waveform and a fast PWM waveform. In this case the frequency modulation ratio with respect to target 1, denoted as $M_{f,1}$, is equal to 75. Because of the high switching frequency, PWM produces a superior sinewave, deviating only slightly for low fundamental voltage amplitudes. The quantized Marx waveform, which is made with significantly fewer switching transitions, still manages to stay within about 5% of the nominal heating factor for fundamental voltage amplitudes in the upper two-thirds range.

For the intermediate target, shown in Figure 5.21 the frequency modulation ratio has been reduced by a factor of five to $M_{f,2} = 15$. At this switching frequency the PWM waveform only yields relative heating profiles that lie within 5% for fundamental voltages above 0.4 V_{dc}. Over this range the quantized waveform is generally better. Lastly, Figure 5.22 has a frequency modulation ratio of only, $M_{f,3} = 3$. It is interesting to note that when stimulating the highest frequency target, additional current harmonics actually increases the relative heating factor as opposed to decreasing this factor as seen in the lower frequency targets.

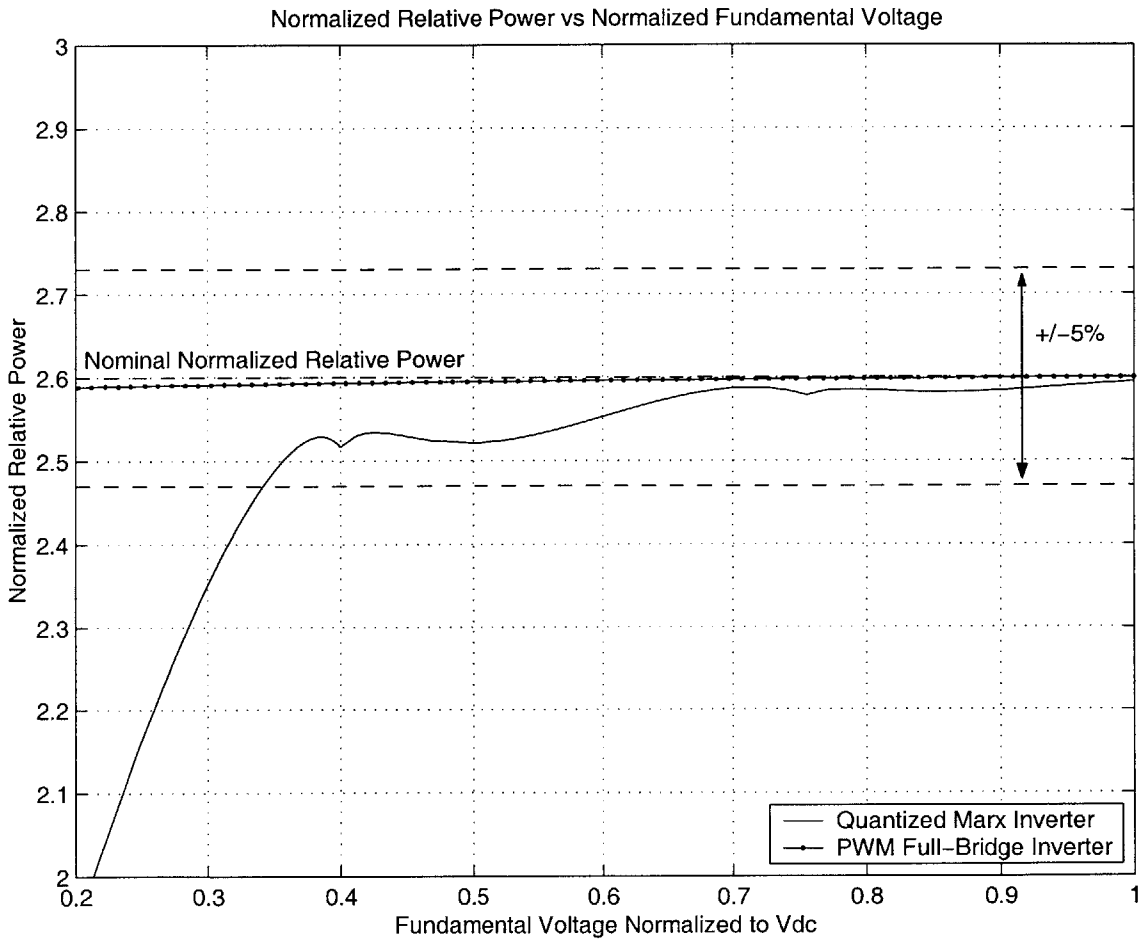

Figure 5.20: 4 kHz Target, $M_{f,1} = 75$.

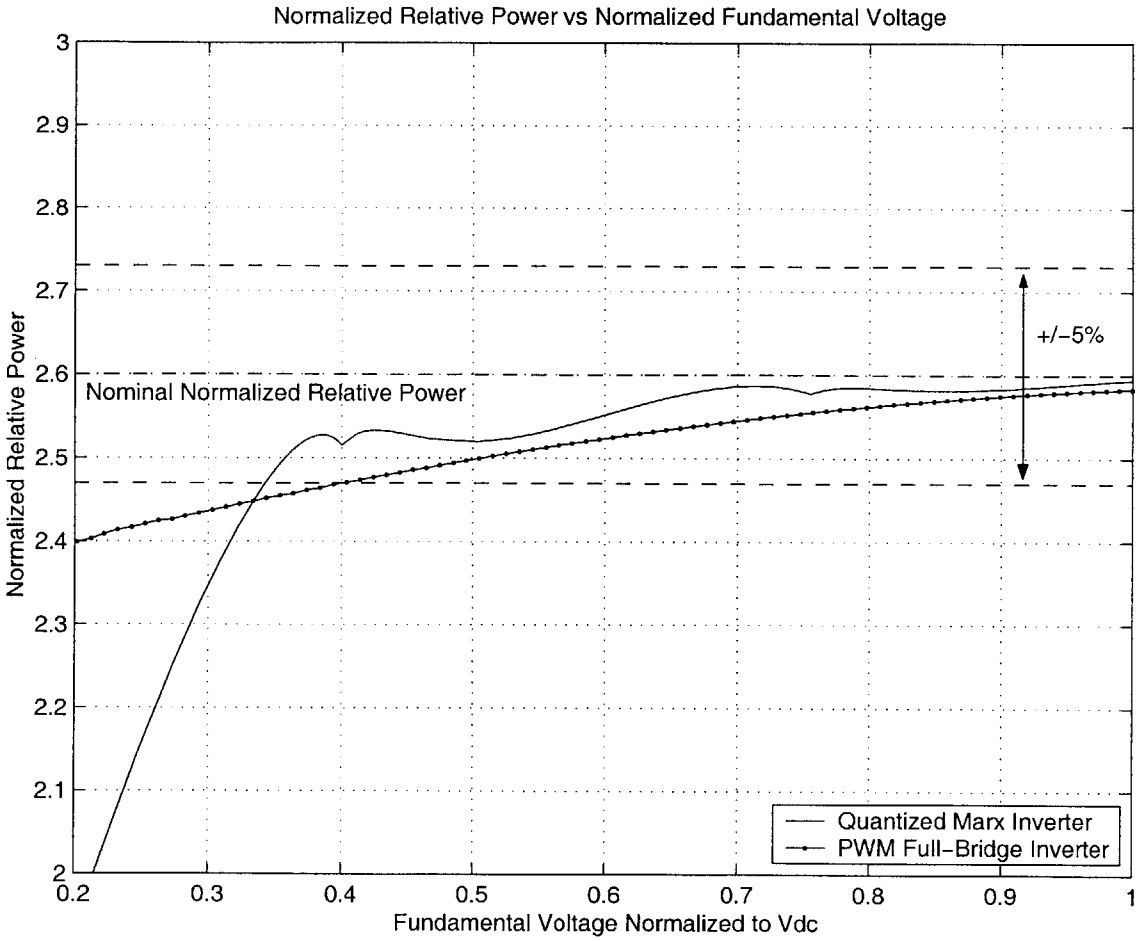

Figure 5.21: 20 kHz Target, $M_{f,2} = 15$.

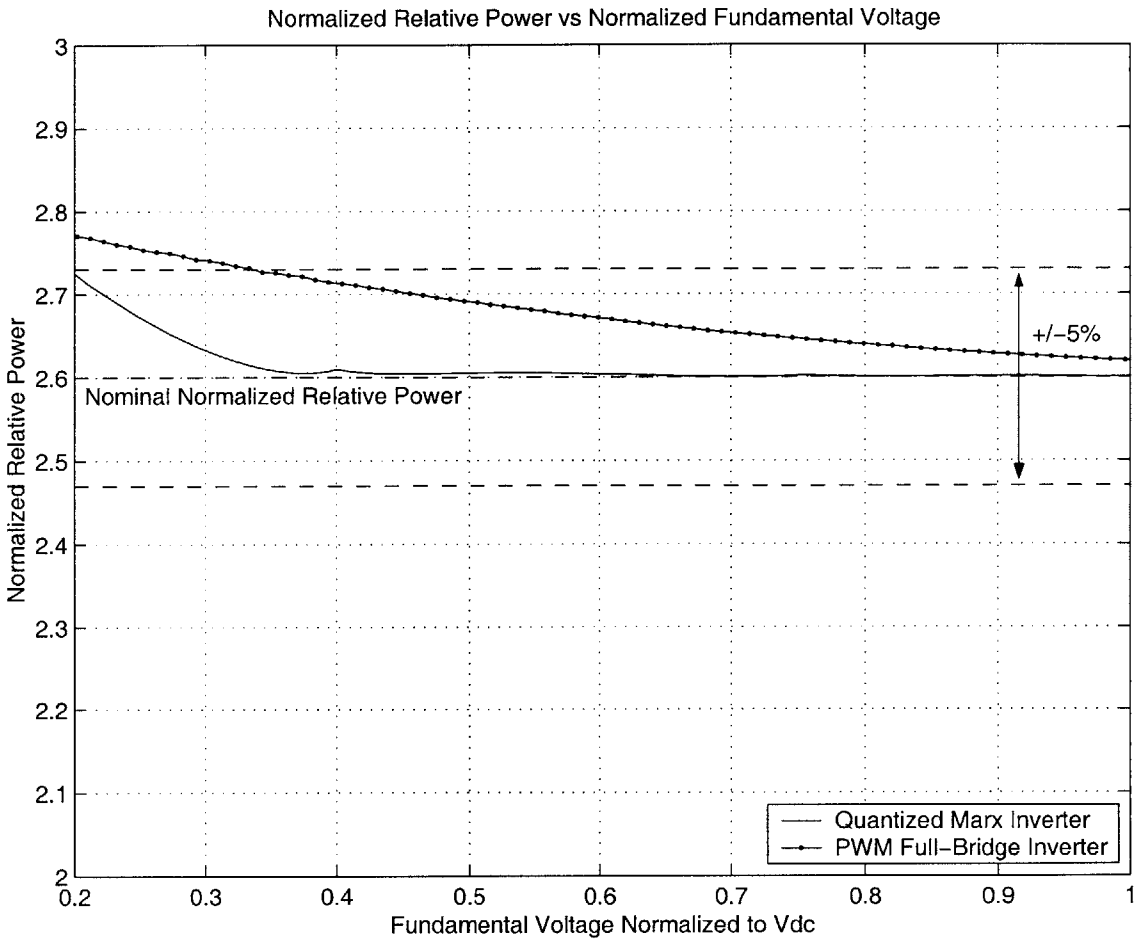

Figure 5.22: 100 kHz Target, $M_{f,3} = 3$.

5.3.2 Comparing Converter Efficiencies

The unipolar PWM scheme is clearly capable of satisfying the THD requirements of the discussed multi-target induction heating system but must use a significant number of switching instances at high frequency to do so. A major limitation of this approach is that the converter will incur roughly the same switching losses for driving any target, even if it's the lowest frequency target. Furthermore, the magnitude of the switching losses are ultimately determined by the frequency of the highest frequency target, hence systems with greater than three targets or with large separations in frequency can incur severe efficiency penalties. The Marx inverter circumvents these problems in two ways. First, by running at a switching frequency related to the frequency of the target being driven, not the frequency of the highest target. And second by only needing to switch one-third as much voltage as the PWM full-bridge to achieve comparable power handling. The result is an additional reduction in switching losses.

For sinewave amplitudes in the range of 0.35 V_{dc} to 1 V_{dc}, it was shown that a PWM inverter with a frequency modulation ratio of about three times the highest target drive frequency was needed to have comparable harmonic performance with a 7-level Marx inverter. As pointed out, in order to have the same power capability the full-bridge requires a bus voltage that is effectively three times the corresponding Marx inverter bus voltage. Having established the PWM switching frequency and the required bus voltage we are now in a position to compare the theoretical efficiencies of each converter. The efficiency of each converter was estimated by considering the following loss mechanisms:

(1) Conduction losses.

(2) Switching loss due to dissipatively charging and discharging the parasitic body diode depletion capacitance.

(3) Switching loss due to non-zero overlap in voltage and current during turn on and turn off.

(4) Gate drive losses.

(5) Losses due to capacitive voltage balancing (unique to the Marx converter).

A comparison of the first four losses are shown side-by-side for both the PWM full-bridge and Marx inverter (assuming all seven levels are used) in Table 5.5. For completeness, the Marx inverter losses when using less than all seven levels are listed in Table 5.6. The conduction loss of the Marx converter is clearly worse, since the load current must traverse more switches, and up to an additional two ESR's associated with the Marx capacitors. As a result, the Marx inverter may not be an obvious choice when conduction losses dominate. However when switching losses dominate, the Marx inverter compares more favorably. The losses associated with charging and discharging the body diode capacitance are reduced by a factor of 6.75. This assumes that this capacitance is linear; the actual nonlinearity of MOSFET capacitance will lessen this penalty.

Table 5.5: Comparison of loss mechanisms.

Loss Mechanism	**PWM Loss**	**Marx Loss (7 levels used)**
Conduction Losses	$I_{rms}^2(2R_{ds,on})$	$I_{rms}^2(6R_{ds,on}+2R_{ESR})$
Parasitic Diode Capacitance	$4C_{diode}(3V_{dc})^2M_f f_s$	$16C_{diode}(V_{dc})^2 f_s$
t_{on} and t_{off} switching losses	$\frac{1}{2}[(3V_{dc})(t_{on}+t_{off})f_s]$ $\times \sum_{t=1}^{4M_f} I(t)$	$\frac{1}{2}[(V_{dc})(t_{on}+t_{off})f_s]$ $\times \sum_{t=1}^{12} I(t)$
Gate Drive Losses	$4V_{cc}Q_g M_f f_s$	$16V_{cc}Q_g f_s$

Table 5.6: Marx inverter losses when using 3 to 5 levels of the quantizer to make sinewaves.

Loss Mechanism	Marx Loss, 3 levels	Marx Loss, 5 levels
Conduction Losses	$I_{rms}^2(6R_{ds,on} + 2R_{ESR})$	$I_{rms}^2(6R_{ds,on} + 2R_{ESR})$
Parasitic Diode Capacitance	$6C_{diode}(V_{dc})^2 f_s$	$12C_{diode}(V_{dc})^2 f_s$
t_{on} and t_{off} switching losses	$\frac{1}{2}[(V_{dc})(t_{on} + t_{off})f_s]$ $\times \sum_{t=1}^{4} I(t)$	$\frac{1}{2}[(V_{dc})(t_{on} + t_{off})f_s]$ $\times \sum_{t=1}^{8} I(t)$
Gate Drive Losses	$6V_{cc}Q_g f_s$	$12V_{cc}Q_g f_s$

The precise calculation of losses due to finite switching speeds requires knowledge of the exact load current value at each switching instant. Of the three load frequencies in our working induction heating example, the Marx inverter executes at most as many load current switch transitions as the PWM inverter when driving the highest frequency target at high voltage. At lower frequencies and voltages, the Marx inverter requires significantly fewer load current switch transitions to create an output waveform with THD comparable or superior to that of the PWM inverter. Even for the highest frequency, highest voltage case, when the number of switching instances for each converter is the same, the full-bridge is penalized by having to switch three times the voltage as the Marx inverter. In terms of the gate drive losses, the Marx converter is 33% higher when all seven levels are used. When only five of the levels are used the gate drive losses become equivalent. In general all switching loss mechanisms in the Marx inverter are reduced when less levels are needed, i.e., three levels or five levels. Perhaps more significant is the fact that losses improve dramatically when we consider driving the intermediate and lowest frequency targets. In the lower frequency cases, the Marx inverter can operate at an effective switching frequency that is an additional factor of five or even 25 times lower than before, while the full-bridge cannot.

The Marx inverter does suffer from an additional loss mechanism not present in the full-bridge. Voltage balancing from capacitor to capacitor incurs dissipation. The conclusions reached in [32] concerning this phenomena also apply here. The energy lost is proportional to the voltage difference between capacitors squared. Furthermore the conclusion that this difference can be minimized by increasing the capacitance C or the switching frequency f_s, also applies here.

Using the simple expressions for these mechanisms the efficiency of each converter was calculated using MATLAB and then compared against actual data. For the purposes of testing and comparison each converter was built using International Rectifier's IRFB59N10D MOSFET. The efficiency for each converter was estimated assuming a series LR load that gave a magnitude of 50 Ω with a phase angle of 45^o at 100 kHz (the drive frequency). The computed MATLAB estimate along with actual measurements are shown in Figure 5.23. The two lowest curves compare the full-bridge efficiency versus the Marx inverter for 3 $V_{dc} = 80$ V. As seen the loss equations predict that the Marx inverter is noticeably more efficient. The measured efficiencies also support this even though it is clear that the estimates are somewhat conservative. This is to be expected because the hand calculations assume that each switching instance is absolutely hard-switched. In truth this is not strictly the case as the inductive load provides opportunities for at least half of the switching transitions to switch with less voltage as the inductor current can discharge the MOSFET capacitance during the dead-time interval. The Marx bus voltage ($V_{dc} = 26.666$ V) in this case was chosen merely for comparative purposes and represents an under utilization of the voltage blocking capability of the IRFB59N10D ($V_{DSS} = 100$ V). If the bus voltage is increased three times this amount, the overall efficiency of the Marx inverter improves dramatically as shown by the top curve. Once again, the top curve represents a conservative figure. For the three normalized fundamental voltages above 0.5 V the measured efficiencies were greater than 90%. Even when the normalized voltage amplitude was as low as 0.25 the efficiency was still about 85%.

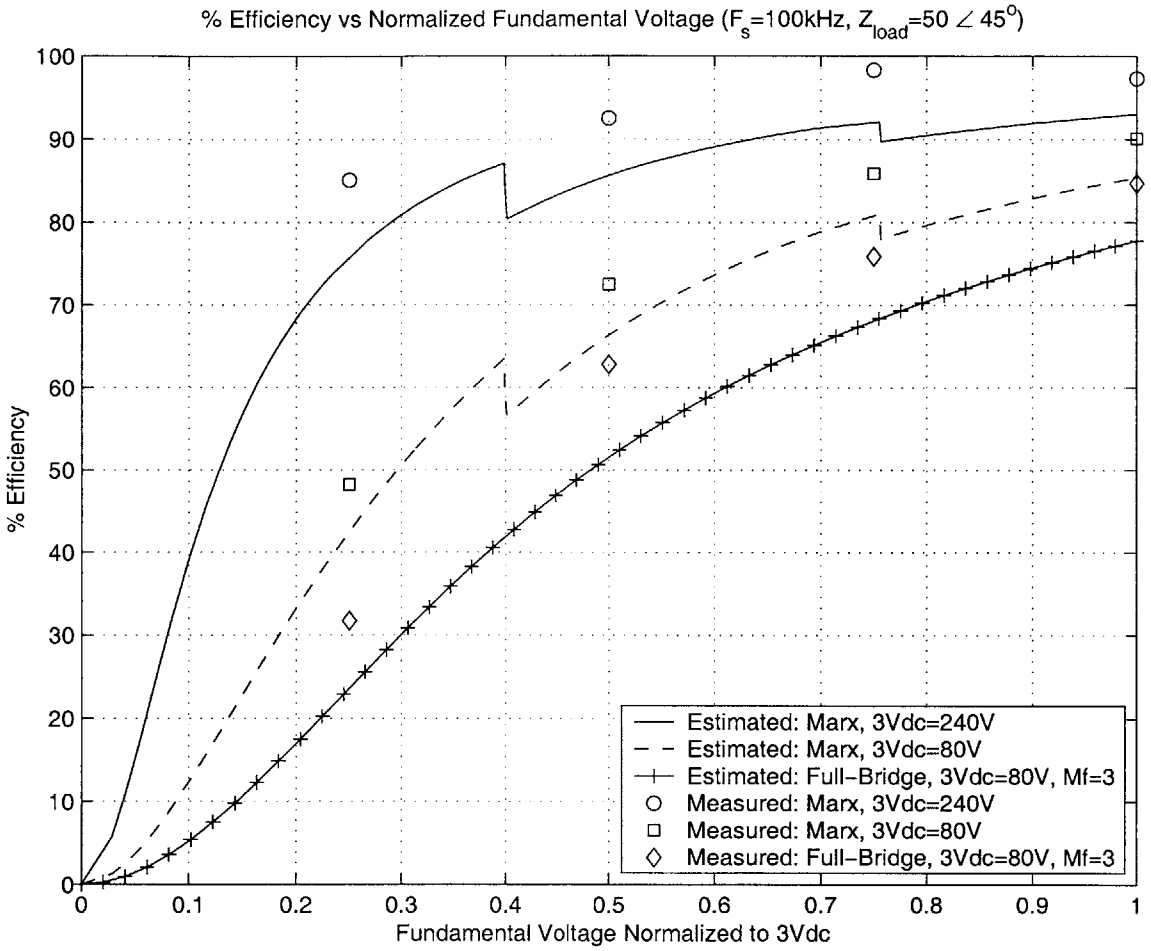

Figure 5.23: Efficiency Comparison.

5.3.3 Comparing MOSFETs Count

For the purpose of comparing efficiencies in the previous subsection, the devices used in both the Marx inverter and full-bridge were identical. While the comparison still favored the Marx inverter in terms of switching losses and as a result efficiency, it was not completely fair. To make this comparison the MOSFETs in the Marx inverter were intentionally underutilized in terms of their rated voltage blocking capability or V_{dss}. A fairer comparison would pit the Marx inverter prototype against a full-bridge designed to operate at 240 V. This would require the full-bridge MOSFETs to have higher voltage ratings. If only 80% of the rated blocking voltage is used, as in the Marx prototype, a MOSFET with a $V_{dss} = 300$ V

would be needed.

While using different devices makes it difficult to draw a comparison solely on the merit of topology, it brings up an important point concerning device count. If a designer is trying to meet an output resistance specification for a full-bridge, the required device count can approach the number of devices used in a comparable Marx topology. This argument is based on the scaling of MOSFET channel resistance and assumes that the ESR of the Marx capacitors is a negligible. Roughly speaking, the channel resistance in power MOSFETS scales according to the following relationship,

$$R_{ds,on} \propto V_{dss}^{k}, \tag{5.17}$$

where the exponent k is typically greater than two [33]. Thus for a 300 V part, one would expect a resistance that is at least nine times greater than a 100 V part using the same technology. To meet the $R_{ds,on}$ goal, the full-bridge would then need to parallel three MOSFETs for each switch in the H-bridge. Doing so brings the device count in the H-bridge to 12 MOSFETs, a number that is much closer to the number of devices needed (16 MOSFETS) in a three-stage Marx inverter. According to (5.17), the Marx inverter part count will always be greater than the full-bridge and will continue to worsen as the number of levels grows. Up to three stages the part count is not significantly greater considering the improved efficiency. Furthermore, all switching devices have real limitations concerning the amount of voltage they can block. The limited number of MOSFETs rated beyond 1 kV is a perfect example. A three-stage Marx inverter could effectively triple this rating over what might otherwise be achieved with a full-bridge.

5.4 Chapter Summary

This chapter introduced a power supply that can be used to excite the frequency selectable induction heating targets discussed in Chapter 3 and 4. This power supply, the Marx

multilevel inverter, is unlike previous multilevel converters in that it generates the required voltage levels by multiplying the dc bus voltage instead of dividing it. This approach to level synthesis allows for a topology that overcomes the power delivery limitations of more traditional multilevel converters. An experimental 1 kW prototype was constructed for evaluation purposes. Through a minimal amount of control hardware the converter was configured to behave as a symmetric mid-tread quantizer. This static input-to-output transfer function allows the Marx inverter to approximate almost arbitrary waveforms using a fundamental switching frequency technique.

Using this control scheme the Marx inverter was compared against a more common means of synthesizing sine waves with a pulse-width-modulated full-bridge inverter. These two topologies were examined in regards to efficiency and total harmonic distortion for a variety of inductive loads consistent with the targets in Chapter 3. Theoretical calculations show that the for a acceptable amount of harmonic distortion the efficiency of the Marx inverter is superior to a full-bridge operated using PWM. The reason for this can be attributed to a variety of factors. Although the Marx inverter requires more components, the multiplying nature of the Marx inverter reduces the voltage requirement on the individual switches in comparison to a full-bridge processing the same amount of power. This reduction in voltage, coupled with fewer switching instances for a given amount of distortion, translates into smaller switching losses in general.

Chapter 6

Thesis Summary and Future Work

DYNAMIC vibration absorbers will continue to play an important role in suppressing structural vibrations. These passive networks (consisting of auxiliary spring-mass systems) can provide excellent attenuation in narrow frequency bands. Finding ways to increase this usable frequency range represents an ongoing and highly active area of research. One area that shows promise, focuses on DVA's that are semi-active in nature, i.e. dampers that can alter key system parameters in a useful way. Often, these parameters are chosen based on their ability to adapt a DVA's anti-resonant frequency. This thesis demonstrates a way of using thermo-responsive gel polymers to control a DVA's anti-resonant frequency. If a DVA consists of a container filled with a gel polymer, its moment of inertia can be changed by exploiting the gel's discontinuous phase property. Changing the inertia in this way allows the anti-resonant frequency to likewise by modified.

The first part of this thesis expanded upon the variable moment of inertia concept, culminating in a gel DVA prototype. Meant as a proof of concept, the DVA prototype lead to a number of interesting questions concerning the thermal triggering of the gel material. The remainder of this thesis confronts the most significant of these problems, how to heat the various gel polymers without ruining the mechanical properties of the damper. To address this problem, an induction heating system that could be used to heat arbitrary combinations of gel polymers was developed. Originally meant for heating gel polymers, this system and its individual components (induction targets and power electronics) can be used, in whole or in part, in a number of different applications. As a result, each of these components has individual engineering merit and deserves mentioning. In general

this thesis makes contributions to three specific areas:

(1) Vibration Damping.

(2) Induction Heating.

(3) Power Electronics.

6.1 Summary of Thesis Contributions

6.1.1 The Gel Polymer Dynamic Vibration Absorber

It is an engineering design challenge to build DVA's that provide sufficient attenuation, while meeting the constraints imposed by physical dimensions and weight. Although, DVA's that can modify their moment of inertia have been cited in the literature, they typically rely on sliding masses to do so. The gel damper suggests yet another approach for changing moment of inertia– the use of variable viscosity fluids. This approach may yield tighter configurations with more uniform weight distributions. If the gel polymers are engineered to take advantage of their hysteretic behavior, a small amount of energy could be used to change and maintain the damper's anti-resonant frequency.

Although there are a number of issues that must be resolved to make the gel damper a viable topology. This thesis has laid the basic ground work for further exploration. The basic concept of using gel polymers to make variable viscosity solutions has been introduced and experimentally tested. Topologies that utilize this idea for damping both torsional and linear vibrations have been illustrated and analyzed. A means of induction heating the gel compartments was also addressed by this thesis and is discussed in greater detail in the following section.

6.1.2 Frequency Selectable Induction Heating Targets

In order to heat the individual gel polymers in a noncontact method, a special collection of induction heating targets was engineered. These targets exhibit preferential heating with frequency allowing the individual targets to be "singled out" if the magnetic field is driven at the right frequency. The induction targets investigated in this thesis can be divided into two categories: nonresonant and resonant. Both types of frequency selectable induction heating targets were examined, modeled and analyzed. For each of these models, the behavior of a multiple induction target system was analyzed for both sinusoidal current and voltage excitations of the induction coil.

Nonresonant induction heating targets were constructed using single-turn conductors whose critical dimensions are small compared to the skin depth over the frequency range of interest. If these single-turn conductors have similar self-inductances, with R/L break-point frequencies that are spaced evenly by factors of α, frequency selectivity can be achieved. That is a target driven at its break-point frequency will heat by an amount $(\alpha^2 + 1)/(2\alpha)$ more than the remaining targets (for the same degree of coupling). These results were verified experimentally for two different geometries: thin-walled cylindrical shells and thin wire loops. In general this class of target is attractive because they are easy to construct, require very little volume, can be submerged in water and when properly designed can dissipate a substantial amount of power.

The second class of target studied, is the resonant induction target. In this thesis, resonant targets are essentially RLC circuits consisting of an air core inductor and capacitor. The effective series resistance of the coil is used as the dissipative element. By picking each capacitor to have a different resonant frequency, frequency selectivity can be achieved. An experimental system consisting of three resonant targets was built and tested. When compared to nonresonant selectable induction heating targets, resonant RLC circuits have the potential for considerably higher preferential heating in a smaller frequency band. However, the drawbacks of this topology include added complexity, and shortcomings associated with

capacitors. For instance capacitors are not well suited to humid environments and have substantially lower limitations on the amount of power that they can dissipate compared to their inductor counterparts.

6.1.3 The Marx Multilevel Inverter

A major triumph of this thesis is a new multilevel inverter topology meant for use as the induction heating power supply. Because higher harmonics in the drive waveform, can lead to unwanted heating in the induction targets described here, the sinusoidal drive must have a low total harmonic distortion. The Marx inverter can meet this requirement with greater efficiency than more traditional approaches such as pulse-width-modulated full-bridge inverters and linear power amplifiers. A 1 kW prototype Marx inverter was built and tested in this thesis. As a point of reference, the prototype achieved efficiencies greater than 90% while driving a 100 kHz sinusoid into an inductive load with a magnitude of 50 Ω and a phase of 45^o. These efficiencies are made possible because inductive loads allow the staircase waveform to be produced using ZVS transitions.

The benefits of this topology, extend beyond the induction heating system developed in this thesis. Many of the advantages pertaining to traditional multilevel inverters apply equally well to the Marx inverter. As already mentioned, voltages with low distortion can be generated with relatively fewer switching instances. Because of its multiplying structure, outputs with voltages exceeding the breakdown limitations of the individual switches can easily be obtained. This allows a designer to use low voltage MOSFETS to achieve efficiencies at power levels that ordinarily could not be obtained. Unlike traditional multilevel converters such as the diode-clamped and capacitor-clamped, the Marx inverter is suitable for real power transfer without the need for complicated control or external voltage balancing networks. When compared to these topologies the Marx inverter requires slightly more components for balancing purposes but certainly fewer than the generalized inverter topology with self voltage balancing.

6.2 Future Work

6.2.1 The Gel Polymer Dynamic Vibration Absorber

A number of important issues must be addressed before the gel damper can become a practical vibration suppression tool. Empirical evidence suggests that even in its least viscous state, the gel solution contributes some mechanical loss within the rotating container. This loss mechanism limits the effective Q of the damper and hence the amount of absolute attenuation that can be achieved. Developing a fluid-mechanics model for these losses will provide valuable information when specifying the dimensions of a gel chamber.

Although this thesis focused on a means by which the individual gel polymers can be heated, it did not address the issue of removing heat from the system. The current prototype relies on heat being lost to the environment. Without an active means of cooling the gel, the system has to rely on its thermal time constants before certain anti-resonant frequencies can be achieved. This suggests that the effective bandwidth of the system is likewise limited. The issue of heat removal will have to eventually be considered. In addition, no attempt has been made to optimize the gel chemistry for this application. By designing the gels with a high degree of hysteresis it may be possible to reduce the amount of energy that must be expended to change the damper's state. For instance if the hysteresis band includes the ambient temperature, the gel could be treated like a latch. Once the latch is set, the gel could maintain its state even after it has cooled down to the ambient temperature. Of course, resetting the gel state will require active heat removal.

Once the issues of active heating and cooling are resolved, a control scheme will have to be developed for the vibration damper. An appropriate control circuit will be needed to detect the frequency of the disturbance and heat the gel chambers appropriately. It might be possible to estimate the frequency of excitation without the need for additional sensors. If the induction coil is designed with some amount of saliency, i.e its inductance changes as the gel container rotates, it should be possible to estimate the frequency of the disturbance

by looking at how the inductance is modulated. In addition to the frequency of excitation, the control system must know what the state of the gel is at any point in time. If the gels are designed to be hysteretic it may not be sufficient to simply know the instantaneous temperature of the gel solution, unless it lies outside of the hysteresis band. One way to estimate the temperature of the gel fluid will be discussed next.

6.2.2 Frequency Selectable Induction Heating Targets

6.2.2.1 Nonresonant Targets

Regulating the gel temperatures under some form of closed-loop control requires that the temperature of the induction targets be known. Because these targets are enclosed in a closed environment it is undesirable to add additional sensors and then route signals from the gel containers to the outside world. An approach that has been suggested, but remains to be explored is estimating the temperature of the induction target by looking at changes in the converter power signature as the gel is heated. As a conductor heats, its resistance changes. In the case of the nonresonant targets, changes in resistance translate into shifts of the break-point frequency as well as the absolute power that is delivered for a given current or voltage. By developing accurate models of the resistance as a function of temperature an exciting parameter-estimation problem can be explored.

The multi-frequency, multi-target system could be used in a wide range of applications, including medical and industrial processes, to provide a wide range of spatial temperature control. One possible application is the treatment of deep-seated tumors using hyperthermia [23, 41, 42]. Currently, the generation of a desired spatial temperature gradient requires a complicated distribution of identical induction targets. The availability of frequency selectable targets would allow more flexibility in the distribution of induction targets, since the temperature profile could be modified after distribution simply by controlling the drive voltage across the primary induction coil. The ability to actively regulate the

temperature of these targets is further reason to pursue the parameter-estimation problem outlined above. Initial work for this application will involve verifying that targets can be constructed with the desired break-points given the small catheter-sized dimensions that must be observed.

6.2.2.2 Resonant Targets

The resonant targets are less suited to the gel damper but offer intriguing possibilities for other applications. One goal to pursue in this area is the design of resonant targets that are fully integrated. The resonant targets in this thesis require a lumped inductor and capacitor. Future targets to consider are those that don't require a discrete capacitor but rely on the inter-winding capacitance of the inductor to make the structure resonant. This approach would increase the absolute power that the target can dissipate since it no longer is bottlenecked by a capacitor. The challenge in this case will be designing the structure with capacitances that are high enough to give reasonable resonant frequencies. Yet another possibility is to consider rectifying the voltage on the resonant target side. Then the induction system could be used to regulate the power to multiple dc buses over one magnetic path. This approach may be of benefit for remote powering of actuators used in a closed environment for medical reasons (or otherwise). All of these applications will eventually depend on being able to drive the desired target at its resonant frequency. To meet this need, additional control circuitry will have to be created to actively track the natural frequency of each target as it varies due to changes in component values or operating conditions.

6.2.3 The Marx Multilevel Inverter

The 1 kW Marx inverter prototype was designed to demonstrate the Marx multilevel concept but has not been optimized in a number of respects. No serious attempt has been made to reduce the volume of this converter. Components were chosen to allow for a wide range

of operating frequencies. But no practical limit on the achievable upper frequency has been established. The high switching frequencies involved required fast analog circuitry for decision making. The control circuitry, while attractive because of its simplicity could be further refined to minimize the potential of glitches at low reference voltage levels. If the converter was operated at lower switching frequencies digital controllers and more sophisticated control schemes could be explored.

The quantized output approach to waveform synthesis has been examined carefully in this thesis for single sinewaves. But it has also demonstrated that the quantizer can be used to replicate more complicated waveforms, such as sums of sinewaves. In this regard, little work has been done to establish how generating multiple sinewaves will impact the spectral purity of each sinewave. In fact, total harmonic distortion is no longer a sufficient metric for this problem and must be redefined. Determining how multiple sinewaves affect the converter's ability to ZVS should also be examined as this will impact the overall efficiency of the inverter. The question of how many levels is reasonable for a given number of simultaneously driven targets should also be addressed. If the one level per target philosophy is observed it might be advantages to modularize the converter. If the basic switching cell could be constructed into a modular section that can be cascaded with cells already in use, the system could grow to meet the additional load requirements without the need to rebuild and entire converter.

Finally, while the Marx converter in this thesis has been configured to act as a multilevel inverter, this topology is theoretically bidirectional. If the input and output ports are switched it should be possible to operate the Marx converter as a rectifier, taking a large sine voltage in and stepping it down to a lower dc bus voltage. The Marx rectifier could replace the role of an intermediate step-down transformer as part of the rectification process. Lastly, by combining two Marx converters back-to-back a high-voltage ac/ac converter could be built for altering the phase or frequency of the ac input.

Appendix A

Hydroxypropyl Cellulose (HPC) Gel Bead Recipe

Inverse Suspension Crosslinkng of Hydroxypropyl Cellulose with Vinyl Sulfone using 0.45 w% Gauex in Mineral Oil.

Twenty grams of HPC (Aqualon, Klucel LF NF, M. 95k) was added to 80 mL of deionized water and allowed to hydrate overnight. To this suspension was added 20 drops of a 5N NaOH solution to form a solution of approximately pH 12.5. The suspension was stirred thoroughly to disperse the basic solution, and was then allowed to stand for 45 minutes.

The continuous phase solvent, mineral oil was added to a baffled reaction vessel equipped with an impeller blade, and stirring was initiated at 450 rpm. To the hydrated polymer suspension was added 170 μl of vinyl sulfone (Sigma, Catalog No. V9501) and then stirred with a glass rod for 30 seconds. This polymer suspension was then poured into the agitating reaction vessel. The mixture was allowed to react at room temperature overnight.

The beads were worked up in the typical manner as described in the Protocol. In the collapsed state (20°C above the LCST), the average diameter of the beads was 841 μm and the median diameter was 819 μm (a mean to median ratio of 1.03). The equilibrium swell ratio measured from 30°C to 55°C was 7.4. The larger bead size was due to the absence of surfactant in the process.

Appendix B

Source Code

Coilgen:

FastHenry:

MATLAB:

B.1 Coilgen

Coilgen [9] is a C program which acts as a preprocessor for FastHenry. This program can generate the node list for a user-specified solenoid. Coilgen helped to produce a number of the coil configurations used in this thesis. Three Coilgen input files are listed below (one for each major experiment). In some cases it was necessary to hand edit the resulting .inp file. Additional comments can be found in the corresponding coilrc file.

B.1.1 coilrc-shim

```
# Configuration file for coilgen
# Cylindrical shim experiment
#
# This file was used to generate the shim models used in FastHenry.
# Coilgen generates wires with rectangular cross-sections. Currently,
# the "wire diameter" is set to the thickness of the copper shim. It
# should be changed for the particular target to be modelled. The .inp
# will also have to be edited to give the right width, i.e. w=25.0 in
# this case. In addition, the spiral aspect should be removed, i.e.
# x=0.0 for all nodes. If AC resistance is needed, then nhinc and nwinc
# must be set accordingly as well as the .freq statement. See the
# FastHenry manual for more information

# Format is:
#  diameter  length  #turns  wire_diameter  centre_x  centre_y  centre_z

# Uncomment the following line if the primary induction coil is needed.
#45.7 45 33 1.363 0.0 0.0 0.0

3.175e-2 7.62e-5 1 7.62e-5 0.0 0.0 0.0
```

B.1.2 coilrc-tuned

```
# Configuration file for coilgen
# 3 tuned loads experiment
#
# Don't forget for increased accuracy you can also add "nwinc=2 nhinc=2"
# or something similar depending on the frequency. Look at the FastHenry
# manual for more details
#
# Remember that these wires have rectangular cross-sections so do not
# expect the DC restistance to match up
```

```
#
# Format is: (meters)
# diameter  length  #turns  wire_diameter  centre_x  centre_y  centre_z

#Primary Coil
4.7e-2 20.4e-2 48 4.25e-3 0.0 0.0 0.0

#Top Coil
6.41438e-2 4.2e-2 59 6.438e-4 6.6e-2 0.0 0.0

#Middle Coil
6.41438e-2 4.0e-2 57 6.438e-4 0.0 0.0 0.0

#Bottom Coil
6.41438e-2 4.1e-2 58 6.438e-4 -6.75e-2 0.0 0.0
```

B.1.3 coilrc-wires

```
# Configuration file for coilgen
# 3 wires experiment
#
# The following changes should be made manually to the .inp file
# Change the conductivity of coil 3, using ".default sigma=6.683567642e3"
# Change the conductivity of coil 4, using ".default sigma=7.518991937e2"
#
# It may be desirable to hand edit the input file to keep the wires from
# spiraling, i.e. keep them in one plane
#
# Don't forget for increased accuracy you can also add "nwinc=2 nhinc=2"
# or something similar depending on the frequency. Look at the FastHenry
# manual for more details
#
# Remember that these wires have rectangular cross-sections so do not
# expect the DC restistance to match up
#
# Format is:
# diameter  length  #turns  wire_diameter  centre_x  centre_y  centre_z

# primary coil
4.481e-2 9.5e-2 109 .8118e-3 0.0 0.0 0.0

# 20AWG copper wire
6.0e-2  .8118e-3 1.01 .8118e-3 2.0e-2 5.5e-3 0.0

# 20AWG alloy 90 wire
6.0e-2  .8118e-3 1.01 .8118e-3 0.0 5.5e-3 0.0

# 20AWG alloy 800 wire
6.0e-2  .8118e-3 1.01 .8118e-3 -2.2e-2 5.5e-3 0.0
```

B.2 FastHenry

A number of the results in this thesis were made possible using a 3-D inductance extraction program called FastHenry [18]. Below are the input files used by FastHenry to determine the inductance and AC resistance of the cylindrical shells used in the calorimetry experiment discussed in Chapter 3. These node lists were generated using Coilgen and are included here because they required the greatest degree of manual editing. The sheer size of the input files for the 3 wires experiment and tuned loads experiment precludes their inclusion. The reader is referred to the appropriate Coilgen source code for reproducing those input files.

B.2.1 ShimBrass.inp

```
* File generated by coilgen, Thu Oct 17 19:54:01 2002
* nhinc and nwinc must be set according to the skin depth for the frequency specified in .freq

.Units mm
.default sigma=1.624e4 nhinc=2 nwinc=2

* Nodes
N0 x=0.0 y=0.000 z=15.879
N1 x=0.0 y=0.997 z=15.848
N2 x=0.0 y=1.990 z=15.754
N3 x=0.0 y=2.975 z=15.598
N4 x=0.0 y=3.949 z=15.380
N5 x=0.0 y=4.907 z=15.102
N6 x=0.0 y=5.845 z=14.764
N7 x=0.0 y=6.761 z=14.368
N8 x=0.0 y=7.650 z=13.915
N9 x=0.0 y=8.508 z=13.407
N10 x=0.0 y=9.333 z=12.846
N11 x=0.0 y=10.122 z=12.235
N12 x=0.0 y=10.870 z=11.575
N13 x=0.0 y=11.575 z=10.870
N14 x=0.0 y=12.235 z=10.122
N15 x=0.0 y=12.846 z=9.333
N16 x=0.0 y=13.407 z=8.508
N17 x=0.0 y=13.915 z=7.650
N18 x=0.0 y=14.368 z=6.761
N19 x=0.0 y=14.764 z=5.845
N20 x=0.0 y=15.102 z=4.907
N21 x=0.0 y=15.380 z=3.949
N22 x=0.0 y=15.598 z=2.975
```

```
N23 x=0.0 y=15.754 z=1.990
N24 x=0.0 y=15.848 z=0.997
N25 x=0.0 y=15.879 z=0.000
N26 x=0.0 y=15.848 z=-0.997
N27 x=0.0 y=15.754 z=-1.990
N28 x=0.0 y=15.598 z=-2.975
N29 x=0.0 y=15.380 z=-3.949
N30 x=0.0 y=15.102 z=-4.907
N31 x=0.0 y=14.764 z=-5.845
N32 x=0.0 y=14.368 z=-6.761
N33 x=0.0 y=13.915 z=-7.650
N34 x=0.0 y=13.407 z=-8.508
N35 x=0.0 y=12.846 z=-9.333
N36 x=0.0 y=12.235 z=-10.122
N37 x=0.0 y=11.575 z=-10.870
N38 x=0.0 y=10.870 z=-11.575
N39 x=0.0 y=10.122 z=-12.235
N40 x=0.0 y=9.333 z=-12.846
N41 x=0.0 y=8.508 z=-13.407
N42 x=0.0 y=7.650 z=-13.915
N43 x=0.0 y=6.761 z=-14.368
N44 x=0.0 y=5.845 z=-14.764
N45 x=0.0 y=4.907 z=-15.102
N46 x=0.0 y=3.949 z=-15.380
N47 x=0.0 y=2.975 z=-15.598
N48 x=0.0 y=1.990 z=-15.754
N49 x=0.0 y=0.997 z=-15.848
N50 x=0.0 y=0.000 z=-15.879
N51 x=0.0 y=-0.997 z=-15.848
N52 x=0.0 y=-1.990 z=-15.754
N53 x=0.0 y=-2.975 z=-15.598
N54 x=0.0 y=-3.949 z=-15.380
N55 x=0.0 y=-4.907 z=-15.102
N56 x=0.0 y=-5.845 z=-14.764
N57 x=0.0 y=-6.761 z=-14.368
N58 x=0.0 y=-7.650 z=-13.915
N59 x=0.0 y=-8.508 z=-13.407
N60 x=0.0 y=-9.333 z=-12.846
N61 x=0.0 y=-10.122 z=-12.235
N62 x=0.0 y=-10.870 z=-11.575
N63 x=0.0 y=-11.575 z=-10.870
N64 x=0.0 y=-12.235 z=-10.122
N65 x=0.0 y=-12.846 z=-9.333
N66 x=0.0 y=-13.407 z=-8.508
N67 x=0.0 y=-13.915 z=-7.650
N68 x=0.0 y=-14.368 z=-6.761
N69 x=0.0 y=-14.764 z=-5.845
N70 x=0.0 y=-15.102 z=-4.907
N71 x=0.0 y=-15.380 z=-3.949
N72 x=0.0 y=-15.598 z=-2.975
N73 x=0.0 y=-15.754 z=-1.990
N74 x=0.0 y=-15.848 z=-0.997
N75 x=0.0 y=-15.879 z=-0.000
N76 x=0.0 y=-15.848 z=0.997
```

```
N77 x=0.0 y=-15.754 z=1.990
N78 x=0.0 y=-15.598 z=2.975
N79 x=0.0 y=-15.380 z=3.949
N80 x=0.0 y=-15.102 z=4.907
N81 x=0.0 y=-14.764 z=5.845
N82 x=0.0 y=-14.368 z=6.761
N83 x=0.0 y=-13.915 z=7.650
N84 x=0.0 y=-13.407 z=8.508
N85 x=0.0 y=-12.846 z=9.333
N86 x=0.0 y=-12.235 z=10.122
N87 x=0.0 y=-11.575 z=10.870
N88 x=0.0 y=-10.870 z=11.575
N89 x=0.0 y=-10.122 z=12.235
N90 x=0.0 y=-9.333 z=12.846
N91 x=0.0 y=-8.508 z=13.407
N92 x=0.0 y=-7.650 z=13.915
N93 x=0.0 y=-6.761 z=14.368
N94 x=0.0 y=-5.845 z=14.764
N95 x=0.0 y=-4.907 z=15.102
N96 x=0.0 y=-3.949 z=15.380
N97 x=0.0 y=-2.975 z=15.598
N98 x=0.0 y=-1.990 z=15.754
N99 x=0.0 y=-0.997 z=15.848
N100 x=0.0 y=-0.000 z=15.879

* Segments
E0 N0 N1 w=25.0 h=0.0508
E1 N1 N2 w=25.0 h=0.0508
E2 N2 N3 w=25.0 h=0.0508
E3 N3 N4 w=25.0 h=0.0508
E4 N4 N5 w=25.0 h=0.0508
E5 N5 N6 w=25.0 h=0.0508
E6 N6 N7 w=25.0 h=0.0508
E7 N7 N8 w=25.0 h=0.0508
E8 N8 N9 w=25.0 h=0.0508
E9 N9 N10 w=25.0 h=0.0508
E10 N10 N11 w=25.0 h=0.0508
E11 N11 N12 w=25.0 h=0.0508
E12 N12 N13 w=25.0 h=0.0508
E13 N13 N14 w=25.0 h=0.0508
E14 N14 N15 w=25.0 h=0.0508
E15 N15 N16 w=25.0 h=0.0508
E16 N16 N17 w=25.0 h=0.0508
E17 N17 N18 w=25.0 h=0.0508
E18 N18 N19 w=25.0 h=0.0508
E19 N19 N20 w=25.0 h=0.0508
E20 N20 N21 w=25.0 h=0.0508
E21 N21 N22 w=25.0 h=0.0508
E22 N22 N23 w=25.0 h=0.0508
E23 N23 N24 w=25.0 h=0.0508
E24 N24 N25 w=25.0 h=0.0508
E25 N25 N26 w=25.0 h=0.0508
E26 N26 N27 w=25.0 h=0.0508
E27 N27 N28 w=25.0 h=0.0508
```

```
E28 N28 N29 w=25.0 h=0.0508
E29 N29 N30 w=25.0 h=0.0508
E30 N30 N31 w=25.0 h=0.0508
E31 N31 N32 w=25.0 h=0.0508
E32 N32 N33 w=25.0 h=0.0508
E33 N33 N34 w=25.0 h=0.0508
E34 N34 N35 w=25.0 h=0.0508
E35 N35 N36 w=25.0 h=0.0508
E36 N36 N37 w=25.0 h=0.0508
E37 N37 N38 w=25.0 h=0.0508
E38 N38 N39 w=25.0 h=0.0508
E39 N39 N40 w=25.0 h=0.0508
E40 N40 N41 w=25.0 h=0.0508
E41 N41 N42 w=25.0 h=0.0508
E42 N42 N43 w=25.0 h=0.0508
E43 N43 N44 w=25.0 h=0.0508
E44 N44 N45 w=25.0 h=0.0508
E45 N45 N46 w=25.0 h=0.0508
E46 N46 N47 w=25.0 h=0.0508
E47 N47 N48 w=25.0 h=0.0508
E48 N48 N49 w=25.0 h=0.0508
E49 N49 N50 w=25.0 h=0.0508
E50 N50 N51 w=25.0 h=0.0508
E51 N51 N52 w=25.0 h=0.0508
E52 N52 N53 w=25.0 h=0.0508
E53 N53 N54 w=25.0 h=0.0508
E54 N54 N55 w=25.0 h=0.0508
E55 N55 N56 w=25.0 h=0.0508
E56 N56 N57 w=25.0 h=0.0508
E57 N57 N58 w=25.0 h=0.0508
E58 N58 N59 w=25.0 h=0.0508
E59 N59 N60 w=25.0 h=0.0508
E60 N60 N61 w=25.0 h=0.0508
E61 N61 N62 w=25.0 h=0.0508
E62 N62 N63 w=25.0 h=0.0508
E63 N63 N64 w=25.0 h=0.0508
E64 N64 N65 w=25.0 h=0.0508
E65 N65 N66 w=25.0 h=0.0508
E66 N66 N67 w=25.0 h=0.0508
E67 N67 N68 w=25.0 h=0.0508
E68 N68 N69 w=25.0 h=0.0508
E69 N69 N70 w=25.0 h=0.0508
E70 N70 N71 w=25.0 h=0.0508
E71 N71 N72 w=25.0 h=0.0508
E72 N72 N73 w=25.0 h=0.0508
E73 N73 N74 w=25.0 h=0.0508
E74 N74 N75 w=25.0 h=0.0508
E75 N75 N76 w=25.0 h=0.0508
E76 N76 N77 w=25.0 h=0.0508
E77 N77 N78 w=25.0 h=0.0508
E78 N78 N79 w=25.0 h=0.0508
E79 N79 N80 w=25.0 h=0.0508
E80 N80 N81 w=25.0 h=0.0508
E81 N81 N82 w=25.0 h=0.0508
```

```
E82 N82 N83 w=25.0 h=0.0508
E83 N83 N84 w=25.0 h=0.0508
E84 N84 N85 w=25.0 h=0.0508
E85 N85 N86 w=25.0 h=0.0508
E86 N86 N87 w=25.0 h=0.0508
E87 N87 N88 w=25.0 h=0.0508
E88 N88 N89 w=25.0 h=0.0508
E89 N89 N90 w=25.0 h=0.0508
E90 N90 N91 w=25.0 h=0.0508
E91 N91 N92 w=25.0 h=0.0508
E92 N92 N93 w=25.0 h=0.0508
E93 N93 N94 w=25.0 h=0.0508
E94 N94 N95 w=25.0 h=0.0508
E95 N95 N96 w=25.0 h=0.0508
E96 N96 N97 w=25.0 h=0.0508
E97 N97 N98 w=25.0 h=0.0508
E98 N98 N99 w=25.0 h=0.0508
E99 N99 N100 w=25.0 h=0.0508

* define the 'port'
.external N0 N100

* frequency range
*   the frequency is 1/(2*pi), so the resulting reactance
*   is numerically equal to the inductance
.freq fmin=0.1592 fmax=0.1592 ndec=1

* The end
.end
```

B.2.2 ShimCu.inp

```
* File generated by coilgen, Thu Oct 17 19:54:01 2002
* nhinc and nwinc must be set according to the skin depth for the frequency specified in .freq

.Units mm
.default sigma=5.8e4 nhinc=2 nwinc=2

* Nodes
N0 x=0.0 y=0.000 z=15.879
N1 x=0.0 y=0.997 z=15.848
N2 x=0.0 y=1.990 z=15.754
N3 x=0.0 y=2.975 z=15.598
N4 x=0.0 y=3.949 z=15.380
N5 x=0.0 y=4.907 z=15.102
N6 x=0.0 y=5.845 z=14.764
N7 x=0.0 y=6.761 z=14.368
N8 x=0.0 y=7.650 z=13.915
N9 x=0.0 y=8.508 z=13.407
N10 x=0.0 y=9.333 z=12.846
N11 x=0.0 y=10.122 z=12.235
```

```
N12 x=0.0 y=10.870 z=11.575
N13 x=0.0 y=11.575 z=10.870
N14 x=0.0 y=12.235 z=10.122
N15 x=0.0 y=12.846 z=9.333
N16 x=0.0 y=13.407 z=8.508
N17 x=0.0 y=13.915 z=7.650
N18 x=0.0 y=14.368 z=6.761
N19 x=0.0 y=14.764 z=5.845
N20 x=0.0 y=15.102 z=4.907
N21 x=0.0 y=15.380 z=3.949
N22 x=0.0 y=15.598 z=2.975
N23 x=0.0 y=15.754 z=1.990
N24 x=0.0 y=15.848 z=0.997
N25 x=0.0 y=15.879 z=0.000
N26 x=0.0 y=15.848 z=-0.997
N27 x=0.0 y=15.754 z=-1.990
N28 x=0.0 y=15.598 z=-2.975
N29 x=0.0 y=15.380 z=-3.949
N30 x=0.0 y=15.102 z=-4.907
N31 x=0.0 y=14.764 z=-5.845
N32 x=0.0 y=14.368 z=-6.761
N33 x=0.0 y=13.915 z=-7.650
N34 x=0.0 y=13.407 z=-8.508
N35 x=0.0 y=12.846 z=-9.333
N36 x=0.0 y=12.235 z=-10.122
N37 x=0.0 y=11.575 z=-10.870
N38 x=0.0 y=10.870 z=-11.575
N39 x=0.0 y=10.122 z=-12.235
N40 x=0.0 y=9.333 z=-12.846
N41 x=0.0 y=8.508 z=-13.407
N42 x=0.0 y=7.650 z=-13.915
N43 x=0.0 y=6.761 z=-14.368
N44 x=0.0 y=5.845 z=-14.764
N45 x=0.0 y=4.907 z=-15.102
N46 x=0.0 y=3.949 z=-15.380
N47 x=0.0 y=2.975 z=-15.598
N48 x=0.0 y=1.990 z=-15.754
N49 x=0.0 y=0.997 z=-15.848
N50 x=0.0 y=0.000 z=-15.879
N51 x=0.0 y=-0.997 z=-15.848
N52 x=0.0 y=-1.990 z=-15.754
N53 x=0.0 y=-2.975 z=-15.598
N54 x=0.0 y=-3.949 z=-15.380
N55 x=0.0 y=-4.907 z=-15.102
N56 x=0.0 y=-5.845 z=-14.764
N57 x=0.0 y=-6.761 z=-14.368
N58 x=0.0 y=-7.650 z=-13.915
N59 x=0.0 y=-8.508 z=-13.407
N60 x=0.0 y=-9.333 z=-12.846
N61 x=0.0 y=-10.122 z=-12.235
N62 x=0.0 y=-10.870 z=-11.575
N63 x=0.0 y=-11.575 z=-10.870
N64 x=0.0 y=-12.235 z=-10.122
N65 x=0.0 y=-12.846 z=-9.333
```

```
N66 x=0.0 y=-13.407 z=-8.508
N67 x=0.0 y=-13.915 z=-7.650
N68 x=0.0 y=-14.368 z=-6.761
N69 x=0.0 y=-14.764 z=-5.845
N70 x=0.0 y=-15.102 z=-4.907
N71 x=0.0 y=-15.380 z=-3.949
N72 x=0.0 y=-15.598 z=-2.975
N73 x=0.0 y=-15.754 z=-1.990
N74 x=0.0 y=-15.848 z=-0.997
N75 x=0.0 y=-15.879 z=-0.000
N76 x=0.0 y=-15.848 z=0.997
N77 x=0.0 y=-15.754 z=1.990
N78 x=0.0 y=-15.598 z=2.975
N79 x=0.0 y=-15.380 z=3.949
N80 x=0.0 y=-15.102 z=4.907
N81 x=0.0 y=-14.764 z=5.845
N82 x=0.0 y=-14.368 z=6.761
N83 x=0.0 y=-13.915 z=7.650
N84 x=0.0 y=-13.407 z=8.508
N85 x=0.0 y=-12.846 z=9.333
N86 x=0.0 y=-12.235 z=10.122
N87 x=0.0 y=-11.575 z=10.870
N88 x=0.0 y=-10.870 z=11.575
N89 x=0.0 y=-10.122 z=12.235
N90 x=0.0 y=-9.333 z=12.846
N91 x=0.0 y=-8.508 z=13.407
N92 x=0.0 y=-7.650 z=13.915
N93 x=0.0 y=-6.761 z=14.368
N94 x=0.0 y=-5.845 z=14.764
N95 x=0.0 y=-4.907 z=15.102
N96 x=0.0 y=-3.949 z=15.380
N97 x=0.0 y=-2.975 z=15.598
N98 x=0.0 y=-1.990 z=15.754
N99 x=0.0 y=-0.997 z=15.848
N100 x=0.0 y=-0.000 z=15.879

* Segments
E0 N0 N1 w=25.0 h=0.0762
E1 N1 N2 w=25.0 h=0.0762
E2 N2 N3 w=25.0 h=0.0762
E3 N3 N4 w=25.0 h=0.0762
E4 N4 N5 w=25.0 h=0.0762
E5 N5 N6 w=25.0 h=0.0762
E6 N6 N7 w=25.0 h=0.0762
E7 N7 N8 w=25.0 h=0.0762
E8 N8 N9 w=25.0 h=0.0762
E9 N9 N10 w=25.0 h=0.0762
E10 N10 N11 w=25.0 h=0.0762
E11 N11 N12 w=25.0 h=0.0762
E12 N12 N13 w=25.0 h=0.0762
E13 N13 N14 w=25.0 h=0.0762
E14 N14 N15 w=25.0 h=0.0762
E15 N15 N16 w=25.0 h=0.0762
E16 N16 N17 w=25.0 h=0.0762
```

```
E17 N17 N18 w=25.0 h=0.0762
E18 N18 N19 w=25.0 h=0.0762
E19 N19 N20 w=25.0 h=0.0762
E20 N20 N21 w=25.0 h=0.0762
E21 N21 N22 w=25.0 h=0.0762
E22 N22 N23 w=25.0 h=0.0762
E23 N23 N24 w=25.0 h=0.0762
E24 N24 N25 w=25.0 h=0.0762
E25 N25 N26 w=25.0 h=0.0762
E26 N26 N27 w=25.0 h=0.0762
E27 N27 N28 w=25.0 h=0.0762
E28 N28 N29 w=25.0 h=0.0762
E29 N29 N30 w=25.0 h=0.0762
E30 N30 N31 w=25.0 h=0.0762
E31 N31 N32 w=25.0 h=0.0762
E32 N32 N33 w=25.0 h=0.0762
E33 N33 N34 w=25.0 h=0.0762
E34 N34 N35 w=25.0 h=0.0762
E35 N35 N36 w=25.0 h=0.0762
E36 N36 N37 w=25.0 h=0.0762
E37 N37 N38 w=25.0 h=0.0762
E38 N38 N39 w=25.0 h=0.0762
E39 N39 N40 w=25.0 h=0.0762
E40 N40 N41 w=25.0 h=0.0762
E41 N41 N42 w=25.0 h=0.0762
E42 N42 N43 w=25.0 h=0.0762
E43 N43 N44 w=25.0 h=0.0762
E44 N44 N45 w=25.0 h=0.0762
E45 N45 N46 w=25.0 h=0.0762
E46 N46 N47 w=25.0 h=0.0762
E47 N47 N48 w=25.0 h=0.0762
E48 N48 N49 w=25.0 h=0.0762
E49 N49 N50 w=25.0 h=0.0762
E50 N50 N51 w=25.0 h=0.0762
E51 N51 N52 w=25.0 h=0.0762
E52 N52 N53 w=25.0 h=0.0762
E53 N53 N54 w=25.0 h=0.0762
E54 N54 N55 w=25.0 h=0.0762
E55 N55 N56 w=25.0 h=0.0762
E56 N56 N57 w=25.0 h=0.0762
E57 N57 N58 w=25.0 h=0.0762
E58 N58 N59 w=25.0 h=0.0762
E59 N59 N60 w=25.0 h=0.0762
E60 N60 N61 w=25.0 h=0.0762
E61 N61 N62 w=25.0 h=0.0762
E62 N62 N63 w=25.0 h=0.0762
E63 N63 N64 w=25.0 h=0.0762
E64 N64 N65 w=25.0 h=0.0762
E65 N65 N66 w=25.0 h=0.0762
E66 N66 N67 w=25.0 h=0.0762
E67 N67 N68 w=25.0 h=0.0762
E68 N68 N69 w=25.0 h=0.0762
E69 N69 N70 w=25.0 h=0.0762
E70 N70 N71 w=25.0 h=0.0762
```

```
E71 N71 N72 w=25.0 h=0.0762
E72 N72 N73 w=25.0 h=0.0762
E73 N73 N74 w=25.0 h=0.0762
E74 N74 N75 w=25.0 h=0.0762
E75 N75 N76 w=25.0 h=0.0762
E76 N76 N77 w=25.0 h=0.0762
E77 N77 N78 w=25.0 h=0.0762
E78 N78 N79 w=25.0 h=0.0762
E79 N79 N80 w=25.0 h=0.0762
E80 N80 N81 w=25.0 h=0.0762
E81 N81 N82 w=25.0 h=0.0762
E82 N82 N83 w=25.0 h=0.0762
E83 N83 N84 w=25.0 h=0.0762
E84 N84 N85 w=25.0 h=0.0762
E85 N85 N86 w=25.0 h=0.0762
E86 N86 N87 w=25.0 h=0.0762
E87 N87 N88 w=25.0 h=0.0762
E88 N88 N89 w=25.0 h=0.0762
E89 N89 N90 w=25.0 h=0.0762
E90 N90 N91 w=25.0 h=0.0762
E91 N91 N92 w=25.0 h=0.0762
E92 N92 N93 w=25.0 h=0.0762
E93 N93 N94 w=25.0 h=0.0762
E94 N94 N95 w=25.0 h=0.0762
E95 N95 N96 w=25.0 h=0.0762
E96 N96 N97 w=25.0 h=0.0762
E97 N97 N98 w=25.0 h=0.0762
E98 N98 N99 w=25.0 h=0.0762
E99 N99 N100 w=25.0 h=0.0762

* define the 'port'
.external N0 N100

* frequency range
*   the frequency is 1/(2*pi), so the resulting reactance
*   is numerically equal to the inductance
.freq fmin=0.1592 fmax=0.1592 ndec=1

* The end
.end
```

B.2.3 ShimSteel.inp

```
* File generated by coilgen, Thu Oct 17 19:54:01 2002
* nhinc and nwinc must be set according to the skin depth for the frequency specified in .freq

.Units mm
.default sigma=1.45e3 nhinc=2nwinc=2

* Nodes
N0 x=0.0 y=0.000 z=15.879
```

```
N1 x=0.0 y=0.997 z=15.848
N2 x=0.0 y=1.990 z=15.754
N3 x=0.0 y=2.975 z=15.598
N4 x=0.0 y=3.949 z=15.380
N5 x=0.0 y=4.907 z=15.102
N6 x=0.0 y=5.845 z=14.764
N7 x=0.0 y=6.761 z=14.368
N8 x=0.0 y=7.650 z=13.915
N9 x=0.0 y=8.508 z=13.407
N10 x=0.0 y=9.333 z=12.846
N11 x=0.0 y=10.122 z=12.235
N12 x=0.0 y=10.870 z=11.575
N13 x=0.0 y=11.575 z=10.870
N14 x=0.0 y=12.235 z=10.122
N15 x=0.0 y=12.846 z=9.333
N16 x=0.0 y=13.407 z=8.508
N17 x=0.0 y=13.915 z=7.650
N18 x=0.0 y=14.368 z=6.761
N19 x=0.0 y=14.764 z=5.845
N20 x=0.0 y=15.102 z=4.907
N21 x=0.0 y=15.380 z=3.949
N22 x=0.0 y=15.598 z=2.975
N23 x=0.0 y=15.754 z=1.990
N24 x=0.0 y=15.848 z=0.997
N25 x=0.0 y=15.879 z=0.000
N26 x=0.0 y=15.848 z=-0.997
N27 x=0.0 y=15.754 z=-1.990
N28 x=0.0 y=15.598 z=-2.975
N29 x=0.0 y=15.380 z=-3.949
N30 x=0.0 y=15.102 z=-4.907
N31 x=0.0 y=14.764 z=-5.845
N32 x=0.0 y=14.368 z=-6.761
N33 x=0.0 y=13.915 z=-7.650
N34 x=0.0 y=13.407 z=-8.508
N35 x=0.0 y=12.846 z=-9.333
N36 x=0.0 y=12.235 z=-10.122
N37 x=0.0 y=11.575 z=-10.870
N38 x=0.0 y=10.870 z=-11.575
N39 x=0.0 y=10.122 z=-12.235
N40 x=0.0 y=9.333 z=-12.846
N41 x=0.0 y=8.508 z=-13.407
N42 x=0.0 y=7.650 z=-13.915
N43 x=0.0 y=6.761 z=-14.368
N44 x=0.0 y=5.845 z=-14.764
N45 x=0.0 y=4.907 z=-15.102
N46 x=0.0 y=3.949 z=-15.380
N47 x=0.0 y=2.975 z=-15.598
N48 x=0.0 y=1.990 z=-15.754
N49 x=0.0 y=0.997 z=-15.848
N50 x=0.0 y=0.000 z=-15.879
N51 x=0.0 y=-0.997 z=-15.848
N52 x=0.0 y=-1.990 z=-15.754
N53 x=0.0 y=-2.975 z=-15.598
N54 x=0.0 y=-3.949 z=-15.380
```

```
N55 x=0.0 y=-4.907 z=-15.102
N56 x=0.0 y=-5.845 z=-14.764
N57 x=0.0 y=-6.761 z=-14.368
N58 x=0.0 y=-7.650 z=-13.915
N59 x=0.0 y=-8.508 z=-13.407
N60 x=0.0 y=-9.333 z=-12.846
N61 x=0.0 y=-10.122 z=-12.235
N62 x=0.0 y=-10.870 z=-11.575
N63 x=0.0 y=-11.575 z=-10.870
N64 x=0.0 y=-12.235 z=-10.122
N65 x=0.0 y=-12.846 z=-9.333
N66 x=0.0 y=-13.407 z=-8.508
N67 x=0.0 y=-13.915 z=-7.650
N68 x=0.0 y=-14.368 z=-6.761
N69 x=0.0 y=-14.764 z=-5.845
N70 x=0.0 y=-15.102 z=-4.907
N71 x=0.0 y=-15.380 z=-3.949
N72 x=0.0 y=-15.598 z=-2.975
N73 x=0.0 y=-15.754 z=-1.990
N74 x=0.0 y=-15.848 z=-0.997
N75 x=0.0 y=-15.879 z=-0.000
N76 x=0.0 y=-15.848 z=0.997
N77 x=0.0 y=-15.754 z=1.990
N78 x=0.0 y=-15.598 z=2.975
N79 x=0.0 y=-15.380 z=3.949
N80 x=0.0 y=-15.102 z=4.907
N81 x=0.0 y=-14.764 z=5.845
N82 x=0.0 y=-14.368 z=6.761
N83 x=0.0 y=-13.915 z=7.650
N84 x=0.0 y=-13.407 z=8.508
N85 x=0.0 y=-12.846 z=9.333
N86 x=0.0 y=-12.235 z=10.122
N87 x=0.0 y=-11.575 z=10.870
N88 x=0.0 y=-10.870 z=11.575
N89 x=0.0 y=-10.122 z=12.235
N90 x=0.0 y=-9.333 z=12.846
N91 x=0.0 y=-8.508 z=13.407
N92 x=0.0 y=-7.650 z=13.915
N93 x=0.0 y=-6.761 z=14.368
N94 x=0.0 y=-5.845 z=14.764
N95 x=0.0 y=-4.907 z=15.102
N96 x=0.0 y=-3.949 z=15.380
N97 x=0.0 y=-2.975 z=15.598
N98 x=0.0 y=-1.990 z=15.754
N99 x=0.0 y=-0.997 z=15.848
N100 x=0.0 y=-0.000 z=15.879

* Segments
E0 N0 N1 w=25.4 h=0.1016
E1 N1 N2 w=25.4 h=0.1016
E2 N2 N3 w=25.4 h=0.1016
E3 N3 N4 w=25.4 h=0.1016
E4 N4 N5 w=25.4 h=0.1016
E5 N5 N6 w=25.4 h=0.1016
```

```
E6 N6 N7 w=25.4 h=0.1016
E7 N7 N8 w=25.4 h=0.1016
E8 N8 N9 w=25.4 h=0.1016
E9 N9 N10 w=25.4 h=0.1016
E10 N10 N11 w=25.4 h=0.1016
E11 N11 N12 w=25.4 h=0.1016
E12 N12 N13 w=25.4 h=0.1016
E13 N13 N14 w=25.4 h=0.1016
E14 N14 N15 w=25.4 h=0.1016
E15 N15 N16 w=25.4 h=0.1016
E16 N16 N17 w=25.4 h=0.1016
E17 N17 N18 w=25.4 h=0.1016
E18 N18 N19 w=25.4 h=0.1016
E19 N19 N20 w=25.4 h=0.1016
E20 N20 N21 w=25.4 h=0.1016
E21 N21 N22 w=25.4 h=0.1016
E22 N22 N23 w=25.4 h=0.1016
E23 N23 N24 w=25.4 h=0.1016
E24 N24 N25 w=25.4 h=0.1016
E25 N25 N26 w=25.4 h=0.1016
E26 N26 N27 w=25.4 h=0.1016
E27 N27 N28 w=25.4 h=0.1016
E28 N28 N29 w=25.4 h=0.1016
E29 N29 N30 w=25.4 h=0.1016
E30 N30 N31 w=25.4 h=0.1016
E31 N31 N32 w=25.4 h=0.1016
E32 N32 N33 w=25.4 h=0.1016
E33 N33 N34 w=25.4 h=0.1016
E34 N34 N35 w=25.4 h=0.1016
E35 N35 N36 w=25.4 h=0.1016
E36 N36 N37 w=25.4 h=0.1016
E37 N37 N38 w=25.4 h=0.1016
E38 N38 N39 w=25.4 h=0.1016
E39 N39 N40 w=25.4 h=0.1016
E40 N40 N41 w=25.4 h=0.1016
E41 N41 N42 w=25.4 h=0.1016
E42 N42 N43 w=25.4 h=0.1016
E43 N43 N44 w=25.4 h=0.1016
E44 N44 N45 w=25.4 h=0.1016
E45 N45 N46 w=25.4 h=0.1016
E46 N46 N47 w=25.4 h=0.1016
E47 N47 N48 w=25.4 h=0.1016
E48 N48 N49 w=25.4 h=0.1016
E49 N49 N50 w=25.4 h=0.1016
E50 N50 N51 w=25.4 h=0.1016
E51 N51 N52 w=25.4 h=0.1016
E52 N52 N53 w=25.4 h=0.1016
E53 N53 N54 w=25.4 h=0.1016
E54 N54 N55 w=25.4 h=0.1016
E55 N55 N56 w=25.4 h=0.1016
E56 N56 N57 w=25.4 h=0.1016
E57 N57 N58 w=25.4 h=0.1016
E58 N58 N59 w=25.4 h=0.1016
E59 N59 N60 w=25.4 h=0.1016
```

```
E60 N60 N61 w=25.4 h=0.1016
E61 N61 N62 w=25.4 h=0.1016
E62 N62 N63 w=25.4 h=0.1016
E63 N63 N64 w=25.4 h=0.1016
E64 N64 N65 w=25.4 h=0.1016
E65 N65 N66 w=25.4 h=0.1016
E66 N66 N67 w=25.4 h=0.1016
E67 N67 N68 w=25.4 h=0.1016
E68 N68 N69 w=25.4 h=0.1016
E69 N69 N70 w=25.4 h=0.1016
E70 N70 N71 w=25.4 h=0.1016
E71 N71 N72 w=25.4 h=0.1016
E72 N72 N73 w=25.4 h=0.1016
E73 N73 N74 w=25.4 h=0.1016
E74 N74 N75 w=25.4 h=0.1016
E75 N75 N76 w=25.4 h=0.1016
E76 N76 N77 w=25.4 h=0.1016
E77 N77 N78 w=25.4 h=0.1016
E78 N78 N79 w=25.4 h=0.1016
E79 N79 N80 w=25.4 h=0.1016
E80 N80 N81 w=25.4 h=0.1016
E81 N81 N82 w=25.4 h=0.1016
E82 N82 N83 w=25.4 h=0.1016
E83 N83 N84 w=25.4 h=0.1016
E84 N84 N85 w=25.4 h=0.1016
E85 N85 N86 w=25.4 h=0.1016
E86 N86 N87 w=25.4 h=0.1016
E87 N87 N88 w=25.4 h=0.1016
E88 N88 N89 w=25.4 h=0.1016
E89 N89 N90 w=25.4 h=0.1016
E90 N90 N91 w=25.4 h=0.1016
E91 N91 N92 w=25.4 h=0.1016
E92 N92 N93 w=25.4 h=0.1016
E93 N93 N94 w=25.4 h=0.1016
E94 N94 N95 w=25.4 h=0.1016
E95 N95 N96 w=25.4 h=0.1016
E96 N96 N97 w=25.4 h=0.1016
E97 N97 N98 w=25.4 h=0.1016
E98 N98 N99 w=25.4 h=0.1016
E99 N99 N100 w=25.4 h=0.1016

* define the 'port'
.external N0 N100

* frequency range
*   the frequency is 1/(2*pi), so the resulting reactance
*   is numerically equal to the inductance
.freq fmin=0.1592 fmax=0.1592 ndec=1

* The end
.end
```

B.3 MATLAB

A number of the plots in this thesis were generated using MATLAB. All of the source code required to produce these results and more are included below. These files were written for MATLAB version 6.0.0.88 release 12 for Windows.

B.3.1 ACR.m

```
%ACR.m
%This function takes the radius of a loop of wire, its diameter, conductivity and a set of
%frequency points in (Hz) and returns the AC resistance of that wire.

function [R]=ACR(r_w,r_c,Sgm,f);

%%%%%%%%%%%%%%%%%%%%%%%%%%%%%%%%%%%%%%%%%%%%%%%%%%%%%%%%%%%%%%%%%%%%%%%%%%%%%%%%%%%%%%%%%%%%
%Wire parameters
%%%%%%%%%%%%%%%%%%%%%%%%%%%%%%%%%%%%%%%%%%%%%%%%%%%%%%%%%%%%%%%%%%%%%%%%%%%%%%%%%%%%%%%%%%%%
N=1;                %One turn assumed b/c proximity effects are ignored.
l_w=N*2*pi*r_c ; %Length of Wire (Meters)
Mo=4*pi*1e-7;     %Permeability of Freespace (H/M)

%Convert frequencies to rps
w=2*pi*f;
%Reciprocal of complex depth of penetration
m=(j*w*Sgm*Mo).^.5;
%Some required Bessel functin calculations
I0=besseli(0,m*r_w);
I1=besseli(1,m*r_w);
%Take the real part of Impedance
R=real(m.*l_w.*I0./(2*pi.*r_w.*Sgm.*I1));
```

B.3.2 ATDVA.m

```
%ATDVA.m
%This script calculates the frequency response of a resonant mechanical structure coupled
%to a tunable semi-active DVA. DVA's with variable spring constants and masses can be
%examined.

clear
%%%%%%%%%%%%%%%%%%%%%%%%%%%%%%%%%%%%%%%%%%%%%%%%%%%%%%%%%%%%%%%%%%%%%%%%%%%%%%%%%%%%%%%%%%%%
%System parameters
%%%%%%%%%%%%%%%%%%%%%%%%%%%%%%%%%%%%%%%%%%%%%%%%%%%%%%%%%%%%%%%%%%%%%%%%%%%%%%%%%%%%%%%%%%%%
m1=1;                                       %Primary mass
```

```
m2=.1;                                       %Secondary mass
k1=1;                                        %Primary compliance
k2=.1;                                       %Secondary compliance
c1=.1;                                       %Primary damping constant
c2=.001;                                     %Secondary damping constant
s=tf('s');                                   %Complex frequency s

%%%%%%%%%%%%%%%%%%%%%%%%%%%%%%%%%%%%%%%%%%%%%%%%%%%%%%%%%%%%%%%%%%%%%%%%%%%%%%%%%%%%%%%%%%%%%%
%1st transfer function
%%%%%%%%%%%%%%%%%%%%%%%%%%%%%%%%%%%%%%%%%%%%%%%%%%%%%%%%%%%%%%%%%%%%%%%%%%%%%%%%%%%%%%%%%%%%%%
H1=[m2*s^2+c2*s+k2]/[[m1*s^2+(c1+c2)*s+(k1+k2)]*[m2*s^2+c2*s+k2]-[c2*s+k2]^2];

%%%%%%%%%%%%%%%%%%%%%%%%%%%%%%%%%%%%%%%%%%%%%%%%%%%%%%%%%%%%%%%%%%%%%%%%%%%%%%%%%%%%%%%%%%%%%%
%1st transfer function
%%%%%%%%%%%%%%%%%%%%%%%%%%%%%%%%%%%%%%%%%%%%%%%%%%%%%%%%%%%%%%%%%%%%%%%%%%%%%%%%%%%%%%%%%%%%%%
%m2=.05;                                      %Secondary mass
k2=.05;                                       %Secondary compliance

H2=[m2*s^2+c2*s+k2]/[[m1*s^2+(c1+c2)*s+(k1+k2)]*[m2*s^2+c2*s+k2]-[c2*s+k2]^2];

%%%%%%%%%%%%%%%%%%%%%%%%%%%%%%%%%%%%%%%%%%%%%%%%%%%%%%%%%%%%%%%%%%%%%%%%%%%%%%%%%%%%%%%%%%%%%%
%3re transfer function
%%%%%%%%%%%%%%%%%%%%%%%%%%%%%%%%%%%%%%%%%%%%%%%%%%%%%%%%%%%%%%%%%%%%%%%%%%%%%%%%%%%%%%%%%%%%%%
%m2=.2;                                       %Secondary mass
k2=.2;                                       %Secondary compliance

H3=[m2*s^2+c2*s+k2]/[[m1*s^2+(c1+c2)*s+(k1+k2)]*[m2*s^2+c2*s+k2]-[c2*s+k2]^2];

%%%%%%%%%%%%%%%%%%%%%%%%%%%%%%%%%%%%%%%%%%%%%%%%%%%%%%%%%%%%%%%%%%%%%%%%%%%%%%%%%%%%%%%%%%%%%%
%Determine frequency response
%%%%%%%%%%%%%%%%%%%%%%%%%%%%%%%%%%%%%%%%%%%%%%%%%%%%%%%%%%%%%%%%%%%%%%%%%%%%%%%%%%%%%%%%%%%%%%
%Frequency vector in rps
w=logspace(-1,1,1000);

%Bode response
[mag1,phase1]=bode(H1,w);
[mag2,phase2]=bode(H2,w);
[mag3,phase3]=bode(H3,w);

%%%%%%%%%%%%%%%%%%%%%%%%%%%%%%%%%%%%%%%%%%%%%%%%%%%%%%%%%%%%%%%%%%%%%%%%%%%%%%%%%%%%%%%%%%%%%%
%Plot results
%%%%%%%%%%%%%%%%%%%%%%%%%%%%%%%%%%%%%%%%%%%%%%%%%%%%%%%%%%%%%%%%%%%%%%%%%%%%%%%%%%%%%%%%%%%%%%
figure(1)
subplot(2,1,1)
semilogx(w,20*log10(mag1(:)),'-',w,20*log10(mag2(:)),'--',w,20*log10(mag3(:)),'-.')
title('Frequency Response (X_1/F) of Resonant Mechanical Structure
    for Different Values of K_{2}')
%title('Frequency Response (\Theta_1/F) of Resonant Mechanical Structure
    for Different Values of J_{2}')
ylabel('[X_{1}/X_{st}| (dB)')
%ylabel('[\Theta_{1}/\Theta_{st}| (dB)')
legend('K_{2,nominal}','K_{2,min}','K_{2,max}')
%legend('J_{2,nominal}','J_{2,min}','J_{2,max}')
grid on
```

```
subplot(2,1,2)
semilogx(w,phase1(:),'-',w,phase2(:),'--',w,phase3(:),'-.');
ylabel('Phase (Degrees)')
xlabel('Normalized Frequency (\omega/\omega_n)')
legend('K_{2,nominal}','K_{2,min}','K_{2,max}')
%legend('J_{2,nominal}','J_{2,min}','J_{2,max}')
grid on
```

B.3.3 Calorimetry.m

```
%Calorimetry.m
%This script plots the measured power curves for three thin-walled shells of shim metal:
%Copper, Brass, Stainless Steel. Each shell was individually coupled to a primary induction
%coil during a calorimetry experiment.

clear
%%%%%%%%%%%%%%%%%%%%%%%%%%%%%%%%%%%%%%%%%%%%%%%%%%%%%%%%%%%%%%%%%%%%%%%%%%%%%%%%%%%%%%%%%%%%%%%%
%Experimental data
%%%%%%%%%%%%%%%%%%%%%%%%%%%%%%%%%%%%%%%%%%%%%%%%%%%%%%%%%%%%%%%%%%%%%%%%%%%%%%%%%%%%%%%%%%%%%%%%
cx(1) = 300e3;
cx(2) = 200e3;
cx(3) = 120e3;
cx(4) = 100e3;
cx(5) = 80e3;
cx(6) = 60e3;
cx(7) = 40e3;
cx(8) = 30e3;
cx(9) = 20e3;
cx(10) = 15e3;
cx(11) = 10e3;
cx(12) = 7e3;
cx(13) = 5e3;
cx(14) = 3e3;

cy(1) = 1.15 * (2.3460/(.80334 * (1.014/1.029)))^2;
cy(2) = 2.4 * (2.3460/(1.18104 * (1.014/1.022)))^2;
cy(3) = 6.25 * (2.3460/(1.9739 * (1.014/1.016)))^2;
cy(4) = 8.7;
cy(5) = 8.45;
cy(6) = 8.3;
cy(7) = 7.7;
cy(8) = 7.3;
cy(9) = 6.36;
cy(10) = 5.75;
cy(11) = 4.7;
cy(12) = 3.65;
cy(13) = 2.5;
cy(14) = 1.2;

cy = cy * (.78597/2.3460) ^2;
```

```
sx(1) = 300e3;
sx(2) = 240e3;
sx(3) = 200e3;
sx(4) = 140e3;
sx(5) = 100e3;
sx(6) = 80e3;
sx(7) = 60e3;
sx(8) = 40e3;
sx(9) = 30e3;
sx(10) = 20e3;
sx(11) = 15e3;

sy(1) = 13.8;
sy(2) = 12.4;
sy(3) = 11.05;
sy(4) = 7.8;
sy(5) = 5.1;
sy(6) = 3.45;
sy(7) = 2.2;
sy(8) = 1.1;
sy(9) = 4.6 * (.79760/(2.1058 * (1.029/1.007)))^2 ;
sy(10) = 4.4 * (.79760/(3.0693 * (1.029/1.006)))^2 ;
sy(11) = 2.6 * (.79760/(3.1011 * (1.029/1.005)))^2 ;

bx(1) = 300e3;
bx(2) = 240e3;
bx(3) = 200e3;
bx(4) = 180e3;
bx(5) = 160e3;
bx(6) = 140e3;
bx(7) = 120e3;
bx(8) = 100e3;
bx(9) = 80e3;
bx(10) = 60e3;
bx(11) = 40e3;
bx(12) = 30e3;
bx(13) = 20e3;
bx(14) = 15e3;
bx(15) = 10e3;
bx(16) = 7e3;

by(1) = 3.9;
by(2) = 3.9;
by(3) = 3.85;
by(4) = 3.8;
by(5) = 3.75;
by(6) = 3.7;
by(7) = 3.6;
by(8) = 3.45;
by(9) = 3.2;
by(10) = 2.8;
by(11) = 2.2;
by(12) = 1.7;
by(13) = 1.0;
```

```
by(14) = 7.6 * (.79760/(2.6606 * (1.029/1.005)))^2 ;
by(15) = 5.0 * (.79760/(3.0503 * (1.029/1.005)))^2 ;
by(16) = 1.8 * (.79760/(2.5492 * (1.029/1.005)))^2 ;

cy = cy * (.1349 * 14.295 / 13.2);
by = by * (.1349 * 14.295 / 13.2);
sy = sy * (.1349 * 14.295 / 13.2);

%%%%%%%%%%%%%%%%%%%%%%%%%%%%%%%%%%%%%%%%%%%%%%%%%%%%%%%%%%%%%%%%%%%%%%%%%%%%%%%%%%%%%%%%%%%%%%%%%%%%%%%
%FastHenry data
%%%%%%%%%%%%%%%%%%%%%%%%%%%%%%%%%%%%%%%%%%%%%%%%%%%%%%%%%%%%%%%%%%%%%%%%%%%%%%%%%%%%%%%%%%%%%%%%%%%%%%%
[header1, data1] =hdrload('FastHCu.txt');
[header1, data2] =hdrload('FastHBrass.txt');
[header1, data3] =hdrload('FastHSteel.txt');

%Frequency vector
F0=data1(:,1)';
%Frequency matrix
F1=[data1(:,1)'; data2(:,1)'; data3(:,1)'];
%Resistance of primary coil
R1=[data1(:,2)'; data2(:,2)'; data3(:,2)'];
%Reactance of primary coil
X1=[data1(:,3)'; data2(:,3)'; data3(:,3)'];
%Average the cross terms
X12=[(data1(:,5)'+data1(:,7)')/2; (data2(:,5)'+data2(:,7)')/2; (data3(:,5)'+data3(:,7)')/2];
%Resistance of targets
R2=[data1(:,8)'; data2(:,8)'; data3(:,8)'];
%Reactance of targets
X2=[data1(:,9)'; data2(:,9)'; data3(:,9)'];

%%%%%%%%%%%%%%%%%%%%%%%%%%%%%%%%%%%%%%%%%%%%%%%%%%%%%%%%%%%%%%%%%%%%%%%%%%%%%%%%%%%%%%%%%%%%%%%%%%%%%%%
%Calculate +/-10% of the FastHenry prediction
%%%%%%%%%%%%%%%%%%%%%%%%%%%%%%%%%%%%%%%%%%%%%%%%%%%%%%%%%%%%%%%%%%%%%%%%%%%%%%%%%%%%%%%%%%%%%%%%%%%%%%%
%Convert F1 to rps
w1=2*pi*F1;
%Inductance of primary coil
L1=X1./w1;
%Inductance of targets
L2=X2./w1;
%Mutual inductance
L12=X12./w1;
%Coupling coefficients
K=L12./sqrt(L1.*L2);

%Convert current from RMS
I=.8*1.414;
%Convert F0 to rps
w0=2*pi*F0;
%Find power dissipated
for n=1:size(K,1)
Pfast(n,:)=0.5.*(I.*K(n,:).*w0).^2.*L1(n,:).*L2(n,:).*R2(n,:)./
    [(L2(n,:).*w0).^2+R2(n,:).^2];
end
Pfast2=[Pfast*.9; Pfast*1.1];
```

```
%%%%%%%%%%%%%%%%%%%%%%%%%%%%%%%%%%%%%%%%%%%%%%%%%%%%%%%%%%%%%%%%%%%%%%%%%%%%%%%%%%%%%%%%%%%%
%Calculate the circuit model prediction
%%%%%%%%%%%%%%%%%%%%%%%%%%%%%%%%%%%%%%%%%%%%%%%%%%%%%%%%%%%%%%%%%%%%%%%%%%%%%%%%%%%%%%%%%%%%
%Inductance of primary coil
L1=100e-6*[1 1 1];
%Inductance of targets
L2=2.51e-8*[1 1 1];
%Coupling coefficients
K=.20*[1 1 1];
%Resistance of targets
R=[.00089,.0047 .0267];
%Frequency range
f=logspace(3,6,1000);
%Convert to rps
w=2*pi*f;
%Find power dissipated
for n=1:length(K);
P(n,:)=0.5*(I*K(n)*w).^2*L1(n)*L2(n)*R(n)./[(L2(n)*w).^2+R(n)^2];
end

%%%%%%%%%%%%%%%%%%%%%%%%%%%%%%%%%%%%%%%%%%%%%%%%%%%%%%%%%%%%%%%%%%%%%%%%%%%%%%%%%%%%%%%%%%%%
%Plot results
%%%%%%%%%%%%%%%%%%%%%%%%%%%%%%%%%%%%%%%%%%%%%%%%%%%%%%%%%%%%%%%%%%%%%%%%%%%%%%%%%%%%%%%%%%%%
figure(1);
loglog(cx,cy,'bo',bx,by,'bd',sx,sy,'bs',f,P(1,:),'k-',F0,Pfast2(1,:),'r-.',f,P,'k-',
    F0,Pfast2,'r-.');
%loglog(cx,cy,'bs-',bx,by, 'bo-', sx,sy, 'bd-',f,P,'r')
title('Plot of Induced Power versus Frequency for Constant Current Drive')
ylabel('Power (Watts)')
xlabel('Frequency (Hz)')
legend('Copper, 110 Annealed','Brass, Alloy 260','Stainless Steel, 302',
    'Circuit Model Prediction','\pm 10% of Fasthenry Prediction',2)
%legend('Copper, 110 Annealed','Brass, Alloy 260','Stainless Steel, 302',
    'Circuit Model Prediction',2)
grid on
axis([3e3,3e5,.019,3])
```

B.3.4 DVA.m

```
%DVA.m
%This script calculates the frequency response of a resonant mechanical structure coupled
%to a DVA. Different DVA parameters can be examined, including constant and optimal
%tuning conditions.

clear
%%%%%%%%%%%%%%%%%%%%%%%%%%%%%%%%%%%%%%%%%%%%%%%%%%%%%%%%%%%%%%%%%%%%%%%%%%%%%%%%%%%%%%%%%%%%
%System parameters
%%%%%%%%%%%%%%%%%%%%%%%%%%%%%%%%%%%%%%%%%%%%%%%%%%%%%%%%%%%%%%%%%%%%%%%%%%%%%%%%%%%%%%%%%%%%
m1=1;                                       %Primary mass
m2=.1;                                      %Secondary mass
```

```
k1=1;                                          %Primay compliance
k2=.1;                                         %Secondary compliance
c1=.1;                                         %Primary damping constant
c2=.001;                                       %Secondary damping constant
mu=.2;                                         %Mass ratio
psi=1/(1+mu);                                  %Frequency ratio: optimal tuning
%psi=1;                                        %Frequency ratio: contant tuning
z1=0;                                          %Primary damping ratio
Xst=1;                                         %Static displacement
wn=1;                                          %Natural frequency
s=tf('s');                                     %Complex frequency s

%%%%%%%%%%%%%%%%%%%%%%%%%%%%%%%%%%%%%%%%%%%%%%%%%%%%%%%%%%%%%%%%%%%%%%%%%%%%%%%%%%%%%%%%%%%%%%%
%1st transfer function
%%%%%%%%%%%%%%%%%%%%%%%%%%%%%%%%%%%%%%%%%%%%%%%%%%%%%%%%%%%%%%%%%%%%%%%%%%%%%%%%%%%%%%%%%%%%%%%%
z2=0.1;                                        %Secondary damping ratio

%X1/F transfer function
H1=[(s/wn)^2+2*z2*psi*(s/wn)+psi^2]/[(s/wn)^4+2*(z1+(1+mu)*psi*z2)*(s/wn)^3+
    (1+(1+mu)*psi^2+4*z1*z2*psi)*(s/wn)^2+2*(z1*psi^2+z2*psi)*(s/wn)+psi^2];
%X2/F transfer function
%H1=[2*z2*psi*(s/wn)+psi^2]/[(s/wn)^4+2*(z1+(1+mu)*psi*z2)*(s/wn)^3+
    (1+(1+mu)*psi^2+4*z1*z2*psi)*(s/wn)^2+2*(z1*psi^2+z2*psi)*(s/wn)+psi^2];
%(X2-X1)/F transfer function
%H1=[(s/wn)^2]/[(s/wn)^4+2*(z1+(1+mu)*psi*z2)*(s/wn)^3+
    (1+(1+mu)*psi^2+4*z1*z2*psi)*(s/wn)^2+2*(z1*psi^2+z2*psi)*(s/wn)+psi^2];

%%%%%%%%%%%%%%%%%%%%%%%%%%%%%%%%%%%%%%%%%%%%%%%%%%%%%%%%%%%%%%%%%%%%%%%%%%%%%%%%%%%%%%%%%%%%%%%%
%2nd transfer function
%%%%%%%%%%%%%%%%%%%%%%%%%%%%%%%%%%%%%%%%%%%%%%%%%%%%%%%%%%%%%%%%%%%%%%%%%%%%%%%%%%%%%%%%%%%%%%%%
z2=.24;                                        %Secondary damping ratio

%X1/F transfer function
H2=[(s/wn)^2+2*z2*psi*(s/wn)+psi^2]/[(s/wn)^4+2*(z1+(1+mu)*psi*z2)*(s/wn)^3+
    (1+(1+mu)*psi^2+4*z1*z2*psi)*(s/wn)^2+2*(z1*psi^2+z2*psi)*(s/wn)+psi^2];
%X2/F transfer function
%H2=[2*z2*psi*(s/wn)+psi^2]/[(s/wn)^4+2*(z1+(1+mu)*psi*z2)*(s/wn)^3+
    (1+(1+mu)*psi^2+4*z1*z2*psi)*(s/wn)^2+2*(z1*psi^2+z2*psi)*(s/wn)+psi^2];
%(X2-X1)/F transfer function
%H2=[(s/wn)^2]/[(s/wn)^4+2*(z1+(1+mu)*psi*z2)*(s/wn)^3+
    (1+(1+mu)*psi^2+4*z1*z2*psi)*(s/wn)^2+2*(z1*psi^2+z2*psi)*(s/wn)+psi^2];

%%%%%%%%%%%%%%%%%%%%%%%%%%%%%%%%%%%%%%%%%%%%%%%%%%%%%%%%%%%%%%%%%%%%%%%%%%%%%%%%%%%%%%%%%%%%%%%%
%3rd transfer function
%%%%%%%%%%%%%%%%%%%%%%%%%%%%%%%%%%%%%%%%%%%%%%%%%%%%%%%%%%%%%%%%%%%%%%%%%%%%%%%%%%%%%%%%%%%%%%%%
z2=1;                                          %Secondary damping ratio

%X1/F transfer function
H3=[(s/wn)^2+2*z2*psi*(s/wn)+psi^2]/[(s/wn)^4+2*(z1+(1+mu)*psi*z2)*(s/wn)^3+
    (1+(1+mu)*psi^2+4*z1*z2*psi)*(s/wn)^2+2*(z1*psi^2+z2*psi)*(s/wn)+psi^2];
%X2/F transfer function
%H3=[2*z2*psi*(s/wn)+psi^2]/[(s/wn)^4+2*(z1+(1+mu)*psi*z2)*(s/wn)^3+
    (1+(1+mu)*psi^2+4*z1*z2*psi)*(s/wn)^2+2*(z1*psi^2+z2*psi)*(s/wn)+psi^2];
%(X2-X1)/F transfer function
```

```
%H3=[(s/wn)^2]/[(s/wn)^4+2*(z1+(1+mu)*psi*z2)*(s/wn)^3+
    (1+(1+mu)*psi^2+4*z1*z2*psi)*(s/wn)^2+2*(z1*psi^2+z2*psi)*(s/wn)+psi^2];

%%%%%%%%%%%%%%%%%%%%%%%%%%%%%%%%%%%%%%%%%%%%%%%%%%%%%%%%%%%%%%%%%%%%%%%%%%%%%%%%%%%%%%%%%%%%
%Determine frequency response
%%%%%%%%%%%%%%%%%%%%%%%%%%%%%%%%%%%%%%%%%%%%%%%%%%%%%%%%%%%%%%%%%%%%%%%%%%%%%%%%%%%%%%%%%%%%
%Frequency vector in rps
w=logspace(-1,1,10000);

%Bode response
[mag1,phase1]=bode(H1,w);
[mag2,phase2]=bode(H2,w);
[mag3,phase3]=bode(H3,w);

%%%%%%%%%%%%%%%%%%%%%%%%%%%%%%%%%%%%%%%%%%%%%%%%%%%%%%%%%%%%%%%%%%%%%%%%%%%%%%%%%%%%%%%%%%%%
%Plot results
%%%%%%%%%%%%%%%%%%%%%%%%%%%%%%%%%%%%%%%%%%%%%%%%%%%%%%%%%%%%%%%%%%%%%%%%%%%%%%%%%%%%%%%%%%%%
figure(1)
subplot(2,1,1)
semilogx(w,20*log10(mag1(:)),'-',w,20*log10(mag2(:)),'--',w,20*log10(mag3(:)),'-.');
title('Frequency Response (X_1/F) of Resonant Mechanical Structure with DVA for
    Different DVA Damping Ratios')
%title('Frequency Response ([X_2-X_1]/F) of DVA with respect to Resonant Structure for
    Different DVA Damping Ratios')
ylabel('|X_{1}/X_{st}| (dB)')
%ylabel('|[X_{2}-X_{1}]/X_{st}| (dB)')
legend('\zeta_{2}=0.1','\zeta_{2}=0.24','\zeta_{2}=1.0')
axis([.1 10 -40 30])
grid on
subplot(2,1,2)
semilogx(w,phase1(:),'-',w,phase2(:),'--',w,phase3(:),'-.');
ylabel('Phase (Degrees)')
xlabel('Normalized Frequency (\omega/\omega_n)')
legend('\zeta_{2}=0.1','\zeta_{2}=0.24','\zeta_{2}=1.0')
grid on
```

B.3.5 Efficiency50.m

```
%Efficiency50.m
%Marx vs PWM efficiency for a single load: 50 Ohm mag, phase of 45 deg, at 100KHz.
%This script can be modified to handle 3 inductively coupled targets.

clear
%%%%%%%%%%%%%%%%%%%%%%%%%%%%%%%%%%%%%%%%%%%%%%%%%%%%%%%%%%%%%%%%%%%%%%%%%%%%%%%%%%%%%%%%%%%%
%Initialize marx parameters
%%%%%%%%%%%%%%%%%%%%%%%%%%%%%%%%%%%%%%%%%%%%%%%%%%%%%%%%%%%%%%%%%%%%%%%%%%%%%%%%%%%%%%%%%%%%
Fc=1;                               %Carrier frequency (Hz)
Tstart=1;                           %Time offset, pick to be greater than 5 time constants
T=1/Fc+Tstart;                      %Carrier period (Secs)
Tpoints=10000;                      %Number of sample points in period T
Mapoints=10;                        %Number Of Ma (amplitude modulation ratio) points
```

```
levels=3;                          %Number of Marx levels
Vdc=80/levels;                     %Marx voltage level
qt=.5;                             %Quantization trigger level
qi=1;                              %Quantization interval

%%%%%%%%%%%%%%%%%%%%%%%%%%%%%%%%%%%%%%%%%%%%%%%%%%%%%%%%%%%%%%%%%%%%%%%%%%%%%%%%%%%%%%%%%%%
%MOSFET parameters
%%%%%%%%%%%%%%%%%%%%%%%%%%%%%%%%%%%%%%%%%%%%%%%%%%%%%%%%%%%%%%%%%%%%%%%%%%%%%%%%%%%%%%%%%%%
ton=55e-9;                         %Turn on time
toff=36e-9;                        %Turn off time
Qg=55e-9;                          %Gate charge
Vcc=11;                            %Gate voltage
%cp=1050e-12;                      %Effective parasitic MOSFET capacitance at 80.0V
cp=2000e-12;                       %Effective parasitic MOSFET capacitance at 26.6V
fs=100e3;                          %Switching frequency
Cmarx=600e-6;                      %Marx capacitance
Rds=.025;                          %MOSFET on resistance
RESR=.05;                          %Capacitor ESR

%%%%%%%%%%%%%%%%%%%%%%%%%%%%%%%%%%%%%%%%%%%%%%%%%%%%%%%%%%%%%%%%%%%%%%%%%%%%%%%%%%%%%%%%%%%
%Load parameters
%%%%%%%%%%%%%%%%%%%%%%%%%%%%%%%%%%%%%%%%%%%%%%%%%%%%%%%%%%%%%%%%%%%%%%%%%%%%%%%%%%%%%%%%%%%
L=[58e-6 1e-9 1e-9 1e-9]*fs        %Inductances
R=[35.73 1e6 1e6 1e6]              %Resistances
C=[Inf,Inf,Inf,Inf];               %Capacitances

%%%%%%%%%%%%%%%%%%%%%%%%%%%%%%%%%%%%%%%%%%%%%%%%%%%%%%%%%%%%%%%%%%%%%%%%%%%%%%%%%%%%%%%%%%%
%Define Ma and time vectors
%%%%%%%%%%%%%%%%%%%%%%%%%%%%%%%%%%%%%%%%%%%%%%%%%%%%%%%%%%%%%%%%%%%%%%%%%%%%%%%%%%%%%%%%%%%
A=linspace(0,1.0*levels,Mapoints);  %Ma varies from 0 to 1
A1=linspace(.5,.51,10);
A2=linspace(.51,.6,20);
A3=linspace(.6,1.50,20);
A4=[1.50001, 1.5001, 1.501, 1.505];
A5=linspace(1.51,2.40,40);
A6=[2.44,2.45,2.4999, 2.500015,2.505];
A7=linspace(2.51,3,40);
A=[A1,A2,A3,A4,A5,A6,A7];
Mapoints=length(A);                %Number Of Ma (amplitude modulation ratio) points
t=linspace (0,T,Tpoints);          %t varies over one period

%%%%%%%%%%%%%%%%%%%%%%%%%%%%%%%%%%%%%%%%%%%%%%%%%%%%%%%%%%%%%%%%%%%%%%%%%%%%%%%%%%%%%%%%%%%
%Build Matlab system representation of load
%%%%%%%%%%%%%%%%%%%%%%%%%%%%%%%%%%%%%%%%%%%%%%%%%%%%%%%%%%%%%%%%%%%%%%%%%%%%%%%%%%%%%%%%%%%
K12=0;
K13=0;
K14=0;
M12=K12*sqrt(L(1)*L(2));
M13=K13*sqrt(L(1)*L(3));
M14=K14*sqrt(L(1)*L(4));

Rmat=[R(1),0,0,0;0,R(2),0,0;0,0,R(3),0;0,0,0,R(4)];
Lmat=[L(1),M12,M13,M14;M12,L(2),0,0;M13,0,L(3),0;M14,0,0,L(4)];
invCmat=[1/C(1),0,0,0;0,1/C(2),0,0;0,0,1/C(3),0;0,0,0,1/C(4)];
```

```
Aload=[-1*inv(Lmat)*Rmat,inv(Lmat); -1*invCmat, zeros(4)];
Bload=[inv(Lmat), zeros(4); zeros(4), zeros(4)];
Cload=[eye(4) zeros(4)];      %Gives currents through resistance
%Cload=[Rmat zeros(4)];       %Gives voltages across resistance
Dload=[zeros(4) zeros(4)];
sys=ss(Aload,Bload,Cload,Dload);
[Num,Den]=ss2tf(Aload,Bload,Cload,Dload,1);
Poles=roots(Den);
Taus=1./Poles

%%%%%%%%%%%%%%%%%%%%%%%%%%%%%%%%%%%%%%%%%%%%%%%%%%%%%%%%%%%%%%%%%%%%%%%%%%%%%%%%%%%%%%%%%%%%%%
%Define quantizer to simulate Marx inverter
%%%%%%%%%%%%%%%%%%%%%%%%%%%%%%%%%%%%%%%%%%%%%%%%%%%%%%%%%%%%%%%%%%%%%%%%%%%%%%%%%%%%%%%%%%%%%%
%Define reference sinewave voltage
v=A'*sin(2*pi*Fc*t);
%Define quantizer characteristics
partition=[(-levels+(1-qt)):qi:0,qt:qi:(levels-(1-qt))];
codebook=[-levels*Vdc:Vdc:levels*Vdc];
%Initialize variables
B1M=zeros(1,Mapoints);
I=zeros(Tpoints,length(R),Mapoints);
indx=zeros(Tpoints,Mapoints);
Vm=zeros(Mapoints,Tpoints);

%Build Marx pattern
for k=1:length(A);
[indx(:,k),Vm(k,:)]=quantiz(v(k,:),partition,codebook);
indx2(:,k)=(indx(:,k)-levels)>1;
indx3(:,k)=(indx(:,k)-levels)<-1;
indx4(:,k)=(indx(:,k)-levels)>2;
indx5(:,k)=(indx(:,k)-levels)<-2;
step0(:,k)=(indx(:,k)-levels)==0;
step1(:,k)=abs((indx(:,k)-levels))==1;
step2(:,k)=abs((indx(:,k)-levels))==2;
step3(:,k)=abs((indx(:,k)-levels))==3;

%Fundamental Marx amplitude
B1M(k)=2/(T)*trapz(t,Vm(k,:).*sin(2*pi*Fc*t));
%Calculate currents using Marx waveform as input
I(:,:,k)=lsim(sys,[Vm(k,:)',zeros(length(t),7)],t);
%Determine Marx inverter switching instances
m=1;
for n=floor((Tstart/T)*Tpoints+1):Tpoints-1;
if indx(n,k) ~=indx(n+1,k);
Sw(m,k)=n-floor((Tstart/T*Tpoints));
m=m+1;
end
end
end

I1=I(:,1:4:length(A)*4);
I2=I(:,2:4:length(A)*4);
I3=I(:,3:4:length(A)*4);
I4=I(:,4:4:length(A)*4);
```

```
%%%%%%%%%%%%%%%%%%%%%%%%%%%%%%%%%%%%%%%%%%%%%%%%%%%%%%%%%%%%%%%%%%%%%%%%%%%%%%%%%%%%%%%%%%%%%%%%%%%%%
%Redefine time vector to avoid transient (5 time constants later)
%%%%%%%%%%%%%%%%%%%%%%%%%%%%%%%%%%%%%%%%%%%%%%%%%%%%%%%%%%%%%%%%%%%%%%%%%%%%%%%%%%%%%%%%%%%%%%%%%%%%%
nut=floor((Tstart/T)*Tpoints+1):Tpoints;
t=t(nut);
v=v(:,nut);
Vm=Vm(:,nut);
I=I(nut,:);

I1=I1(nut,:);
I2=I2(nut,:);
I3=I3(nut,:);
I4=I4(nut,:);

indx2=indx2(nut,:);
indx3=indx3(nut,:);
indx4=indx4(nut,:);
indx5=indx5(nut,:);

step0=step0(nut,:);
step1=step1(nut,:);
step2=step2(nut,:);
step3=step3(nut,:);

%%%%%%%%%%%%%%%%%%%%%%%%%%%%%%%%%%%%%%%%%%%%%%%%%%%%%%%%%%%%%%%%%%%%%%%%%%%%%%%%%%%%%%%%%%%%%%%%%%%%%
%Calculate the mean-square of the inductor current
%%%%%%%%%%%%%%%%%%%%%%%%%%%%%%%%%%%%%%%%%%%%%%%%%%%%%%%%%%%%%%%%%%%%%%%%%%%%%%%%%%%%%%%%%%%%%%%%%%%%%
%Mean-square of the marx voltage using half of T
VMS=1/(T-Tstart)*trapz(t',Vm.^2');

%Determine DC offset of inductor current
DCoffset1=(max(I1)+min(I1))/2;
DCoffset2=(max(I2)+min(I2))/2;
DCoffset3=(max(I3)+min(I3))/2;
DCoffset4=(max(I4)+min(I4))/2;

%Needed for matrix math in next step
DCoffset1=diag(DCoffset1);
DCoffset2=diag(DCoffset2);
DCoffset3=diag(DCoffset3);
DCoffset4=diag(DCoffset4);

%Remove DC offset from current
I1=I1-ones(length(A),length(t))'*DCoffset1;
I2=I2-ones(length(A),length(t))'*DCoffset2;
I3=I3-ones(length(A),length(t))'*DCoffset3;
I4=I4-ones(length(A),length(t))'*DCoffset4;

%Mean-square of the current
IMS1=1/(T-Tstart)*trapz(t',I1.^2);
IMS2=1/(T-Tstart)*trapz(t',I2.^2);
IMS3=1/(T-Tstart)*trapz(t',I3.^2);
IMS4=1/(T-Tstart)*trapz(t',I4.^2);
```

```
%%%%%%%%%%%%%%%%%%%%%%%%%%%%%%%%%%%%%%%%%%%%%%%%%%%%%%%%%%%%%%%%%%%%%%%%%%%%%%%%%%%%%%%%%%%%%%%%%%
%Calculate losses in converter
%%%%%%%%%%%%%%%%%%%%%%%%%%%%%%%%%%%%%%%%%%%%%%%%%%%%%%%%%%%%%%%%%%%%%%%%%%%%%%%%%%%%%%%%%%%%%%%%%%
for z=1:2
if z==2;
I1=3*I1;
IMS1=9*IMS1;
Vdc=3*Vdc;
cp=1050e-12;
end

%Initialize variables
Psw1=zeros(m-1,Mapoints);
Psw2=zeros(1,Mapoints);
Psw3=zeros(1,Mapoints);
Psw4=zeros(1,Mapoints);
Psw5=zeros(1,Mapoints);

for k=1:Mapoints;
for n=1:m-1;
if Sw(n,k)~=0;
Psw1(n,k)=.5*Vdc*abs(I1(Sw(n,k),k))*(ton+toff)/(T-Tstart);
end
end

if A(k)<0.5
Psw2(k)=0;
Psw3(k)=0;
Psw4(k)=0;

else if A(k)<1.5
Psw2(k)=6*cp*Vdc^2;
Psw3(k)=6*Vcc*Qg;
Psw4(k)=0;
Psw5(k)=1/(T-Tstart)*trapz(t',(I1(:,k).*(step0(:,k)+step1(:,k))).^2)*6*Rds;

else if A(k)< 2.5
Psw2(k)=12*cp*Vdc^2;
Psw3(k)=12*Vcc*Qg;
Psw4(k)=1/(2*Cmarx)*((trapz(t',I1(:,k).*indx2(:,k))/fs).^2+
    (trapz(t',I1(:,k).*indx3(:,k))/fs).^2);
Psw5(k)=1/(T-Tstart)*trapz(t',(I1(:,k).*(step0(:,k)+step1(:,k))).^2)*6*Rds;
Psw5(k)=Psw5(k)+1/(T-Tstart)*trapz(t',(I1(:,k).*(step2(:,k))).^2)*(6*Rds+RESR);

else
Psw2(k)=16*cp*Vdc^2;
Psw3(k)=16*Vcc*Qg;
dv1=1/Cmarx*trapz(t',I1(:,k).*indx2(:,k))/fs;
dv2=1/Cmarx*trapz(t',I1(:,k).*indx3(:,k))/fs;
dv3=1/Cmarx*trapz(t',I1(:,k).*indx4(:,k))/fs;
dv4=1/Cmarx*trapz(t',I1(:,k).*indx5(:,k))/fs;
Psw4(k)=.25*Cmarx*((dv1-dv2).^2+(dv3-dv4).^2+(dv1+dv2).^2+(dv3+dv4).^2);
Psw5(k)=1/(T-Tstart)*trapz(t',(I1(:,k).*(step0(:,k)+step1(:,k))).^2)*6*Rds;
```

```
Psw5(k)=Psw5(k)+1/(T-Tstart)*trapz(t',(I1(:,k).*(step2(:,k))).^2)*(6*Rds+RESR);
Psw5(k)=Psw5(k)+1/(T-Tstart)*trapz(t',(I1(:,k).*(step3(:,k))).^2)*(6*Rds+2*RESR);

end
end
end
end
Psw6=2.563;                                %Quiescent power for logic board

PonoffM=sum(Psw1*fs);
PcpM=Psw2*fs;
PgateM=Psw3*fs+Psw6;
PcapeqM=Psw4*fs;
PcondM=Psw5;
PlogicM=Psw6;

Psw(z,:)=(sum(Psw1)+Psw2+Psw3+Psw4)*fs+Psw5+Psw6;

%%%%%%%%%%%%%%%%%%%%%%%%%%%%%%%%%%%%%%%%%%%%%%%%%%%%%%%%%%%%%%%%%%%%%%%%%%%%%%%%%%%%%%%%%%%%
%Determine power in each load and calculate efficiency
%%%%%%%%%%%%%%%%%%%%%%%%%%%%%%%%%%%%%%%%%%%%%%%%%%%%%%%%%%%%%%%%%%%%%%%%%%%%%%%%%%%%%%%%%%%%
Pload1(z,:)=IMS1*R(1);
Pload2(z,:)=IMS2*R(2);
Pload3(z,:)=IMS3*R(3);
Pload4(z,:)=IMS4*R(4);
Pload(z,:)=Pload1(z,:)+Pload2(z,:)+Pload3(z,:)+Pload4(z,:);

EffM(z,:)=Pload(z,:)./(Pload(z,:)+Psw(z,:));
end

Im=I1';

%%%%%%%%%%%%%%%%%%%%%%%%%%%%%%%%%%%%%%%%%%%%%%%%%%%%%%%%%%%%%%%%%%%%%%%%%%%%%%%%%%%%%%%%%%%%
%Initialize parameters
%%%%%%%%%%%%%%%%%%%%%%%%%%%%%%%%%%%%%%%%%%%%%%%%%%%%%%%%%%%%%%%%%%%%%%%%%%%%%%%%%%%%%%%%%%%%
Mf=[3];                                    %PWM frequency modulation ratios
Fs=Mf*Fc;                                  %PWM sampling frequency (Hz)
Mapoints=50;                               %Number Of Ma (Amplitude Modulation Ratio) points
Vdc=80;                                    %PWM voltage level
cp=1050e-12;                               %Effective parasitic MOSFET capacitance at 80.0V

for z=1:length(Mf);

%%%%%%%%%%%%%%%%%%%%%%%%%%%%%%%%%%%%%%%%%%%%%%%%%%%%%%%%%%%%%%%%%%%%%%%%%%%%%%%%%%%%%%%%%%%%
%Define Ma and time vectors
%%%%%%%%%%%%%%%%%%%%%%%%%%%%%%%%%%%%%%%%%%%%%%%%%%%%%%%%%%%%%%%%%%%%%%%%%%%%%%%%%%%%%%%%%%%%
A=linspace(0,1,Mapoints);                     %Ma varies from 0 to 1
t=linspace (0,T,Tpoints);                     %t varies over one period

%%%%%%%%%%%%%%%%%%%%%%%%%%%%%%%%%%%%%%%%%%%%%%%%%%%%%%%%%%%%%%%%%%%%%%%%%%%%%%%%%%%%%%%%%%%%
%Define reference sine voltages-- one for each phase leg
%%%%%%%%%%%%%%%%%%%%%%%%%%%%%%%%%%%%%%%%%%%%%%%%%%%%%%%%%%%%%%%%%%%%%%%%%%%%%%%%%%%%%%%%%%%%
Va=A'*sin(2*pi*Fc*t);                         %Phase leg A
Vb=-Va;                                       %Phase leg B
```

```
%%%%%%%%%%%%%%%%%%%%%%%%%%%%%%%%%%%%%%%%%%%%%%%%%%%%%%%%%%%%%%%%%%%%%%%%%%%%%%%%%%%%%%%%%%%%
%Generate triangle waveform for sampling
%%%%%%%%%%%%%%%%%%%%%%%%%%%%%%%%%%%%%%%%%%%%%%%%%%%%%%%%%%%%%%%%%%%%%%%%%%%%%%%%%%%%%%%%%%%%
%phi=pi/2;                                    %Phase of triangle waveform
phi=0;                                        %Phase of triangle waveform; Use this one
tri=sawtooth(2*pi*Fs(z)*t+phi, 0.5);          %Triangle waveform

%%%%%%%%%%%%%%%%%%%%%%%%%%%%%%%%%%%%%%%%%%%%%%%%%%%%%%%%%%%%%%%%%%%%%%%%%%%%%%%%%%%%%%%%%%%%
%Generate unipolar natural sampling PWM waveform
%%%%%%%%%%%%%%%%%%%%%%%%%%%%%%%%%%%%%%%%%%%%%%%%%%%%%%%%%%%%%%%%%%%%%%%%%%%%%%%%%%%%%%%%%%%%
PWMa=zeros(length(A),length(t));              %Initialize matrix
PWMb=zeros(length(A),length(t));              %Initialize matrix

tri=ones(length(A),1)*tri;                    %Create matrix of triangle waveforms

PWMa=sign(Va-tri);                            %Compare reference A with triangle waveform
PWMa=.5*Vdc*(PWMa+ones(length(A),length(t))); %Generate PWMa Matrix
PWMb=sign(Vb-tri);                            %Compare reference B with triangle waveform
PWMb=.5*Vdc*(PWMb+ones(length(A),length(t))); %Generate PWMb matrix
PWM=(PWMa-PWMb)';                             %Difference is PWM waveform across L

%%%%%%%%%%%%%%%%%%%%%%%%%%%%%%%%%%%%%%%%%%%%%%%%%%%%%%%%%%%%%%%%%%%%%%%%%%%%%%%%%%%%%%%%%%%%
%Determine response of system to PWM input and determine switching instances
%%%%%%%%%%%%%%%%%%%%%%%%%%%%%%%%%%%%%%%%%%%%%%%%%%%%%%%%%%%%%%%%%%%%%%%%%%%%%%%%%%%%%%%%%%%%
%Initialize variables
B1P=zeros(1,Mapoints);
I=zeros(Tpoints,length(R),Mapoints);
%Find PWM fundamental, and resulting current waveforms for PWM input
for k=1:length(A)
B1P(k)=2/(T)*trapz(t,PWM(:,k)'.*sin(2*pi*Fc*t));
I(:,:,k)=lsim(sys,[PWM(:,k),zeros(length(t),7)],t);
%Determine PWM switching instances
m=1;
for n=floor((Tstart/T)*Tpoints+1):Tpoints-1;
if PWM(n,k) ~=PWM(n+1,k)
Sw(m,k)=n-floor((Tstart/T*Tpoints));
m=m+1;
end
end
end

I1=I(:,1:4:length(A)*4);
I2=I(:,2:4:length(A)*4);
I3=I(:,3:4:length(A)*4);
I4=I(:,4:4:length(A)*4);

%%%%%%%%%%%%%%%%%%%%%%%%%%%%%%%%%%%%%%%%%%%%%%%%%%%%%%%%%%%%%%%%%%%%%%%%%%%%%%%%%%%%%%%%%%%%
%Redefine time vector to avoid transient (5 time constants later)
%%%%%%%%%%%%%%%%%%%%%%%%%%%%%%%%%%%%%%%%%%%%%%%%%%%%%%%%%%%%%%%%%%%%%%%%%%%%%%%%%%%%%%%%%%%%
nut=floor((Tstart/T)*Tpoints+1):Tpoints;
t=t(nut);
Va=Va(:,nut);
PWM=PWM(nut,:);
```

```
I=I(nut,:);
tri=tri(:,nut);

I1=I1(nut,:);
I2=I2(nut,:);
I3=I3(nut,:);
I4=I4(nut,:);

%%%%%%%%%%%%%%%%%%%%%%%%%%%%%%%%%%%%%%%%%%%%%%%%%%%%%%%%%%%%%%%%%%%%%%%%%%%%%%%%%
%Calculate the mean-square of the inductor current
%%%%%%%%%%%%%%%%%%%%%%%%%%%%%%%%%%%%%%%%%%%%%%%%%%%%%%%%%%%%%%%%%%%%%%%%%%%%%%%%%
%Mean-square of the PWM voltage using half of T
VMS=2/T*trapz(t',PWM.^2);

%Determine DC offset of inductor current
DCoffset1=(max(I1)+min(I1))/2;
DCoffset2=(max(I2)+min(I2))/2;
DCoffset3=(max(I3)+min(I3))/2;
DCoffset4=(max(I4)+min(I4))/2;

%Needed for matrix math in next step
DCoffset1=diag(DCoffset1);
DCoffset2=diag(DCoffset2);
DCoffset3=diag(DCoffset3);
DCoffset4=diag(DCoffset4);

%Remove DC offset from current
I1=I1-ones(length(A),length(t))'*DCoffset1;
I2=I2-ones(length(A),length(t))'*DCoffset2;
I3=I3-ones(length(A),length(t))'*DCoffset3;
I4=I4-ones(length(A),length(t))'*DCoffset4;

%Mean-square of the current
IMS1=1/(T-Tstart)*trapz(t',I1.^2);
IMS2=1/(T-Tstart)*trapz(t',I2.^2);
IMS3=1/(T-Tstart)*trapz(t',I3.^2);
IMS4=1/(T-Tstart)*trapz(t',I4.^2);

%%%%%%%%%%%%%%%%%%%%%%%%%%%%%%%%%%%%%%%%%%%%%%%%%%%%%%%%%%%%%%%%%%%%%%%%%%%%%%%%%
%Calculate losses in converter
%%%%%%%%%%%%%%%%%%%%%%%%%%%%%%%%%%%%%%%%%%%%%%%%%%%%%%%%%%%%%%%%%%%%%%%%%%%%%%%%%
%Initialize variables
Psw1=zeros(m-1,Mapoints);
Psw2=zeros(1,Mapoints);
Psw3=zeros(1,Mapoints);
Psw4=zeros(1,Mapoints);

for k=1:Mapoints;
for n=1:m-1;
if Sw(n,k)~=0;
Psw1(n,k)=.5*Vdc*abs(I1(Sw(n,k),k))*(ton+toff);
end
Psw2(k)=4*cp*Vdc^2*Mf(z);
Psw3(k)=4*Vcc*Qg*Mf(z);
```

```
end
end
Psw4=IMS1*(2*Rds);
Psw5=.766;                                  %Quiescent logic power
PonoffP=sum(Psw1*fs);
PcpP=Psw2*fs;
PgateP=Psw3*fs+Psw5;
PcondP=Psw4;

Psw=(sum(Psw1)+Psw2+Psw3)*fs+Psw4;

%%%%%%%%%%%%%%%%%%%%%%%%%%%%%%%%%%%%%%%%%%%%%%%%%%%%%%%%%%%%%%%%%%%%%%%%%%%%%%%%%%%%%%%%%%
%Determine power in each load and calculate efficiency
%%%%%%%%%%%%%%%%%%%%%%%%%%%%%%%%%%%%%%%%%%%%%%%%%%%%%%%%%%%%%%%%%%%%%%%%%%%%%%%%%%%%%%%%%%
Pload1=IMS1*R(1);
Pload2=IMS2*R(2);
Pload3=IMS3*R(3);
Pload4=IMS4*R(4);
Pload=Pload1+Pload2+Pload3+Pload4;

EffP(z,:)=Pload./(Pload+Psw);
end

%%%%%%%%%%%%%%%%%%%%%%%%%%%%%%%%%%%%%%%%%%%%%%%%%%%%%%%%%%%%%%%%%%%%%%%%%%%%%%%%%%%%%%%%%%
%Measured efficiencies
%%%%%%%%%%%%%%%%%%%%%%%%%%%%%%%%%%%%%%%%%%%%%%%%%%%%%%%%%%%%%%%%%%%%%%%%%%%%%%%%%%%%%%%%%%
Vdc1=[20 40 60 80]/80;
MarxP1=[2.82 10.67 23.27 42.1];
PWMP1=[3.47 11.62 23.79 42.18];
Marx1=[48.2 72.5 85.9 90.1];
PWM1=[31.7 62.8 75.9 84.7];

Vdc2=[60 120 180 240]/240;
Marx2=[85.1 92.5 98.3 97.3];

%%%%%%%%%%%%%%%%%%%%%%%%%%%%%%%%%%%%%%%%%%%%%%%%%%%%%%%%%%%%%%%%%%%%%%%%%%%%%%%%%%%%%%%%%%
%Plot efficiency
%%%%%%%%%%%%%%%%%%%%%%%%%%%%%%%%%%%%%%%%%%%%%%%%%%%%%%%%%%%%%%%%%%%%%%%%%%%%%%%%%%%%%%%%%%
figure(1)
plot(B1M/(Vdc),100*EffM(2,:),'b-',B1M/(Vdc),100*EffM(1,:),'r--',
    A,100*EffP(1,:),'g+-',Vdc2,Marx2,'bo',Vdc1,Marx1,'rs',Vdc1,PWM1,'gd')
grid on
title('% Efficiency vs Normalized Fundamental Voltage
    (F_{s}=100kHz, Z_{load}=50 \angle 45^o)')
ylabel('% Efficiency')
xlabel('Fundamental Voltage Normalized to 3Vdc')
legend('Estimated: Marx, 3Vdc=240V','Estimated: Marx, 3Vdc=80V',
    'Estimated: Full-Bridge, 3Vdc=80V, Mf=3','Measured: Marx, 3Vdc=240V',
    'Measured: Marx, 3Vdc=80V','Measured: Full-Bridge, 3Vdc=80V, Mf=3',4)
axis([0,1,0,100])
```

B.3.6 Gelcontainer.m

```
%Gelcontainer.m
%This script calculates the inertias of a 3 gel-chamber vibration absorber given the
%dimensions of the gel chambers.

clear
%%%%%%%%%%%%%%%%%%%%%%%%%%%%%%%%%%%%%%%%%%%%%%%%%%%%%%%%%%%%%%%%%%%%%%%%%%%%%%%%%%%%%%%%%%%%
%Gel container dimensions (in cm's) and material densities
%%%%%%%%%%%%%%%%%%%%%%%%%%%%%%%%%%%%%%%%%%%%%%%%%%%%%%%%%%%%%%%%%%%%%%%%%%%%%%%%%%%%%%%%%%%%
%Inner radius
r1=1.5875;
%Outer radius of chamber 1
r2=3*r1;
%Outer radius of chamber 2
r3=((r2^4+r1^4)/2)^.25;
%Outer radius of chamber 3
r4=((r3^4+r1^4)/2)^.25;
%Height of chamber
h=2.54;
%Thickness of chamber wall
t=.254;
%length of container
l=12.7;
%Thickness of hollow post wall
w=t;

%Density of plastic
rho_HDPE=.955;
%density of water
rho_h20=1;

%%%%%%%%%%%%%%%%%%%%%%%%%%%%%%%%%%%%%%%%%%%%%%%%%%%%%%%%%%%%%%%%%%%%%%%%%%%%%%%%%%%%%%%%%%%%
%Calculate inertias
%%%%%%%%%%%%%%%%%%%%%%%%%%%%%%%%%%%%%%%%%%%%%%%%%%%%%%%%%%%%%%%%%%%%%%%%%%%%%%%%%%%%%%%%%%%%
%Chamber a (1) inertia
Ja=rho_HDPE*pi*h/2*((r2+t)^4-r2^4)+rho_HDPE*pi*t*(r2^4-r1^4);
%Chamber b (2) inertia
Jb=rho_HDPE*pi*h/2*((r3+t)^4-r3^4)+rho_HDPE*pi*t*(r3^4-r1^4);
%Chamber c (3) inertia
Jc=rho_HDPE*pi*h/2*((r4+t)^4-r4^4)+rho_HDPE*pi*t*(r4^4-r1^4);
%Hollow post inertia
Jaxis=rho_HDPE*l*pi/2*((r1^4-(r1-w)^4));
%Total inertia of container
J0=Ja+Jb+Jc+Jaxis;
%Gel 1 inertia
J1=rho_h20*pi*h/2*(r2^4-r1^4);
%Gel 2 inertia
J2=rho_h20*pi*h/2*(r3^4-r1^4);
%Gel 3 inertia
J3=rho_h20*pi*h/2*(r4^4-r1^4);

%%%%%%%%%%%%%%%%%%%%%%%%%%%%%%%%%%%%%%%%%%%%%%%%%%%%%%%%%%%%%%%%%%%%%%%%%%%%%%%%%%%%%%%%%%%%
%Calculate masses
%%%%%%%%%%%%%%%%%%%%%%%%%%%%%%%%%%%%%%%%%%%%%%%%%%%%%%%%%%%%%%%%%%%%%%%%%%%%%%%%%%%%%%%%%%%%
%Chamber a (1) mass
```

```
Ma=rho_HDPE*pi*h*((r2+t)^2-r2^2)+2*rho_HDPE*pi*t*(r2^2-r1^2);
%Chamber b (2) mass
Mb=rho_HDPE*pi*h*((r3+t)^2-r3^2)+2*rho_HDPE*pi*t*(r3^2-r1^2);
%Chamber c (3) mass
Mc=rho_HDPE*pi*h*((r4+t)^2-r4^2)+2*rho_HDPE*pi*t*(r4^2-r1^2);
%Hollow post mass
Maxis=rho_HDPE*l*pi*((r1^2-(r1-w)^2));
%Total mass of container
M0=Ma+Mb+Mc+Maxis;
%Gel 1 inertia
M1=rho_h20*pi*h*(r2^2-r1^2);
%Gel 2 inertia
M2=rho_h20*pi*h*(r3^2-r1^2);
%Gel 3 inertia
M3=rho_h20*pi*h*(r4^2-r1^2);
%Total mass of container and gel
Mtotal=M0+M1+M2+M3;

%%%%%%%%%%%%%%%%%%%%%%%%%%%%%%%%%%%%%%%%%%%%%%%%%%%%%%%%%%%%%%%%%%%%%%%%%%%%%%%%%%%%%%%%%%%%%%
%Verify ratios to insure container mass/inertia is small compared to gel mass/inertia
%%%%%%%%%%%%%%%%%%%%%%%%%%%%%%%%%%%%%%%%%%%%%%%%%%%%%%%%%%%%%%%%%%%%%%%%%%%%%%%%%%%%%%%%%%%%%%
ratioM=M2/M1
ratioJ=J0/J1

%%%%%%%%%%%%%%%%%%%%%%%%%%%%%%%%%%%%%%%%%%%%%%%%%%%%%%%%%%%%%%%%%%%%%%%%%%%%%%%%%%%%%%%%%%%%%%
%Simulate the nominal frequency response of a torsional gel-damper using this container
%%%%%%%%%%%%%%%%%%%%%%%%%%%%%%%%%%%%%%%%%%%%%%%%%%%%%%%%%%%%%%%%%%%%%%%%%%%%%%%%%%%%%%%%%%%%%%
JATDVA([J0, J1, J2, J3]);
```

B.3.7 hdrload.m

```
function [header, data] = hdrload(file)

    % HDRLOAD Load data from an ASCII file containing a text header.
    %     [header, data] = HDRLOAD('filename.ext') reads a data file
    %     called 'filename.ext', which contains a text header.  There
    %     is no default extension; any extensions must be explicitly
    %     supplied.
    %
    %     The first output, HEADER, is the header information, returned
    %     as a text array.
    %     The second output, DATA, is the data matrix.  This data matrix
    %     has the same dimensions as the data in the file, one row per
    %     line of ASCII data in the file.  If the data is not regularly
    %     spaced (i.e., each line of ASCII data does not contain the
    %     same number of points), the data is returned as a column
    %     vector.
    %
    %     Limitations:  No line of the text header can begin with
    %     a number.  Only one header and data set will be read,
    %     and the header must come before the data.
```

```
%
%     See also LOAD, SAVE, SPCONVERT, FSCANF, FPRINTF, STR2MAT.
%     See also the IOFUN directory.

% check number and type of arguments
if nargin < 1
  error('Function requires one input argument');
elseif ~isstr(file)
  error('Input argument must be a string representing a filename');
end

% Open the file.  If this returns a -1, we did not open the file
% successfully.
fid = fopen(file);
if fid==-1
  error('File not found or permission denied');
  end

% Initialize loop variables
% We store the number of lines in the header, and the maximum length
% of any one line in the header.  These are used later in assigning
% the 'header' output variable.
no_lines = 0;
max_line = 0;

% We also store the number of columns in the data we read.  This way
% we can compute the size of the output based on the number of
% columns and the total number of data points.
ncols = 0;

% Finally, we initialize the data to [].
data = [];

% Start processing.
line = fgetl(fid);
if ~isstr(line)
  disp('Warning: file contains no header and no data')
  end;
[data, ncols, errmsg, nxtindex] = sscanf(line, '%f');

% One slight problem, pointed out by Peter vanderWal: If the first
% character of the line is 'e', then this will scan as 0.00e+00.
% We can trap this case specifically by using the 'next index'
% output: in the case of a stripped 'e' the next index is one,
% indicating zero characters read.  See the help entry for 'sscanf'
% for more information on this output parameter.
% We loop through the file one line at a time until we find some
% data.  After that point we stop checking for header information.
% This part of the program takes most of the processing time, because
% fgetl is relatively slow (compared to fscanf, which we will use
% later).
while isempty(data)|(nxtindex==1)
  no_lines = no_lines+1;
  max_line = max([max_line, length(line)]);
```

```
  % Create unique variable to hold this line of text information.
  % Store the last-read line in this variable.
  eval(['line', num2str(no_lines), '=line;']);
  line = fgetl(fid);
  if ~isstr(line)
    disp('Warning: file contains no data')
    break
    end;
  [data, ncols, errmsg, nxtindex] = sscanf(line, '%f');
  end % while

% Now that we have read in the first line of data, we can skip the
% processing that stores header information, and just read in the
% rest of the data.
data = [data; fscanf(fid, '%f')];
fclose(fid);

% Create header output from line information. The number of lines and
% the maximum line length are stored explicitly, and each line is
% stored in a unique variable using the 'eval' statement within the
% loop. Note that, if we knew a priori that the headers were 10 lines
% or less, we could use the STR2MAT function and save some work.
% First, initialize the header to an array of spaces.
header = setstr(' '*ones(no_lines, max_line));
for i = 1:no_lines
  varname = ['line' num2str(i)];
  % Note that we only assign this line variable to a subset of this
  % row of the header array.  We thus ensure that the matrix sizes in
  % the assignment are equal.

  %I commented out the next line because it was causing problems.
  %eval(['header(i, 1:length(' varname ')) = ' varname ';']);
  end

% Resize output data, based on the number of columns (as returned
% from the sscanf of the first line of data) and the total number of
% data elements. Since the data was read in row-wise, and MATLAB
% stores data in columnwise format, we have to reverse the size
% arguments and then transpose the data.  If we read in irregularly
% spaced data, then the division we are about to do will not work.
% Therefore, we will trap the error with an EVAL call; if the reshape
% fails, we will just return the data as is.
eval('data = reshape(data, ncols, length(data)/ncols)'';', '');

% And we're done!
```

B.3.8 JATDVA.m

```
%JATDVA
%This function generates the frequency response of a hypothetical 3 gel-chamber torsional
%adaptive vibration absorber given the 4 possible inertia's
```

```
function ans = JATDVA(J)
%%%%%%%%%%%%%%%%%%%%%%%%%%%%%%%%%%%%%%%%%%%%%%%%%%%%%%%%%%%%%%%%%%%%%%%%%%%%%%%%%%%%%%%%%%%
%System Parameters
%%%%%%%%%%%%%%%%%%%%%%%%%%%%%%%%%%%%%%%%%%%%%%%%%%%%%%%%%%%%%%%%%%%%%%%%%%%%%%%%%%%%%%%%%%%
%Damper inertias
J0=J(1);
J1=J(2);
J2=J(3);
J3=J(4);

m1=10*(J0+J2);                             %Primary mass (inertia)
k1=m1;                                     %Primary compliance
c1=.1*sqrt(m1*k1);                         %Primary damping constant
m2=J0+J1+J2+J3;                            %Highest possible secondary mass (inertia)
k2=.1*k1;                                  %Secondary compliance
c2=.05*sqrt(m2*k2);                        %Secondary damping constant
DC=k1;                                     %DC gain
s=tf('s');                                  %Complex frequency s

%%%%%%%%%%%%%%%%%%%%%%%%%%%%%%%%%%%%%%%%%%%%%%%%%%%%%%%%%%%%%%%%%%%%%%%%%%%%%%%%%%%%%%%%%%%
%Transfer function without DVA
%%%%%%%%%%%%%%%%%%%%%%%%%%%%%%%%%%%%%%%%%%%%%%%%%%%%%%%%%%%%%%%%%%%%%%%%%%%%%%%%%%%%%%%%%%%
H0=DC/[m1*s^2+c1*s+k1];

%%%%%%%%%%%%%%%%%%%%%%%%%%%%%%%%%%%%%%%%%%%%%%%%%%%%%%%%%%%%%%%%%%%%%%%%%%%%%%%%%%%%%%%%%%%
%Transfer functions with DVA
%%%%%%%%%%%%%%%%%%%%%%%%%%%%%%%%%%%%%%%%%%%%%%%%%%%%%%%%%%%%%%%%%%%%%%%%%%%%%%%%%%%%%%%%%%%
m2=J0+J1+J2+J3;                            %Secondary mass (inertia) 1
H1=DC*[m2*s^2+c2*s+k2]/[[m1*s^2+(c1+c2)*s+(k1+k2)]*[m2*s^2+c2*s+k2]-[c2*s+k2]^2];

m2=J0+J2+J3;                               %Secondary mass (inertia) 2
H2=DC*[m2*s^2+c2*s+k2]/[[m1*s^2+(c1+c2)*s+(k1+k2)]*[m2*s^2+c2*s+k2]-[c2*s+k2]^2];

m2=J0+J1+J3;                               %Secondary mass (inertia) 3
H3=DC*[m2*s^2+c2*s+k2]/[[m1*s^2+(c1+c2)*s+(k1+k2)]*[m2*s^2+c2*s+k2]-[c2*s+k2]^2];

m2=J0+J3;                                  %Secondary mass (inertia) 4
H4=DC*[m2*s^2+c2*s+k2]/[[m1*s^2+(c1+c2)*s+(k1+k2)]*[m2*s^2+c2*s+k2]-[c2*s+k2]^2];

m2=J0+J1+J2;                               %Secondary mass (inertia) 5
H5=DC*[m2*s^2+c2*s+k2]/[[m1*s^2+(c1+c2)*s+(k1+k2)]*[m2*s^2+c2*s+k2]-[c2*s+k2]^2];

m2=J0+J2;                                  %Secondary mass (inertia) 6
H6=DC*[m2*s^2+c2*s+k2]/[[m1*s^2+(c1+c2)*s+(k1+k2)]*[m2*s^2+c2*s+k2]-[c2*s+k2]^2];

m2=J0+J1;                                  %Secondary mass (inertia) 7
H7=DC*[m2*s^2+c2*s+k2]/[[m1*s^2+(c1+c2)*s+(k1+k2)]*[m2*s^2+c2*s+k2]-[c2*s+k2]^2];

m2=J0;                                     %Secondary mass (inertia) 8
H8=DC*[m2*s^2+c2*s+k2]/[[m1*s^2+(c1+c2)*s+(k1+k2)]*[m2*s^2+c2*s+k2]-[c2*s+k2]^2];

%%%%%%%%%%%%%%%%%%%%%%%%%%%%%%%%%%%%%%%%%%%%%%%%%%%%%%%%%%%%%%%%%%%%%%%%%%%%%%%%%%%%%%%%%%%
%Determine frequency response
```

```
%%%%%%%%%%%%%%%%%%%%%%%%%%%%%%%%%%%%%%%%%%%%%%%%%%%%%%%%%%%%%%%%%%%%%%%%%%%%%%%%%%%%%%%%%%%%
%Frequency vector in rps
w=logspace(-1,1,10000);

%Bode response
[mag0,phase0]=bode(H0,w);
[mag1,phase1]=bode(H1,w);
[mag2,phase2]=bode(H2,w);
[mag3,phase3]=bode(H3,w);
[mag4,phase4]=bode(H4,w);
[mag5,phase5]=bode(H5,w);
[mag6,phase6]=bode(H6,w);
[mag7,phase7]=bode(H7,w);
[mag8,phase8]=bode(H8,w);

%Construct a magnitude matrix
Mag=[mag0(:), mag1(:), mag2(:), mag3(:), mag4(:), mag5(:), mag6(:), mag7(:), mag8(:)];

%Determine minimum frequency response using all possible states
MyMag=min(Mag');

%%%%%%%%%%%%%%%%%%%%%%%%%%%%%%%%%%%%%%%%%%%%%%%%%%%%%%%%%%%%%%%%%%%%%%%%%%%%%%%%%%%%%%%%%%%%
%Plot results
%%%%%%%%%%%%%%%%%%%%%%%%%%%%%%%%%%%%%%%%%%%%%%%%%%%%%%%%%%%%%%%%%%%%%%%%%%%%%%%%%%%%%%%%%%%%
figure(1)
semilogx(w,20*log10(mag0(:)),'--',w,20*log10(MyMag),'-')
title('Magnitude of Angular Displacement versus Frequency')
ylabel('Magnitude(dB) / DC Gain')
xlabel('Frequency (rads/sec) / \omega_{n}')
legend('Without GEL DVA','With Minimum Response of all GEL states')
grid on
```

B.3.9 Prototype.m

```
%Prototype.m
%This script plots the measured acceleration for an experimental geldamper prototype.
%The damper uses two gel chambers and is capable of 4 distinct anti-resonant frequencies

clear
%%%%%%%%%%%%%%%%%%%%%%%%%%%%%%%%%%%%%%%%%%%%%%%%%%%%%%%%%%%%%%%%%%%%%%%%%%%%%%%%%%%%%%%%%%%%
%Read network analyzer data files
%%%%%%%%%%%%%%%%%%%%%%%%%%%%%%%%%%%%%%%%%%%%%%%%%%%%%%%%%%%%%%%%%%%%%%%%%%%%%%%%%%%%%%%%%%%%
%RMS voltage input
Vinrms=.707;
%Calculate voltage amplitude
Vinamp=Vinrms*sqrt(2);

[header1, data1] =hdrload('da0.txt');
F1=data1(:,1);
Mag1=10.^(data1(:,2)/20);
%Acceration in g's
```

```
Acc1=Vinamp*Mag1/300e-3;
%Displacement
%Disp1=Acc1./(F1*2*pi).^2*9.8;

[header1, data2] =hdrload('da1.txt');
F2=data2(:,1);
Mag2=10.^(data2(:,2)/20);
%Acceleration in g's
Acc2=Vinamp*Mag2/300e-3;
%Displacement
%Disp2=Acc2./(F1*2*pi).^2*9.8;

[header1, data3] =hdrload('da2.txt');
F3=data3(:,1);
Mag3=10.^(data3(:,2)/20);
%Acceleration in g's
Acc3=Vinamp*Mag3/300e-3;
%Displacement
%Disp3=Acc3./(F1*2*pi).^2*9.8;

[header1, data4] =hdrload('da3.txt');
F4=data4(:,1);
Mag4=10.^(data4(:,2)/20);
%Acceleration in g's
Acc4=Vinamp*Mag4/300e-3;
%Displacement
%Disp4=Acc4./(F1*2*pi).^2*9.8;

%%%%%%%%%%%%%%%%%%%%%%%%%%%%%%%%%%%%%%%%%%%%%%%%%%%%%%%%%%%%%%%%%%%%%%%%%%%%%%%%
%Scale acceleration and displacement
%%%%%%%%%%%%%%%%%%%%%%%%%%%%%%%%%%%%%%%%%%%%%%%%%%%%%%%%%%%%%%%%%%%%%%%%%%%%%%%%
%Acceleration in mg's
Acc1m=Acc1*1000;
Acc2m=Acc2*1000;
Acc3m=Acc3*1000;
Acc4m=Acc4*1000;

%Disp1m=Disp1*1000;
%Disp2m=Disp2*1000;
%Disp3m=Disp3*1000;
%Disp4m=Disp4*1000;

%Downsample data points for plotting symbols
x=length(F1);
for i=0:10
F(i+1)=F1(floor(x/10)*i+1);
Acc1ds(i+1)=Acc1m(floor(x/10)*i+1);
Acc2ds(i+1)=Acc2m(floor(x/10)*i+1);
Acc3ds(i+1)=Acc3m(floor(x/10)*i+1);
Acc4ds(i+1)=Acc4m(floor(x/10)*i+1);
end

%%%%%%%%%%%%%%%%%%%%%%%%%%%%%%%%%%%%%%%%%%%%%%%%%%%%%%%%%%%%%%%%%%%%%%%%%%%%%%%%
%Plot results
```

```
%%%%%%%%%%%%%%%%%%%%%%%%%%%%%%%%%%%%%%%%%%%%%%%%%%%%%%%%%%%%%%%%%%%%%%%%%%%%%%%%%%%%%%%%
figure(1)
semilogy(F,Acc1ds,'s',F,Acc2ds,'d',F,Acc3ds,'o',F,Acc4ds,'v');
axis([10, 16,1,1000])
grid on
title('Servomechanism Acceleration with Multiple Gel Chamber Vibration Damper')
xlabel('Frequency (Hz)')
ylabel('Acceleration (mg)')
legend('No Gel Chambers Active','1st Gel Chamber Active','2nd Gel Chamber Active',
    '1st and 2nd Gel Chambers Active',4)
hold on
semilogy(F1,Acc1m,'-',F2,Acc2m,'-',F3,Acc3m,'-',F4,Acc4m,'-');
hold off
```

B.3.10 RelativePower.m

```
%RelativePower.m
%This script can calculate the normalized relative power delivered to multiple induction
%loads for a Marx and PWM waveforms as a function of synthesized fundamental amplitude.

clear
%%%%%%%%%%%%%%%%%%%%%%%%%%%%%%%%%%%%%%%%%%%%%%%%%%%%%%%%%%%%%%%%%%%%%%%%%%%%%%%%%%%%%%%%
%Initialize parameters
%%%%%%%%%%%%%%%%%%%%%%%%%%%%%%%%%%%%%%%%%%%%%%%%%%%%%%%%%%%%%%%%%%%%%%%%%%%%%%%%%%%%%%%%
Fc=5;                               %Carrier frequency (Hz)
Tstart=1;                           %Time offset, pick to be greater than 5 time constants
T=1/Fc+Tstart;                      %Carrier period (Secs)
Mapoints=10;                        %Number Of Ma (amplitude modulation ratio) points
Tpoints=2000;                       %Number of sample points in period T
levels=3;                           %Number of Marx levels
Vdc=1/levels;                       %Marx voltage level
qt=.5;                              %Quantization trigger level
qi=1;                               %Quantization interval


L=[1 1e-3 1e-3 1e-3]/(2*pi);        %Inductances
R=[0 .001 .005 .025];               %Resistances
C=[Inf,Inf,Inf,Inf];                %Capacitances

%%%%%%%%%%%%%%%%%%%%%%%%%%%%%%%%%%%%%%%%%%%%%%%%%%%%%%%%%%%%%%%%%%%%%%%%%%%%%%%%%%%%%%%%
%Define Ma and time vectors
%%%%%%%%%%%%%%%%%%%%%%%%%%%%%%%%%%%%%%%%%%%%%%%%%%%%%%%%%%%%%%%%%%%%%%%%%%%%%%%%%%%%%%%%
A=linspace(0,1.0*levels,Mapoints);  %Ma varies from 0 to 1
A1=linspace(0,1.5,40);
A2=linspace(1.5,1.52,40);
A3=linspace(1.52,2.5,40);
A4=linspace(2.5,2.54,40);
A5=linspace(2.54,3,40);
A=[A1,A2,A3,A4,A5];
t=linspace (0,T,Tpoints);           %t varies over one period
```

```
%%%%%%%%%%%%%%%%%%%%%%%%%%%%%%%%%%%%%%%%%%%%%%%%%%%%%%%%%%%%%%%%%%%%%%%%%%%%%%%%%%%%%%%%%%%%
%Build Matlab system representation of load
%%%%%%%%%%%%%%%%%%%%%%%%%%%%%%%%%%%%%%%%%%%%%%%%%%%%%%%%%%%%%%%%%%%%%%%%%%%%%%%%%%%%%%%%%%%%
K12=.3;
K13=.3;
K14=.3;
M12=K12*sqrt(L(1)*L(2));
M13=K13*sqrt(L(1)*L(3));
M14=K14*sqrt(L(1)*L(4));

Rmat=[R(1),0,0,0;0,R(2),0,0;0,0,R(3),0;0,0,0,R(4)];
Lmat=[L(1),M12,M13,M14;M12,L(2),0,0;M13,0,L(3),0;M14,0,0,L(4)];
invCmat=[1/C(1),0,0,0;0,1/C(2),0,0;0,0,1/C(3),0;0,0,0,1/C(4)];
Aload=[-1*inv(Lmat)*Rmat,inv(Lmat); -1*invCmat, zeros(4)];
Bload=[inv(Lmat), zeros(4); zeros(4), zeros(4)];
Cload=[eye(4) zeros(4)];  %Gives currents through resistance
%Cload=[Rmat zeros(4)];  %Gives voltages across resistance
Dload=[zeros(4) zeros(4)];
sys=ss(Aload,Bload,Cload,Dload);
[Num,Den]=ss2tf(Aload,Bload,Cload,Dload,1);
Poles=roots(Den);
Taus=1./Poles

%%%%%%%%%%%%%%%%%%%%%%%%%%%%%%%%%%%%%%%%%%%%%%%%%%%%%%%%%%%%%%%%%%%%%%%%%%%%%%%%%%%%%%%%%%%%
%Define quantizer to simulate Marx inverter
%%%%%%%%%%%%%%%%%%%%%%%%%%%%%%%%%%%%%%%%%%%%%%%%%%%%%%%%%%%%%%%%%%%%%%%%%%%%%%%%%%%%%%%%%%%%
%Define reference sinewave voltage
v=A'*sin(2*pi*Fc*t);
%Define quantizer characteristics
partition=[(-levels+(1-qt)):qi:0,qt:qi:(levels-(1-qt))];
codebook=[-levels*Vdc:Vdc:levels*Vdc];
%Build Marx pattern
for k=1:length(A);
[indx,Vm(k,:)]=quantiz(v(k,:),partition,codebook);
%Fundamental Marx amplitude
B1M(k)=2/(T)*trapz(t,Vm(k,:).*sin(2*pi*Fc*t));
%Calculate currents using Marx waveform as input
I(:,:,k)=lsim(sys,[Vm(k,:)',zeros(length(t),7)],t);
end

I1=I(:,1:4:length(A)*4);
I2=I(:,2:4:length(A)*4);
I3=I(:,3:4:length(A)*4);
I4=I(:,4:4:length(A)*4);

%%%%%%%%%%%%%%%%%%%%%%%%%%%%%%%%%%%%%%%%%%%%%%%%%%%%%%%%%%%%%%%%%%%%%%%%%%%%%%%%%%%%%%%%%%%%
%Calculate fundamental current waveforms
%%%%%%%%%%%%%%%%%%%%%%%%%%%%%%%%%%%%%%%%%%%%%%%%%%%%%%%%%%%%%%%%%%%%%%%%%%%%%%%%%%%%%%%%%%%%
%Define unit sinewave voltage
vunit=sin(2*pi*Fc*t);

%Calculate currents
Iunit=lsim(sys,[vunit',zeros(length(t),7)],t);
Iunit1=Iunit(:,1);
```

```
Iunit2=Iunit(:,2);
Iunit3=Iunit(:,3);
Iunit4=Iunit(:,4);

%Scale currents
Ifun1=Iunit1*B1M;
Ifun2=Iunit2*B1M;
Ifun3=Iunit3*B1M;
Ifun4=Iunit4*B1M;

%%%%%%%%%%%%%%%%%%%%%%%%%%%%%%%%%%%%%%%%%%%%%%%%%%%%%%%%%%%%%%%%%%%%%%%%%%%%%%%%%%%%%%%%%%%%%%%
%Take second half of vectors to avoid transient (5 time constants later)
%%%%%%%%%%%%%%%%%%%%%%%%%%%%%%%%%%%%%%%%%%%%%%%%%%%%%%%%%%%%%%%%%%%%%%%%%%%%%%%%%%%%%%%%%%%%%%%
nut=floor((Tstart/T)*Tpoints+1):Tpoints;
t=t(nut);
v=v(:,nut);
Vm=Vm(:,nut);
I=I(nut,:);

I1=I1(nut,:);
I2=I2(nut,:);
I3=I3(nut,:);
I4=I4(nut,:);

Ifun1=Ifun1(nut,:);
Ifun2=Ifun2(nut,:);
Ifun3=Ifun3(nut,:);
Ifun4=Ifun4(nut,:);

%%%%%%%%%%%%%%%%%%%%%%%%%%%%%%%%%%%%%%%%%%%%%%%%%%%%%%%%%%%%%%%%%%%%%%%%%%%%%%%%%%%%%%%%%%%%%%%
%Calculate total harmonic distortion
%%%%%%%%%%%%%%%%%%%%%%%%%%%%%%%%%%%%%%%%%%%%%%%%%%%%%%%%%%%%%%%%%%%%%%%%%%%%%%%%%%%%%%%%%%%%%%%
%Mean-square of the Marx voltage using half of T
VMS=1/(T-Tstart)*trapz(t',Vm.^2');

%Determine DC offset of inductor current
DCoffset1=(max(I1)+min(I1))/2;
DCoffset2=(max(I2)+min(I2))/2;
DCoffset3=(max(I3)+min(I3))/2;
DCoffset4=(max(I4)+min(I4))/2;

%Needed for matrix math in next step
DCoffset1=diag(DCoffset1);
DCoffset2=diag(DCoffset2);
DCoffset3=diag(DCoffset3);
DCoffset4=diag(DCoffset4);

%Remove DC offset from current
I1=I1-ones(length(A),length(t))'*DCoffset1;
I2=I2-ones(length(A),length(t))'*DCoffset2;
I3=I3-ones(length(A),length(t))'*DCoffset3;
I4=I4-ones(length(A),length(t))'*DCoffset4;

%Determine DC offset of inductor current
```

```
DCoffsetfun1=(max(Ifun1)+min(Ifun1))/2;
DCoffsetfun2=(max(Ifun2)+min(Ifun2))/2;
DCoffsetfun3=(max(Ifun3)+min(Ifun3))/2;
DCoffsetfun4=(max(Ifun4)+min(Ifun4))/2;

%Needed for matrix math in next step
DCoffsetfun1=diag(DCoffsetfun1);
DCoffsetfun2=diag(DCoffsetfun2);
DCoffsetfun3=diag(DCoffsetfun3);
DCoffsetfun4=diag(DCoffsetfun4);

%Remove DC offset from current
Ifun1=Ifun1-ones(length(A),length(t))'*DCoffsetfun1;
Ifun2=Ifun2-ones(length(A),length(t))'*DCoffsetfun2;
Ifun3=Ifun3-ones(length(A),length(t))'*DCoffsetfun3;
Ifun4=Ifun4-ones(length(A),length(t))'*DCoffsetfun4;

%Find %THD of Marx voltage
THD=100*[(2*VMS-B1M.^2)./B1M.^2].^.5;

%%%%%%%%%%%%%%%%%%%%%%%%%%%%%%%%%%%%%%%%%%%%%%%%%%%%%%%%%%%%%%%%%%%%%%%%%%%%%%%%%%%%%%%%%%%%%%
%Calculate the weighted total harmonic distortion
%%%%%%%%%%%%%%%%%%%%%%%%%%%%%%%%%%%%%%%%%%%%%%%%%%%%%%%%%%%%%%%%%%%%%%%%%%%%%%%%%%%%%%%%%%%%%%
%Sum of current harmonics minus fundamental
Ih1=I1-Ifun1;
Ih2=I2-Ifun2;
Ih3=I3-Ifun3;
Ih4=I4-Ifun4;

%Calculate the mean-square of the extra current harmonics
HMS1=1/(T-Tstart)*trapz(t',Ih1.^2);
HMS2=1/(T-Tstart)*trapz(t',Ih2.^2);
HMS3=1/(T-Tstart)*trapz(t',Ih3.^2);
HMS4=1/(T-Tstart)*trapz(t',Ih4.^2);

%Calculate current THD
MTHD1=100*sqrt(HMS1./(.5*max(Ifun1).^2));
MTHD2=100*sqrt(HMS2./(.5*max(Ifun2).^2));
MTHD3=100*sqrt(HMS3./(.5*max(Ifun3).^2));
MTHD4=100*sqrt(HMS4./(.5*max(Ifun4).^2));

%%%%%%%%%%%%%%%%%%%%%%%%%%%%%%%%%%%%%%%%%%%%%%%%%%%%%%%%%%%%%%%%%%%%%%%%%%%%%%%%%%%%%%%%%%%%%%
%Calculate power delivered to induction targets
%%%%%%%%%%%%%%%%%%%%%%%%%%%%%%%%%%%%%%%%%%%%%%%%%%%%%%%%%%%%%%%%%%%%%%%%%%%%%%%%%%%%%%%%%%%%%%
P1=0.5*(max(Ifun1)).^2*R(1).*(1+(MTHD1/100).^2);
P2=0.5*(max(Ifun2)).^2*R(2).*(1+(MTHD2/100).^2);
P3=0.5*(max(Ifun3)).^2*R(3).*(1+(MTHD3/100).^2);
P4=0.5*(max(Ifun4)).^2*R(4).*(1+(MTHD4/100).^2);

Pr=[P2;P3;P4];
Pr=sort(Pr);
factorM=Pr(3,:)./Pr(2,:);

%%%%%%%%%%%%%%%%%%%%%%%%%%%%%%%%%%%%%%%%%%%%%%%%%%%%%%%%%%%%%%%%%%%%%%%%%%%%%%%%%%%%%%%%%%%%%%
```

```
%Initialize parameters
%%%%%%%%%%%%%%%%%%%%%%%%%%%%%%%%%%%%%%%%%%%%%%%%%%%%%%%%%%%%%%%%%%%%%%%%%%%%%%%%%%%%%%%%%%%%
clear I

Mf=15;                               %PWM frequency modulation ratio
Fs=Mf*Fc;                            %PWM sampling frequency (Hz)
%Mapoints=10;                        %Number Of Ma (amplitude modulation ratio) points
Tpoints=20000;                       %Number of sample points in period T
Vdc=1;                               %PWM voltage level

%%%%%%%%%%%%%%%%%%%%%%%%%%%%%%%%%%%%%%%%%%%%%%%%%%%%%%%%%%%%%%%%%%%%%%%%%%%%%%%%%%%%%%%%%%%%
%Define Ma and time vectors
%%%%%%%%%%%%%%%%%%%%%%%%%%%%%%%%%%%%%%%%%%%%%%%%%%%%%%%%%%%%%%%%%%%%%%%%%%%%%%%%%%%%%%%%%%%%
A=linspace(0,1,Mapoints);            %Ma varies from 0 to 1
t=linspace (0,T,Tpoints);            %t varies over one period

%%%%%%%%%%%%%%%%%%%%%%%%%%%%%%%%%%%%%%%%%%%%%%%%%%%%%%%%%%%%%%%%%%%%%%%%%%%%%%%%%%%%%%%%%%%%
%Define reference sine voltages-- one for each phase leg
%%%%%%%%%%%%%%%%%%%%%%%%%%%%%%%%%%%%%%%%%%%%%%%%%%%%%%%%%%%%%%%%%%%%%%%%%%%%%%%%%%%%%%%%%%%%
Va=A'*sin(2*pi*Fc*t);                %Phase leg A
Vb=-Va;                              %Phase leg B

%%%%%%%%%%%%%%%%%%%%%%%%%%%%%%%%%%%%%%%%%%%%%%%%%%%%%%%%%%%%%%%%%%%%%%%%%%%%%%%%%%%%%%%%%%%%
%Generate triangle waveform for sampling
%%%%%%%%%%%%%%%%%%%%%%%%%%%%%%%%%%%%%%%%%%%%%%%%%%%%%%%%%%%%%%%%%%%%%%%%%%%%%%%%%%%%%%%%%%%%
%phi=pi/2;                           %Phase of triangle waveform
phi=0;                               %Phase of triangle waveform; This one appears correct
tri=sawtooth(2*pi*Fs*t+phi, 0.5);    %Triangle waveform

%%%%%%%%%%%%%%%%%%%%%%%%%%%%%%%%%%%%%%%%%%%%%%%%%%%%%%%%%%%%%%%%%%%%%%%%%%%%%%%%%%%%%%%%%%%%
%Generate unipolar natural sampling PWM waveform
%%%%%%%%%%%%%%%%%%%%%%%%%%%%%%%%%%%%%%%%%%%%%%%%%%%%%%%%%%%%%%%%%%%%%%%%%%%%%%%%%%%%%%%%%%%%
PWMa=zeros(length(A),length(t));     %Initialize matrix
PWMb=zeros(length(A),length(t));     %Initialize matrix

tri=ones(length(A),1)*tri;                       %Create matrix of triangle waveforms

PWMa=sign(Va-tri);                               %Compare reference A with triangle waveform
PWMa=.5*Vdc*(PWMa+ones(length(A),length(t)));    %Generate PWMa matrix
PWMb=sign(Vb-tri);                               %Compare reference B with triangle waveform
PWMb=.5*Vdc*(PWMb+ones(length(A),length(t)));    %Generate PWMb matrix
PWM=(PWMa-PWMb)';                                %Difference is PWM waveform across L


%%%%%%%%%%%%%%%%%%%%%%%%%%%%%%%%%%%%%%%%%%%%%%%%%%%%%%%%%%%%%%%%%%%%%%%%%%%%%%%%%%%%%%%%%%%%
%Build system response
%%%%%%%%%%%%%%%%%%%%%%%%%%%%%%%%%%%%%%%%%%%%%%%%%%%%%%%%%%%%%%%%%%%%%%%%%%%%%%%%%%%%%%%%%%%%
for k=1:length(A);
%Calculate currents using PWM waveform as input
I(:,:,k)=lsim(sys,[PWM(:,k),zeros(length(t),7)],t);
%Fundamental PWM amplitude
B1P(k)=2/(T)*trapz(t,PWM(:,k)'.*sin(2*pi*Fc*t));
end
```

```
I1=I(:,1:4:length(A)*4);
I2=I(:,2:4:length(A)*4);
I3=I(:,3:4:length(A)*4);
I4=I(:,4:4:length(A)*4);

%%%%%%%%%%%%%%%%%%%%%%%%%%%%%%%%%%%%%%%%%%%%%%%%%%%%%%%%%%%%%%%%%%%%%%%%%%%%%%%%%%%%%%%%%%%%
%Calculate fundamental current waveforms
%%%%%%%%%%%%%%%%%%%%%%%%%%%%%%%%%%%%%%%%%%%%%%%%%%%%%%%%%%%%%%%%%%%%%%%%%%%%%%%%%%%%%%%%%%%%
%Define reference sinewave voltage
vunit=sin(2*pi*Fc*t);

%Calculate currents
Iunit=lsim(sys,[vunit',zeros(length(t),7)],t);
Iunit1=Iunit(:,1);
Iunit2=Iunit(:,2);
Iunit3=Iunit(:,3);
Iunit4=Iunit(:,4);

%Scale currents
Ifun1=Iunit1*B1P;
Ifun2=Iunit2*B1P;
Ifun3=Iunit3*B1P;
Ifun4=Iunit4*B1P;

%%%%%%%%%%%%%%%%%%%%%%%%%%%%%%%%%%%%%%%%%%%%%%%%%%%%%%%%%%%%%%%%%%%%%%%%%%%%%%%%%%%%%%%%%%%%
%Take second half of vectors to avoid transient (5 time constants later)
%%%%%%%%%%%%%%%%%%%%%%%%%%%%%%%%%%%%%%%%%%%%%%%%%%%%%%%%%%%%%%%%%%%%%%%%%%%%%%%%%%%%%%%%%%%%
nut=floor((Tstart/T)*Tpoints+1):Tpoints;
t=t(nut);
Va=Va(:,nut);
PWM=PWM(nut,:);
I=I(nut,:);
tri=tri(:,nut);
I1=I1(nut,:);
I2=I2(nut,:);
I3=I3(nut,:);
I4=I4(nut,:);
Ifun1=Ifun1(nut,:);
Ifun2=Ifun2(nut,:);
Ifun3=Ifun3(nut,:);
Ifun4=Ifun4(nut,:);

%%%%%%%%%%%%%%%%%%%%%%%%%%%%%%%%%%%%%%%%%%%%%%%%%%%%%%%%%%%%%%%%%%%%%%%%%%%%%%%%%%%%%%%%%%%%
%Calculate Total Harmonic Distortion
%%%%%%%%%%%%%%%%%%%%%%%%%%%%%%%%%%%%%%%%%%%%%%%%%%%%%%%%%%%%%%%%%%%%%%%%%%%%%%%%%%%%%%%%%%%%
%Mean-square of the PWM voltage using half of T
VMS=2/T*trapz(t',PWM.^2);

%Determine DC offset of inductor current
DCoffset1=(max(I1)+min(I1))/2;
DCoffset2=(max(I2)+min(I2))/2;
DCoffset3=(max(I3)+min(I3))/2;
DCoffset4=(max(I4)+min(I4))/2;
```

```
%Needed for matrix math in next step
DCoffset1=diag(DCoffset1);
DCoffset2=diag(DCoffset2);
DCoffset3=diag(DCoffset3);
DCoffset4=diag(DCoffset4);

%Remove DC offset from current
I1=I1-ones(length(A),length(t))'*DCoffset1;
I2=I2-ones(length(A),length(t))'*DCoffset2;
I3=I3-ones(length(A),length(t))'*DCoffset3;
I4=I4-ones(length(A),length(t))'*DCoffset4;

%Determine DC offset of inductor current
DCoffsetfun1=(max(Ifun1)+min(Ifun1))/2;
DCoffsetfun2=(max(Ifun2)+min(Ifun2))/2;
DCoffsetfun3=(max(Ifun3)+min(Ifun3))/2;
DCoffsetfun4=(max(Ifun4)+min(Ifun4))/2;

%Needed for matrix math in next step
DCoffsetfun1=diag(DCoffsetfun1);
DCoffsetfun2=diag(DCoffsetfun2);
DCoffsetfun3=diag(DCoffsetfun3);
DCoffsetfun4=diag(DCoffsetfun4);

%Remove DC offset from current
Ifun1=Ifun1-ones(length(A),length(t))'*DCoffsetfun1;
Ifun2=Ifun2-ones(length(A),length(t))'*DCoffsetfun2;
Ifun3=Ifun3-ones(length(A),length(t))'*DCoffsetfun3;
Ifun4=Ifun4-ones(length(A),length(t))'*DCoffsetfun4;

%Find %THD of PWM voltage
THD=100*[(VMS-.5*(B1P*Vdc).^2)./(.5*(B1P*Vdc).^2)].^.5;

%%%%%%%%%%%%%%%%%%%%%%%%%%%%%%%%%%%%%%%%%%%%%%%%%%%%%%%%%%%%%%%%%%%%%%%%%%%%%%%%%%%%%%%%%%%%
%Calculate the weighted total harmonic distortion
%%%%%%%%%%%%%%%%%%%%%%%%%%%%%%%%%%%%%%%%%%%%%%%%%%%%%%%%%%%%%%%%%%%%%%%%%%%%%%%%%%%%%%%%%%%%
%Sum of current harmonics minus fundamental
Ih1=I1-Ifun1;
Ih2=I2-Ifun2;
Ih3=I3-Ifun3;
Ih4=I4-Ifun4;

%Calculate the mean-square of the extra current harmonics
HMS1=1/(T-Tstart)*trapz(t',Ih1.^2);
HMS2=1/(T-Tstart)*trapz(t',Ih2.^2);
HMS3=1/(T-Tstart)*trapz(t',Ih3.^2);
HMS4=1/(T-Tstart)*trapz(t',Ih4.^2);

%Calculate current THD
PTHD1=100*sqrt(HMS1./(.5*max(Ifun1).^2));
PTHD2=100*sqrt(HMS2./(.5*max(Ifun2).^2));
PTHD3=100*sqrt(HMS3./(.5*max(Ifun3).^2));
PTHD4=100*sqrt(HMS4./(.5*max(Ifun4).^2));
```

```
%%%%%%%%%%%%%%%%%%%%%%%%%%%%%%%%%%%%%%%%%%%%%%%%%%%%%%%%%%%%%%%%%%%%%%%%%%%%%%%%%%%%%%%%%%%
%Calculate power delivered to induction targets
%%%%%%%%%%%%%%%%%%%%%%%%%%%%%%%%%%%%%%%%%%%%%%%%%%%%%%%%%%%%%%%%%%%%%%%%%%%%%%%%%%%%%%%%%%%
P1=0.5*(max(Ifun1)).^2*R(1).*(1+(PTHD1/100).^2);
P2=0.5*(max(Ifun2)).^2*R(2).*(1+(PTHD2/100).^2);
P3=0.5*(max(Ifun3)).^2*R(3).*(1+(PTHD3/100).^2);
P4=0.5*(max(Ifun4)).^2*R(4).*(1+(PTHD4/100).^2);

Pr=[P2;P3;P4];
Pr=sort(Pr);
factorP=Pr(3,:)./Pr(2,:);

%%%%%%%%%%%%%%%%%%%%%%%%%%%%%%%%%%%%%%%%%%%%%%%%%%%%%%%%%%%%%%%%%%%%%%%%%%%%%%%%%%%%%%%%%%%
%Plot normalized relativer power vs normalized fundamental voltage
%%%%%%%%%%%%%%%%%%%%%%%%%%%%%%%%%%%%%%%%%%%%%%%%%%%%%%%%%%%%%%%%%%%%%%%%%%%%%%%%%%%%%%%%%%%
x=linspace(0,1,100);
y0=2.6*ones(1,100);
y1=2.6*1.05*ones(1,100);
y2=2.6*.95*ones(1,100);
figure(1)
plot(B1M/(1),factorM,'-',B1P/Vdc,factorP,'.-',x,y0,'--',x,y1,'--',x,y2,'--')
grid on
title('Normalized Relative Power vs Normalized Fundamental Voltage')
ylabel('Normalized Relative Power')
xlabel('Fundamental Voltage Normalized to Vdc')
legend('Quantized Marx Inverter','PWM Full-Bridge Inverter',4)
axis([0.2,1,1,3])
```

B.3.11 SDOF.m

```
%SDOF.m
%This script calculates the frequency response of a SDOF resonant mechanical structure
%for different system parameters.

clear
%%%%%%%%%%%%%%%%%%%%%%%%%%%%%%%%%%%%%%%%%%%%%%%%%%%%%%%%%%%%%%%%%%%%%%%%%%%%%%%%%%%%%%%%%%%
%System parameters
%%%%%%%%%%%%%%%%%%%%%%%%%%%%%%%%%%%%%%%%%%%%%%%%%%%%%%%%%%%%%%%%%%%%%%%%%%%%%%%%%%%%%%%%%%%
m1=1;                                       %Primary mass
k1=1;                                       %Primary compliance
s=tf('s');                                  %Complex frequency s

%%%%%%%%%%%%%%%%%%%%%%%%%%%%%%%%%%%%%%%%%%%%%%%%%%%%%%%%%%%%%%%%%%%%%%%%%%%%%%%%%%%%%%%%%%%
%1st transfer function
%%%%%%%%%%%%%%%%%%%%%%%%%%%%%%%%%%%%%%%%%%%%%%%%%%%%%%%%%%%%%%%%%%%%%%%%%%%%%%%%%%%%%%%%%%%
c1=.1;                                      %Primary damping constant
z1=.5*c1/sqrt(m1*k1);                       %Primary damping ratio

H1=1/[m1*s^2+c1*s+k1];

%%%%%%%%%%%%%%%%%%%%%%%%%%%%%%%%%%%%%%%%%%%%%%%%%%%%%%%%%%%%%%%%%%%%%%%%%%%%%%%%%%%%%%%%%%%
```

```
%2nd transfer function
%%%%%%%%%%%%%%%%%%%%%%%%%%%%%%%%%%%%%%%%%%%%%%%%%%%%%%%%%%%%%%%%%%%%%%%%%%%%%%%%%%%%%%%%%%%%
c1=.4;                                      %Primary damping constant
z2=.5*c1/sqrt(m1*k1);                       %Primary damping ratio

H2=1/[m1*s^2+c1*s+k1];

%%%%%%%%%%%%%%%%%%%%%%%%%%%%%%%%%%%%%%%%%%%%%%%%%%%%%%%%%%%%%%%%%%%%%%%%%%%%%%%%%%%%%%%%%%%%
%3rd transfer function
%%%%%%%%%%%%%%%%%%%%%%%%%%%%%%%%%%%%%%%%%%%%%%%%%%%%%%%%%%%%%%%%%%%%%%%%%%%%%%%%%%%%%%%%%%%%
c1=2/sqrt(2)*1;                             %Primary damping constant
z3=.5*c1/sqrt(m1*k1);                       %Primary damping ratio

H3=1/[m1*s^2+c1*s+k1];

%%%%%%%%%%%%%%%%%%%%%%%%%%%%%%%%%%%%%%%%%%%%%%%%%%%%%%%%%%%%%%%%%%%%%%%%%%%%%%%%%%%%%%%%%%%%
%Determine frequency response
%%%%%%%%%%%%%%%%%%%%%%%%%%%%%%%%%%%%%%%%%%%%%%%%%%%%%%%%%%%%%%%%%%%%%%%%%%%%%%%%%%%%%%%%%%%%
%Frequency vector in rps
w=logspace(-1,1,1000);

%Bode response
[mag1,phase1]=bode(H1,w);
[mag2,phase2]=bode(H2,w);
[mag3,phase3]=bode(H3,w);

%%%%%%%%%%%%%%%%%%%%%%%%%%%%%%%%%%%%%%%%%%%%%%%%%%%%%%%%%%%%%%%%%%%%%%%%%%%%%%%%%%%%%%%%%%%%
%Plot results
%%%%%%%%%%%%%%%%%%%%%%%%%%%%%%%%%%%%%%%%%%%%%%%%%%%%%%%%%%%%%%%%%%%%%%%%%%%%%%%%%%%%%%%%%%%%
figure(1)
subplot(2,1,1)
semilogx(w,20*log10(mag1(:)),'-',w,20*log10(mag2(:)),'--',w,20*log10(mag3(:)),'-.');
title('Frequency Response (X_1/F) of Resonant Mechanical Structure for
    Different Damping Ratios')
ylabel('|X_{1}/X_{st}| (dB)')
%xlabel('Frequency (rads/sec)')
legend('\zeta_{1}=0.05','\zeta_{1}=0.2','\zeta_{1}=0.707')
grid on
axis([.1 10 -40 30])
subplot(2,1,2)
semilogx(w,phase1(:),'-',w,phase2(:),'--',w,phase3(:),'-.');
ylabel('Phase (Degrees)')
xlabel('Normalized Frequency (\omega/\omega_n)')
legend('\zeta_{1}=0.05','\zeta_{1}=0.2','\zeta_{1}=0.707')
grid on
```

B.3.12 TargetRLCI.m

```
%TargetsRLCI.m
%This script calculates the frequency response of 3 inductively coupled RLC targets for a
%current driven primary coil. This script uses a state space description that allows the
```

```
%full inductance matrix to be used.
clear
%%%%%%%%%%%%%%%%%%%%%%%%%%%%%%%%%%%%%%%%%%%%%%%%%%%%%%%%%%%%%%%%%%%%%%%%%%%%%%
%System parameters
%%%%%%%%%%%%%%%%%%%%%%%%%%%%%%%%%%%%%%%%%%%%%%%%%%%%%%%%%%%%%%%%%%%%%%%%%%%%%%
%Input current amplitude
Iin=1;

%Resistances
R=[1.0 1.0 1.0 1.0];
%Primary side inductance
Lp=10e-6;
%Target inductances
Ls=100e-6;
%Inductances
L=[Lp Ls Ls Ls];
%Capacitances
C=1e-6*[1e10, .03957858736, .03127197, .025330295];

%Target Q's
Q2=sqrt(L(2)/C(2))/R(2);
Q3=sqrt(L(3)/C(3))/R(3);
Q4=sqrt(L(4)/C(4))/R(4);

%Coupling coefficients
K12=.3;
K13=.3;
K14=.3;
%K14=.0;
K23=0.0;
%K23=0.03;
K24=0.0;
K34=0.0;
%Mutual inductances
M12=K12*sqrt(L(1)*L(2));
M13=K13*sqrt(L(1)*L(3));
M14=K14*sqrt(L(1)*L(4));
M23=K23*sqrt(L(2)*L(3));
M24=K24*sqrt(L(2)*L(4));
M34=K34*sqrt(L(3)*L(4));

%Resistance, inductance and capacitance matrices
Rmat=[R(2),0,0;0,R(3),0;0,0,R(4)];
Lmat=[L(2),M23,M24; M23,L(3),M34; M24,M34,L(4)];
Cmat=[C(2),0,0;0,C(3),0;0,0,C(4)];

%%%%%%%%%%%%%%%%%%%%%%%%%%%%%%%%%%%%%%%%%%%%%%%%%%%%%%%%%%%%%%%%%%%%%%%%%%%%%%
%State space representation
%%%%%%%%%%%%%%%%%%%%%%%%%%%%%%%%%%%%%%%%%%%%%%%%%%%%%%%%%%%%%%%%%%%%%%%%%%%%%%
A=[-1*inv(Lmat)*Rmat,inv(Lmat); -1*inv(Cmat), zeros(3)];
B=[-1*inv(Lmat)*[M12;M13;M14];zeros(3,1)];
D=B;
B=A*B;
C=[eye(3), zeros(3); zeros(3), zeros(3)];  %Gives currents through resistance
```

```
%C=[Rmat, zeros(3); zeros(3), zeros(3)];   %Gives voltages across resistance
D;
sys=ss(A,B,C,D);
[Num,Den]=ss2tf(A,B,C,D,1);

%%%%%%%%%%%%%%%%%%%%%%%%%%%%%%%%%%%%%%%%%%%%%%%%%%%%%%%%%%%%%%%%%%%%%%%%%%%%%%%%%%%%%%%%%%%%%%%%%%%%%%%%
%Calculate magnitude responses and normalized relative power between targets
%%%%%%%%%%%%%%%%%%%%%%%%%%%%%%%%%%%%%%%%%%%%%%%%%%%%%%%%%%%%%%%%%%%%%%%%%%%%%%%%%%%%%%%%%%%%%%%%%%%%%%%%
%Frequency range
f=logspace(2,6,1000);
w=2*pi*f;

%Bode response
[Mag(:,1),Phase(:,1)]=bode(Iin*Num(1,:),Den,w);
[Mag(:,2),Phase(:,2)]=bode(Iin*Num(2,:),Den,w);
[Mag(:,3),Phase(:,3)]=bode(Iin*Num(3,:),Den,w);

%Target magnitude responses
Mag2=Mag(:,1);
Mag3=Mag(:,2);
Mag4=Mag(:,3);

%Power calculations
P2=R(2)*Mag2.^2/2;
P3=R(3)*Mag3.^2/2;
P4=R(4)*Mag4.^2/2;

%Sort power and determine ratios
P=[P2,P3,P4]';
P1=sort(P);
factor=P1(3,:)./P1(2,:);

%Downsample vectors
for i=1:floor(length(f)/10)-1;
fs(i)=f(i*10);
P2s(i)=P2(i*10);
P3s(i)=P3(i*10);
P4s(i)=P4(i*10);
Mag2s(i)=Mag2(i*10);
Mag3s(i)=Mag3(i*10);
Mag4s(i)=Mag4(i*10);
end

%%%%%%%%%%%%%%%%%%%%%%%%%%%%%%%%%%%%%%%%%%%%%%%%%%%%%%%%%%%%%%%%%%%%%%%%%%%%%%%%%%%%%%%%%%%%%%%%%%%%%%%%
%Plot results
%%%%%%%%%%%%%%%%%%%%%%%%%%%%%%%%%%%%%%%%%%%%%%%%%%%%%%%%%%%%%%%%%%%%%%%%%%%%%%%%%%%%%%%%%%%%%%%%%%%%%%%%
figure(1)
loglog(fs,Mag2s,'bo',fs,Mag3s,'gd',fs,Mag4s,'rs',f,Mag2,'b',f,Mag3,'g',f,Mag4,'r')
title('I_{in} to I_{n} Transfer Function for Three Different Targets: Current Drive')
ylabel('Magnitude')
xlabel('Frequency (Hz)')
legend('Target 1: 80kHz', 'Target 2: 90kHz', 'Target 3: 100kHz')
grid on
axis([3e4,3e5,1e-2,1e1])
```

```
figure(2)
loglog(fs,P2s,'bo',fs,P3s,'gd',fs,P4s,'rs',f,P2,'b',f,P3,'g',f,P4,'r')
title('Induced Heating Versus Frequency For Three Different Targets: Current Drive')
%title('Induced Heating Versus Frequency For Two Lightly Cross-Coupled Targets:
    Current Drive')
ylabel('Power (Watts)')
xlabel('Frequency (Hz)')
legend('Target 1: 80kHz', 'Target 2: 90kHz', 'Target 3: 100kHz')
%legend('Target 1: 80kHz','Target 2: 90kHz')
grid on
axis([3e4,3e5,1e-4, 2e2])

figure(3)
loglog(f,factor)
grid on
title('Ratio of Target with Greatest Power Dissipation to Target with
    Second Greatest Power Dissipation')
ylabel('Power Ratio')
xlabel('Frequency (Hz)')
axis([3e4,3e5,1e0,2e2])
```

B.3.13 TargetRLCV.m

```
%TargetsRLCV.m
%This script calculates the frequency response of 3 inductively coupled RLC targets for a
%voltage driven primary coil. This script uses a state space description that allows the
%full inductance matrix to be used.

clear
%%%%%%%%%%%%%%%%%%%%%%%%%%%%%%%%%%%%%%%%%%%%%%%%%%%%%%%%%%%%%%%%%%%%%%%%%%%%%%%%%%%%%%%%%%%%%%%%
%System parameters
%%%%%%%%%%%%%%%%%%%%%%%%%%%%%%%%%%%%%%%%%%%%%%%%%%%%%%%%%%%%%%%%%%%%%%%%%%%%%%%%%%%%%%%%%%%%%%%%
%Input voltage amplitude
vin=1;

%Resistances
R=[1.0 1.0 1.0 1.0];
%Primary side inductance
Lp=10e-6;
%Target inductances
Ls=100e-6;
%Inductances
L=[Lp Ls Ls Ls];
%Capacitances
C=1e-6*[1, .03957858736, .03127197, .025330295];

%Coupling coefficients
K12=.3;
K13=.3;
K14=.3;
```

```
%Mutual inductances
M12=K12*sqrt(L(1)*L(2));
M13=K13*sqrt(L(1)*L(3));
M14=K14*sqrt(L(1)*L(4));

%Resistance, inductance and capacitance matrices
Rmat=[R(1),0,0,0;0,R(2),0,0;0,0,R(3),0;0,0,0,R(4)];
Lmat=[L(1),M12,M13,M14;M12,L(2),0,0;M13,0,L(3),0;M14,0,0,L(4)];
Cmat=[C(1),0,0,0;0,C(2),0,0;0,0,C(3),0;0,0,0,C(4)];

%%%%%%%%%%%%%%%%%%%%%%%%%%%%%%%%%%%%%%%%%%%%%%%%%%%%%%%%%%%%%%%%%%%%%%%%%%%%%%%%%%%%%%%%%%%%%%%%%%
%State space representation
%%%%%%%%%%%%%%%%%%%%%%%%%%%%%%%%%%%%%%%%%%%%%%%%%%%%%%%%%%%%%%%%%%%%%%%%%%%%%%%%%%%%%%%%%%%%%%%%%%
A=[-1*inv(Lmat)*Rmat,inv(Lmat); -1*inv(Cmat), zeros(4)];
B=[inv(Lmat), zeros(4); zeros(4), zeros(4)];
C=[eye(4) zeros(4)];  %Gives currents through resistance
%C=[Rmat zeros(4)];   %Gives voltages across resistance
D=[zeros(4) zeros(4)];
sys=ss(A,B,C,D);
[Num,Den]=ss2tf(A,B,C,D,1);

%%%%%%%%%%%%%%%%%%%%%%%%%%%%%%%%%%%%%%%%%%%%%%%%%%%%%%%%%%%%%%%%%%%%%%%%%%%%%%%%%%%%%%%%%%%%%%%%%%
%Calculate magnitude responses and normalized relative power between targets
%%%%%%%%%%%%%%%%%%%%%%%%%%%%%%%%%%%%%%%%%%%%%%%%%%%%%%%%%%%%%%%%%%%%%%%%%%%%%%%%%%%%%%%%%%%%%%%%%%
%Frequency range
f=logspace(2,6,1000);
w=2*pi*f;

%Bode response
[Mag(:,1),Phase(:,1)]=bode(vin*Num(1,:),Den,w);
[Mag(:,2),Phase(:,2)]=bode(vin*Num(2,:),Den,w);
[Mag(:,3),Phase(:,3)]=bode(vin*Num(3,:),Den,w);
[Mag(:,4),Phase(:,4)]=bode(vin*Num(4,:),Den,w);

%Target magnitude responses
Mag1=Mag(:,1);
Mag2=Mag(:,2);
Mag3=Mag(:,3);
Mag4=Mag(:,4);

%Power calculations
P1=R(1)*Mag1.^2/2;
P2=R(2)*Mag2.^2/2;
P3=R(3)*Mag3.^2/2;
P4=R(4)*Mag4.^2/2;

%Sort power and determine ratios
P=[P2,P3,P4]';
P1=sort(P);
factor=P1(3,:)./P1(3-1,:);

%Downsample vectors
for i=1:floor(length(f)/10)-1;
fs(i)=f(i*10);
```

```
P2s(i)=P2(i*10);
P3s(i)=P3(i*10);
P4s(i)=P4(i*10);
Mag1s(i)=Mag1(i*10);
Mag2s(i)=Mag2(i*10);
Mag3s(i)=Mag3(i*10);
Mag4s(i)=Mag4(i*10);
end

%%%%%%%%%%%%%%%%%%%%%%%%%%%%%%%%%%%%%%%%%%%%%%%%%%%%%%%%%%%%%%%%%%%%%%%%%%%%%%%%%%%%%%%%%%%%%%%%%%%%%%%%%%%%
%Plot results
%%%%%%%%%%%%%%%%%%%%%%%%%%%%%%%%%%%%%%%%%%%%%%%%%%%%%%%%%%%%%%%%%%%%%%%%%%%%%%%%%%%%%%%%%%%%%%%%%%%%%%%%%%%%
figure(1)
loglog(fs,Mag2s,'bo',fs,Mag3s,'gd',fs,Mag4s,'rs',f,Mag2,'b',f,Mag3,'g',f,Mag4,'r')
title('V_{in} to I_{n} Transfer Function for Three Different Targets: Voltage Drive')
ylabel('Magnitude')
xlabel('Frequency (Hz)')
legend('Target 1: 80kHz', 'Target 2: 90kHz', 'Target 3: 100kHz')
grid on
axis([3e4,3e5,1e-3,1e0])

figure(2)
loglog(fs,P2s,'bo',fs,P3s,'gd',fs,P4s,'rs',f,P2,'b',f,P3,'g',f,P4,'r')
title('Induced Heating Versus Frequency For Three Different Targets: Voltage Drive')
ylabel('Power (Watts)')
xlabel('Frequency (Hz)')
legend('Target 1: 80kHz', 'Target 2: 90kHz', 'Target 3: 100kHz')
grid on
axis([3e4,3e5,1e-6,1e-1])

figure(3)
subplot(2,1,1)
loglog(f,1./Mag1,'b')
title('Magnitude and Phase of Primary Side Impedance')
ylabel('Magnitude (Ohms)')
grid on
axis([3e4,3e5,1e0, 1e2])
subplot(2,1,2)
semilogx(f,-1*Phase(:,1),'b')
ylabel('Phase (Degrees)')
xlabel('Frequency (Hz)')
grid on
axis([3e4,3e5,-90, 90])

figure(4)
loglog(f,factor)
grid on
title('Relative Power Dissipation For Three Different Targets')
ylabel('Relative Power')
xlabel('Frequency (Hz)')
axis([3e4,3e5,1e0,2e2])
```

B.3.14 TargetsRLI.m

```
%TargetsRLI.m
%This script is designed to calculate the needed resistances of three RL induction
%targets, assuming that the targets have different coupling coefficients with the induction
%coil and must heat different amounts of mass. This script also plots the associated power
%curves assuming a current fed primary coil.

clear
%%%%%%%%%%%%%%%%%%%%%%%%%%%%%%%%%%%%%%%%%%%%%%%%%%%%%%%%%%%%%%%%%%%%%%%%%%%%%%%%%%%%%%%%%%%%
%System parameters
%%%%%%%%%%%%%%%%%%%%%%%%%%%%%%%%%%%%%%%%%%%%%%%%%%%%%%%%%%%%%%%%%%%%%%%%%%%%%%%%%%%%%%%%%%%%
%Input current amplitude
I=1;
%Primary side inductances
L1=100e-3*[1 1 1];
%Target self inductances
L2=2.5e-8*[1 1 1];
%Coupling coefficients
K=[.3 .3 .3];
%First target breakpoint frequency
f1=4e3;
w1=2*pi*f1;
%First target resistance
R1=1*L2(1)*w1;
%Desired separation in temperature (or power if masses are equal)
alpha=2.6;
%Mass ratios
M=[1 1 1];
%Weighting factor
G=M./K.^2;

%%%%%%%%%%%%%%%%%%%%%%%%%%%%%%%%%%%%%%%%%%%%%%%%%%%%%%%%%%%%%%%%%%%%%%%%%%%%%%%%%%%%%%%%%%%%
%Solve for R2
%%%%%%%%%%%%%%%%%%%%%%%%%%%%%%%%%%%%%%%%%%%%%%%%%%%%%%%%%%%%%%%%%%%%%%%%%%%%%%%%%%%%%%%%%%%%
a=1;
b=-alpha*G(1)/G(2)/R1*[(L2(1)*w1)^2+R1^2];
c=(L2(1)*w1)^2;
R2=(-b + sqrt(b^2-4*a*c))/(2*a);

%%%%%%%%%%%%%%%%%%%%%%%%%%%%%%%%%%%%%%%%%%%%%%%%%%%%%%%%%%%%%%%%%%%%%%%%%%%%%%%%%%%%%%%%%%%%
%Solve for w2
%%%%%%%%%%%%%%%%%%%%%%%%%%%%%%%%%%%%%%%%%%%%%%%%%%%%%%%%%%%%%%%%%%%%%%%%%%%%%%%%%%%%%%%%%%%%
w2=1/L2(1)*sqrt((R1^2-alpha*G(2)/G(1)*R1*R2)/(alpha*G(2)/G(1)*R1/R2-1));

%%%%%%%%%%%%%%%%%%%%%%%%%%%%%%%%%%%%%%%%%%%%%%%%%%%%%%%%%%%%%%%%%%%%%%%%%%%%%%%%%%%%%%%%%%%%
%Solve for R3
%%%%%%%%%%%%%%%%%%%%%%%%%%%%%%%%%%%%%%%%%%%%%%%%%%%%%%%%%%%%%%%%%%%%%%%%%%%%%%%%%%%%%%%%%%%%
a=1;
b=-alpha*G(2)/G(3)/R2*((L2(1)*w2)^2+R2^2);
c=(L2(1)*w2)^2;
R3=(-b + sqrt(b^2-4*a*c))/(2*a);
```

```
%%%%%%%%%%%%%%%%%%%%%%%%%%%%%%%%%%%%%%%%%%%%%%%%%%%%%%%%%%%%%%%%%%%%%%%%%%%%%%%%%%%%%%%%%%%%%
%Solve for w3
%%%%%%%%%%%%%%%%%%%%%%%%%%%%%%%%%%%%%%%%%%%%%%%%%%%%%%%%%%%%%%%%%%%%%%%%%%%%%%%%%%%%%%%%%%%%%
w3=1/L2(1)*sqrt((R2^2-alpha*G(3)/G(2)*R2*R3)/(alpha*G(3)/G(2)*R2/R3-1));

%%%%%%%%%%%%%%%%%%%%%%%%%%%%%%%%%%%%%%%%%%%%%%%%%%%%%%%%%%%%%%%%%%%%%%%%%%%%%%%%%%%%%%%%%%%%%
%Determine resistances and breakpoint frequencies
%%%%%%%%%%%%%%%%%%%%%%%%%%%%%%%%%%%%%%%%%%%%%%%%%%%%%%%%%%%%%%%%%%%%%%%%%%%%%%%%%%%%%%%%%%%%%
%Target resistances
R=[R1 R2 R3];
%Target breakpoint frequencies
f1=w1/(2*pi);
f2=w2/(2*pi);
f3=w3/(2*pi);
%Mass ratios
M=G.*K.^2;
%Target frequency spread
spread=f3/f1;

%%%%%%%%%%%%%%%%%%%%%%%%%%%%%%%%%%%%%%%%%%%%%%%%%%%%%%%%%%%%%%%%%%%%%%%%%%%%%%%%%%%%%%%%%%%%%
%Calculate normalized relative power and temperature rises between targets
%%%%%%%%%%%%%%%%%%%%%%%%%%%%%%%%%%%%%%%%%%%%%%%%%%%%%%%%%%%%%%%%%%%%%%%%%%%%%%%%%%%%%%%%%%%%%
%Frequency range
f=logspace(3,6,10000);
w=2*pi*f;

%Power and temperature rise calculations
for i=1:length(K);
P(i,:)=0.5*(I*K(i)*w).^2*L1(i)*L2(i)*R(i)./[(L2(i)*w).^2+R(i)^2];
T(i,:)=0.5*(I*K(i)*w).^2*L1(i)*L2(i)*R(i)./[(L2(i)*w).^2+R(i)^2]/M(i);
end

%Downsample vectors
for i=1:floor(length(f)/1000)-1;
fs(i)=f(i*1000);
P1s(i)=P(1,i*1000);
P2s(i)=P(2,i*1000);
P3s(i)=P(3,i*1000);
T1s(i)=T(1,i*1000);
T2s(i)=T(2,i*1000);
T3s(i)=T(3,i*1000);
end

%Sort power and determine ratios
P1=sort(P);
factorP=P1(length(K),:)./P1(length(K)-1,:);

%Sort temperature and determine ratios
T1=sort(T);
factorT=T1(length(K),:)./T1(length(K)-1,:);

%%%%%%%%%%%%%%%%%%%%%%%%%%%%%%%%%%%%%%%%%%%%%%%%%%%%%%%%%%%%%%%%%%%%%%%%%%%%%%%%%%%%%%%%%%%%%
%Plot results
%%%%%%%%%%%%%%%%%%%%%%%%%%%%%%%%%%%%%%%%%%%%%%%%%%%%%%%%%%%%%%%%%%%%%%%%%%%%%%%%%%%%%%%%%%%%%
```

```
figure(1)
loglog(fs,P1s,'o',fs,P2s,'d',fs,P3s,'s',f,P(1,:),'b',f,P(2,:),'g',f,P(3,:),'r')
grid on
title('Induced Heating Versus Frequency For Three Different Targets: Current Drive')
ylabel('Power (Watts)')
xlabel('Frequency (Hz)')
legend('Target 1: 4kHz','Target 2: 20kHz', 'Target 3: 100kHz',4)

figure(2)
semilogx(f,factorP)
title('Ratio of Target with Greatest Power Dissipation to Target with
    Second Greatest Power Dissipation')
ylabel('Power Ratio')
xlabel('Frequency (Hz)')
grid on

figure(3)
semilogx(f,factorT)
title('Ratio of Target with Greatest Temperature Rise to Target with
    Second Greatest Temperature Rise')
ylabel('Temperature Rise Ratio')
xlabel('Frequency (Hz)')
grid on
```

B.3.15 TargetsRLV.m

```
%TargetsRLV.m
%This script calculates the frequency response of 3 inductively coupled RL targets for a
%voltage driven primary coil. This script uses a state space description that allows the
%full inductance matrix to be used.

clear
%%%%%%%%%%%%%%%%%%%%%%%%%%%%%%%%%%%%%%%%%%%%%%%%%%%%%%%%%%%%%%%%%%%%%%%%%%%%%%%%%%%%%%%%%%%%%%%%
%System parameters
%%%%%%%%%%%%%%%%%%%%%%%%%%%%%%%%%%%%%%%%%%%%%%%%%%%%%%%%%%%%%%%%%%%%%%%%%%%%%%%%%%%%%%%%%%%%%%%%
%Input voltage amplitude
vin=1;

%Resistances
R=[.1 .001 .005 .025];
%Inductances
L=[200e-6 3.979e-8 3.979e-8 3.979e-8];

%Coupling coefficients
K12=.3;
K13=.3;
K14=.3;
%Mutual inductances
M12=K12*sqrt(L(1)*L(2));
M13=K13*sqrt(L(1)*L(3));
M14=K14*sqrt(L(1)*L(4));
```

```
%Resistance and inductance matrices
Rmat=-1*[R(1),0,0,0;0,R(2),0,0;0,0,R(3),0;0,0,0,R(4)];
Lmat=[L(1),M12,M13,M14;M12,L(2),0,0;M13,0,L(3),0;M14,0,0,L(4)];

%%%%%%%%%%%%%%%%%%%%%%%%%%%%%%%%%%%%%%%%%%%%%%%%%%%%%%%%%%%%%%%%%%%%%%%%%%%%%%%%%%%%%%%%%%%%%%
%State space representation
%%%%%%%%%%%%%%%%%%%%%%%%%%%%%%%%%%%%%%%%%%%%%%%%%%%%%%%%%%%%%%%%%%%%%%%%%%%%%%%%%%%%%%%%%%%%%%
n=length(R);
A=inv(Lmat)*Rmat;
B=inv(Lmat);
B=B(1:n,1);
C=eye(n);   %Gives current through resistances
%C=Rmat;    %Gives voltage across resistances
D=zeros(n);
D=D(1:n,1);
sys=ss(A,B,C,D);
[Num,Den]=ss2tf(A,B,C,D,1);


%%%%%%%%%%%%%%%%%%%%%%%%%%%%%%%%%%%%%%%%%%%%%%%%%%%%%%%%%%%%%%%%%%%%%%%%%%%%%%%%%%%%%%%%%%%%%%
%Calculate magnitude responses and normalized relative power between targets
%%%%%%%%%%%%%%%%%%%%%%%%%%%%%%%%%%%%%%%%%%%%%%%%%%%%%%%%%%%%%%%%%%%%%%%%%%%%%%%%%%%%%%%%%%%%%%
%Frequency range
f=logspace(2,6,1000);
w=2*pi*f;

%Bode response and power calculations
for k=1:n;
[Mag(:,k),Phase(:,k)]=bode(vin*Num(k,1:n+1),Den,w);
P(:,k)=R(k)*Mag(:,k).^2/2;
if k>1
    Pr(:,k-1)=P(:,k);
end
end

%Sort power and determine ratios
Pr=sort(Pr');
factor=Pr(n-1,:)./Pr(n-2,:);

%Target magnitude responses
Mag1=Mag(:,1);
Mag2=Mag(:,2);
Mag3=Mag(:,3);
Mag4=Mag(:,4);

%Dissipated power in targets
P2=P(:,2);
P3=P(:,3);
P4=P(:,4);

%Downsample vectors
for i=1:floor(length(f)/100)-1;
fs(i)=f(i*100);
```

```
P2s(i)=P2(i*100);
P3s(i)=P3(i*100);
P4s(i)=P4(i*100);
Mag1s(i)=Mag1(i*100);
Mag2s(i)=Mag2(i*100);
Mag3s(i)=Mag3(i*100);
Mag4s(i)=Mag4(i*100);
end

%%%%%%%%%%%%%%%%%%%%%%%%%%%%%%%%%%%%%%%%%%%%%%%%%%%%%%%%%%%%%%%%%%%%%%%%%%%%%%%%%%%%
%Plot results
%%%%%%%%%%%%%%%%%%%%%%%%%%%%%%%%%%%%%%%%%%%%%%%%%%%%%%%%%%%%%%%%%%%%%%%%%%%%%%%%%%%%
figure(1)
loglog(fs,Mag2s,'o',fs,Mag3s,'d',fs,Mag4s,'s',f,Mag2,'b',f,Mag3,'g',f,Mag4,'r')
legend('Target 1: 4kHz','Target 2: 20kHz', 'Target 3: 100kHz',3)
title('V_{in} to I_{n} Transfer Function for Three Different Targets: Voltage Drive')
ylabel('Magnitude')
xlabel('Frequency (Hz)')
grid on

figure(2)
loglog(fs,P2s,'o',fs,P3s,'d',fs,P4s,'s',f,P2,'b',f,P3,'g',f,P4,'r')
legend('Target 1: 4kHz','Target 2: 20kHz', 'Target 3: 100kHz',3)
grid on
title('Induced Heating Versus Frequency For Three Different Targets: Voltage Drive')
ylabel('Power (Watts)')
xlabel('Frequency (Hz)')
axis([1e2,1e6,1e-6,1e-2])

figure(3)
semilogx(f,factor)
grid on
title('Relative Power Dissipation For Three Different Targets')
ylabel('Relative Power')
xlabel('Frequency (Hz)')
```

B.3.16 THDcomparison.m

```
%THDComparison.m
%Calculates THD for Marx and PWM converters driving an RL load at its breakpoint
%This script can be modified to handle 3 inductively coupled targets.

clear
%%%%%%%%%%%%%%%%%%%%%%%%%%%%%%%%%%%%%%%%%%%%%%%%%%%%%%%%%%%%%%%%%%%%%%%%%%%%%%%%%%%%
%Initialize parameters
%%%%%%%%%%%%%%%%%%%%%%%%%%%%%%%%%%%%%%%%%%%%%%%%%%%%%%%%%%%%%%%%%%%%%%%%%%%%%%%%%%%%
Fc=1;                             %Carrier frequency (Hz)
Tstart=1;                         %Time offset, pick greater than 5 time constants
T=1/Fc+Tstart;                    %Carrier period (Secs)

Mapoints=10;                      %Number of Ma (amplitude modulation ratio) points
```

```
Tpoints=2000;                       %Number of sample points in period T
levels=3;                           %Number of Marx levels
Vdc=1/levels;                       %Marx voltage level
qt=.5;                              %Quantization trigger level
qi=1;                               %Quantization interval

L=[1 1e-3 1e-3 1e-3]/(2*pi);        %Inductances
R=[1, 1e6, 1e6, 1e6];               %Resistances
C=[Inf,Inf,Inf,Inf];                %Capacitances

%%%%%%%%%%%%%%%%%%%%%%%%%%%%%%%%%%%%%%%%%%%%%%%%%%%%%%%%%%%%%%%%%%%%%%%%%%%%%%%%%%%%%%%%%%%%
%Define Ma and time vectors
%%%%%%%%%%%%%%%%%%%%%%%%%%%%%%%%%%%%%%%%%%%%%%%%%%%%%%%%%%%%%%%%%%%%%%%%%%%%%%%%%%%%%%%%%%%%
A=linspace(0,1.0*levels,Mapoints);  %Ma varies from 0 to 1
A1=linspace(0,1.5,40);
A2=linspace(1.5,1.52,40);
A3=linspace(1.52,2.5,40);
A4=linspace(2.5,2.54,40);
A5=linspace(2.54,3,40);
A=[A1,A2,A3,A4,A5];
t=linspace (0,T,Tpoints);           %t varies over one period

%%%%%%%%%%%%%%%%%%%%%%%%%%%%%%%%%%%%%%%%%%%%%%%%%%%%%%%%%%%%%%%%%%%%%%%%%%%%%%%%%%%%%%%%%%%%
%Build matlab system representation of load
%%%%%%%%%%%%%%%%%%%%%%%%%%%%%%%%%%%%%%%%%%%%%%%%%%%%%%%%%%%%%%%%%%%%%%%%%%%%%%%%%%%%%%%%%%%%
K12=.0;
K13=.0;
K14=.0;
M12=K12*sqrt(L(1)*L(2));
M13=K13*sqrt(L(1)*L(3));
M14=K14*sqrt(L(1)*L(4));

Rmat=[R(1),0,0,0;0,R(2),0,0;0,0,R(3),0;0,0,0,R(4)];
Lmat=[L(1),M12,M13,M14;M12,L(2),0,0;M13,0,L(3),0;M14,0,0,L(4)];
invCmat=[1/C(1),0,0,0;0,1/C(2),0,0;0,0,1/C(3),0;0,0,0,1/C(4)];
Aload=[-1*inv(Lmat)*Rmat,inv(Lmat); -1*invCmat, zeros(4)];
Bload=[inv(Lmat), zeros(4); zeros(4), zeros(4)];
Cload=[eye(4) zeros(4)];  %Gives currents through resistance
%Cload=[Rmat zeros(4)];  %Gives voltages across resistance
Dload=[zeros(4) zeros(4)];
sys=ss(Aload,Bload,Cload,Dload);
[Num,Den]=ss2tf(Aload,Bload,Cload,Dload,1);
Poles=roots(Den);
Taus=1./Poles

%%%%%%%%%%%%%%%%%%%%%%%%%%%%%%%%%%%%%%%%%%%%%%%%%%%%%%%%%%%%%%%%%%%%%%%%%%%%%%%%%%%%%%%%%%%%
%Define quantizer to simulate Marx inverter
%%%%%%%%%%%%%%%%%%%%%%%%%%%%%%%%%%%%%%%%%%%%%%%%%%%%%%%%%%%%%%%%%%%%%%%%%%%%%%%%%%%%%%%%%%%%
%Define reference sinewave voltage
v=A'*sin(2*pi*Fc*t);
%Define quantizer characteristics
partition=[(-levels+(1-qt)):qi:0,qt:qi:(levels-(1-qt))];
codebook=[-levels*Vdc:Vdc:levels*Vdc];
%Generate Marx waveform, find fundamental and calculate currents using Marx input
```

```
for k=1:length(A);
[indx,Vm(k,:)]=quantiz(v(k,:),partition,codebook);
%Fundamental Marx amplitude
B1M(k)=2/(T)*trapz(t,Vm(k,:).*sin(2*pi*Fc*t));
%Calculate currents using Marx waveform as input
I(:,:,k)=lsim(sys,[Vm(k,:)',zeros(length(t),7)],t);
end

I1=I(:,1:4:length(A)*4);
I2=I(:,2:4:length(A)*4);
I3=I(:,3:4:length(A)*4);
I4=I(:,4:4:length(A)*4);

%%%%%%%%%%%%%%%%%%%%%%%%%%%%%%%%%%%%%%%%%%%%%%%%%%%%%%%%%%%%%%%%%%%%%%%%%%%%%%%%%%%%%%%%%%%%%%%%%%%%%%
%Calculate fundamental current waveforms
%%%%%%%%%%%%%%%%%%%%%%%%%%%%%%%%%%%%%%%%%%%%%%%%%%%%%%%%%%%%%%%%%%%%%%%%%%%%%%%%%%%%%%%%%%%%%%%%%%%%%%
%Define unit sinewave voltage
vunit=sin(2*pi*Fc*t);

%Calculate currents
Iunit=lsim(sys,[vunit',zeros(length(t),7)],t);
Iunit1=Iunit(:,1);
Iunit2=Iunit(:,2);
Iunit3=Iunit(:,3);
Iunit4=Iunit(:,4);

%Scale currents
Ifun1=Iunit1*B1M;
Ifun2=Iunit2*B1M;
Ifun3=Iunit3*B1M;
Ifun4=Iunit4*B1M;

%%%%%%%%%%%%%%%%%%%%%%%%%%%%%%%%%%%%%%%%%%%%%%%%%%%%%%%%%%%%%%%%%%%%%%%%%%%%%%%%%%%%%%%%%%%%%%%%%%%%%%
%Take second half of vectors to avoid transient (5 time constants later)
%%%%%%%%%%%%%%%%%%%%%%%%%%%%%%%%%%%%%%%%%%%%%%%%%%%%%%%%%%%%%%%%%%%%%%%%%%%%%%%%%%%%%%%%%%%%%%%%%%%%%%
nut=floor((Tstart/T)*Tpoints+1):Tpoints;
t=t(nut);
v=v(:,nut);
Vm=Vm(:,nut);
I=I(nut,:,:);

I1=I1(nut,:);
I2=I2(nut,:);
I3=I3(nut,:);
I4=I4(nut,:);

Ifun1=Ifun1(nut,:);
Ifun2=Ifun2(nut,:);
Ifun3=Ifun3(nut,:);
Ifun4=Ifun4(nut,:);

%%%%%%%%%%%%%%%%%%%%%%%%%%%%%%%%%%%%%%%%%%%%%%%%%%%%%%%%%%%%%%%%%%%%%%%%%%%%%%%%%%%%%%%%%%%%%%%%%%%%%%
%Calculate total harmonic distortion
%%%%%%%%%%%%%%%%%%%%%%%%%%%%%%%%%%%%%%%%%%%%%%%%%%%%%%%%%%%%%%%%%%%%%%%%%%%%%%%%%%%%%%%%%%%%%%%%%%%%%%
```

```
%Mean-square of the Marx voltage using half of T
VMS=1/(T-Tstart)*trapz(t',Vm.^2');

%Determine DC offset of inductor current
DCoffset1=(max(I1)+min(I1))/2;
DCoffset2=(max(I2)+min(I2))/2;
DCoffset3=(max(I3)+min(I3))/2;
DCoffset4=(max(I4)+min(I4))/2;

%Needed for matrix math in next step
DCoffset1=diag(DCoffset1);
DCoffset2=diag(DCoffset2);
DCoffset3=diag(DCoffset3);
DCoffset4=diag(DCoffset4);

%Remove DC offset from current
I1=I1-ones(length(A),length(t))'*DCoffset1;
I2=I2-ones(length(A),length(t))'*DCoffset2;
I3=I3-ones(length(A),length(t))'*DCoffset3;
I4=I4-ones(length(A),length(t))'*DCoffset4;

%Determine DC offset of inductor current
DCoffsetfun1=(max(Ifun1)+min(Ifun1))/2;
DCoffsetfun2=(max(Ifun2)+min(Ifun2))/2;
DCoffsetfun3=(max(Ifun3)+min(Ifun3))/2;
DCoffsetfun4=(max(Ifun4)+min(Ifun4))/2;

%Needed for matrix math in next step
DCoffsetfun1=diag(DCoffsetfun1);
DCoffsetfun2=diag(DCoffsetfun2);
DCoffsetfun3=diag(DCoffsetfun3);
DCoffsetfun4=diag(DCoffsetfun4);

%Remove DC offset from current
Ifun1=Ifun1-ones(length(A),length(t))'*DCoffsetfun1;
Ifun2=Ifun2-ones(length(A),length(t))'*DCoffsetfun2;
Ifun3=Ifun3-ones(length(A),length(t))'*DCoffsetfun3;
Ifun4=Ifun4-ones(length(A),length(t))'*DCoffsetfun4;

%Find %THD of Marx voltage
THD=100*[(2*VMS-B1M.^2)./B1M.^2].^.5;

%%%%%%%%%%%%%%%%%%%%%%%%%%%%%%%%%%%%%%%%%%%%%%%%%%%%%%%%%%%%%%%%%%%%%%%%%%%%%%%%%%%%%%%%%%%%
%Calculate the weighted total harmonic distortion
%%%%%%%%%%%%%%%%%%%%%%%%%%%%%%%%%%%%%%%%%%%%%%%%%%%%%%%%%%%%%%%%%%%%%%%%%%%%%%%%%%%%%%%%%%%%
%Sum of current harmonics minus fundamental
Ih1=I1-Ifun1;
Ih2=I2-Ifun2;
Ih3=I3-Ifun3;
Ih4=I4-Ifun4;

%Calculate the mean-square of the extra harmonics
HMS1=1/(T-Tstart)*trapz(t',Ih1.^2);
HMS2=1/(T-Tstart)*trapz(t',Ih2.^2);
```

```
HMS3=1/(T-Tstart)*trapz(t',Ih3.^2);
HMS4=1/(T-Tstart)*trapz(t',Ih4.^2);

%Calculate current THD
MTHD1=100*sqrt(HMS1./(.5*max(Ifun1).^2));
MTHD2=100*sqrt(HMS2./(.5*max(Ifun2).^2));
MTHD3=100*sqrt(HMS3./(.5*max(Ifun3).^2));
MTHD4=100*sqrt(HMS4./(.5*max(Ifun4).^2));

%%%%%%%%%%%%%%%%%%%%%%%%%%%%%%%%%%%%%%%%%%%%%%%%%%%%%%%%%%%%%%%%%%%%%%%%%%%%%%%%%%%%%%%%%%%%
%Save for plotting
%%%%%%%%%%%%%%%%%%%%%%%%%%%%%%%%%%%%%%%%%%%%%%%%%%%%%%%%%%%%%%%%%%%%%%%%%%%%%%%%%%%%%%%%%%%%
MI1=I1';
MI2=I2';
MI3=I3';
MI4=I4';
AM=A;

%%%%%%%%%%%%%%%%%%%%%%%%%%%%%%%%%%%%%%%%%%%%%%%%%%%%%%%%%%%%%%%%%%%%%%%%%%%%%%%%%%%%%%%%%%%%
%Initialize parameters
%%%%%%%%%%%%%%%%%%%%%%%%%%%%%%%%%%%%%%%%%%%%%%%%%%%%%%%%%%%%%%%%%%%%%%%%%%%%%%%%%%%%%%%%%%%%
for z=1:3;

clear I

Mf=[3 5 10];                        %PWM frequency modulation ratios
Fs=Mf(z)*Fc;                        %PWM sampling frequency (Hz)
Tpoints=2000;                       %Number of sample points in period T
Vdc=1;                              %PWM voltage level

%%%%%%%%%%%%%%%%%%%%%%%%%%%%%%%%%%%%%%%%%%%%%%%%%%%%%%%%%%%%%%%%%%%%%%%%%%%%%%%%%%%%%%%%%%%%
%Define Ma and time vectors
%%%%%%%%%%%%%%%%%%%%%%%%%%%%%%%%%%%%%%%%%%%%%%%%%%%%%%%%%%%%%%%%%%%%%%%%%%%%%%%%%%%%%%%%%%%%
A=linspace(0,1,Mapoints);           %Ma varies from 0 to 1
t=linspace (0,T,Tpoints);           %t varies over one period

%%%%%%%%%%%%%%%%%%%%%%%%%%%%%%%%%%%%%%%%%%%%%%%%%%%%%%%%%%%%%%%%%%%%%%%%%%%%%%%%%%%%%%%%%%%%
%Define reference sine voltages-- one for each phase leg
%%%%%%%%%%%%%%%%%%%%%%%%%%%%%%%%%%%%%%%%%%%%%%%%%%%%%%%%%%%%%%%%%%%%%%%%%%%%%%%%%%%%%%%%%%%%
Va=A'*sin(2*pi*Fc*t);               %Phase leg A
Vb=-Va;                             %Phase leg B

%%%%%%%%%%%%%%%%%%%%%%%%%%%%%%%%%%%%%%%%%%%%%%%%%%%%%%%%%%%%%%%%%%%%%%%%%%%%%%%%%%%%%%%%%%%%
%Generate Triangle waveform for sampling
%%%%%%%%%%%%%%%%%%%%%%%%%%%%%%%%%%%%%%%%%%%%%%%%%%%%%%%%%%%%%%%%%%%%%%%%%%%%%%%%%%%%%%%%%%%%
%phi=pi/2;                          %Phase of triangle waveform
phi=0;                              %Phase of triangle waveform; Use this one
tri=sawtooth(2*pi*Fs*t+phi, 0.5);   %Triangle waveform

%%%%%%%%%%%%%%%%%%%%%%%%%%%%%%%%%%%%%%%%%%%%%%%%%%%%%%%%%%%%%%%%%%%%%%%%%%%%%%%%%%%%%%%%%%%%
%Generate unipolar natural sampling PWM waveform
%%%%%%%%%%%%%%%%%%%%%%%%%%%%%%%%%%%%%%%%%%%%%%%%%%%%%%%%%%%%%%%%%%%%%%%%%%%%%%%%%%%%%%%%%%%%
PWMa=zeros(length(A),length(t));    %Initialize matrix
PWMb=zeros(length(A),length(t));    %Initialize matrix
```

```
tri=ones(length(A),1)*tri;                          %Create matrix of triangle waveforms

PWMa=sign(Va-tri);                                  %Compare reference A with triangle waveform
PWMa=.5*Vdc*(PWMa+ones(length(A),length(t)));       %Generate PWMa matrix
PWMb=sign(Vb-tri);                                  %Compare reference B with triangle waveform
PWMb=.5*Vdc*(PWMb+ones(length(A),length(t)));       %Generate PWMb matrix
PWM=(PWMa-PWMb)';                                   %Difference is PWM waveform across L

%%%%%%%%%%%%%%%%%%%%%%%%%%%%%%%%%%%%%%%%%%%%%%%%%%%%%%%%%%%%%%%%%%%%%%%%%%%%%%%%%%%%%%%%%%%%%%
%Build system response
%%%%%%%%%%%%%%%%%%%%%%%%%%%%%%%%%%%%%%%%%%%%%%%%%%%%%%%%%%%%%%%%%%%%%%%%%%%%%%%%%%%%%%%%%%%%%%
for k=1:length(A)
%Fundamental PWM amplitude
B1P(k)=2/(T)*trapz(t,PWM(:,k)'.*sin(2*pi*Fc*t));
%Calculate currents using PWM waveform as input
I(:,:,k)=lsim(sys,[PWM(:,k),zeros(length(t),7)],t);
end

I1=I(:,1:4:length(A)*4);
I2=I(:,2:4:length(A)*4);
I3=I(:,3:4:length(A)*4);
I4=I(:,4:4:length(A)*4);

%%%%%%%%%%%%%%%%%%%%%%%%%%%%%%%%%%%%%%%%%%%%%%%%%%%%%%%%%%%%%%%%%%%%%%%%%%%%%%%%%%%%%%%%%%%%%%
%Calculate fundamental current waveforms
%%%%%%%%%%%%%%%%%%%%%%%%%%%%%%%%%%%%%%%%%%%%%%%%%%%%%%%%%%%%%%%%%%%%%%%%%%%%%%%%%%%%%%%%%%%%%%
%Define reference sinewave voltage
vunit=sin(2*pi*Fc*t);

%Calculate currents
Iunit=lsim(sys,[vunit',zeros(length(t),7)],t);
Iunit1=Iunit(:,1);
Iunit2=Iunit(:,2);
Iunit3=Iunit(:,3);
Iunit4=Iunit(:,4);

%Scale currents
Ifun1=Iunit1*B1P;
Ifun2=Iunit2*B1P;
Ifun3=Iunit3*B1P;
Ifun4=Iunit4*B1P;

%%%%%%%%%%%%%%%%%%%%%%%%%%%%%%%%%%%%%%%%%%%%%%%%%%%%%%%%%%%%%%%%%%%%%%%%%%%%%%%%%%%%%%%%%%%%%%
%Take second half of vectors to avoid transient (5 time constants later)
%%%%%%%%%%%%%%%%%%%%%%%%%%%%%%%%%%%%%%%%%%%%%%%%%%%%%%%%%%%%%%%%%%%%%%%%%%%%%%%%%%%%%%%%%%%%%%
nut=floor((Tstart/T)*Tpoints+1):Tpoints;
t=t(nut);
Va=Va(:,nut);
PWM=PWM(nut,:);
I=I(nut,:,:);
tri=tri(:,nut);
I1=I1(nut,:);
I2=I2(nut,:);
```

```
I3=I3(nut,:);
I4=I4(nut,:);
Ifun1=Ifun1(nut,:);
Ifun2=Ifun2(nut,:);
Ifun3=Ifun3(nut,:);
Ifun4=Ifun4(nut,:);

%%%%%%%%%%%%%%%%%%%%%%%%%%%%%%%%%%%%%%%%%%%%%%%%%%%%%%%%%%%%%%%%%%%%%%%%%%%%%%%%%%%%%%%%%%%%%%%%%%%
%Calculate total harmonic distortion
%%%%%%%%%%%%%%%%%%%%%%%%%%%%%%%%%%%%%%%%%%%%%%%%%%%%%%%%%%%%%%%%%%%%%%%%%%%%%%%%%%%%%%%%%%%%%%%%%%%
%Mean-square of the PWM voltage using half of T
VMS=2/T*trapz(t',PWM.^2);

%Determine DC offset of inductor current
DCoffset1=(max(I1)+min(I1))/2;
DCoffset2=(max(I2)+min(I2))/2;
DCoffset3=(max(I3)+min(I3))/2;
DCoffset4=(max(I4)+min(I4))/2;

%Needed for matrix math in next step
DCoffset1=diag(DCoffset1);
DCoffset2=diag(DCoffset2);
DCoffset3=diag(DCoffset3);
DCoffset4=diag(DCoffset4);

%Remove DC offset from current
I1=I1-ones(length(A),length(t))'*DCoffset1;
I2=I2-ones(length(A),length(t))'*DCoffset2;
I3=I3-ones(length(A),length(t))'*DCoffset3;
I4=I4-ones(length(A),length(t))'*DCoffset4;

%Determine DC offset of inductor current
DCoffsetfun1=(max(Ifun1)+min(Ifun1))/2;
DCoffsetfun2=(max(Ifun2)+min(Ifun2))/2;
DCoffsetfun3=(max(Ifun3)+min(Ifun3))/2;
DCoffsetfun4=(max(Ifun4)+min(Ifun4))/2;

%Needed for matrix math in next step
DCoffsetfun1=diag(DCoffsetfun1);
DCoffsetfun2=diag(DCoffsetfun2);
DCoffsetfun3=diag(DCoffsetfun3);
DCoffsetfun4=diag(DCoffsetfun4);

%Remove DC offset from Current
Ifun1=Ifun1-ones(length(A),length(t))'*DCoffsetfun1;
Ifun2=Ifun2-ones(length(A),length(t))'*DCoffsetfun2;
Ifun3=Ifun3-ones(length(A),length(t))'*DCoffsetfun3;
Ifun4=Ifun4-ones(length(A),length(t))'*DCoffsetfun4;

%Find %THD of PWM voltage
THD=100*[(VMS-.5*(B1P*Vdc).^2)./(.5*(B1P*Vdc).^2)].^.5;

%%%%%%%%%%%%%%%%%%%%%%%%%%%%%%%%%%%%%%%%%%%%%%%%%%%%%%%%%%%%%%%%%%%%%%%%%%%%%%%%%%%%%%%%%%%%%%%%%%%
%Calculate the weighted harmonic distortion
```

```
%%%%%%%%%%%%%%%%%%%%%%%%%%%%%%%%%%%%%%%%%%%%%%%%%%%%%%%%%%%%%%%%%%%%%%%%%%%%%%%%%%%%%%%%%%%%
%Sum of current harmonics minus fundamental
Ih1=I1-Ifun1;
Ih2=I2-Ifun2;
Ih3=I3-Ifun3;
Ih4=I4-Ifun4;

%Calculate the mean-square of the extra current harmonics
HMS1=1/(T-Tstart)*trapz(t',Ih1.^2);
HMS2=1/(T-Tstart)*trapz(t',Ih2.^2);
HMS3=1/(T-Tstart)*trapz(t',Ih3.^2);
HMS4=1/(T-Tstart)*trapz(t',Ih4.^2);

%Calculate current THD
PTHD1(z,:)=100*sqrt(HMS1./(.5*max(Ifun1).^2));
PTHD2(z,:)=100*sqrt(HMS2./(.5*max(Ifun2).^2));
PTHD3(z,:)=100*sqrt(HMS3./(.5*max(Ifun3).^2));
PTHD4(z,:)=100*sqrt(HMS4./(.5*max(Ifun4).^2));

%%%%%%%%%%%%%%%%%%%%%%%%%%%%%%%%%%%%%%%%%%%%%%%%%%%%%%%%%%%%%%%%%%%%%%%%%%%%%%%%%%%%%%%%%%%%
%Save and transpose for easy plotting
%%%%%%%%%%%%%%%%%%%%%%%%%%%%%%%%%%%%%%%%%%%%%%%%%%%%%%%%%%%%%%%%%%%%%%%%%%%%%%%%%%%%%%%%%%%%
PWM=PWM';
PI1=I1';
PI2=I2';
PI3=I3';
PI4=I4';
AP=A;
end

%%%%%%%%%%%%%%%%%%%%%%%%%%%%%%%%%%%%%%%%%%%%%%%%%%%%%%%%%%%%%%%%%%%%%%%%%%%%%%%%%%%%%%%%%%%%
%Plot THD versus amplitude
%%%%%%%%%%%%%%%%%%%%%%%%%%%%%%%%%%%%%%%%%%%%%%%%%%%%%%%%%%%%%%%%%%%%%%%%%%%%%%%%%%%%%%%%%%%%
figure(1)
plot(B1M/(1),MTHD1,'b-',B1P/Vdc,PTHD1(1,:),'gs-',B1P/Vdc,PTHD1(2,:),'go-',B1P/Vdc,PTHD1(3,:),'gd-')
grid on
title('%THD vs Normalized Fundamental Voltage')
ylabel('%THD of Load Current')
xlabel('Fundamental Voltage Normalized to 3 Vdc')
legend('Quantized Marx Inverter, 7-Levels','PWM Full-Bridge Inverter, Mf=3','PWM Full-Bridge Inverter, Mf=5'
axis([0.2,1,0,35])

%%%%%%%%%%%%%%%%%%%%%%%%%%%%%%%%%%%%%%%%%%%%%%%%%%%%%%%%%%%%%%%%%%%%%%%%%%%%%%%%%%%%%%%%%%%%
%Plot converter voltage and current as a sanity check
%%%%%%%%%%%%%%%%%%%%%%%%%%%%%%%%%%%%%%%%%%%%%%%%%%%%%%%%%%%%%%%%%%%%%%%%%%%%%%%%%%%%%%%%%%%%
figure(2)
plot(t,Vm(length(AM),:),'b',t,MI1(length(AM),:),'r')
grid on

figure(3)
plot(t,PWM(length(AP),:),'b',t,PI1(length(AP),:),'r')
grid on
```

B.3.17 Tuned.m

```
%Tuned.m
%This script plots the measured Vin-to-Iout transfer function for three tuned targets
%coupled to a single primary coil. Their frequencies are roughly 56.1kHz, 67.2kHz, 81.9kHz
%single primary coil. These measurements were made with a network analyzer.

clear
%%%%%%%%%%%%%%%%%%%%%%%%%%%%%%%%%%%%%%%%%%%%%%%%%%%%%%%%%%%%%%%%%%%%%%%%%%%%%%%%%%%%%%%%%%%
%Read network analyzer data files
%%%%%%%%%%%%%%%%%%%%%%%%%%%%%%%%%%%%%%%%%%%%%%%%%%%%%%%%%%%%%%%%%%%%%%%%%%%%%%%%%%%%%%%%%%%
%Magnitude of current in primary induction coil
[header1, data1] =hdrload('IM.txt');
F1=data1(:,1);
TPM=10.^(data1(:,2)/20);
%Phase of current in primary induction coil
[header1, data1] =hdrload('IP.txt');
TPP=data1(:,2);
%Magnitude of current in bottom target
[header1, data1] =hdrload('BM.txt');
TBM=10.^(data1(:,2)/20);
%Magnitude of current in middle target
[header1, data1] =hdrload('MM.txt');
TMM=10.^(data1(:,2)/20);
%Magnitude of current in top target
[header1, data1] =hdrload('TM.txt');
TTM=10.^(data1(:,2)/20);
%Magnitude of voltage across primary induction coil
[header1, data1] =hdrload('VM.txt');
%Need a factor of .5 here to account for the gain of the diff amp and current probe
VM=10.^(data1(:,2)/20)*.5;

%%%%%%%%%%%%%%%%%%%%%%%%%%%%%%%%%%%%%%%%%%%%%%%%%%%%%%%%%%%%%%%%%%%%%%%%%%%%%%%%%%%%%%%%%%%
%System parameters
%%%%%%%%%%%%%%%%%%%%%%%%%%%%%%%%%%%%%%%%%%%%%%%%%%%%%%%%%%%%%%%%%%%%%%%%%%%%%%%%%%%%%%%%%%%
%Input voltage amplitude
vin=1

%Target coil resistances measured at different frequencies
R=[.117 1.29 1.26 1.30]; %56.088kHz
%R=[.136 1.54 1.52 1.55]; %67.22kHz
%R=[.165 1.92 1.88 1.92]; %81.87kHz
%Capacitances
C=1e-6*[10e6, .0212, .0306, .0412]; %[ top, mid, bot]

%Resistance, inductance and capacitance matrices
Rmat=[R(1),0,0,0;0,R(2),0,0;0,0,R(3),0;0,0,0,R(4)];
Lmat=[2.09941e-005, 2.62083e-005, 2.79574e-005, 2.55882e-005;
2.61779e-005, 0.000196622, 1.76656e-005, 2.76007e-006;
2.79071e-005, 1.76631e-005, 0.000188768, 1.63797e-005;
2.55452e-005,  2.71534e-006, 1.63682e-005, 0.000192675];
Cmat=[C(1),0,0,0;0,C(2),0,0;0,0,C(3),0;0,0,0,C(4)];
```

```
%%%%%%%%%%%%%%%%%%%%%%%%%%%%%%%%%%%%%%%%%%%%%%%%%%%%%%%%%%%%%%%%%%%%%%%%%%%%%%%%%%%%%%%%%%%%%%%%%%
%State space representation
%%%%%%%%%%%%%%%%%%%%%%%%%%%%%%%%%%%%%%%%%%%%%%%%%%%%%%%%%%%%%%%%%%%%%%%%%%%%%%%%%%%%%%%%%%%%%%%%%%
A=[-1*inv(Lmat)*Rmat,inv(Lmat); -1*inv(Cmat), zeros(4)]
B=[inv(Lmat), zeros(4); zeros(4), zeros(4)]
C=[eye(4) zeros(4)]  %Gives currents through resistance
%C=[Rmat zeros(4)]   %Gives voltages across resistance
D=[zeros(4) zeros(4)]
sys=ss(A,B,C,D);
[Num,Den]=ss2tf(A,B,C,D,1);

%%%%%%%%%%%%%%%%%%%%%%%%%%%%%%%%%%%%%%%%%%%%%%%%%%%%%%%%%%%%%%%%%%%%%%%%%%%%%%%%%%%%%%%%%%%%%%%%%%
%Calculate target (Vin-2-Iout) magnitude responses
%%%%%%%%%%%%%%%%%%%%%%%%%%%%%%%%%%%%%%%%%%%%%%%%%%%%%%%%%%%%%%%%%%%%%%%%%%%%%%%%%%%%%%%%%%%%%%%%%%
%Frequency range
f=logspace(2,6,10000);
w=2*pi*f;

%Bode response
[Mag(:,1),Phase(:,1)]=bode(vin*Num(1,:),Den,w);
[Mag(:,2),Phase(:,2)]=bode(vin*Num(2,:),Den,w);
[Mag(:,3),Phase(:,3)]=bode(vin*Num(3,:),Den,w);
[Mag(:,4),Phase(:,4)]=bode(vin*Num(4,:),Den,w);

%Target magnitude responses
Mag1=Mag(:,1);
Mag2=Mag(:,2);
Mag3=Mag(:,3);
Mag4=Mag(:,4);

%%%%%%%%%%%%%%%%%%%%%%%%%%%%%%%%%%%%%%%%%%%%%%%%%%%%%%%%%%%%%%%%%%%%%%%%%%%%%%%%%%%%%%%%%%%%%%%%%%
%Plot results
%%%%%%%%%%%%%%%%%%%%%%%%%%%%%%%%%%%%%%%%%%%%%%%%%%%%%%%%%%%%%%%%%%%%%%%%%%%%%%%%%%%%%%%%%%%%%%%%%%
figure(1)
loglog(f,Mag1,'k',F1,TPM./VM,'k.-')
ylabel('Magnitude')
title('Theoretical and Measured V_{in}-to-I_{n} Transfer Functions')
grid on
legend('Theoretical V_{in}-to-I_{1}','Measured V_{in}-to-I_{1}',2)
axis([5e4,1e5,1e-3,1e1])

figure(2)
loglog(f,Mag2,'r',F1,TTM./VM,'r.-')
ylabel('Magnitude')
grid on
legend('Theoretical V_{in}-to-I_{2}','Measured V_{in}-to-I_{2}',2)
axis([5e4,1e5,1e-3,1e1])

figure(3)
loglog(f,Mag3,'g',F1,TMM./VM,'g.-')
ylabel('Magnitude')
grid on
legend('Theoretical V_{in}-to-I_{3}','Measured V_{in}-to-I_{3}',2)
axis([5e4,1e5,1e-3,1e1])
```

```
figure(4)
loglog(f,Mag4,'b',F1,TBM./VM,'b.-')
ylabel('Magnitude')
xlabel('Frequency (Hz)')
grid on
legend('Theoretical V_{in}-to-I_{4}','Measured V_{in}-to-I_{4}',2)
axis([5e4,1e5,1e-3,1e1])

figure(5)
subplot(3,1,1)
loglog(f,Mag2,'k',F1,TTM./VM,'r.')
axis([5e4,1e5,1e-3,1e0])
grid on
legend('81.9kHz Frequency Target, Predicted','81.9kHz Frequency Target, Measured',2)
title('V_{in} to I_{n} Transfer Function for Three Experimental Tuned Targets')
subplot(3,1,2)
loglog(f,Mag3,'k',F1,TMM./VM,'g.')
axis([5e4,1e5,1e-3,1e0])
grid on
legend('67.2kHz Frequency Target, Predicted','67.2kHz Frequency Target, Measured',3)
ylabel('Magnitude')
subplot(3,1,3)
loglog(f,Mag4,'k',F1,TBM./VM,'b.')
axis([5e4,1e5,1e-3,1e0])
grid on
legend('56.1kHz Frequency Target, Predicted','56.1kHz Frequency Target, Measured',3)
xlabel('Frequency (Hz)')
```

B.3.18 Wires.m

```
%Wires.m
%This script plots the measured Vin-to-Iout transfer function for three 20AWGC wires of
%different conductivity: Copper, alloy 90, alloy 800. All three wire were inductively
%coupled to a single primary coil. These mesurements were made with a network analyzer.

clear
%%%%%%%%%%%%%%%%%%%%%%%%%%%%%%%%%%%%%%%%%%%%%%%%%%%%%%%%%%%%%%%%%%%%%%%%%%%%%%%%%%%%%%%%%%%
%Read network analyzer data files
%%%%%%%%%%%%%%%%%%%%%%%%%%%%%%%%%%%%%%%%%%%%%%%%%%%%%%%%%%%%%%%%%%%%%%%%%%%%%%%%%%%%%%%%%%%
%Magnitude of current in 20AWG copper wire
[header1, data1] =hdrload('CU3.txt');
F1=data1(:,1);
CuS=10.^(data1(:,2)/20);

%Magnitude of current in 20AWG alloy 90 wire
[header1, data1] =hdrload('A903.txt');
F2=data1(:,1);
A90S=10.^(data1(:,2)/20);

%Magnitude of currentin 20AWGC alloy 800 wire
```

```
[header1, data1] =hdrload('A8003.txt');
F3=data1(:,1);
A8S=10.^(data1(:,2)/20);

%Magnitude of current in primary induction coil
[header1, data1] =hdrload('I3.txt');
F4=data1(:,1);
PI=10.^(data1(:,2)/20);

%Magnitude of voltage across primary induction coil
[header1, data1] =hdrload('V3H.txt');
F5=data1(:,1);
%Need a factor of ten here to account for the gain of the diff amp and current probe
V3=10.^(data1(:,2)/20)*10;

%%%%%%%%%%%%%%%%%%%%%%%%%%%%%%%%%%%%%%%%%%%%%%%%%%%%%%%%%%%%%%%%%%%%%%%%%%%%%%%%%%%%%%%%%%%%%
%System parameters
%%%%%%%%%%%%%%%%%%%%%%%%%%%%%%%%%%%%%%%%%%%%%%%%%%%%%%%%%%%%%%%%%%%%%%%%%%%%%%%%%%%%%%%%%%%%%%
%Input voltage amplitude
vin=1;

%Resistance of copper wire
Rcu=.006279;
%Wire resistances (primary, copper, 90, 800)
R=[.562 Rcu 8.678*Rcu 77.138*Rcu];

%These values were computed using FastHenry
%Primary side inductance
Lp=201.88e-6;
%Target inductances
Ls=0.169e-6;
%Inductances
L=[Lp Ls Ls Ls];
L11=Lp
L22=Ls
L33=Ls
L44=Ls
L12=1.86298e-6;
L13=1.95859e-6;
L14=1.84152e-6;
L23=2.492e-8;
L24=8.53672e-9;
L34=2.21394e-8;

%Coupling coefficients
K12=L12/sqrt(L(1)*L(2))
K13=L13/sqrt(L(1)*L(3))
K14=L14/sqrt(L(1)*L(4))
K23=L23/sqrt(L(2)*L(3));
K24=L24/sqrt(L(2)*L(4));
K34=L34/sqrt(L(3)*L(4));

%Resistance and inductance matrices
Rmat=-1*[R(1),0,0,0;0,R(2),0,0;0,0,R(3),0;0,0,0,R(4)];
```

```
Lmat=[L(1),L12,L13,L14;L12,L(2),L23,L24;L13,L23,L(3),L34;L14,L24,L34,L(4)];

%%%%%%%%%%%%%%%%%%%%%%%%%%%%%%%%%%%%%%%%%%%%%%%%%%%%%%%%%%%%%%%%%%%%%%%%%%%%%%%%%%%%%%%%%%%%
%State space representation
%%%%%%%%%%%%%%%%%%%%%%%%%%%%%%%%%%%%%%%%%%%%%%%%%%%%%%%%%%%%%%%%%%%%%%%%%%%%%%%%%%%%%%%%%%%%
A=inv(Lmat)*Rmat;
B=inv(Lmat);
B=B(1:4,1);
C=eye(4);
D=zeros(4);
D=D(1:4,1);
sys=ss(A,B,C,D);
[Num,Den]=ss2tf(A,B,C,D,1);

%%%%%%%%%%%%%%%%%%%%%%%%%%%%%%%%%%%%%%%%%%%%%%%%%%%%%%%%%%%%%%%%%%%%%%%%%%%%%%%%%%%%%%%%%%%%
%Calculate target (Vin-2-Iout) magnitude responses
%%%%%%%%%%%%%%%%%%%%%%%%%%%%%%%%%%%%%%%%%%%%%%%%%%%%%%%%%%%%%%%%%%%%%%%%%%%%%%%%%%%%%%%%%%%%
%Frequency range
f=logspace(2,6,1000);
w=2*pi*f;

%Bode response
[Mag(:,1),Phase(:,1)]=bode(vin*Num(1,:),Den,w);
[Mag(:,2),Phase(:,2)]=bode(vin*Num(2,:),Den,w);
[Mag(:,3),Phase(:,3)]=bode(vin*Num(3,:),Den,w);
[Mag(:,4),Phase(:,4)]=bode(vin*Num(4,:),Den,w);

%Target magnitude responses
Mag1=Mag(:,1);
Mag2=Mag(:,2);
Mag3=Mag(:,3);
Mag4=Mag(:,4);

%%%%%%%%%%%%%%%%%%%%%%%%%%%%%%%%%%%%%%%%%%%%%%%%%%%%%%%%%%%%%%%%%%%%%%%%%%%%%%%%%%%%%%%%%%%%
%Corrections to model, i.e. second order effects and instrumentation
%%%%%%%%%%%%%%%%%%%%%%%%%%%%%%%%%%%%%%%%%%%%%%%%%%%%%%%%%%%%%%%%%%%%%%%%%%%%%%%%%%%%%%%%%%%%
%Account from probe insertion impedance at these discrete frequencies
f0=[1e3,2e3,3e3,4e3,5e3,6e3,7e3,8e3,9e3,1e4,2e4,3e4,4e4,5e4,6e4,7e4,8e4,9e4,1e5,2e5,3e5,4e5,
    5e5];
%Probe resistance
Rpb=[.038,.072,.079,.096,.099,.106,.110,.114,.118,.120,.124,.123,.121,.122,.123,.127,.129,
    .133,.136,.136,.100,.066,.126]/25;
%Probe inductance
Lpb=[8.1,4.4,2.9,2.0,1.6,1.3,1.04,.87,.75,.65,.34,.30,.28,.28,.29,.287,.284,.292,.276,.242,
    .258,.293,.337]*1e-6/25;

%Primary coil resistance with frequency
R1=[.562,.563,.566,.568,.572,.575,.580,.585,.589,.597,.68,.79,.91,1.04,1.16,1.27,1.38,1.49,
    1.59,2.5,3.4,4.3,5.5];

%Account for AC resistance in targets
R2=ACR(8.118e-4/2,3e-2,5.80e7,f0);
R3=ACR(8.118e-4/2,3e-2,6.683567642e6,f0);
R4=ACR(8.118e-4/2,3e-2,7.518991937e5,f0);
```

```
%Don't account for AC resistance in targets
%R1=R(1)
%R2=R(2)
%R3=R(3)
%R4=R(4)

%%%%%%%%%%%%%%%%%%%%%%%%%%%%%%%%%%%%%%%%%%%%%%%%%%%%%%%%%%%%%%%%%%%%%%%%%%%%%%%%%%%%%%%%%%%%
%Recompute model parameters with corrections
%%%%%%%%%%%%%%%%%%%%%%%%%%%%%%%%%%%%%%%%%%%%%%%%%%%%%%%%%%%%%%%%%%%%%%%%%%%%%%%%%%%%%%%%%%%%
%Convert frequency points to rps
w=2*pi*f0;
%Convert to S-domain
s=j*w;

%Recompute inductances and resistances to include probe on primary side winding
L11=Lp+Lpb;
L12=K12*sqrt(L(1)*L(2));
L13=K13*sqrt(L(1)*L(3));
L14=K14*sqrt(L(1)*L(4));
L23=K23*sqrt(L(2)*L(3));
L24=K24*sqrt(L(2)*L(4));
L34=K34*sqrt(L(3)*L(4));
R1=R1+Rpb;
I1_num= (-L22.*L33.*L44+L22.*L34.^2+L23.^2.*L44-2.*L23.*L24.*L34+L24.^2.*L33).*s.^3+
    (-L44.*R3.*L22-L22.*L33.*R4-L44.*R2.*L33+L23.^2.*R4+R3.*L24.^2+L34.^2.*R2).*s.^2+
    (-R3.*L22.*R4-L44.*R3.*R2-R2.*L33.*R4).*s-R3.*R2.*R4;
Den1=((-L11.*L22.*L33.*L44+L11.*L22.*L34.^2+L11.*L23.^2.*L44-2.*L11.*L23.*L24.*L34+
    L11.*L24.^2.*L33+L12.^2.*L33.*L44-L12.^2.*L34.^2-2.*L12.*L23.*L13.*L44+
    2.*L12.*L23.*L14.*L34+2.*L12.*L24.*L13.*L34-2.*L12.*L24.*L14.*L33+L22.*L13.^2.*L44-
    2.*L13.*L22.*L14.*L34-L13.^2.*L24.^2+2.*L13.*L24.*L14.*L23+L22.*L14.^2.*L33-
    L14.^2.*L23.^2).*s.^4+(-L44.*R3.*L11.*L22-L44.*R1.*L22.*L33-L44.*R2.*L11.*L33+
    L24.^2.*R3.*L11+L12.^2.*R4.*L33+L22.*R3.*L14.^2+L12.^2.*L44.*R3-2.*L13.*R2.*L14.*L34+
    L11.*L23.^2.*R4+L11.*L34.^2.*R2+L13.^2.*R2.*L44+R2.*L14.^2.*L33+L13.^2.*L22.*R4+
    L44.*R1.*L23.^2+L22.*R1.*L34.^2+R1.*L33.*L24.^2-2.*L13.*L12.*L23.*R4-
    2.*R1.*L23.*L24.*L34-R4.*L11.*L22.*L33-2.*R3.*L12.*L14.*L24).*s.^3+(R1.*R3.*L24.^2+
    R3.*L12.^2.*R4-L44.*R1.*R2.*L33-L22.*R3.*L11.*R4-R1.*L22.*L33.*R4+R2.*R3.*L14.^2-
    L44.*R1.*R3.*L22-R2.*L11.*L33.*R4-L44.*R2.*R3.*L11+R1.*L34.^2.*R2+L13.^2.*R2.*R4+
    R1.*L23.^2.*R4).*s.^2+(-R1.*R3.*L22.*R4-R1.*R2.*L33.*R4-R2.*R3.*L11.*R4-
    L44.*R1.*R3.*R2).*s-R1.*R3.*R2.*R4);
R1=R1-Rpb;
L11=Lp;

%Recompute inductances and resistances to include probe on copper target
L22=Ls+Lpb;
L12=K12*sqrt(L(1)*L(2));
L13=K13*sqrt(L(1)*L(3));
L14=K14*sqrt(L(1)*L(4));
L23=K23*sqrt(L(2)*L(3));
L24=K24*sqrt(L(2)*L(4));
L34=K34*sqrt(L(3)*L(4));
R2=R2+Rpb;
I2_num= -((-L12.*L33.*L44+L12.*L34.^2+L23.*L13.*L44-L23.*L14.*L34-L24.*L13.*L34+
    L24.*L14.*L33).*s.^2+(R3.*L14.*L24+L13.*L23.*R4-L44.*R3.*L12-L12.*L33.*R4).*s-
```

```
    L12.*R3.*R4).*s;
Den2=((-L11.*L22.*L33.*L44+L11.*L22.*L34.^2+L11.*L23.^2.*L44-2.*L11.*L23.*L24.*L34+
    L11.*L24.^2.*L33+L12.^2.*L33.*L44-L12.^2.*L34.^2-2.*L12.*L23.*L13.*L44+
    2.*L12.*L23.*L14.*L34+2.*L12.*L24.*L13.*L34-2.*L12.*L24.*L14.*L33+L22.*L13.^2.*L44-
    2.*L13.*L22.*L14.*L34-L13.^2.*L24.^2+2.*L13.*L24.*L14.*L23+L22.*L14.^2.*L33-
    L14.^2.*L23.^2).*s.^4+(-L44.*R3.*L11.*L22-L44.*R1.*L22.*L33-L44.*R2.*L11.*L33+
    L24.^2.*R3.*L11+L12.^2.*R4.*L33+L22.*R3.*L14.^2+L12.^2.*L44.*R3-2.*L13.*R2.*L14.*L34+
    L11.*L23.^2.*R4+L11.*L34.^2.*R2+L13.^2.*R2.*L44+R2.*L14.^2.*L33+L13.^2.*L22.*R4+
    L44.*R1.*L23.^2+L22.*R1.*L34.^2+R1.*L33.*L24.^2-2.*L13.*L12.*L23.*R4-
    2.*R1.*L23.*L24.*L34-R4.*L11.*L22.*L33-2.*R3.*L12.*L14.*L24).*s.^3+(R1.*R3.*L24.^2+
    R3.*L12.^2.*R4-L44.*R1.*R2.*L33-L22.*R3.*L11.*R4-R1.*L22.*L33.*R4+R2.*R3.*L14.^2-
    L44.*R1.*R3.*L22-R2.*L11.*L33.*R4-L44.*R2.*R3.*L11+R1.*L34.^2.*R2+L13.^2.*R2.*R4+
    R1.*L23.^2.*R4).*s.^2+(-R1.*R3.*L22.*R4-R1.*R2.*L33.*R4-R2.*R3.*L11.*R4-
    L44.*R1.*R3.*R2).*s-R1.*R3.*R2.*R4);
R2=R(2)
L22=Ls;

%Recompute inductances and resistances to include probe on alloy 90 target
L33=Ls+Lpb;
L12=K12*sqrt(L(1)*L(2));
L13=K13*sqrt(L(1)*L(3));
L14=K14*sqrt(L(1)*L(4));
L23=K23*sqrt(L(2)*L(3));
L24=K24*sqrt(L(2)*L(4));
L34=K34*sqrt(L(3)*L(4));
R3=R3+Rpb;
I3_num= ((-L12.*L23.*L44+L12.*L24.*L34+L22.*L13.*L44-L22.*L14.*L34-L13.*L24.^2+
    L24.*L14.*L23).*s.^2+(L13.*L22.*R4+L13.*R2.*L44-R2.*L14.*L34-L12.*L23.*R4).*s+
    L13.*R2.*R4).*s;
Den3=((-L11.*L22.*L33.*L44+L11.*L22.*L34.^2+L11.*L23.^2.*L44-2.*L11.*L23.*L24.*L34+
    L11.*L24.^2.*L33+L12.^2.*L33.*L44-L12.^2.*L34.^2-2.*L12.*L23.*L13.*L44+
    2.*L12.*L23.*L14.*L34+2.*L12.*L24.*L13.*L34-2.*L12.*L24.*L14.*L33+L22.*L13.^2.*L44-
    2.*L13.*L22.*L14.*L34-L13.^2.*L24.^2+2.*L13.*L24.*L14.*L23+L22.*L14.^2.*L33-
    L14.^2.*L23.^2).*s.^4+(-L44.*R3.*L11.*L22-L44.*R1.*L22.*L33-L44.*R2.*L11.*L33+
    L24.^2.*R3.*L11+L12.^2.*R4.*L33+L22.*R3.*L14.^2+L12.^2.*L44.*R3-2.*L13.*R2.*L14.*L34+
    L11.*L23.^2.*R4+L11.*L34.^2.*R2+L13.^2.*R2.*L44+R2.*L14.^2.*L33+L13.^2.*L22.*R4+
    L44.*R1.*L23.^2+L22.*R1.*L34.^2+R1.*L33.*L24.^2-2.*L13.*L12.*L23.*R4-
    2.*R1.*L23.*L24.*L34-R4.*L11.*L22.*L33-2.*R3.*L12.*L14.*L24).*s.^3+(R1.*R3.*L24.^2+
    R3.*L12.^2.*R4-L44.*R1.*R2.*L33-L22.*R3.*L11.*R4-R1.*L22.*L33.*R4+R2.*R3.*L14.^2-
    L44.*R1.*R3.*L22-R2.*L11.*L33.*R4-L44.*R2.*R3.*L11+R1.*L34.^2.*R2+L13.^2.*R2.*R4+
    R1.*L23.^2.*R4).*s.^2+(-R1.*R3.*L22.*R4-R1.*R2.*L33.*R4-R2.*R3.*L11.*R4-
    L44.*R1.*R3.*R2).*s-R1.*R3.*R2.*R4);
R3=R(3)
L33=Ls;

%Recompute inductances and resistances to include probe on alloy 800 target
L44=Ls+Lpb;
L12=K12*sqrt(L(1)*L(2));
L13=K13*sqrt(L(1)*L(3));
L14=K14*sqrt(L(1)*L(4));
L23=K23*sqrt(L(2)*L(3));
L24=K24*sqrt(L(2)*L(4));
L34=K34*sqrt(L(3)*L(4));
R4=R4+Rpb;
```

```
I4_num= ((L12.*L23.*L34-L12.*L24.*L33-L22.*L13.*L34+L22.*L14.*L33+L23.*L13.*L24-
L14.*L23.^2).*s.^2+(-L13.*L34.*R2+L22.*R3.*L14+L14.*L33.*R2-R3.*L12.*L24).*s+
R2.*R3.*L14).*s;
Den4=((-L11.*L22.*L33.*L44+L11.*L22.*L34.^2+L11.*L23.^2.*L44-2.*L11.*L23.*L24.*L34+
    L11.*L24.^2.*L33+L12.^2.*L33.*L44-L12.^2.*L34.^2-2.*L12.*L23.*L13.*L44+
    2.*L12.*L23.*L14.*L34+2.*L12.*L24.*L13.*L34-2.*L12.*L24.*L14.*L33+L22.*L13.^2.*L44-
    2.*L13.*L22.*L14.*L34-L13.^2.*L24.^2+2.*L13.*L24.*L14.*L23+L22.*L14.^2.*L33-
    L14.^2.*L23.^2).*s.^4+(-L44.*R3.*L11.*L22-L44.*R1.*L22.*L33-L44.*R2.*L11.*L33+
    L24.^2.*R3.*L11+L12.^2.*R4.*L33+L22.*R3.*L14.^2+L12.^2.*L44.*R3-2.*L13.*R2.*L14.*L34+
    L11.*L23.^2.*R4+L11.*L34.^2.*R2+L13.^2.*R2.*L44+R2.*L14.^2.*L33+L13.^2.*L22.*R4+
    L44.*R1.*L23.^2+L22.*R1.*L34.^2+R1.*L33.*L24.^2-2.*L13.*L12.*L23.*R4-
    2.*R1.*L23.*L24.*L34-R4.*L11.*L22.*L33-2.*R3.*L12.*L14.*L24).*s.^3+(R1.*R3.*L24.^2+
    R3.*L12.^2.*R4-L44.*R1.*R2.*L33-L22.*R3.*L11.*R4-R1.*L22.*L33.*R4+R2.*R3.*L14.^2-
    L44.*R1.*R3.*L22-R2.*L11.*L33.*R4-L44.*R2.*R3.*L11+R1.*L34.^2.*R2+L13.^2.*R2.*R4+
    R1.*L23.^2.*R4).*s.^2+(-R1.*R3.*L22.*R4-R1.*R2.*L33.*R4-R2.*R3.*L11.*R4-
    L44.*R1.*R3.*R2).*s-R1.*R3.*R2.*R4);
R4=R(4)
L44=Ls;

%Compute current magnitude from complex transfer function
I1=abs(I1_num./Den1);
I2=abs(I2_num./Den2);
I3=abs(I3_num./Den3);
I4=abs(I4_num./Den4);

%%%%%%%%%%%%%%%%%%%%%%%%%%%%%%%%%%%%%%%%%%%%%%%%%%%%%%%%%%%%%%%%%%%%%%%%%%%%%%%%%%%%%%%%%%%%%
%Plot results
%%%%%%%%%%%%%%%%%%%%%%%%%%%%%%%%%%%%%%%%%%%%%%%%%%%%%%%%%%%%%%%%%%%%%%%%%%%%%%%%%%%%%%%%%%%%%
%Check +/- 10% bounds
%I1=[.90*I1;  1.10*I1];
%I2=[.90*I2;  1.10*I2];
%I3=[.90*I3;  1.10*I3];
%I4=[.90*I4;  1.10*I4];

%Check +/- 5% bounds
%I1=[.95*I1;  1.05*I1];
%I2=[.95*I2;  1.05*I2];
%I3=[.95*I3;  1.05*I3];
%I4=[.95*I4;  1.05*I4];

figure(1)
loglog(f,Mag1','k-',F1,CuS./V3,'r.-',f0,I1,'bo');
legend('Circuit Model Prediction','Measured','Model with Correction for Probe Insertion
    Impedance',3)
hold on
loglog(f,Mag','k-',F1,CuS./V3,'r.-',F2,A90S./V3,'r.-',F3,A8S./V3,'r.-',F4,PI./V3,'r.-',
    f0,I2,'bo',f0,I3,'bo',f0,I4,'bo');
hold off
title('V_{in} to I_{n} Transfer Function for Three Wire Loops with Different
    Conductivities')
xlabel('Frequency(Hz)')
ylabel('Magnitude')
grid on
axis([1e3,.5e6,2e-3,2e0]);
```

Appendix C

Circuit Schematics, Layout and Parts

Circuit Schematics

Printed Circuit Board (PCB) Layout

Parts List

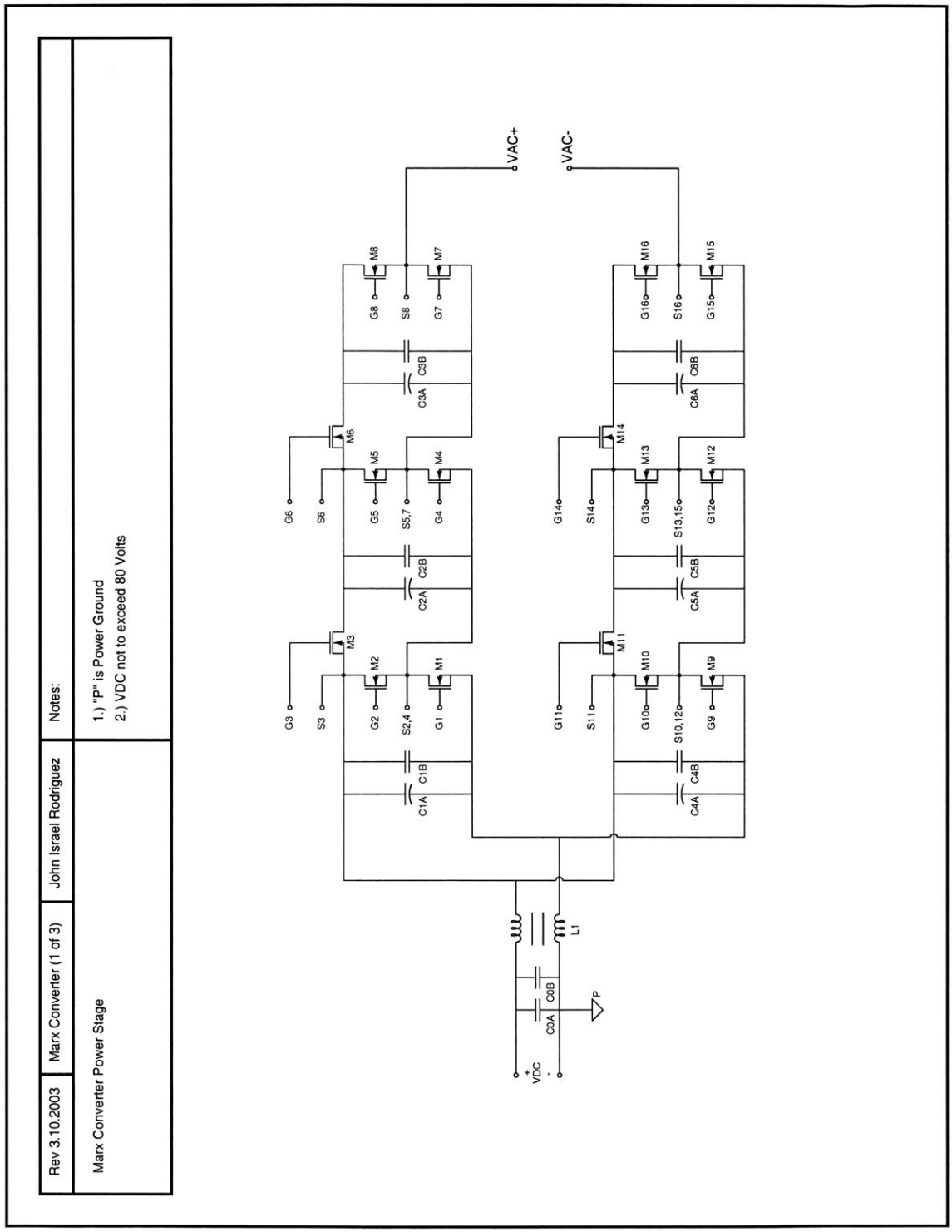

Figure C.1: Marx inverter power stage

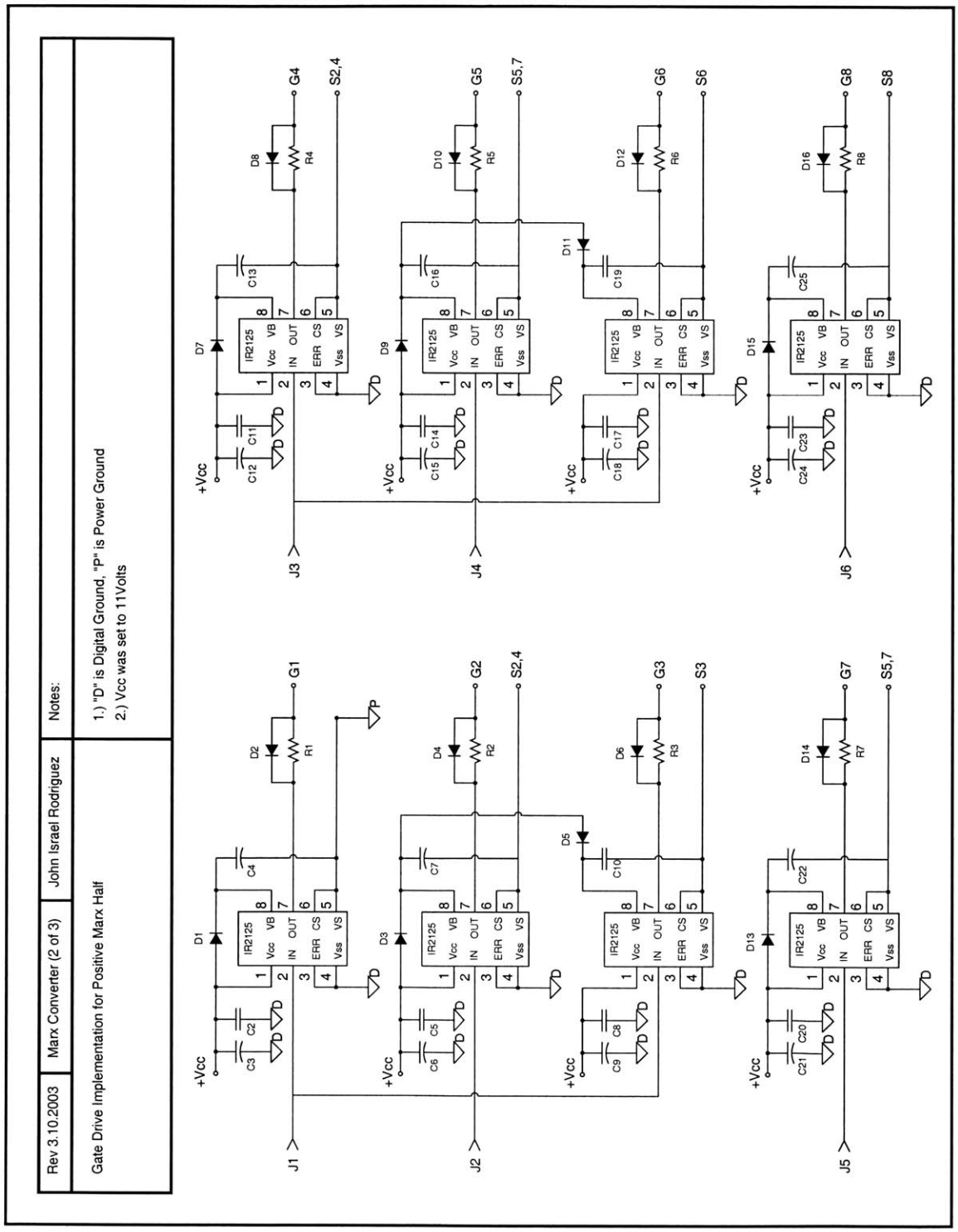

Figure C.2: Gate drives for positive Marx phase leg

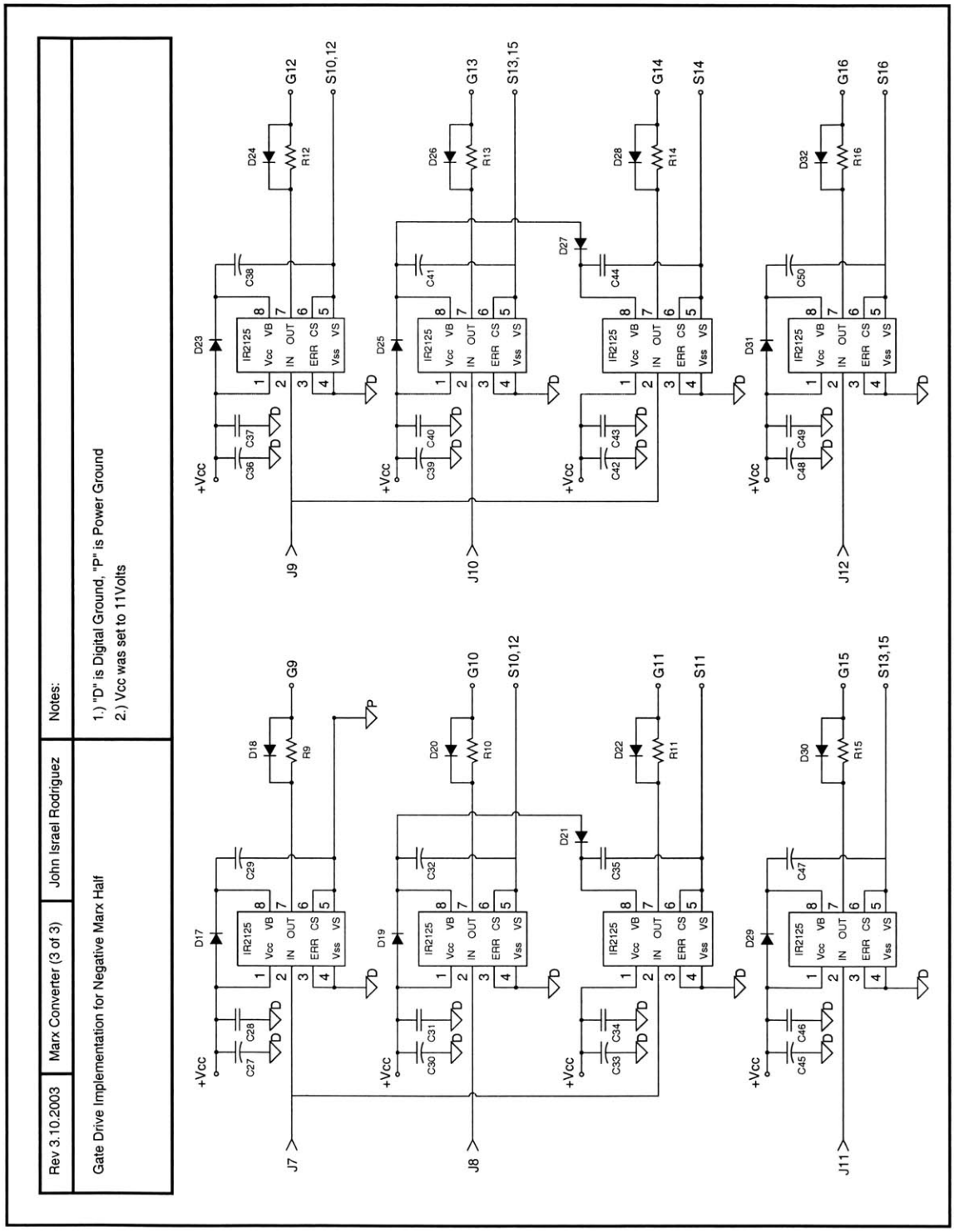

Figure C.3: Gate drives for negative Marx phase leg

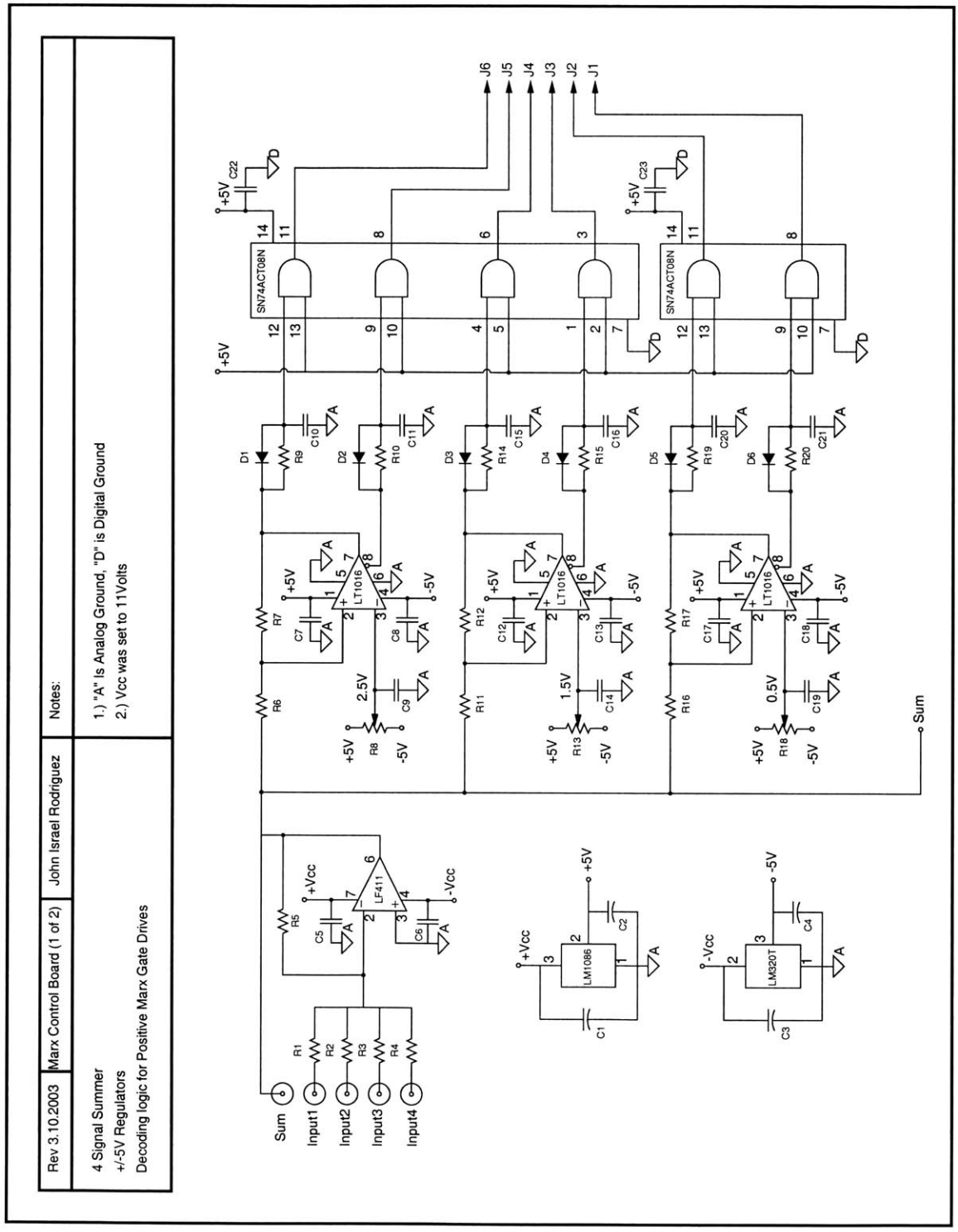

Figure C.4: Control for positive Marx phase leg gate drives

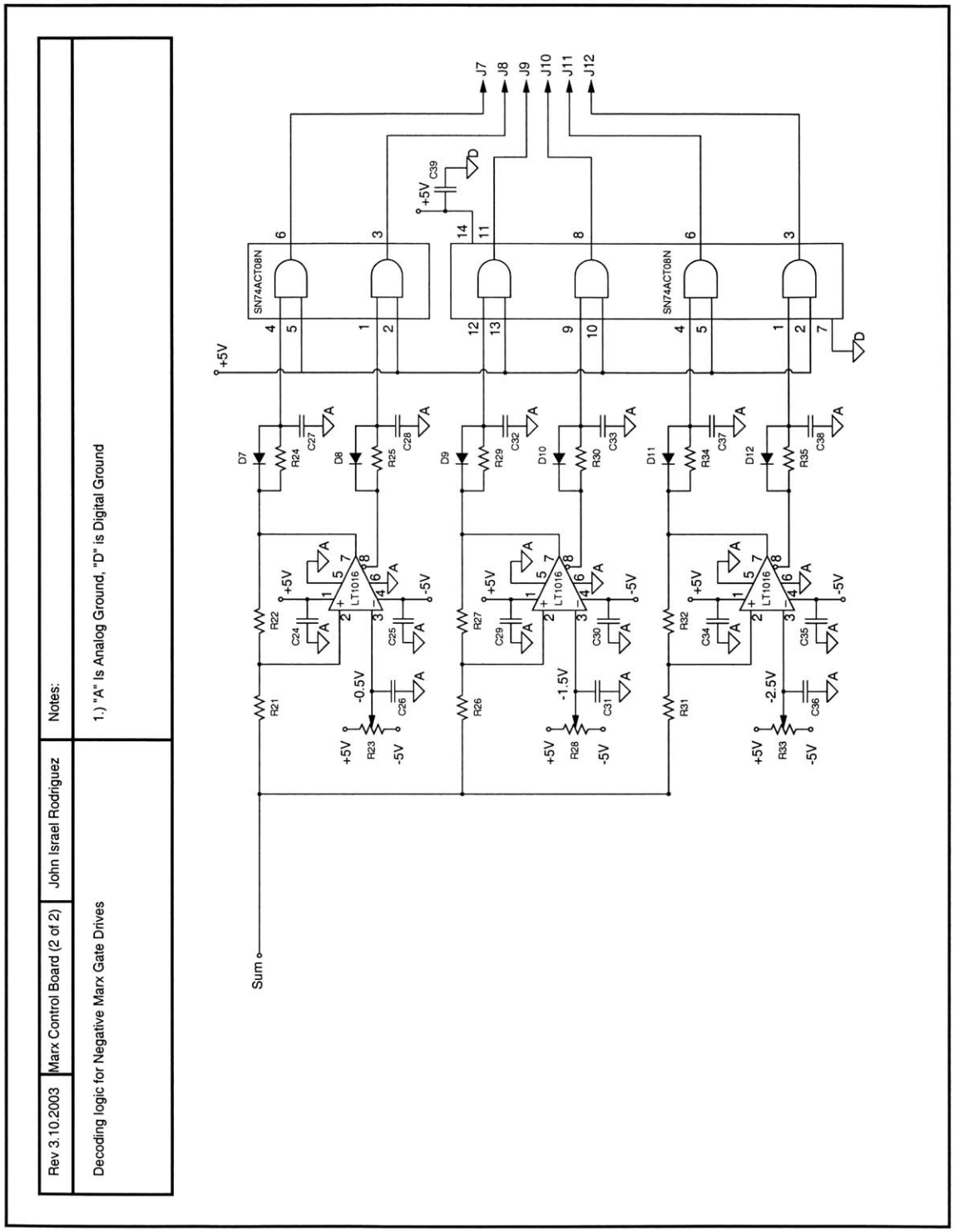

Figure C.5: Control for negative Marx phase leg gate drives

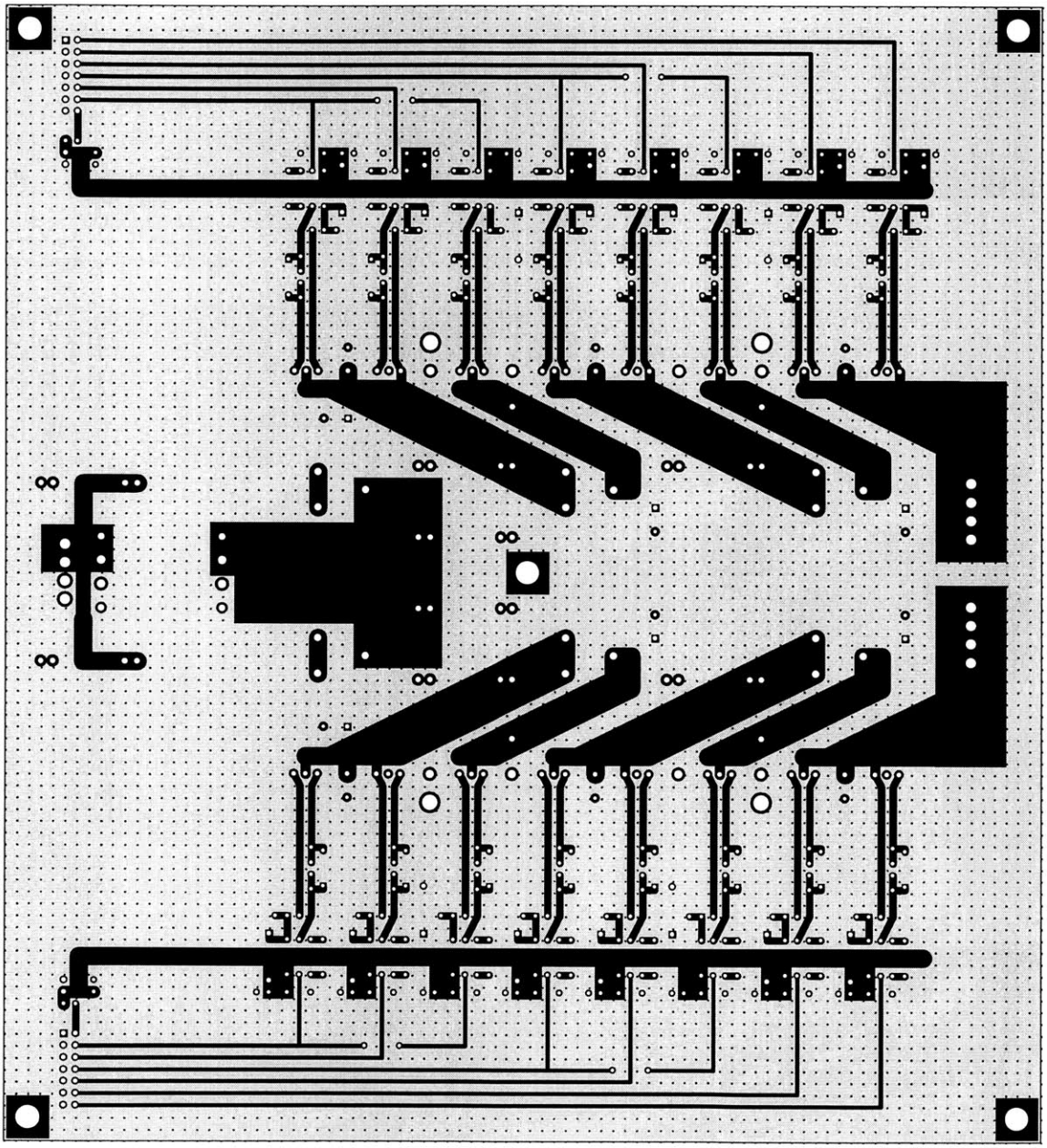

Figure C.6: Marx Converter PCB: Top layer of copper

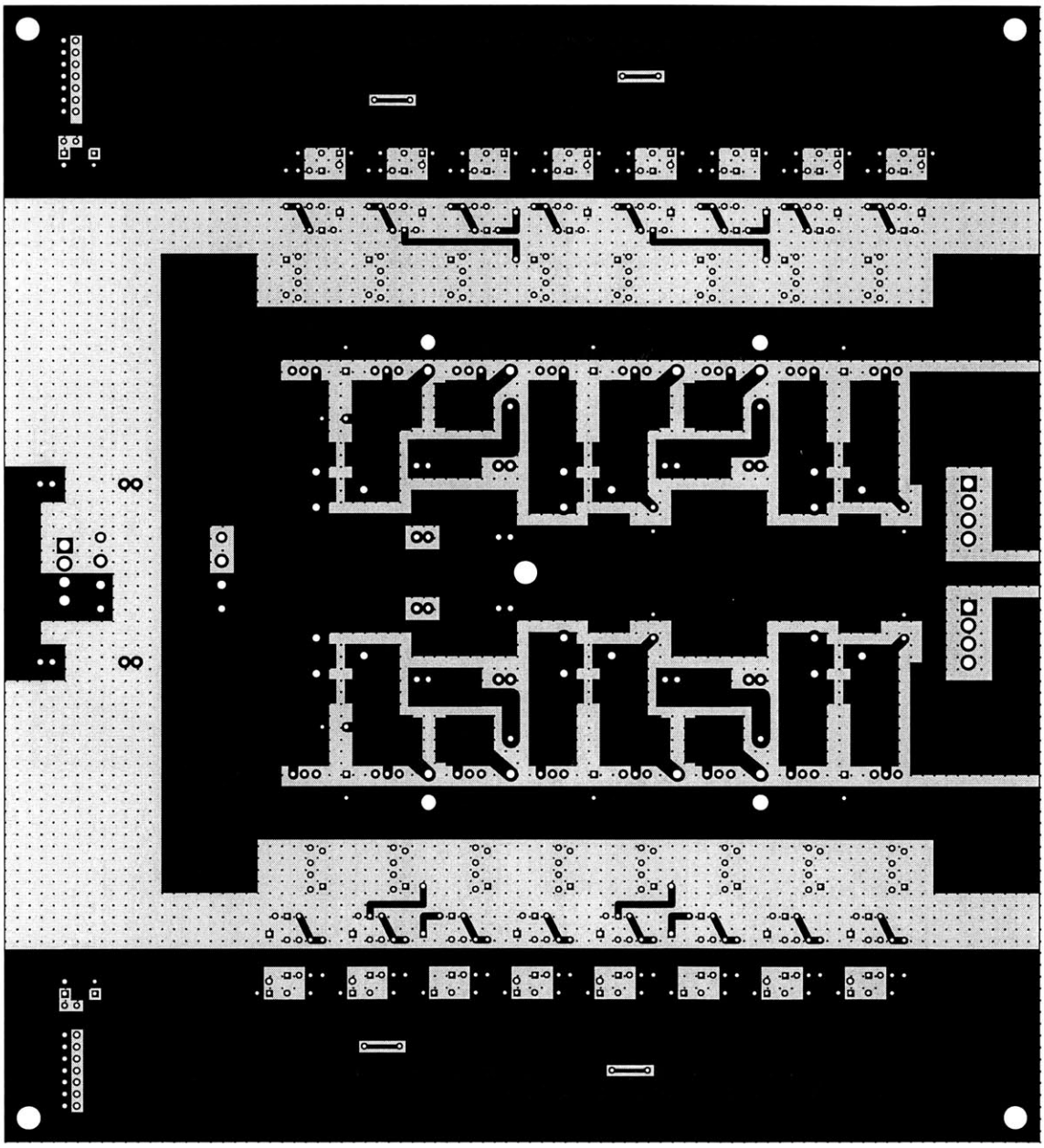

Figure C.7: Marx Converter PCB: Bottom layer of copper

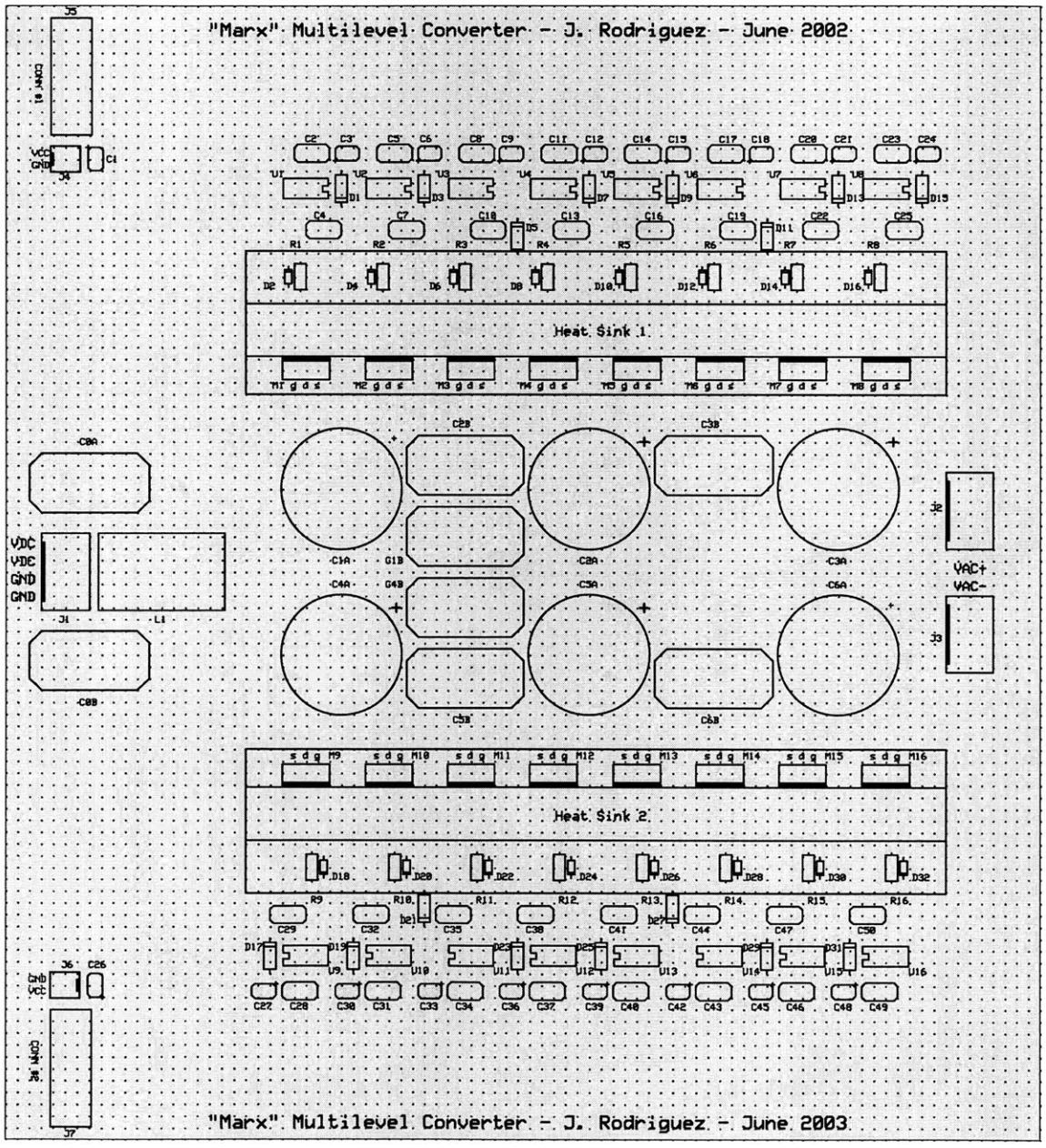

Figure C.8: Marx Converter PCB: Silkscreen

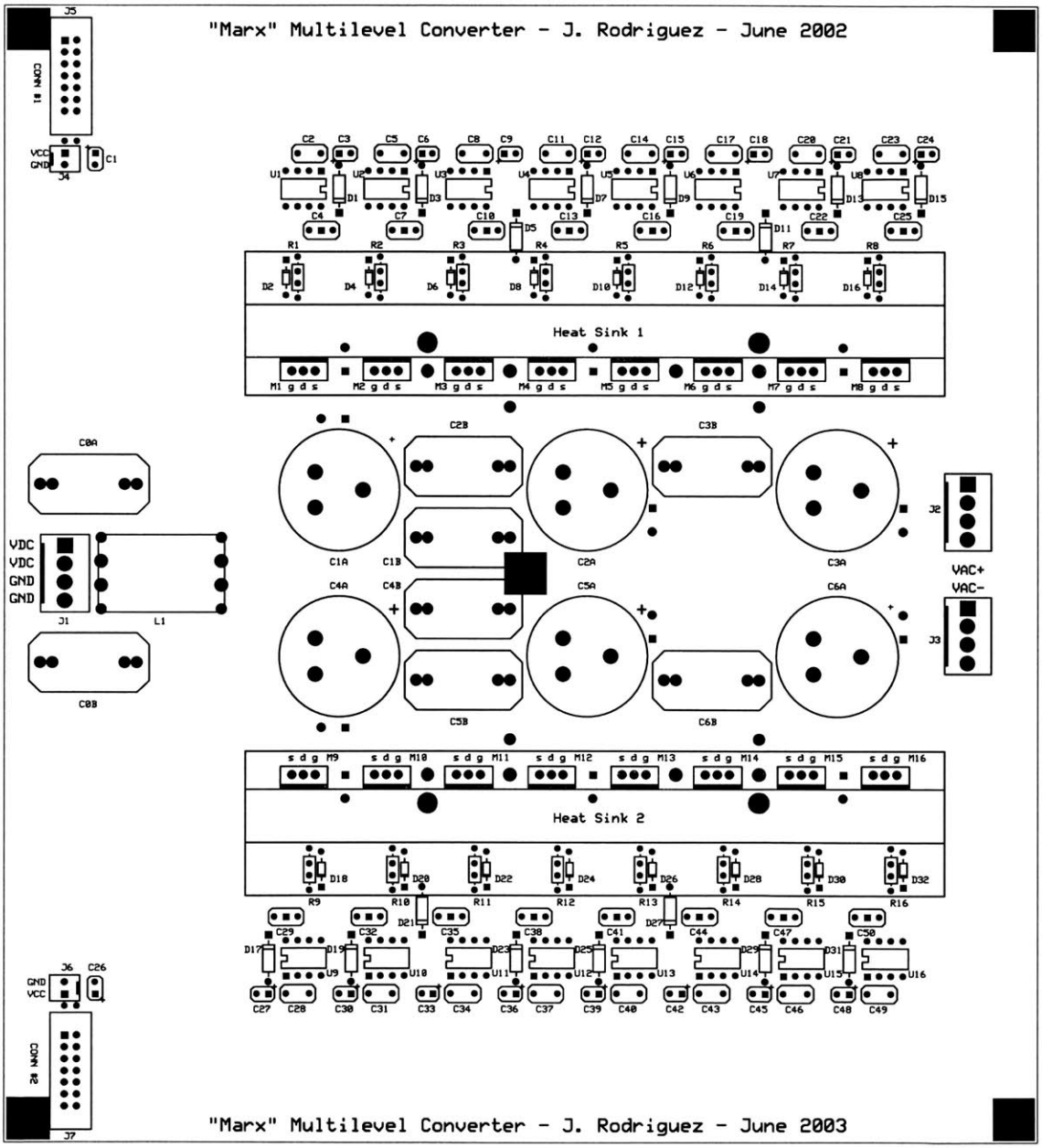

Figure C.9: Marx Converter PCB: Silkscreen with pads

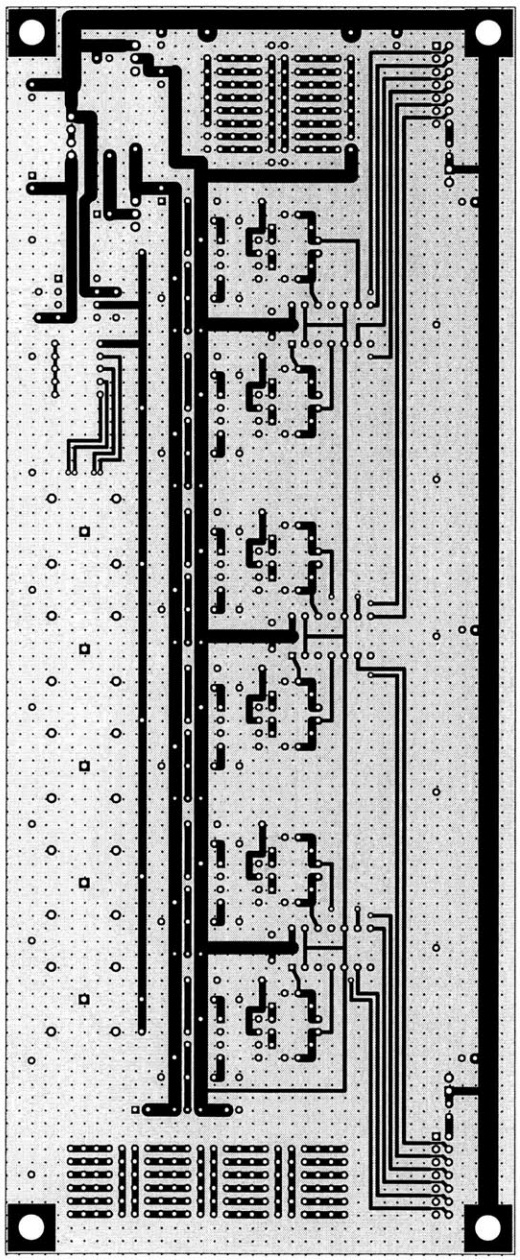

Figure C.10: Marx Control Board PCB: Top layer of copper

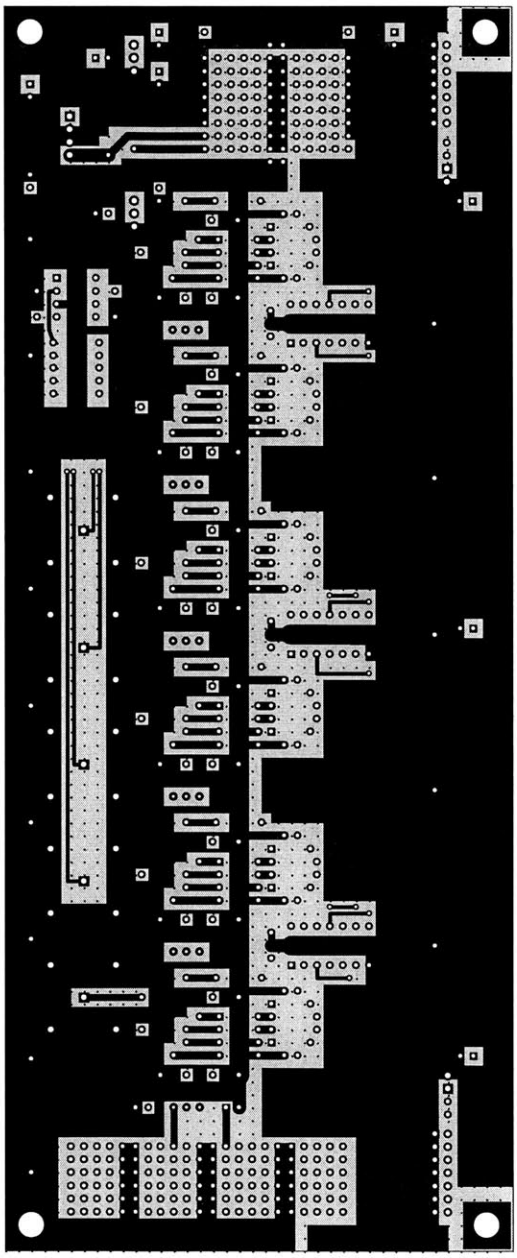

Figure C.11: Marx Control Board PCB: Bottom layer of copper

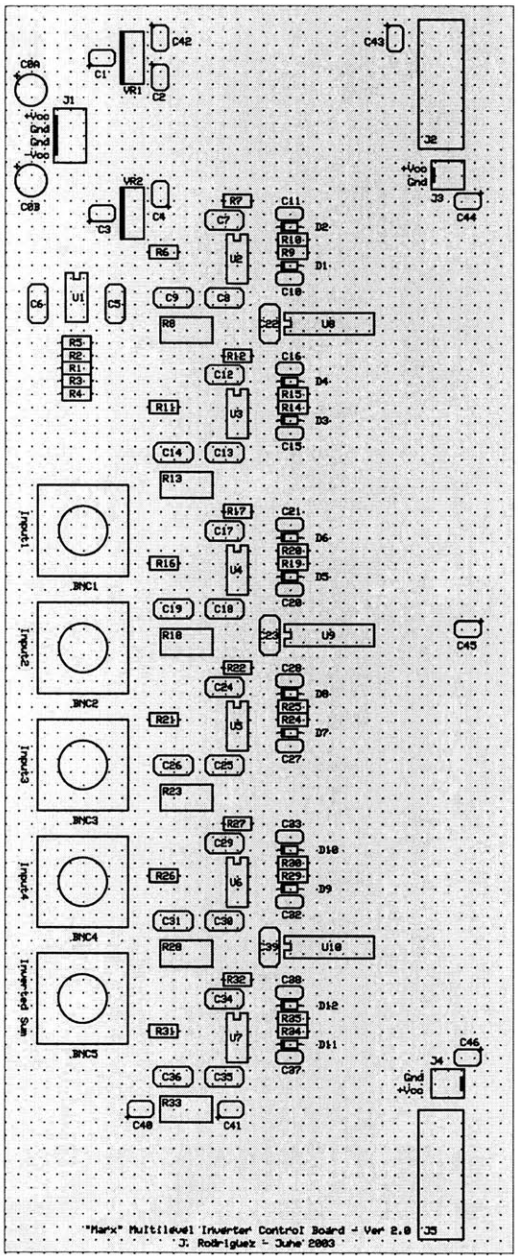

Figure C.12: Marx Control Board PCB: Silkscreen

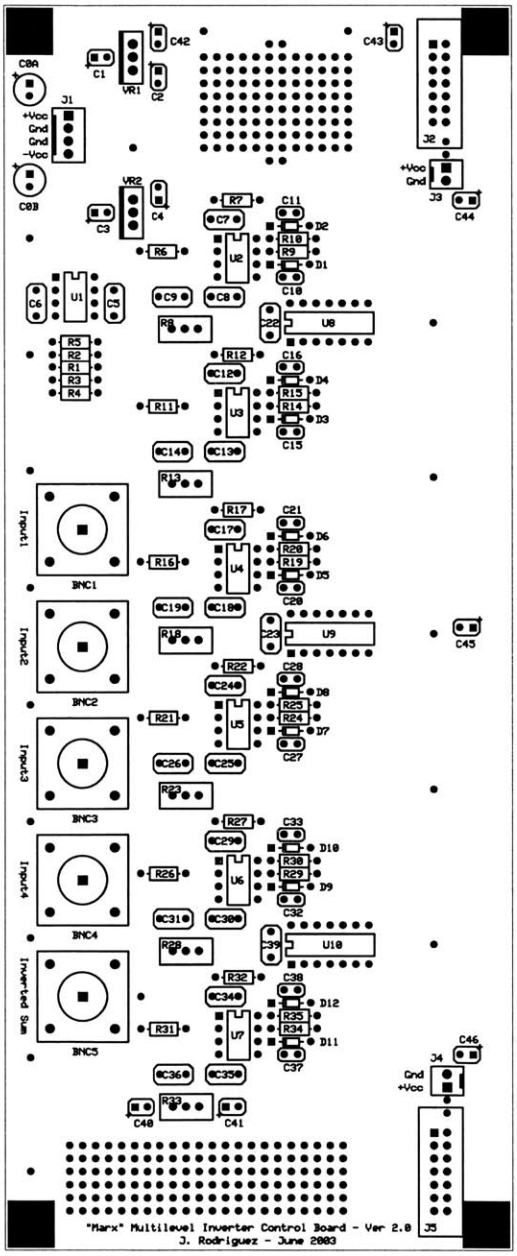

Figure C.13: Marx Control Board PCB: Silkscreen with pads

Marx Converter Board Components	Value	Notes
C_{1A}, C_{2A}, C_{3A}, C_{4A}, C_{5A}, C_{6A}	460 μF	Electrolytic (100V) Cornell Dublier 350JL461U100B
C_{0A}, C_{0B}, C_{1B}, C_{2B}, C_{3B}, C_{4B}, C_{5B}, C_{6B}	1 μF	Polypropylene (250 V)
C_1, C_3, C_6, C_9, C_{12}, C_{15}, C_{18}, C_{21}, C_{24}, C_{26}, C_{27}, C_{30}, C_{33}, C_{36}, C_{39}, C_{42}, C_{45}, C_{48}	10 μF	Tantalum (16 V)
C_4, C_7, C_{13}, C_{16}, C_{22}, C_{25}, C_{29}, C_{32}, C_{38}, C_{41}, C_{47}, C_{50}	1 μF	Tantalum (16 V)
C_2, C_5, C_8, C_{11}, C_{14}, C_{17}, C_{20}, C_{23}, C_{28}, C_{31}, C_{34}, C_{37}, C_{40}, C_{43}, C_{46}, C_{49}	0.47μF	Ceramic (50 V)
C_{10}, C_{19}, C_{35}, C_{44}	0.1 μF	Ceramic (50 V)
D_1, D_3, D_5, D_7, D_9, D_{11}, D_{13}, D_{15}, D_{17}, D_{19}, D_{21}, D_{23}, D_{25}, D_{27}, D_{29}, D_{31}		HER105CT, 1 A, 400V, DO-41
D_2, D_4, D_6, D_8, D_{10}, D_{12}, D_{14}, D_{16}, D_{18}, D_{20}, D_{22}, D_{24}, D_{26}, D_{28}, D_{30}, D_{32}		1N4148, 75 V, 500 mW, DO-35
Heat Sinks 1 and 2		KM150-1 Thermalloy, discontinued
J_1, J_2, J_3		Molex, 0.156in, 4-pin, straight
J_4, J_6		Molex, 0.1in, 2-pin, straight
J_5, J_7		Ribbon cable header, 14-pin
L_1	250 μH	Common Mode Choke CM1011-254
M_1, M_2, M_3, M_4, M_5, M_6, M_7, M_8 M_9, M_{10}, M_{11}, M_{12}, M_{13}, M_{14}, M_{15}, M_{16}		IRFB59N10D, V_{dss}=100 V, $R_{ds,on}$=25m Ω, T0-220
R_1, R_2, R_3, R_4, R_5, R_6, R_7, R_8, R_9, R_{10}, R_{11}, R_{12}, R_{13}, R_{14}, R_{15}, R_{16}	10 Ω	Carbon Film
U_1, U_2, U_3, U_4, U_5, U_6, U_7, U_8, U_9, U_{10}, U_{11}, U_{12}, U_{13}, U_{14}, U_{15}, U_{16}		IR2125, 8-pin DIP

Control Board Components	Value	Notes
BNC_1, BNC_2, BNC_3, BNC_4, BNC_5		50 Ω BNC connector
C_{0A}, C_{0B},	100 μF	Electrolytic (25 V)
C_1, C_2, C_3, C_4, C_{40}, C_{41}, C_{42}, C_{43}, C_{44}, C_{45}, C_{46}	10 μF	Tantalum (16 V)
C_5, C_6, C_7, C_8, C_9, C_{12}, C_{13}, C_{14}, C_{17}, C_{18}, C_{19}, C_{22}, C_{23}, C_{24}, C_{25}, C_{26}, C_{29}, C_{30}, C_{31},C_{34}, C_{35}, C_{36}, C_{39}	0.1 μF	Ceramic (50 V)
C_{10}, C_{11}, C_{15}, C_{16}, C_{20}, C_{21}, C_{27}, C_{28}, C_{32}, C_{33}, C_{37}, C_{38}	100 pF	Ceramic G0G (50 V)
D_1, D_2, D_3, D_4, D_5, D_6, D_7, D_8, D_9, D_{10}, D_{11}, D_{12}		1N4148, 75 V, 500 mW, DO-35
J_1		Molex, 0.1in, 4-pin, straight
J_2, J_5		Ribbon cable header, 14-pin
J_3, J_4		Molex, 0.1in, 2-pin, straight
R_1, R_2, R_3, R_4, R_5	1 kΩ	Carbon Film
R_6, R_{11}, R_{16}, R_{21}, R_{26}, R_{31}	27 Ω	Carbon Film
R_7, R_{12}, R_{17}, R_{22}, R_{27}, R_{32}	27 kΩ	Carbon Film
R_8, R_{13}, R_{18}, R_{23}, R_{28}, R_{33}	10 kΩ	Potentiometer
R_9, R_{10}, R_{14}, R_{15}, R_{19}, R_{20}, R_{24}, R_{25}, R_{29}, R_{30}, R_{34}, R_{35},	7.3 kΩ	Carbon Film
U_1		LF411, Op-Amp, 8-pin DIP
U_2, U_3, U_4, U_5, U_6, U_7		LT1016, Fast Comparator, 8-pin DIP
U_8, U_9, U_{10}		SN74ACT08N, 2-Input-And-Gates, 14-pin DIP
VR_1		LM1086, +5 V Regulator
VR_1		LM1086, -5 V Regulator

Bibliography

[1] "Data sheet: Adxl202/adxl210," Analog Devices, One Technology Way, P.O.Box 9106, Norwood, MA 02062-9106, U.S.A., 1999. [Online]. Available: http://www.analog.com/UploadedFiles/Data_Sheets/70885338ADXL202_10_b.pdf

[2] L. Bromberg, "Personal correspondence," June 2003.

[3] A. D. Dimarogonas and A. Kollias, "A "smart" electrorheological fluid dynamic vibration absorber," in *Intelligent Structures, Materials, and Vibration*, vol. 58. ASME Design Engineering Division, Sept. 1993, pp. 7–15.

[4] R. C. Dorf, Ed., *The Electrical Engineering Handbook.* Boca Raton: CRC, Press, 1993.

[5] "Fastmodel," Fast Field Solvers, Mar. 2001. [Online]. Available: http://www.fastfieldsolvers.com/main.htm

[6] F. Forest, E. Laboure, F. Costa, and J. Y. Gaspard, "Principle of a multi-load/single converter system for low power induction heating," *IEEE Transactions on Power Electronics*, vol. 15, no. 2, pp. 223–230, Mar. 2000.

[7] H. Frahm, "Device for damping vibration of bodies," U.S. Patent 989 958, 1911.

[8] T. Fujinami, S. Yamamoto, and A. Sone, "Dynamic absorber using lever and pendulum mechanism for vibration control of structure (the method of deciding parameters for the system)," *Transactions of the Japan Society of Mechanical Engineers, Part C*, vol. 57, pp. 3490–3496, 1991.

[9] C. Girardi, "coilgen.c," 2002. [Online]. Available: http://www.qsl.net/in3otd/programs.html

[10] F. W. Grover, *Inductance Calculations: Working Formulas and Tables.* New York: Dover Publications, Inc., 1946.

[11] C. M. Harris and C. E. Crede, *Shock and Vibration Handbook.* New York: McGraw-Hill, 1961.

[12] J. P. D. Hartog, *Mechanical Vibrations.* New York: McGraw-Hill, 1956.

[13] H. A. Haus and J. R. Melcher, *Electromagnetic Fields and Energy.* Prentice-Hall, 1989.

[14] R. He, "Power dissipation in untuned targets as a function of frequency," Massachusetts Institute of Technology, Cambridge, MA, Advanced Undergraduate Project, Dec. 2002.

[15] D. G. Holmes, "A general analytical method for determining the theoretical harmonic components of carrier based pwm strategies," in *Thirty-Third IAS Annual Meeting*, vol. 2, Oct. 1998, pp. 1207–1214.

[16] D. Jackson, "Inductively coupled power transfer for electromechanical systems," Ph.D. dissertation, Massachusetts Institute of Technology, Cambridge, MA, May 1998.

[17] D. K. Jackson, S. B. Leeb, A. H. Mitwalli, P. Narvaez, D. Fusco, and E. C. L. Jr., "Power electronic drives for magnetically trigger gels," *IEEE Transactions on Industrial Electronics*, vol. 44, no. 2, pp. 217–225, Apr. 1997.

[18] M. Kamon, M. J. Ttsuk, and J. K. White, "Fasthenry:a multipole-accelerated 3-d inductance extraction program," *IEEE Transactions on Microwave Theory and Techniques*, vol. 42, pp. 1750–1758, Sept. 1994.

[19] K. B. Kim, E. Levi, Z. Zabar, and L. Birenbaum, "Mutual inductance of noncoaxial circular coils with constant current density," *IEEE Transactions on Magnetics*, vol. 33, pp. 4303–4309, Sept. 1997.

[20] I. Kimura and T. Katsuki, "Vlf induction heating for clinical hyperthermia," *IEEE Transactions on Magnetics*, vol. 22, no. 6, pp. 1897–1900, Nov. 1986.

[21] H. Kobayashi and S. Aida, "Development of a houde damper using magnetic damping," in *Vibration Isolation, Acoustics, and Damping in Mechanical Systems*, vol. 62. ASME Design Engineering Division, Sept. 1993, pp. 25–29.

[22] J. Lai and F. Z. Peng, "Multilevel converters– a new breed of power converters," *IEEE Transactions on Industrial Applications*, vol. 32, no. 3, pp. 509–517, May/Jun 1996.

[23] A. Matloubieh, R. Roemer, and T. Cetas, "Numerical simulation of magnetic induction heating of tumors with ferromagnetic seed implants," *IEEE Transactions on Biomedical Engineering*, vol. BME31, pp. 227–234, Feb. 1984.

[24] H. Matsuki, K. Murakami, T. Satoh, and T. Hoshino, "An optimum design of a soft heating system for local hyperthermia," *IEEE Transactions on Magnetics*, vol. 23, no. 5, pp. 2440–2442, Sept. 1987.

[25] H. Matsuki, T. Satoh, K. Murakami, T. Hoshino, T. Yanada, and S. Kikuchi, "Local hyperthermia based on soft heating method utilizing temperature-sensitive ferrite rod," *IEEE Transactions on Magnetics*, vol. 26, no. 5, pp. 1551–1553, Sept. 1990.

[26] A. H. Mitwalli, "Polymer gel actuators and sensors," Ph.D. dissertation, Massachusetts Institute of Technology, Cambridge, MA, May 1998.

[27] N. Mohan, T. Undeland, and W. Robins, *Power Electronics Converter, Applications, and Design*. Wiley, 1995.

[28] A. Nabae, I. Takahashi, and H. Akagi, "A new neutral-point-clamped inverter," *IEEE Transactions on Industrial Applications*, vol. 17, no. 5, pp. 518–523, September/October 1981.

[29] Y. Okada, K. Matsuda, and H. Hashitani, "Self-sensing active vibration control using the moving-coil-type actuator," *Journal of Vibrations and Acoustics*, vol. 117, pp. 411–415, Oct. 1995.

[30] Y. Okada and R. Okashita, "Adaptive control of an active mass damper to reduce structural vibration," *JSME International Journal, series 3: Vibration, Control Engineering, Engineering for Industry*, vol. 33, pp. 435–440, 1990.

[31] C. Pascual and P. T. Krein, "Switched capacitor system for automatic series battery equalization," in *Applied Power Electronics Conference Proceedings*, vol. 2, Feb. 1997, pp. 848–854.

[32] F. Z. Peng, "A generalized multilevel inverter topology with self voltage balancing," *IEEE Transactions on Industrial Applications*, vol. 37, no. 2, pp. 611–618, March/May 2001.

[33] D. Perreault, "Personal correspondence concerning the $r_{ds,in}$ of mosfets versus v_{dss}," MIT, Laboratory for Electromagnetic and Electronic Systems, June 2003.

[34] J. Rodriguez, J. S. Lai, and F. Z. Peng, "Multilevel inverters: A survey of topologies, controls, and applications," *IEEE Transactions on Industrial Electronics*, vol. 49, pp. 724–738, Aug. 2002.

[35] J. Rodriguez, L. Moran, P. Correa, and C. Silva, "A vector control technique for medium-voltage multilevel inverters," *IEEE Transactions on Industrial Electronics*, vol. 49, pp. 882–888, Aug. 2002.

[36] J. I. Rodriguez, R. He, and S. Leeb, "Frequency selectable induction heating targets," in *The 34th IEEE Power Electronics Specialists Conference*, June 2003, pp. 1943–1950.

[37] J. I. Rodriguez and S. Leeb, "A multilevel inverter topology for inductively coupled power transfer," in *Applied Power Electronics Conference Proceedings*, Feb. 2003, pp. 1118–1126.

[38] "Marx generator," RPI Plasma Dynamics Laboratory. [Online]. Available: http://hibp.ecse.rpi.edu/~leij/febetron/marx.html

[39] E. Scholtz, "Personal correspondence," MIT, Laboratory for Electromagnetic and Electronic Systems, May 2003.

[40] S. Sirisukprasert, J. S. Lai, and T. H. Liu, "Optimum harmonic reduction with a wide range of modulation indexes for multilevel converters," *IEEE Transactions on Industrial Electronics*, vol. 49, pp. 875–881, Aug. 2002.

[41] P. Stauffer, T. Cetas, A. Fletcher, D. DeYoung, M. Dewhirst, J. Oleson, and R. Roemer, "Observations on the user of ferromagnetic implants for inducing hyperthermia," *IEEE Transactions on Biomedical Engineering*, vol. BME31, pp. 76–90, Feb. 1984.

[42] P. Stauffer, T. Cetas, and R. Jones, "Magnetic induction heating of ferromagnetic implants for inducing localized hyperthermia in deep-seated tumors," *IEEE Transactions on Biomedical Engineering*, vol. BME31, pp. 235–251, Feb. 1984.

[43] J. Sun, M. R. Jolly, and M. A. Norris, "Passive, adaptive and active tuned vibration absorbers– a survey," *Transactions of the ASME*, vol. 117, pp. 234–242, June 1995.

[44] S. Takeuchi, N. Futai, and I. Shimoyama, "Selective drive of electrostatic acutators using remote inductive powering," in *The 14th IEEE Conference on Micro Electro Mechanical Systems*, Jan. 2001, pp. 574–577.

[45] Y. Takita and K. Seto, "An investigation of adjustable pendulum-type vibration controlling equipment (semi-active vibration control by application of an anti-resonance point," in *Current topics in structural mechanics, 1989*, vol. 117. Pressure Vessels and Piping Division, July 1989, pp. 109–115.

[46] T. Tanaka, "Gels," *Scientific American*, vol. 244, no. 1, pp. 124–138, Jan. 1981.

[47] L. B. Tentor, "Characterization of an electromagnetic tuned vibration absorber," Ph.D. dissertation, Virginia Polytechnic Institute and State University, Blacksburg, Virginia, Aug. 2001.

[48] C. Ting-Kong, "Design of an adaptive dynamic vibration absorber," Master's thesis, The University of Adelaide, South Australia 5005, Apr. 1999.

[49] D. T. Tompkins, R. V. Vanderby, S. A. Klein, W. A. Beckman, R. A. Steeves, and B. R. Paliwal, "Effect of interseed spacing, tissues perfusion, thermoseed temperatures and catheters in ferromagnetic hyperthermia: Results from simulations using finite element models of thermoseeds and catheters," *IEEE Transactions on Biomedical Engineering*, vol. 41, no. 10, pp. 975–985, Oct. 1994.

[50] H. Yamaura, K. Ono, and K. Toyota, "Optimal tuning method for swing reduction of gondola lift by an inclined pendulum-type dynamic vibration absorber," *Transactions of the Japan Society of Mechanical Engineers, Part C*, vol. 59, pp. 3071–3077, 1993.